Advances in Polymer Science 255

Martin Müller *Editor*

# Polyelectrolyte Complexes in the Dispersed and Solid State I

## Principles and Theory

Springer

# 255
# Advances in Polymer Science



For further volumes:
http://www.springer.com/series/12

## Aims and Scope

The series Advances in Polymer Science presents critical reviews of the present and future trends in polymer and biopolymer science. It covers all areas of research in polymer and biopolymer science including chemistry, physical chemistry, physics, material science.

The thematic volumes are addressed to scientists, whether at universities or in industry, who wish to keep abreast of the important advances in the covered topics.

Advances in Polymer Science enjoys a longstanding tradition and good reputation in its community. Each volume is dedicated to a current topic, and each review critically surveys one aspect of that topic, to place it within the context of the volume. The volumes typically summarize the significant developments of the last 5 to 10 years and discuss them critically, presenting selected examples, explaining and illustrating the important principles, and bringing together many important references of primary literature. On that basis, future research directions in the area can be discussed. Advances in Polymer Science volumes thus are important references for every polymer scientist, as well as for other scientists interested in polymer science - as an introduction to a neighboring field, or as a compilation of detailed information for the specialist.

Review articles for the individual volumes are invited by the volume editors. Single contributions can be specially commissioned.

Readership: Polymer scientists, or scientists in related fields interested in polymer and biopolymer science, at universities or in industry, graduate students.

Special offer:
For all clients with a standing order we offer the electronic form of Advances in Polymer Science free of charge.

Martin Müller
Editor

# Polyelectrolyte Complexes in the Dispersed and Solid State I

## Principles and Theory

With contributions by

A.G. Cherstvy · M.A. Cohen Stuart · C. Cramer · N.I. Lebovka · S. Lindhoud · A.H.E. Müller · D.V. Pergushov · M. Schönhoff · R.G. Winkler · A.A. Zezin · A.B. Zezin

Springer

*Editor*
Martin Müller
Leibniz Institute of Polymer Research Dresden
Department of Polyelectrolytes and Dispersions
Hohe Straße 6
D-01069 Dresden
Germany

ISSN 0065-3195 ISSN 1436-5030 (electronic)
ISBN 978-3-642-40733-8 ISBN 978-3-642-40734-5 (eBook)
DOI 10.1007/978-3-642-40734-5
Springer Heidelberg New York Dordrecht London

# Preface

Nearly one decade ago, a two volume edition "Polyelectrolytes with Defined Molecular Architecture" edited by M. Schmidt appeared in the series *Advances in Polymer Science* and summarized progress in the field at that date. Within the total of 11 chapters, one was dedicated to polyelectrolyte complexes, which addressed interpolyelectrolyte and polyelectrolyte/surfactant complexes as well as theoretical aspects of polyelectrolyte (PEL) complexation.

This new two-volume edition "Polyelectrolyte Complexes in the Dispersed and Solid State: Principles and Applications" is intended to extend the content of this former chapter by bringing together selected state-of-the-art contributions on principles and theory (Volume I) as well as on current application aspects (Volume II) of polyelectrolyte complex (PEC)-based particles and soft matter. In Volume I, progress and new knowledge on theoretical aspects of electrosorption phenomena between PEL and oppositely charged surfaces (A.G. Cherstvy and R.G.Winkler) and of the practically always apparent aggregation and clustering tendency of PEC particles (N.I. Lebovka) are reviewed. Recently identified important dynamic aspects of ion conductivity (C. Cramer and M. Schönhoff) within PEC soft matter and relaxation phenomena within PEL/protein PEC particles (S. Lindhoud and M.A. Cohen-Stuart) as well as structural aspects of interpolyelectrolyte complexes of novel synthetic polyionic species with nonlinear topology and polymer–inorganic hybrids (D.V. Pergushov, A.A. Zezin, A.B. Zezin, A.H.E. Müller) are reviewed. In Volume II, prominent recent applications of PEC particles are reviewed together with an outline of relevant key properties concerning colloidal stability, size, shape, compactness, surface, and biointeraction. The use and tailoring of PEC particle-modified relevant surfaces for paper making (C. Ankerfors and L. Wagberg), solid–liquid separation and water treatment (G. Petzold and S. Schwarz) are addressed. The last three contributions review PEC applications in the life sciences, including the role of PEL/protein complex assemblies in food (S. Bouhallab and

T. Croguennec), the use of DNA/polycation complexes for gene delivery and protection (A. Bertin), and the potential of sizable and shapable nanosized PEC particles in pharmaceutical applications such as controlled drug release (M. Müller).

Dresden, Germany Martin Müller

# Contents

Adv Polym Sci (2014) 255: 1–56
DOI: 10.1007/12_2012_183

Published online: 15 March 2013

# Strong and Weak Polyelectrolyte Adsorption onto Oppositely Charged Curved Surfaces

**Roland G. Winkler and Andrey G. Cherstvy**

**Abstract** Polyelectrolytes are macromolecules composed of charged monomers and exhibit unique properties due to the interplay of their flexibility and electrostatic interactions. In solution, they are attracted to oppositely charged surfaces and interfaces and exhibit a transition to an adsorbed state when certain conditions are met concerning the charge densities of the polymer and surface and the properties of the solution. In this review, we discuss two limiting cases for adsorption of flexible polyelectrolytes on curved surfaces: weak and strong adsorption. In the first case, adsorption is strongly influenced by the entropic degrees of freedom of a flexible polyelectrolyte. By contrast, in the strong adsorption limit, electrostatic interactions dominate, which leads to particular adsorption patterns, specifically on spherical surfaces. We discuss the corresponding theoretical approaches, applying a mean-field description for the polymer and the polymer–surface interaction. For weak adsorption, we discuss the critical adsorption behavior by exactly solvable models for planar and spherical geometries and a generic approximation scheme, which is additionally applied to cylindrical surfaces. For strong adsorption, we investigate various polyelectrolyte patterns on cylinders and spheres and evaluate their stability. The results are discussed in the light of experimental results, mostly of DNA adsorption experiments.

## Contents



R.G. Winkler (✉)
Theoretical Soft Matter and Biophysics, Institute for Advanced Simulation, Forschungszentrum Jülich, 52425 Jülich, Germany
e-mail: r.winkler@fzjuelich.de

A.G. Cherstvy (✉)
Institute for Physics and Astronomy, University of Potsdam, 14476 Potsdam, Germany
e-mail: a.cherstvy@gmail.com

## 1 Introduction

Adsorption of charged macromolecules, and polyelectrolytes in particular, onto charged surfaces is of paramount importance in a wide range of technological applications [1, 2], such as surface coating [3], colloid stabilization [4], and paper making [5–7] and for a variety of biological systems [8–12]. Because of their charges, most charged polymers are water-soluble, which makes them interesting candidates for water-based, environmentally friendly technology. This aspect is even more important for a number of biological systems. Here, examples include wrapping of double-stranded DNA in nucleosomes [13–20], adsorption of single-stranded RNA onto the interior of viral capsides [21–29], and polyelectrolyte multilayered vesicles [30, 31]. Correspondingly, polyelectrolyte adsorption has received substantial attention for many decades. There are several valuable books and review articles on the subject [8, 9, 32–34]. However, electrostatically driven polymer adsorption shows a broad range of facets, not all of which have been addressed adequately in the literature.

A fundamental step in polyelectrolyte adsorption is the transition from a free state in solution to a bound polymer on an interface. Figure 1 illustrates such a transition for the adsorption of a polyelectrolyte onto spherical colloidal particles [35]. In the unbound state, the polymer chain explores the entropic degrees of freedom, whereas in the bound state the attractive polymer–surface electrostatic interactions dominate [8, 33, 36–39]. These two antagonistic trends dictate the properties of adsorption. Theoretical studies of the adsorption behavior of polyelectrolytes onto planar and curved surfaces suggest a phase-transition-like behavior, i.e., a bound polymer state appears at certain critical conditions, which depend upon, e.g., the temperature, the charge density and curvature of the surface, the polyelectrolyte linear charge density and its mechanical persistence [40–44]. An important aspect of this review is to discuss recent advances on this issue.

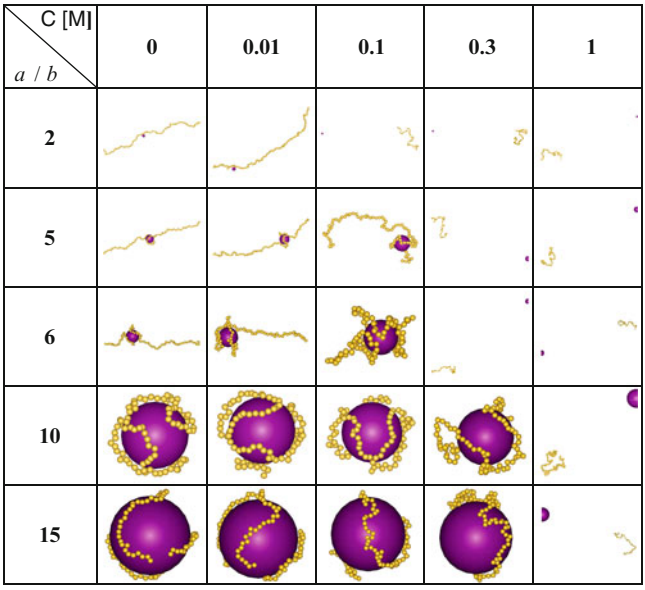


**Fig. 1** Adsorption of a polyelectrolyte chain onto spherical colloidal particles for various salt concentrations $C$ (from [35]). The ratio $a/b$ between the colloid radius $a$ and monomer bond length $b$ increases from top to bottom. The colloid surface charge density is constant, hence, the colloidal charge increases with $a$. The adsorption threshold depends on the salt concentration and the size ratio. More details of the underlying Monte Carlo simulations are provided in Ref. [35]

The formation of thermodynamically stable charged complexes is determined by a large number of parameters, the most important of which are the length of the polymer, its linear charge distribution and persistence length, the size, charge and curvature of the complexing object, and the salt concentration. This renders the development of a comprehensive theory difficult. Moreover, the long-range character of electrostatic interactions poses an extra challenge and exact analytical results are the exception rather than the rule. This explains why the understanding of charged complexes is still in an unsatisfactory state despite significant efforts and progress in recent years.

During the last decade, a wealth of theoretical results have been presented on weak polyelectrolyte adsorption onto oppositely charged planar and curved surfaces (see, e.g., [45–54] for the latest results). The spectrum of applied methods is wide and is often dictated by the particular aspect that the authors are addressing. In terms of critical adsorption, one of the first fundamental exact analytical studies was performed by Wiegel [40] for a planar surface. Odijk [55] investigated the binding of polyelectrolytes to an oppositely charged cylinder using a perturbation theory. Later, Muthukumar et al. [41, 56] used a variational method to study the adsorption onto planar, cylindrical, and spherical surfaces. In particular, Muthukumar [41] has taken into account the conformational changes of the polyelectrolyte upon altering

the salt concentration of the electrolyte solution. The adsorption onto a spherical surface has been studied by a self-consistent variational approach by Haronska et al. [57]. We recently presented exact analytical results for critical adsorption onto a sphere by replacing the Debye–Hückel potential with the Hulthén potential [58–60]. We have proposed a unified approach for polyelectrolyte adsorption onto planar, cylindrical and spherical surfaces [48] by applying the Wentzel–Kramers–Brillouin (WKB) approximation of quantum mechanics [61–64]. In addition, Linse and Shubin [65, 66] used lattice models to study polyelectrolyte adsorption at planar oppositely charged surfaces, thereby extending previous approaches [67, 68]. A scaling theory has been developed by Borisov et al. [69] and Dobrynin et al. [70] (see also [8, 9] and references therein), which predicts strong conformational changes of the adsorbed polyelectrolytes when the surface charged density is varied.

More specific models have been used to study the limit of strong polyelectrolyte adsorption. Here, in contrast to the weak adsorption case, the adsorption energy per persistence length of the adsorbing polyelectrolyte chain is large compared with the energy of thermal fluctuations, and the structure of the adsorbed polyelectrolyte is determined by the surface attraction and intramolecular repulsion rather than chain entropy. This leads to the formation of well-defined patterns of polyelectrolytes on the interfaces. In the case of attractive spheres, tennis-ball patterns [71, 72], rosettes [73, 74], or solenoids [59, 71, 75, 76] have been predicted (see Fig. 2 for examples). For cylinders, helical structures [77–79] or strip patterns have been suggested [77, 80–82]. The investigated systems also diversify according to the polyelectrolyte flexibility. In some of the above references and others [83–90], flexible chains are considered, whereas the influence of polymer persistence has been addressed in Refs. [71, 73, 74, 76–79, 91–94].

Computer simulations of polyelectrolyte adsorption – in particular Monte Carlo studies – confirmed a number of theoretical predictions (see [96–101] for recent advances). In a series of articles, Wallin and Linse [102–104] investigated the influence of chain flexibility, linear charge density, and sphere radius on the complexation of polyelectrolytes with micelles. Akinchina and Linse [105] found transitions between tennis-ball-like, solenoid, and rosette-like structures by varying the polyelectrolyte persistence length only. Taking into account the intramolecular charge–charge interactions by a Debye–Hückel potential, Stoll and colleagues [35, 95, 106] and Kong and Muthukumar [107] undertook similar studies on the adsorption of polyelectrolytes onto oppositely charged spheres. Figure 2 illustrates various conformations of a semiflexible polyelectrolyte. Such studies are of particular interest because the results can directly be compared to theoretical predictions, which are often also based on Debye–Hückel potentials. Messina and coworkers [108–110] demonstrated that in the case of strong electrostatic coupling it is even possible to adsorb a polyelectrolyte with charges of the same sign as a sphere. In addition, the adsorption of polyelectrolytes onto oppositely charged planar surfaces has been studied by Yamakov et al. [111], Ellis et al. [112], and Messina [113, 114], who also considered the influence of image charges on the adsorption characteristics. We would also like to mention simulation studies addressing counterion condensation onto polyelectrolyte chains [115–120]. This corresponds to strong adsorption of (several) small spherical particles.

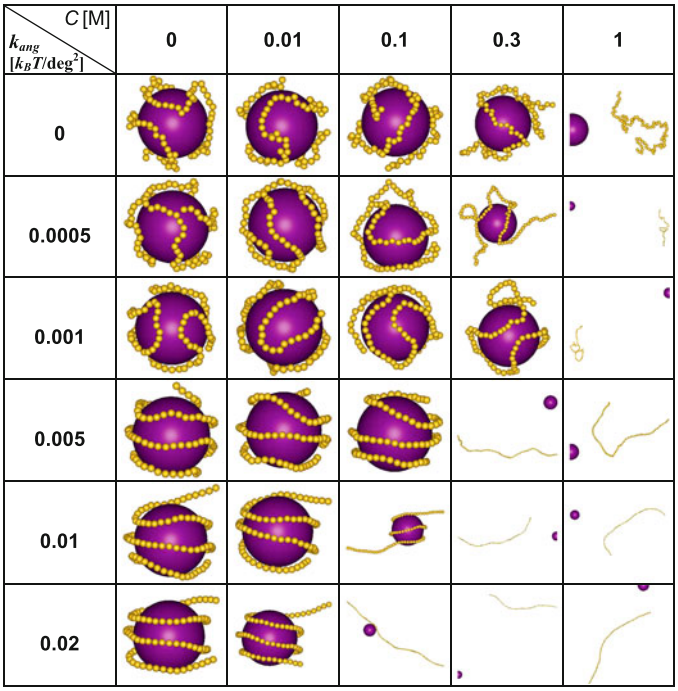


**Fig. 2** Conformations of semiflexible polyelectrolyte chains adsorbed on a spherical colloidal particle for various salt concentrations $C$ and stiffness $k_{ang}$ (from [95]). With increasing stiffness, the adsorbed polyelectrolyte undergoes conformational changes from tennis ball-like patterns to solenoid-like structures. The adsorption threshold depends on salt concentration and polyelectrolyte stiffness. More details of the underlying Monte Carlo simulations are provided in Ref. [95]

Experimentally, a large number of similar studies on the influence of chain stiffness, colloid charge density, and salt concentration have been performed [43, 44, 121–138]. Some theoretical trends regarding the effect of surface curvature and salt concentration on critical adsorption and polyelectrolyte–colloid complexation are supported by experimental observations. These studies, however, also revealed a number of discrepancies and additional physical parameters to be taken into account, as compared with the outcomes of theoretical studies and computer simulations.

In this review article, we focus on two aspects of polyelectrolyte adsorption – first, the critical adsorption transition and its dependence on the surface geometry and, second, the particular charge patterns of strongly adsorbed polyelectrolytes on cylinders and spheres – and study their properties using analytical theory. The first aspect is the limit of what we denote as weak adsorption. Here, the polyelectrolyte entropy plays a major role and determines the critical parameters. In the second case, the strong adsorption limit, the electrostatic energy dominates over the conformational degrees of freedom and the charge–charge interactions determine the complexation properties [139]. In both cases, we adopt the linearized Poisson–Boltzmann equation as the basis for determining the electrostatic potential

for the considered surface geometry. Specifically, we consider planar, cylindrical, and spherical surfaces. This review is motivated by the adsorption of biological molecules onto, typically, cylinders and spheres. Our studies are geared towards a better understanding of the physico-chemical properties of nucleosome core particles of eucaryotic genomic DNA and an understanding of the complexation of flexible nucleic acid genomes with oppositely charged highly basic interiors of capsid shells, which are typical of many spherical and filamentous viruses. Naturally, the applicability of the ideas is much broader and applications in various fields will be discussed.

In general, we will not discuss adsorption onto planar surfaces and structure formation on such surfaces as they occur in polyelectrolyte multilayer formation [2, 140–143]. Such systems are addressed in a review by Lindholm and Cohen Stuart in this series [144].

## 2 Weak Adsorption: Theoretical Model

The weakly charged polyelectrolyte chain is described by a continuous space curve with the linear charge density $\rho = e/l_0$, where $e$ is the elementary charge and $l_0$ the intercharge separation. The intramolecular Coulomb and intersegmental excluded-volume interactions are not taken into account explicitly, but are instead incorporated into the Kuhn segment of the length $l$. Expressions for its dependence on the Debye screening length $\lambda_D = 1/\kappa$ are provided in the literature [56, 145–149]. We assume that intramolecular charge–charge interactions perturb the polymer statistics only slightly. Hence, we consider a polymer chain under $\Theta$-solvent conditions. Under bad or good solvent conditions, the scaling properties for critical adsorption might be altered [9]. Taking counterions and salt ions into account using the Debye–Hückel potential, this corresponds to the limit where the Debye–Hückel potential between two Kuhn segments with the charge $q = \rho l$ separated by $l$ obeys $q^2 \, \mathrm{e}^{-\kappa l}/\epsilon l \ll k_B T$. For $\kappa = 0$, this means $l_B/l \ll 1$, where $l_B = e^2/(\epsilon k_B T)$ is the Bjerrum length, $\epsilon$ the dielectric permittivity, $T$ the temperature, and $k_B$ Boltzmann's constant. The oppositely charged surface has a homogeneous charge density $\sigma$ and is impenetrable to solvent molecules and polyelectrolyte chains. The solvent is treated as a continuous medium of constant dielectric permittivity with $\epsilon = 80$. The counterions and salt ions are taken into account on the level of the linearized Poisson–Boltzmann equation [59]. Its solution yields the polyelectrolyte–surface interaction potential, i.e., the Debye–Hückel potential for the particular geometry. The latter is derived assuming a constant surface charge density, without accounting for possible charge regulation effects or for coupling of the surface potential to the density profile of a polyelectrolyte in the proximity of the interface (see Sects. 6.1.1 and 6.2.1). Because the polyelectrolyte and the surface are weakly charged, no release of counterions upon adsorption will occur. Other approximations employed include the same value of the dielectric

constant in solution and below the adsorbing interface. Some implications of these assumptions are discussed in Sect. 8.

## 2.1 Equation for the Green Function

The conformational properties of a flexible polyelectrolyte chain of length $L$ ($L \to \infty$) and its spatial distribution of monomers follow from the probability density $G(\mathbf{r}, L|\mathbf{r}', 0)$ (Green function), where $\mathbf{r}(0) = \mathbf{r}'$ and $\mathbf{r}(L) = \mathbf{r}$ denote the positions of the polymer end points. The Green function itself follows from the equation [40, 41, 58–60, 150]:

$$\left(\frac{\partial}{\partial L} - \frac{l}{6}\Delta + \frac{V_{\mathrm{DH}}(\mathbf{r})}{k_{\mathrm{B}}T}\right) G(\mathbf{r}, L|\mathbf{r}', 0) = \delta(\mathbf{r} - \mathbf{r}')\delta(L), \tag{1}$$

with $\Delta$ being the Laplace operator. The Laplace term $\Delta G(\mathbf{r}, L|\mathbf{r}', 0)$ accounts for the entropic degrees of freedom of the polymer and $V_{\mathrm{DH}}$ is the Debye–Hückel potential of the surface. Equation (1) has to be solved with the boundary conditions $G = 0$ at the surface, it is impenetrable for the polymer, and $\lim_{|r|\to\infty} G = 0$. Unfortunately, no analytical solution of (1) exists for complex geometries such as cylinders and spheres.

Because the equation for $G$ is linear, it can be solved by an eigenfunction expansion:

$$G(\mathbf{r}, L|\mathbf{r}', 0) = \sum_n \psi_n^*(\mathbf{r}')\,\psi_n(\mathbf{r})\,\mathrm{e}^{-\lambda_n L} \tag{2}$$

in terms of the eigenfunctions $\psi_n$ of the eigenvalue equation:

$$\left(-\frac{l}{6}\Delta + \frac{V_{\mathrm{DH}}(\mathbf{r})}{k_{\mathrm{B}}T}\right)\psi_n(\mathbf{r}) = \lambda_n \psi_n(\mathbf{r}) \tag{3}$$

with the corresponding eigenvalues $\lambda_n$. As is well known, in the limit $L/l \gg 1$ the Green function is dominated by the eigenfunction corresponding to the ground state. Thus, we can restrict our considerations to the lowest eigenvalue $\lambda_0$ [40, 41, 58–60, 150].

The term "weak adsorption" implies that the entropic free energy of a chain is comparable to its electrostatic attraction energy to the interface. The chain is assumed to be Gaussian and its conformations are only weakly perturbed by interactions with the surface. This is the most severe approximation of the current model. We also assume that the polyelectrolyte–density profile is built up near the adsorbing surface without disturbing the electrostatic potential and ionic distribution near the interface prescribed by the Poisson–Boltzmann theory. A more general

self-consistent field theory, with a coupling of polymer and ionic distributions next to the interface, has been presented [151, 152].

### 2.2 Density Distribution Function

The density distribution $P(\mathbf{r})$ of a point $\mathbf{r}(s)$ along the polymer contour ($0 < s < L$) follows from:

$$P(\mathbf{r}) = \int \langle \delta(\mathbf{r} - \mathbf{r}(s)) \rangle \, \mathrm{d}s \tag{4}$$

with:

$$\begin{aligned} \langle \delta(\mathbf{r} - \mathbf{r}(s)) \rangle &\sim \int G(\mathbf{r}_\mathrm{L}, L|\mathbf{r}', s) \, \delta(\mathbf{r} - \mathbf{r}') G(\mathbf{r}', s|\mathbf{r}_0, 0) \, \mathrm{d}^3\mathbf{r}_\mathrm{L} \, \mathrm{d}^3\mathbf{r}_0 \, \mathrm{d}^3\mathbf{r}' \\ &= \int G(\mathbf{r}_\mathrm{L}, L|\mathbf{r}, s) G(\mathbf{r}, s|\mathbf{r}_0, 0) \, \mathrm{d}^3\mathbf{r}_\mathrm{L} \, \mathrm{d}^3\mathbf{r}_0. \end{aligned} \tag{5}$$

Using the ground-state Green function $G(\mathbf{r}, s|\mathbf{r}', s') = \psi_0^*(\mathbf{r}')\psi_0(\mathbf{r}) \, \mathrm{e}^{-\lambda_0|s-s'|}$ (2), we obtain (note that $\psi_0(\mathbf{r})$ is a real function):

$$P(\mathbf{r}) \sim \psi_0(\mathbf{r}) \, \psi_0(\mathbf{r}) \, \mathrm{e}^{-\lambda_0 L}, \tag{6}$$

or, with the normalization $\int P(\mathbf{r}) \, \mathrm{d}^3\mathbf{r} = 1$:

$$P(\mathbf{r}) = \frac{\psi_0(\mathbf{r})^2}{\int \psi_0(\mathbf{r})^2 \, \mathrm{d}^3\mathbf{r}}. \tag{7}$$

## 3 Weak Adsorption: Exactly Solvable Models

In this section, we will discuss the adsorption behavior on planar and spherical surfaces. Figure 3 illustrates the various geometries.

### 3.1 Planar Surface

Analytical results for the Green function are obtained for a planar geometry only. For a planar surface, the linearized Poisson–Boltzmann equation yields the screened potential:

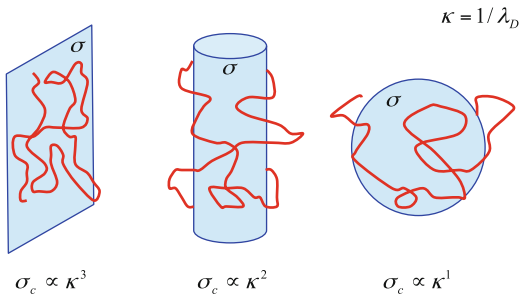


**Fig. 3** Illustration of the adsorption behavior of a polyelectrolyte on planar, cylindrical, and spherical surfaces with the corresponding dependencies of the critical surface charge densities $\sigma_c$ on the inverse Debye screening length $\kappa$ [48]

$$V_{\mathrm{DH}}(z) = \frac{4\pi|\rho\sigma|}{\epsilon\kappa} e^{-\kappa z}, \tag{8}$$

when the $z$-axis is normal to the surface. Parallel to the surface, the polymer conformations are unperturbed and the corresponding Green function is give by a Gaussian [40]. The ground-state eigenvalue equation for the Green function (3) normal to the surface becomes:

$$\left(-\frac{l}{6}\frac{\partial^2}{\partial z^2} - \theta\, \mathrm{e}^{-\kappa z}\right)\psi_0(z) = \lambda_0\psi_0(z), \tag{9}$$

where we introduced the abbreviation:

$$\theta = \frac{4\pi|\rho\sigma|}{\epsilon\kappa k_{\mathrm{B}}T}. \tag{10}$$

The eigenvalue $\lambda_0$ can be positive or negative, corresponding to free and bound states, respectively [40]. The transition between free and bound states appears for $\lambda_0 = 0$. As discussed [40, 41], the bound states are given by:

$$\psi_0(z) \sim J_v\left(\sqrt{24\theta}/(\kappa l)\, \mathrm{e}^{-\kappa z/2}\right), \tag{11}$$

with $J_\nu$ being the Bessel functions of the first kind [153]. The critical values for adsorption follow for $\lambda_0 = 0$ and the boundary condition at the surface:

$$\psi_0(0) = J_0\left(\sqrt{24\theta}/(\kappa l)\right) = 0. \tag{12}$$

This yields the critical surface charge density:

$$|\sigma_c| = \frac{j_0^2\, \epsilon\, k_B T l}{96\, \pi |\rho|} \kappa^3, \tag{13}$$

where $j_0 = 2.4048\ldots$ is the first zero of $J_0(x)$ for $x > 0$ [153].

Smaller surface charge densities will be necessary to trigger polyelectrolyte adsorption for other boundary conditions, when, e.g., the maximum of the polymer peak is positioned right on the adsorbing interface, instead of being displaced from it by entropic repulsion of polymer chains from the surface, as assumed above. Also note that for weak adsorption, we work in the limit of vanishing polymer concentration in the bulk, to avoid a nontrivial computation of the conformational entropy of free polyelectrolytes in an electrolyte solution.

The critical charge density (13) is only half of the value provided in publications by Wiegel and Muthukumar [40, 41]. This is related to the calculation of the surface potential, which is quite complicated in general [76, 154]. We use the solution of the Poisson–Boltzmann equation in the limit of a strong electrolyte [154] instead of the large separation Debye–Hückel potential [40, 41]. The latter underestimates the potential at contact by a factor of two.

The density distribution (7) for a polyelectrolyte in front of the planar surface is given by:

$$P(z) = \frac{\psi_0(z)^2}{\int_0^\infty \psi_0(z)^2\, \mathrm{d}z}. \tag{14}$$

## 3.2 Spherical Surface

For a sphere, the linearized Poisson–Boltzmann equation yields the polymer–sphere interaction energy (per polymer length) (see Sect. 6.2.1):

$$V_{DH}(r) = -\frac{4\pi a^2 |\sigma\rho|}{\epsilon(1+\kappa a)} \frac{\mathrm{e}^{-\kappa(r-a)}}{r}, \tag{15}$$

where $r$ is the radial distance from the sphere center and $a$ is the sphere radius. No analytical solution of (3) exists with the potential (15). To find an analytical solution for polyelectrolyte–sphere adsorption, we approximate the Debye–Hückel potential by the Hulthén potential [155, 156]:

$$V_H(r) = \frac{4\pi a |\sigma\rho| (\mathrm{e}^{\kappa a} - 1)}{\epsilon(1+\kappa a)} \frac{\mathrm{e}^{-\kappa r}}{1 - \mathrm{e}^{-\kappa r}}. \tag{16}$$

The potentials are identical for $r = a$. Moreover, the difference between the two expressions is small for $\kappa a \leq \kappa r \ll 1$ as well as for $\kappa a \gg 1$ because, in the latter limit, $r$ in the denominator of (15) is slowly varying and can be replaced by $a$ and $\mathrm{e}^{-\kappa r} \ll 1$.

Because the Hulthén potential is spherically symmetric, the Green function can be expanded in terms of radial eigenfunctions $\psi_n(r)$ and the spherical harmonics [40, 41, 150]. In the ground-state dominance approximation, this leads to $G(r, L|r', 0) = \psi_0^*(r')\psi_0(r)\,\mathrm{e}^{-\lambda_n L}$ with:

$$\frac{l}{6}\left(\frac{\mathrm{d}^2\psi_0(r)}{\mathrm{d}r^2} + \frac{2}{r}\frac{\mathrm{d}\psi_0(r)}{\mathrm{d}r}\right) - \frac{V_\mathrm{H}(r)}{k_\mathrm{B}T}\psi_0(r) = -\lambda_0\psi_0(r). \tag{17}$$

In the limit of a small curvature, i.e., $a \to \infty$, the curvature term $1/r$ can be neglected and the potentials (15) and (16) assume the form of the potential (8). Hence, the equation of a polyelectrolyte in front of a planar surface (9) is recovered.

To solve the differential equation with the Hulthen potential, we introduce the new variable $\chi(r)$ via:

$$\psi_0(r) = \frac{1}{r}\,\mathrm{e}^{-\xi_0\kappa r}(1 - \mathrm{e}^{-\kappa r})\chi(r) \tag{18}$$

and $x = 1 - \mathrm{e}^{-\kappa r}$, where $\xi_0$ is related with $\lambda_0$ via $\lambda_0 = -l\xi_0^2\kappa^2/6$. Equation (17) then turns into the hypergeometric differential equation:

$$x(1-x)\frac{\mathrm{d}^2}{\mathrm{d}x^2}\chi(x) + [2 - x(3 + 2\xi_0]\frac{\mathrm{d}}{\mathrm{d}x}\chi(x) - \left(1 + 2\xi_0 - \frac{2}{p}\right)\chi(x) = 0, \tag{19}$$

for $\chi$ with the variable $x$, where:

$$p = \frac{\kappa^2\epsilon k_\mathrm{B}Tl(1+\kappa a)}{12\pi a|\sigma\,\rho|(\mathrm{e}^{\kappa a} - 1)}. \tag{20}$$

The solution of (19) in the vicinity of the point $x = 1$ is given by $\chi(x) = F(\alpha,\ \beta;\ \alpha + \beta - \gamma + 1;\ 1 - x)$, where $F = {}_2F_1$ is the Gauss hypergeometric function, and $\alpha = \xi_0 + 1 - \sqrt{\xi_0^2 + 2/p}$, $\beta = \xi_0 + 1 + \sqrt{\xi_0^2 + 2/p}$, and $\gamma = 2$ [153].

The eigenvalue $\lambda_0$ (or $\xi_0$) is determined from the boundary conditions. Similar to the planar case, the eigenvalues can be positive or negative. The critical adsorption conditions follow for $\lambda_0 = \xi_0 = 0$. Because $F(\alpha, \beta; \alpha + \beta - \gamma + 1; 1 - x) = 0$ converges for $|1 - x| < 1$, and $\alpha + \beta - \gamma + 1$ is neither zero nor a negative integer, the boundary condition for $r \to \infty$, i.e., $x = 1$, is satisfied. Hence, the eigenvalue $\xi_0$ is determined by the boundary condition $F(\alpha, \beta; \alpha + \beta - \gamma + 1; \mathrm{e}^{-\kappa a}) = 0$. For $\xi_0 = 0$, the dimensionless parameter $p$ then assumes a particular value $p_\mathrm{c}$ for a given $\kappa a$, which follows from the condition:

$$F\left(1-\sqrt{2/p_c},\ 1+\sqrt{2/p_c};\ 1;\ \mathrm{e}^{-\kappa a}\right)=0. \tag{21}$$

### 3.2.1 Critical Adsorption

The numerical solution of (21) is presented in Fig. 4. Polyelectrolyte adsorption takes place for $p < p_c$. The $p_c$ curve monotonically decrease with increasing $\kappa a$. For small $\kappa a$, it is well approximated by $p_c \approx 2 - 4\kappa a$. This dependence is consistent with the necessary condition for the existence of zeros for $F$, namely, $p < 2$ [157].

An analytical approximation for the "critical" function $\chi_c$ in the large curvature limit $\kappa a \to 0$ is obtained when $p = 2$ is used in (19). Then, the equation reduces to:

$$x(1-x)\frac{\mathrm{d}^2}{\mathrm{d}x^2}\chi_c(x)+(2-3x)\frac{\mathrm{d}}{\mathrm{d}x}\chi_c(x)=0, \tag{22}$$

i.e., it is dominated by the curvature terms. The solution of the equation is:

$$\chi_c(r)=\chi_c^0\left(\frac{1}{\mathrm{e}^{\kappa a}-1}-\frac{1}{\mathrm{e}^{\kappa r}-1}+\ln\frac{\mathrm{e}^{\kappa r}-1}{\mathrm{e}^{\kappa a}-1}\right) \tag{23}$$

for $\kappa a \le \kappa r \to 0$.

As mentioned above, in the small curvature limit ($\kappa a \to \infty$), the spherical adsorption problem turns into the problem of a polyelectrolyte in front of a charged planar surface. The corresponding eigenfunction and critical adsorption condition [40] follow also from the properties of the hypergeometric function. In the limit $\kappa a \to \infty$, the boundary condition (21) can be expressed in terms of Legendre functions of the first kind $P_\nu$ and the Bessel function $J_0$ according to:

$$\begin{aligned}\lim_{\kappa a\to\infty} F(\alpha_c, 2-\alpha_c;\ 1;\ \mathrm{e}^{-\kappa a}) &= \lim_{\kappa a\to\infty} P_{-\alpha_c}(1-2\,\mathrm{e}^{-\kappa a})\\ &= \lim_{\kappa a\to\infty} J_0\left(\sqrt{8/p_c}\,\mathrm{e}^{-\kappa a/2}\right)=0,\end{aligned}$$

with $\alpha_c = 1-\sqrt{2/p_c}$ [153]. The latter condition is identical to the boundary condition (12) for critical adsorption onto a planar surface. Hence, we find the critical value $p_c = (8/j_0^2)\,\mathrm{e}^{-\kappa a}$ for large $\kappa a$. Figure 4 shows the agreement between this approximation and the full numerical solution of (21).

The critical $p_c$ presented in Fig. 4 is determined using the Hulthén potential rather than the Debye–Hückel potential. The above discussion demonstrates that, in the small curvature limit, the difference between the Debye–Hückel potential and the Hulthén potential vanishes. From the following considerations, it will be evident that the function $F_c(r) = F\left(1-\sqrt{2/p_c},\ 1+\sqrt{2/p_c};\ 1;\ \mathrm{e}^{-\kappa r}\right)$

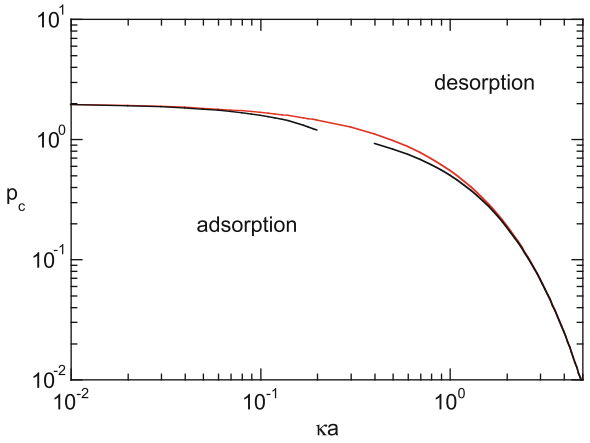


**Fig. 4** Critical values $p_c$ obtained from the boundary condition at the sphere surface. Polyelectrolyte adsorption takes place for $p < p_c$. The *black lines* are the approximations $p_c \approx 2 - 4\kappa a$ for $\kappa a \ll 1$ and $p_c = (8/j_0^2)\,e^{-\kappa a}$, where $j_0 = 2.4048\ldots$, for $\kappa a \gg 1$ [58]

also provides the appropriate critical $p_c$ for the Debye–Hückel potential in the limit $\kappa a \leq \kappa r \ll 1$. Using the Debye–Hückel potential, (19) becomes:

$$x(1-x)\frac{d^2}{dx^2}\chi_c(x) + (2-3x)\frac{d}{dx}\chi_c(x) - \left(1 + \frac{2a\kappa x}{p_c \ln(1-x)(1-e^{-\kappa a})}\right)\chi_c(x) = 0 \tag{24}$$

Again, the first two terms are satisfied by the function (23) and the remaining part disappears at $r = a$ for $p_c = 2$. Hence, the critical value $p_c = 2$ is identical for the Hulthén and the Debye–Hückel potential in the limit $ka \ll 1$ and $(r-a)/a \ll 1$.

The critical value $p_c$ allows us to calculate other critical quantities for polyelectrolyte adsorption, such as the critical temperature [41, 59], the critical colloid surface charge density $\sigma_c$ [58, 59], or the critical colloid radius $a_c$ via (20). Results for the critical temperature and the critical surface charge density have been presented and discussed [58, 59]. Thus, we summarize here our findings for $\sigma_c$ only. Using the above limiting values for $p_c$, we obtain the following approximations:

$$|\sigma_c| = \begin{cases} \dfrac{\epsilon k_B T l}{24\pi a^2 |\rho|}\kappa, & \kappa a \ll 1 \\ \dfrac{j_0^2 \epsilon k_B T l}{96\pi |\rho|}\kappa^3, & \kappa a \gg 1. \end{cases} \tag{25}$$

The exact solution for the Debye–Hückel potential predicts a linear dependence of the critical colloid charge density on the inverse Debye screening length for $\kappa a \ll 1$ (Fig. 5). This is different from the predicted dependence $|\sigma_c| \sim \kappa^2$ based on

the variational calculation of van Goeler and Muthukumar [56]. However, the variational calculation of Haronsa et al. [57] predicts the same dependence on $\kappa$, but the numerical factor is rather different. The Kuhn segment length $l$ of the polymer is independent of $\kappa$ in this limit [41]. In the opposite limit of small curvature ( $\kappa a \gg 1$ ), the obtained $\kappa$ dependence is identical to that found by variational calculations [56–58]. The adsorption–desorption transitions in all these limits are of second order.

The analytical approximation for $\kappa a \ll 1$ [see (25)] not only predicts a critical surface charge density but also a critical colloid charge $Q_c = 4\pi a^2|\sigma_c| \sim \kappa$ itself. This implies that for sufficiently small colloids, critical adsorption is independent of the size of the colloid; it only depends on $\kappa$. In this limit, the Debye screening length defines the region in space where the potential is large enough to capture the dissolved polyelectrolyte and to trigger adsorption.

So far, we have assumed that the Kuhn length (or persistence length) is independent of the Debye screening length. It is, however, well known that the persistence length of flexible polyelectrolytes exhibits a $\kappa$ dependence [158–160]. There exist various power-law predictions $l \sim \kappa^{-b_l}$ for such a dependence, with exponents in the range $b_l = \frac{4}{5}$ to $b_l = \frac{6}{5}$ [41, 146–148, 161–163]. A detailed discussion of the $\kappa$ dependence of the persistence length by far exceeds the focus of the current paper, but we would like to point out that recent simulations and scaling considerations for long flexible polyelectrolytes [146–148, 162] are in agreement with the original prediction $l \sim \kappa^{-2}$ by Odijk [164] and Skolnick and Fixman [165] for semiflexible polyelectrolytes. In this limit, the polyelectrolyte can be mimicked as a linear assembly of weakly interacting de Gennes–Pincus electrostatic blobs with the electrostatic persistence scaling similar to that of Odijk–Skolnick–Fixman stiffness for weakly bendable polyelectrolyte chains. For our purposes, we use the definition of the projection length presented by Ullner [148] as a measure of persistence length, which exhibits the exponent $b_l = 1.2$.

The complex formation of a polyelectrolyte with oppositely charged micelles and proteins has been studied (for example, see [44, 123, 124, 126, 128]). These experiments confirm that complexation occurs only when the surface charge density exceeds a critical value, which typically grows with the reciprocal Debye screening length as $|\sigma_c| \sim \kappa^b$ with $b = 1-1.4$ [44, 59, 124, 126, 128]. Our scaling results agree with the experimental findings when we take the above $\kappa$ dependence of $l$ into account [58, 59].

Instead of the charge density $\sigma_c$, a critical sphere radius $a_c$ can be determined [35, 56, 107] that separates adsorbed from desorbed polyelectrolyte states. By introducing the abbreviation:

$$\bar{\kappa} = \left(\frac{96\pi|\sigma\,\rho|}{j_0^2 \epsilon k_B T l}\right)^{1/3}, \tag{26}$$

and using the definition (20), we obtain the following equation for $a_c$:

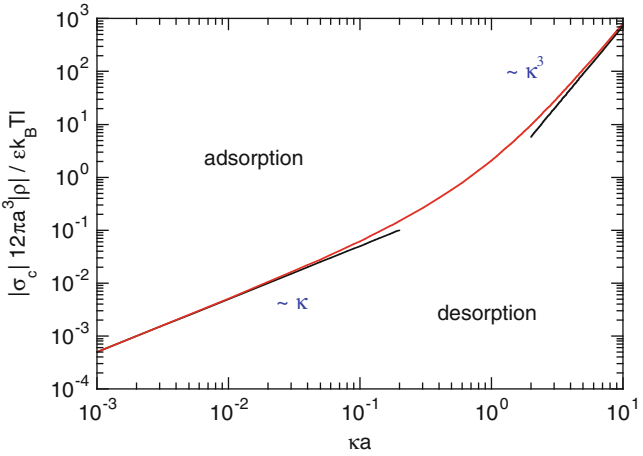


**Fig. 5** Critical charge density $|\sigma_c|$ as function of the inverse Debye screening length. The *black lines* are the analytical approximations (25) for $\kappa a \ll 1$ and $\kappa a \gg 1$, respectively. No adsorption is obtained in the area on the *right* of the curve [58]

$$p_c(\kappa a_c)(e^{\kappa a_c} - 1) - \frac{8\kappa^2}{j_0^2 a_c \bar{\kappa}^3}(1 + \kappa a_c) = 0. \tag{27}$$

Its solution yields a universal curve for $a_c\bar{\kappa}$ as a function of $\kappa/\bar{\kappa}$.

The numerical solution of (27) is shown in Fig. 6 together with the analytical approximations:

$$a_c\bar{\kappa} = \begin{cases} \sqrt{4\kappa/\bar{\kappa}j_0^2}, & \kappa \ll \bar{\kappa} \\ (\kappa/\bar{\kappa})^2/(1 - (\kappa/\bar{\kappa})^3), & \kappa \to \bar{\kappa}. \end{cases} \tag{28}$$

No adsorption is obtained in the region located to the right of the curve. At a fixed $\kappa < \bar{\kappa}$, the entropy penalty due to adsorption of the chain monomers decreases with increasing sphere radius. Beyond the critical radius, the energy gain exceeds the entropy loss and the polymer adsorbs at the sphere surface. As is obvious from the analytical expression, $\bar{\kappa}$ is the maximum value of the inverse Debye screening length; no adsorption is obtained for larger values neither for a sphere nor for a planar surface. Hence, $\bar{\kappa}$ plays a key role in critical adsorption.

This is qualitatively consistent with the variational calculations [56, 107]. These calculations predict the same dependence of the maximum value of $\kappa$ on the polymer and sphere parameters as our solution does. Quantitatively, however, the value of the variational calculation is smaller by the factor $8/j_0^2$. In addition, the shape of the critical curve is rather different, as shown in Fig. 6.

The adsorption of a polyelectrolyte onto a spherical particle has been studied using Monte Carlo simulations [35]. In particular, the critical sphere radius has been determined as a function of $\kappa$. Aside from the interactions considered in our model,

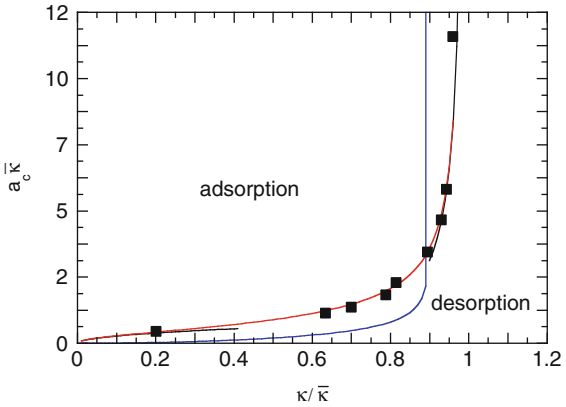


**Fig. 6** Critical radius $a_c$ as a function of the Debye screening length according to (27) (*red*) [58]. The *black lines* are the approximations of (28). The *blue line* represents the critical radius according to the variational calculations of Muthukumar and colleagues [56, 107]. The *symbols* are Monte Carlo simulation results published by Chodanowski and Stoll [35]

the intramolecular charge–charge interactions have been taken into account in simulations by using the Debye–Hückel potential as well as excluded-volume interactions. As a consequence, the simulated systems exhibit significant conformational changes in the polymer when changing the Debye screening length (see Figs. 1 and 2). By examining the simulation results (particularly Figs. 1 and 3 in [35]) for a chain of $N = 100$ monomers, we conclude that the polyelectrolyte molecule exhibits nearly the same conformational behavior for $\kappa$ values close to the adsorption transition, independent of the colloidal radius ($\kappa \gtrsim 0.1/\text{Å}$). Thus, a direct comparison of the theoretical with the simulation results is feasible.

By adjusting the $\kappa$ values of the simulation data [35] such that the singularity appears at unity and multiplying the critical radii by an adequate factor, we achieve a remarkably good agreement with our universal $a_c$ curve, as shown in Fig. 6. This procedure yields the maximum $\kappa$ value $\bar{\kappa}_s \approx 0.25/\text{Å}$, where $\bar{\kappa}_s$ denotes the $\bar{\kappa}$ value used for scaling of the simulation results. Hence, the $\kappa$ values of the simulations presented in Fig. 6 are multiplied by 4.02 and the critical radii are divided by 16.16. The latter value is four times larger than expected. The difference might be related to the different adsorption criteria applied by Chodanowski and Stoll [35] and in our theoretical approach. We clearly expect a larger critical radius from the simulations because, in simulations, a polymer is considered adsorbed when it is in contact with the particle for more than 50% of the simulation time during the minimization period [35], whereas in our analytical approach adsorption is characterized by a transition from free to bound states [see (21)]. Hence, the difference between the simulation data and the results of the variational calculations [56, 107] is not due to the ground state dominance approximation, as speculated [35], it is instead a consequence of the limited applicability of the variational ansatz [56].

Using the simulation parameters presented by Chodanowski and Stoll [35], (26) yields the maximum $\kappa$ value 0.35/Å, when we use the Kuhn length $l = 7.14$ Å. This value is approximately 40% larger than the above $\bar{\kappa}_s$ value. The difference is largely caused by a too-small Kuhn length (persistence length) used in the theoretical model. The excluded volume interactions and the electrostatic repulsion of the equally charged monomers lead to a swelling of the polyelectrolyte compared to the Gaussian chain used in the present calculations. An appropriate persistence length can partially account for this swelling. By using a Kuhn length twice as long, we find that the maximum $\kappa$ value is $\approx$0.28/Å, which is close to $\bar{\kappa}_s$ and thus demonstrates the correct trend.

We finally would like to emphasize that the variational approach of Muthukumar and colleagues [56, 107] provides a good description of the scaling behavior of the critical charge density for polyelectrolyte–sphere interactions, whereas the same approach fails to predict the correct $\kappa^2$ dependence in the case of adsorption onto a cylindrical surface in the limit $\kappa a \ll 1$ (see Sect. 4.3).

### 3.2.2 Conformational Properties of Adsorbed Polyelectrolytes

The radial monomer (or segment) distribution (7) in the vicinity of a sphere is given by:

$$P(r) = \frac{\psi_0(r)^2 r^2}{\int_a^\infty \psi_0(r)^2 r^2 \, \mathrm{d}r} \tag{29}$$

within the ground state dominance approximation [60]. The eigenfunction $\psi_0(r)$ follows from (18) and (19) with $\xi_0 > 0$, where the eigenvalue $\xi_0$ itself is determined by the boundary condition:

$$F\left(\xi_0 + 1 - \sqrt{\xi_0^2 + 2/p},\ \xi_0 + 1 + \sqrt{\xi_0^2 + 2/p};\ 2\xi_0 + 1;\ \mathrm{e}^{-\kappa a}\right) = 0 \tag{30}$$

for a given $p < p_c$ (20). For small $p$ values, multiple solutions of this equation are obtained that correspond to the various "excited states." The largest value $\xi_0$ corresponds to the smallest eigenvalue, i.e., the ground-state value $\lambda_0$. A detailed discussion of the eigenvalues has been published [59].

Figures 7 and 8 provide examples of such distributions for various effective charge densities and Debye screening lengths, respectively. The $\sigma$ values in Figs. 7 and 8 cover the experimental range of colloid and polyelectrolyte parameters (see Fig. 11 in [59]). For the critical parameters, the density distribution $P$ is very broad and reaches a finite value for $r \to \infty$. This corresponds to a uniform polyelectrolyte monomer density and reflects the thermodynamic equilibrium between the bound and free states of the polymer. With increasing colloid surface charge density or decreasing $\kappa$ [65, 66], the distribution becomes more confined and

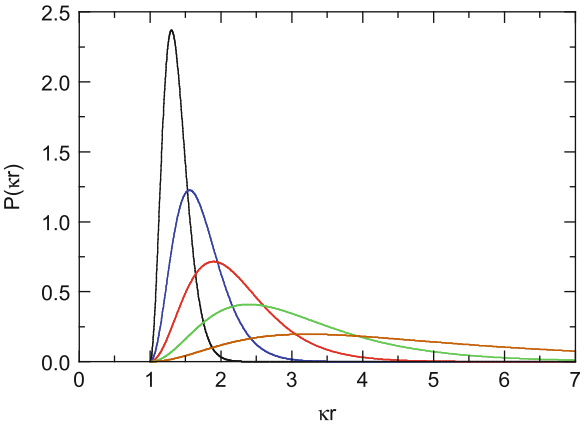


**Fig. 7** Radial monomer density distribution for $\kappa a = 1$ and the surface charge densities $\sigma/(12\pi a^3|\sigma\rho|/(\epsilon k_B T l)) = 3, 5, 10, 25,$ and 100 (from *right* to *left*) [60]

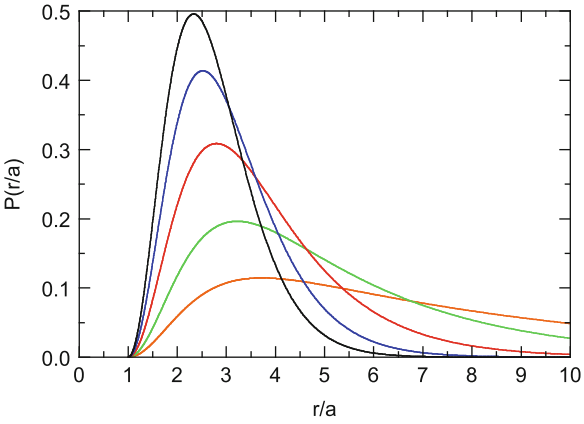


**Fig. 8** Radial monomer density distribution for the charge density $\sigma/(12\pi a^3|\sigma\rho|/(\epsilon k_B T l)) = 3$ and the Debye–Hückel screening parameters $\kappa a = 0.1, 0.5, 0.8, 1.0,$ and 1.1 (from *left* to *right*) [60]

decays exponentially at large distances. In both cases, a larger interaction strength between the colloid and the polyelectrolyte naturally results in a stronger adsorption. Smaller spheres require larger $|\sigma|$ values for the polyelectrolyte adsorption to take place, as is evident from (25). The position of the peak shifts to larger radial distances with decreasing surface charge density and increasing $\kappa$, respectively. However, this change is small compared to the dramatic increase in the thickness of the adsorbed layer.

A measure for the thickness $\Delta$ of the adsorbed layer is the full width at half maximum of the distribution function $P(r)$ [59]. Scaling considerations predict the dependence $\Delta \sim |\sigma|^{-1/3}$ for the layer thickness of a adsorbed polyelectrolyte on a

planar surface [8, 9, 69, 70, 166]. Our results approximately agree with this dependence, as discussed in Sect. 5.1 (see also [59, 60]).

The conformational properties of an adsorbed polyelectrolyte differ from those of a free polyelectrolyte [35]. To characterize the modifications, we determined its mean-square radius of gyration:

$$r_g^2 = \int_a^\infty r^2 P(r)\, dr. \tag{31}$$

Figure 9 shows $r_g^2$ as a function of the colloid radius for various values $\kappa/\bar{\kappa}$. Close to the adsorption transition, the radius of gyration of the polyelectrolyte is almost identical to that of the free polymer. Because we consider an infinitely long polymer, $r_g^2$ diverges when $\bar{\kappa}a \to \bar{\kappa}a_c$. For $a > a_c$, the polymer is adsorbed and confined in the vicinity of the sphere. This is accompanied by an initial decrease in the radius of gyration with increasing sphere radius. At larger $a$, the polymer is confined in a narrow layer close to the sphere surface. An increase in the sphere radius causes an increase in the layer radius, which is not compensated by a decrease in the layer thickness. Hence, the radius of gyration again increases with increasing $a$. The shift of the curves in Fig. 9 to larger $r_g^2$ and $\bar{\kappa}a$ with increasing $\kappa/\bar{\kappa}$ is explained by the reduced attraction of the polyelectrolyte at larger $\kappa$. With increasing $\kappa$, the adsorption is weakened and the polymer become less and less confined near the surface.

Qualitatively, the theoretically obtained dependence of the radius of gyration on the sphere radius is in agreement with the simulation results of Chodanowski and Stoll [35] and Muthukumar [107]. There, also an initial decrease and a later increase in the radius of gyration is found. However, the results cannot be compared quantitatively for several reasons. On the one hand, we did not take into account the conformational changes of the polyelectrolyte due to intramolecular charge–charge interactions. Our results apply as long as the conformational changes by such interactions are small. On the other hand, we consider an infinitely long polyelectrolyte. Published results (see Figs. 3 and 4 in [35]) demonstrate that polyelectrolyte finite size effects might be important in the adsorption process. A polyelectrolyte chain of finite length can be completely adsorbed on a sphere for a certain polymer length-to-radius ratio ( Fig. 1) (see also Table II in [35]). As a consequence, the radius of gyration is mainly determined by the sphere size and to a lesser extent by the screening length. $r_g^2$ is then independent of the salt concentration (as show in Figs. 3 and 4 of [35]). The situation is different for an infinitely long polymer, which is not able to cover a finite size sphere by a monolayer (or less than a monolayer) only. Here, larger $\kappa$ values will lead to larger layer thicknesses and larger radii of gyration.

It has been suggested that polyelectrolytes become trapped in the vicinity of a sphere when the attraction energy of a monomer exceeds the penalty of its entropic confinement ($\sim k_B T$) close to the sphere [121, 128]. This region of high potential around the sphere should become thinner as $\kappa$ increases because the electrostatic

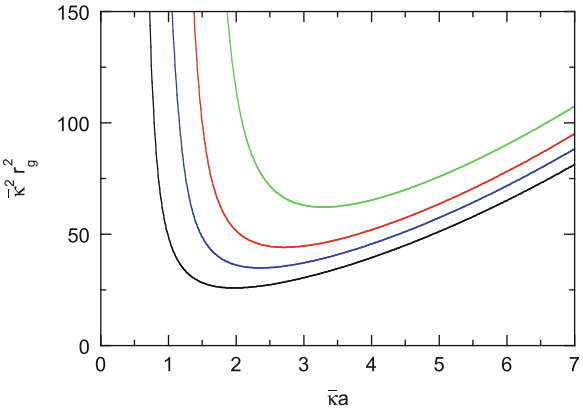


**Fig. 9** Mean square radius of gyration of an adsorbed polyelectrolyte as a function of the sphere radius for the Debye–Hückel parameters $\kappa/\bar{\kappa} = 0.3$, 0.5, 0.6, and 0.7 (*bottom* to *top*) [60]. $\bar{\kappa}$ is defined in (26)

potential decays faster away from the sphere, and the region should become larger with increasing sphere charge density. Thus, larger $|\sigma|$ values would be required to form polyelectrolyte–sphere complexes at higher salt concentrations. Clearly, this statement is qualitatively consistent with our analytical result (25). Using the same crude model as described by McQuigg et al. [121], however, leads to a completely different dependence of the critical charge density on $\kappa$, namely $|\sigma_c| \sim (\kappa a + 1)$ [60, 121]. This yields a dependence on $\kappa$ that is far too weak for $\kappa a \gg 1$ and $\sigma_c$ is independent of $\kappa a$ for $\kappa a \ll 1$. These differences reflect the different underlying physical adsorption mechanisms. In the first case, it is assumed that the gain in adsorption energy compensates for the loss in translational entropy (of either some part of the polymer or the colloid), neglecting any conformational entropy changes. In our approach, however, conformational entropy changes play the dominate role – adsorption is achieved when the gain in adsorption energy compensates the loss in conformational entropy. Even for very small colloids, the spatial distribution of monomers is different from that of a polyelectrolyte in free space (see Figs. 4 and 5), particularly because of the boundary condition on the colloid surface. Thus, the presence of the colloid always affects the conformational properties of the polyelectrolyte. The adsorption process is governed by the polyelectrolyte conformational entropy rather than the translational entropy (of some segments or the colloid), which we of course account for by using (1) as the starting point of our considerations.

The Debye–Hückel attraction energy per polymer length (15) depends on $\kappa$. In particular, it decreases with decreasing $\kappa$ because the monomer distribution becomes narrower. Interestingly, at the transition from an adsorbed to a desorbed state, the average energy is zero because the critical eigenfunction decays very slowly with increasing radial distance and cannot be normalized. As a consequence, the polyelectrolyte fraction close to the sphere becomes zero when the desorption transition is approached.

## 4 Weak Adsorption: WKB Approximation

Exact solutions for critical adsorption of polyelectrolytes have been presented for planar and spherical surfaces. Adsorption onto a cylindrical surface can no longer be treated analytically. Here, a suitable principle for an approximate solution is desirable. We have proposed the WKB approximation as such a scheme [48].

### *4.1 WKB Approximation Scheme*

The WKB scheme is typically used in quantum mechanics to find an approximate solution of a time-independent one-dimensional Schrödinger equation of the form:

$$\frac{\partial^2\psi(x)}{\partial x^2} + Q(x)^2\psi(x) = 0 \tag{32}$$

in the vicinity of the simple zero $x_0$ of the potential $Q(x_0)^2 = 0$ [61–64]. More precisely, the WKB method yields a solution of the more general equation:

$$\frac{\partial^2\psi(x)}{\partial x^2} + [Q(x)^2 - \Omega(x)]\psi(x) = 0 \tag{33}$$

in the form:

$$\psi(x) = S(x)[\alpha\xi^{1/3}J_{-1/3}(\xi) + \beta\xi^{1/3}J_{1/3}(\xi)], \tag{34}$$

with the definitions $\Omega(x) = S(x)^{-1}\partial^2 S(x)/\mathrm{d}x^2$, $S(x) = Q(x)^{-1/2}\xi(x)^{1/6}$ and $\alpha$, $\beta$ being constant coefficients. $\xi$ is related to $Q$ according to [64]:

$$\xi(x) = \begin{cases} \int_x^{x_0} Q(x')\mathrm{d}x' & \text{for } x < x_0 \text{ in the region } Q(x)^2 > 0 \\ \mathrm{e}^{-3\pi i/2}\int_{x_0}^{x} |Q(x')|\mathrm{d}x' & \text{for } x > x_0 \text{ in the region } Q(x)^2 < 0 \end{cases}. \tag{35}$$

Note, that we exchanged the interval over which $Q^2$ is positive and negative, respectively, compared to [64]. In the limit $|\Omega(x)| \ll \sqrt{|Q(x)|}$, the general solution of (34) yields an approximate solution of (32).

Using the properties of Bessel functions, $\psi(x)$ can be expressed in terms of Airy functions *Ai* of negative and positive arguments, respectively [153]. Then, we obtain the uniformly valid Langer solution [48, 64]:

$$\psi(x) = \begin{cases} N_c \frac{\xi^{1/6}}{\sqrt{Q(x)}} Ai\left(-[3\xi/2]^{2/3}\right) & \text{for } x < x_0 \\ N_c \frac{|\xi|^{1/6}}{\sqrt{|Q(x)|}} Ai\left([3|\xi|/2]^{2/3}\right) & \text{for } x > x_0 \end{cases}, \tag{36}$$

with normalization constant $N_c$. For large arguments, the corresponding Airy functions can be asymptotically expanded in sinusoidal and exponentially decaying functions.

In the next section, we present the results of this approach for polyelectrolyte adsorption onto planar, cylindrical, and spherical surfaces. This is possible because the equation for the Green function reduces, in the corresponding separable coordinates, to a one-dimensional equation comparable to (32) in the ground-state approximation. We confirmed that the WKB applicability condition $|\Omega(x)/Q(x)| \ll 1$ is satisfied for all three geometries. The approach applies particularly well above the adsorption–desorption transition, whereas it naturally fails in the proximity of the zero-potential point $x_0$ at which $Q(x_0) = 0$.

## 4.2 Planar Surface

For a planar surface, (9) is of the form (32) with:

$$Q(z)^2 = \frac{6}{l}(\lambda_0 + \theta\, e^{-\kappa z}). \tag{37}$$

Because $\lambda_0 < 0$ for a bound state, the expression is zero for $\kappa z_0 = -\ln(|\lambda_0|/\theta)$. Moreover, $|\lambda_0|/\theta \leq 1$, because $z_0 \geq 0$. The adsorption–desorption transition occurs at $\lambda_0 = 0$, which implies $z_0 \to \infty$. Hence, the critical adsorption parameters are determined by the solution for $0 < z < z_0$. The boundary condition at the surface $\psi_0(0) = 0$, i.e., $Ai(-[3\xi(0)/2]^{2/3}) = 0$ yields $\xi(0) = 2ai_1^{3/2}/3$, where $ai_1 = 2.338$ is the first zero of the Airy function $Ai(-x)$. Evaluation of the integral for $\xi(0)$ (35) yields the critical surface charge density:

$$|\sigma_c| = \frac{ai_1^3 \epsilon k_B T l}{216\pi|\rho|}\kappa^3. \tag{38}$$

Hence, we obtain the same scaling relation as for the exact solution (13). More importantly, the two results deviate quantitatively by only 2%. The dependence of $\sigma_c$ on $\kappa a$ is displayed in Fig. 10.

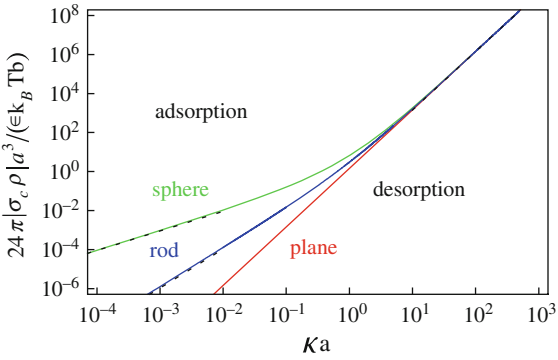


**Fig. 10** Critical surface charge densities obtained by the WKB approach for polyelectrolyte adsorption onto planar, cylindrical, and spherical surfaces. The asymptotic scaling relations for a cylinder (*rod*) (45) and a sphere (53) are indicated by *dotted lines* [48]

## *4.3 Cylindrical Surface*

The linearized Poisson–Boltzmann equation yields the interaction potential between a polyelectrolyte chain and the surface of an infinitely long, uniformly charged cylinder:

$$V_{\mathrm{DH}}(r) = -\frac{4\pi|\rho\sigma|}{\varepsilon\kappa}\frac{K_0(\kappa r)}{K_1(\kappa a)}, \tag{39}$$

where $K_0$ and $K_1$ denote modified Bessel functions of the second kind and $a$ is the radius of the cylinder. The equation for the radial component of the Green function of the cylinder is [48]:

$$\frac{l}{6}\left(\frac{\partial^2\psi_0(r)}{\partial r^2}+\frac{1}{r}\frac{\partial\psi_0(r)}{\partial r}\right)+\theta\frac{K_0(\kappa r)}{K_1(\kappa a)}\psi_0(r) = -\lambda_0\psi_0(r). \tag{40}$$

By the substitution $\kappa r = \mathrm{e}^u$, we obtain the equation $\partial^2\psi_0(u)/\partial u^2 + Q^2\psi_0(u) = 0$ suitable for the WKB approximation, with:

$$Q(u)^2 = \frac{6\mathrm{e}^{2u}}{l\kappa^2}\left(\lambda_0+\theta\frac{K_0(\mathrm{e}^u)}{K_1(\kappa a)}\right). \tag{41}$$

The point $r_0$, where the potential is zero, follows from the equation $K_0(\kappa r_0) = |\lambda_0|K_1(\kappa a)/\theta$, because $\lambda_0 < 0$ for a bound state. In the interval $a < r < r_0$, (35) becomes:

$$\xi(r) = \int_r^{r_0}\sqrt{\frac{6}{l}\left(\theta\frac{K_0(\kappa r)}{K_1(\kappa a)}-|\lambda_0|\right)}\,\mathrm{d}r, \tag{42}$$

which defines $\lambda_0$ via the boundary condition $Ai(-(3\xi(a)/2)^{2/3}) = 0$ or $\xi(a) = 2ai_1^{3/2}/3$ and:

$$\int_a^{r_0} \sqrt{\frac{6}{l}\left(\theta\frac{K_0(\kappa r)}{K_1(\kappa a)} - |\lambda_0|\right)}\mathrm{d}r = \frac{2}{3}ai_1^{3/2}. \tag{43}$$

For $\lambda_0 = 0$, this equation yields the condition:

$$\sqrt{\frac{24\pi|\rho\sigma_c|}{\varepsilon k_B T\kappa^3 l K_1(\kappa a)}}\int_{\kappa a}^{\infty}\sqrt{K_0(x)}\,dx = \frac{2}{3}ai_1^{3/2} \tag{44}$$

for the critical charge density.

As displayed in Fig. 10, $\sigma_c$ reveals a crossover from a planar-like scaling $\sigma_c \sim (\kappa a)^3$ for $\kappa a \gg 1$ to the dependence $\sigma_c \sim (\kappa a)^2$ for $\kappa a \ll 1$. The latter relation follows by an asymptotic expansion of the Bessel functions $K_1(\kappa a)$ for small arguments, which yields:

$$|\sigma_c| = \frac{ai_1^3\epsilon k_B T l}{54\pi|\rho|a}\left(\int_0^{\infty}\sqrt{K_0(x)}\,\mathrm{d}x\right)^{-2}\kappa^2, \tag{45}$$

with $\int_0^{\infty}\sqrt{K_0(x)}\mathrm{d}x = 2.12$.

In the adsorbed state, the eigenfunctions $\psi$ follow from (36). In particular, the asymptotic radial dependence of the eigenfunction in the regime $r > r_0$ can be determined. Here, $\xi$ is given by:

$$|\xi(r)| = \frac{1}{\kappa}\int_{\kappa r_0}^{\kappa r}\sqrt{\frac{6}{l}\left(|\lambda_0| - \theta\frac{K_0(\kappa r)}{K_1(\kappa a)}\right)}\mathrm{d}r, \tag{46}$$

which yields for $\kappa r_0 \gg 1$ the relation $|\xi(r)| = \sqrt{6|\lambda_0|/l}r$. Then, expansion of the Airy function yields:

$$\psi_0(r) = N_c\left(\frac{l\kappa}{6|\lambda_0|r^2}\right)^{1/4}\mathrm{e}^{-r\sqrt{6|\lambda_0|/l}} \tag{47}$$

for $r \gg r_0$. We emphasize the rather strong dependence of the decay length in this equation on the eigenvalue $\lambda_0$.

The radial polyelectrolyte density profile follows from:

$$P(r) = \frac{r\psi_0(r)^2}{\int r\psi_0(r)^2\mathrm{d}r}. \tag{48}$$

### 4.4 Spherical Surface

The radial equation for the Green function is given by (17) with $V_{\mathrm{H}}(r)$ replaced by the potential $V_{\mathrm{DH}}(r)$ of (15). The substitution $\varphi_0(r) = r\psi_0(r)$ for the eigenfunction yields the WKB-like equation $d^2\varphi_0/dr^2 + Q(r)^2\varphi_0 = 0$, with [48]:

$$Q^2 = \frac{6}{l}\left(\lambda_0 + \theta\frac{\kappa a^2}{1+\kappa a}\frac{\mathrm{e}^{-\kappa(r-a)}}{r}\right). \tag{49}$$

The point $r_0$ of zero potential follows from the equation:

$$\frac{\mathrm{e}^{-\kappa r_0}}{r_0} = \frac{6|\lambda_0|(1+\kappa a)}{\theta\kappa a^2 l}\mathrm{e}^{-\kappa a}. \tag{50}$$

As before, the boundary condition at the surface of the sphere leads to the equation:

$$\int_a^{r_0}\sqrt{\frac{6}{l}\left(\frac{\theta\kappa a^2}{1+\kappa a}\frac{\mathrm{e}^{-\kappa(r-a)}}{r} - |\lambda_0|\right)}\mathrm{d}r = \frac{2}{3}ai_1^{3/2} \tag{51}$$

in the interval $a < r < r_0$, which determines the eigenvalue $\lambda_0$. At the adsorption transition, when $\lambda_0 = 0$ implying $r_0 \to \infty$, we find the critical surface charge density:

$$|\sigma_{\mathrm{c}}| = \frac{ai_1^3\epsilon k_{\mathrm{B}}Tl\kappa(1+\kappa a)}{108\pi^2 a^2|\rho|}\frac{\mathrm{e}^{-\kappa a}}{\left[\mathrm{erfc}\left(\sqrt{\kappa a/2}\right)\right]^2}, \tag{52}$$

with the complementary error function $\mathrm{erfc}(x)$. The dependence of $\sigma_{\mathrm{c}}$ on $\kappa$ is shown in Fig. 10. For $\kappa a \gg 1$, the result (38) of a planar surface is obtained, which also follows analytically from (52). In the limit $\kappa a \ll 1$, we find the relation:

$$|\sigma_{\mathrm{c}}| = \frac{ai_1^3\epsilon k_{\mathrm{B}}Tl}{108\pi^2 a^2|\rho|}\kappa. \tag{53}$$

Hence, we find the same dependence on $\kappa$ as for the analytical solution exploiting the Hulthén potential [see (25)]. The ratio of (53) and (25) in the limit $\kappa a \ll 1$ gives 0.6. Thus, the two results deviate quantitatively by approximately 40%.

As before, the ground-state eigenfunctions $\psi_0$ for the regimes $r \gtrless r_0$ follow from (36). The radial density distribution is then obtained via (29).

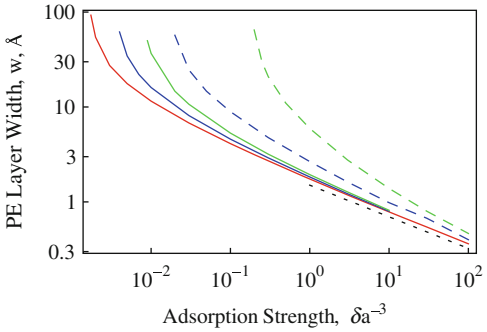


**Fig. 11** Thickness of the adsorbed polyelectrolyte layer near a planar (*red*), cylindrical (*blue*), and spherical (*green*) surface. The scaling relation $\Delta \sim |\sigma_c|^{-1/3}$ is indicated by the *black dotted line*. Parameters: $l = 30$ Å, $1/\kappa = 10$ Å, and $a = 1$ Å for the *dashed*, and $a = 10$ Å for the *solid curves* (for the cylinder and sphere case) [48]

## 4.5 Conformational Properties of Adsorbed Polyelectrolytes

As indicated for the various geometries, the density distribution of polyelectrolytes can be calculated within the WKB approximation. The profiles are comparable with those presented in Sect. 3.2.2 for the adsorption of polyelectrolytes onto a sphere. An interesting quantity is the thickness $\Delta$ of the polyelectrolyte layer. We define $\Delta$ as the full width at half maximum of the respective radial distribution function $P(r)$ [48, 59, 60]. As shown in Fig. 11, $\Delta$ behaves similar for all three geometries. It becomes more compact with increasing surface charge density and decreasing $\kappa$. Naturally, the width diverges when $\kappa a$ approaches the critical value for the adsorption threshold. Far from the adsorption transition, the various curves in Fig. 11 seem to exhibit the scaling dependence $\Delta \sim |\sigma|^{-1/3}$, consistent with scaling considerations for planar surfaces [8, 9, 69, 70]. We emphasize here that this scaling prediction is to be taken with caution for all three adsorbing geometries because it is assumed for very large adsorption strengths only. At such conditions, the spatial extension of very dense polyelectrolyte layers can be influenced by the presence of additional specific intrachain interactions neglected in the current model. Interestingly, the scaling relation suggests that the width $\Delta$ is independent of the radius of the cylinder or sphere. The scaling relations $\Delta \sim |\sigma|^{-3/8}$ and $\Delta \sim |\sigma|^{-2/5}$ have been discussed for planar and spherical surfaces, respectively [59, 60]. Both relations are close to the dependence $|\sigma|^{-1/3}$. For a sphere, however, an exponent different from 1/3 would imply a dependence of $\Delta$ on the sphere radius. The exponent 2/5 suggests a weak dependence $\Delta \sim a^{-1/5}$ on the radius $a$ [60].

# 5 Weak Adsorption: Discussion

## 5.1 Comparing Geometries

Applying various approaches (see Sects. 3 and 4), we determined the distinct scaling behavior for the critical surface charge density required to trigger adsorption of flexible polyelectrolyte chains onto a plane, a cylinder and a spherical surface as function of the Debye screening length $1/\kappa$ (see Fig. 3). A main conclusion is that the critical surface charge density scales as $\sigma_c \sim \kappa^3$ for a planar interface and all $\kappa$, whereas for cylindrical and spherical surfaces in the large-curvature or low-salt limit we find the relations $\sigma_c \sim \kappa^2$ and $\sigma_c \sim \kappa^1$, respectively. Generally, as the radius of surface curvature increases and the parameter $\kappa a$ grows, a transition takes place from the large curvature limit to the planar limit. For both the cylinder and sphere cases, this change in scaling laws appears at $\kappa a \approx 1$, i.e., when the radii of surface curvature become comparable to the Debye screening length (Fig. 10). For adsorption onto a cylindrical surface, the crossover to the planar limit occurs at somewhat smaller $\kappa a$ values than for the sphere situation.

Comparing the results obtained by the WKB method with the exact solutions for the planar and spherical surface, we find, within 2% error, quantitative agreement in the planar case. For a sphere, we find the same asymptotic dependence of $\sigma_c$ on $\kappa$ in the limit $\kappa a \ll 1$ and $\kappa a \gg 1$ for both approaches. Quantitatively, the results deviate somewhat for $\kappa a \ll 1$. Hence, the WKB method is a very valuable approach for studying critical adsorption behavior for a wide range of geometries. The main advantage of the WKB method is a unified approach for the various geometries based on the same level of approximations. It can be applied at the same level of complexity to virtually any shape of the polylectrolyte–surface adsorption potential. Recent advances in polyelectrolyte adsorption under confinement [49, 167] and adsorption onto low-dielectric interfaces [50] have been presented.

For a given $\kappa a$ value, the critical surface charge density required to initiate polyelectrolyte adsorption onto a sphere is always larger than that for adsorption on a cylinder. This, in turn, is larger than $|\sigma_c|$ required for adsorption onto a plane. Physically, as one changes from a plane to a rod and to a sphere, the entropic penalty of polyelectrolyte confinement near the surface is likely to grow. Correspondingly, the necessary surface charge densities $|\sigma_c|$ to initiate adsorption increase as well. Another, energy-based explanation is that a spherical surface offers less contact area [129] and thus larger surface charge densities are necessary for polyelectrolyte adsorption as compared with cylindrical and planar complexation. In the limit of $\kappa a \ll 1$, the reduction in the number of translational degrees of freedom for adsorbed polyelectrolytes appears to be coupled to the power of $|\sigma_c| \sim (\kappa a)^{\gamma+1}$. Namely, $\gamma = 2$ for the planar case with possible chain translations in two dimensions, $\gamma = 1$ for a cylinder with possible translations along its axis, and $\gamma = 0$ for sphere adsorption with no chain translational freedom at all.

It is also interesting to note that such a regular decrease in the power of $\kappa$ resembles the change in the laws of electrostatic repulsion between the particles of corresponding geometry in simple-salt solutions. Namely, at large interparticle separations $R$, $\kappa R \gg 1$, two uniformly charged planes, cylinders, or spheres repel each other according to the dependencies $\sim \mathrm{e}^{-\kappa R}$, $\sim \mathrm{e}^{-\kappa R}(\kappa R)^{-1/2}$, and $\sim \mathrm{e}^{-\kappa R}(\kappa R)^{-1}$ [168].

## 5.2 Comparison Between Theory and Experiment

An alternative technique to the described approaches is the variational principle to determine critical parameters [41, 56, 57]. The quality of the result, however, depends crucially on the applied trial function. Such an approach has been pursued for cylindrical and spherical surfaces [41, 56, 57]. For adsorption on a cylindrical surface, this method yields very good quantitative agreement with the WKB result for the critical adsorption condition $\sigma_c$. By contrast, for adsorption onto a sphere, the results of van Goeler and Muthukumar [56] disagree with the scaling predictions from the WKB model as well as from the approximate solution employing the Hulthén potential. Namely, in the limit of $\kappa a \ll 1$, the variational calculation predicts the dependence $|\sigma_c| \sim (\kappa a)^2$, both for the rod and sphere situations. Note that this variational technique employs a specific dependence of trial functions on the eigenvalues. Variational calculations have also been used to study polyelectrolyte adsorption onto a sphere [57]. As a result, the same dependence on $\sigma_c$ has been found as for the solution with the Hulthén potential and the WKB approach, but the numerical factor is different.

The complex formation between flexible and semiflexible, both biological and synthetic, polyelectrolytes with oppositely charged spherical colloidal particles, cationic or nonionic micelles, and dendrimers has been systematically studied experimentally by Dubin and coworkers [43, 44, 121–126, 128, 129]. The considered cationic micelles possess a homogeneously charged surface, which can be tuned continuously by addition of charged and uncharged groups up to several $e$ per 1,000 Å$^2$. Typically, the sphere diameter is 20–40 Å; however, considerably larger particles have also been studied. The polyelectrolyte persistence length $l_p = l/2$ is on the order of the sphere radius or smaller (approximately 30 Å for NaPSS, AMPS/AAm copolymers, and PDADMAC; 40 Å for hyaluronic acid; and 12 Å for PAA) [44, 130]. More flexible and more rigid polyelectrolytes have also been considered. The polyelectrolytes were in the intermediate charge density regime, typically below the threshold for the Manning counterion condensation [116, 163, 169–171].

Experiments have shown that no polyelectrolyte–micelle complexation occurs when the micellar surface charge density is below the critical charge density $|\sigma_c|$. Above this density, the turbidimetric titration curves reveal a dramatic increase in turbidity that indicates complexation, because the average molecular mass of the complexes is much larger than that of polyelectrolytes alone. The complexes may

consist of many chains and many colloidal spheres. A total charge close to zero of this polyelectrolyte–colloidal assembly is often a necessary condition for higher-order aggregation and phase separation in polyelectrolyte–colloid mixtures.

The critical density was shown to be nearly independent of the polyelectrolyte molecular weight and of the concentration in solution. Experiments have shown that, as the salt concentration in solution increases, the value of $|\sigma_c|$ grows and scales for spherical colloidal particles as [121, 128, 130]:

$$|\sigma_c| \sim \kappa^{b_l} \text{ with } b_l = 1 - 1.8. \tag{54}$$

The exponent $b_l$ depends also on the polyelectrolyte linear charge density $\rho$ and on the polyelectrolyte stiffness [130], which make it a nonuniversal characteristic for the used polyelectrolytes. Typically, polyelectrolytes with smaller $\rho$ reveal a stronger dependence of $\sigma_c$ on $\kappa$. The polyelectrolyte–sphere binding affinity was shown to decrease with the polymer persistence length and to increase with the polyelectrolyte linear charge density. Note that for complexation of polyelectrolytes of different $\rho$ with the spherical dimethyl dodecylamine oxide (DMDAO) micelles, a modified dependence on the critical micelle charge density has been suggested, namely $|\sigma_c| \sim \kappa^{1.8}\rho^{-0.6}$ [128].

The size of some micelles, e.g., DMDAO, as well as their shape can change with $\kappa$. At large salt content, cylindrical rather than spherical micelle shapes are observed. For cylindrical micelles, larger scaling exponents are usually measured than for spherical micelles of the same composition, e.g., from $b_l \approx 1.4$ for PVAS-DMDAO to $b_l \approx 2.5$ for P(AMPS/AAm)-DMDAO complexes [128, 129]. DMDAO micelles also form complexes with quite persistent polyelectrolytes such as double-stranded DNA, with an exponent $b_l \approx 1.6$ [129]. This weaker $\kappa$ dependence on the polyelectrolyte–sphere critical adsorption is consistent with our theoretical result in the low-salt limit. Moreover, although the micelle surface charge density is proportional to the degree of micelle protonation, which is controlled in experiments via the pH value, the exact relation for every micelle type is not known. The surface charge density has therefore been obtained for some systems from the pH titration data via calculation of the surface potential of the micelle using the Debye–Hückel solution (15) on the sphere surface.

Experimental values of $\sigma_c$ ($\kappa$) extracted from several studies on polyelectrolyte–sphere complexation performed by Dubin and coworkers have been presented [59]. The experimentally determined exponents $b_l$ are typically smaller than those obtained theoretically over the relevant range of $\kappa a$ values; the prediction of the model in this range is already close to the regime $|\sigma_c| \sim \kappa^3$. However, the electrostatic part of the polyelectrolyte persistence length $l_p^{el}$ decreases with $\kappa$, where the scaling relation $l_p^{el} \sim \kappa^{-1}$ is observed experimentally for flexible polyelectrolytes, e.g., polyacrylamides such as P(AMPS/AAm) [172]. Theoretical calculations [41, 149, 163] and computer simulations [148, 161] predict:

$$l_p^{el} \sim \kappa^{-4/5} - \kappa^{-6/5}, \tag{55}$$

whereas Odijk [164] and Skolnick and Fixman [165] suggest the rod limit $l_p^{el} \sim \rho^2 \kappa^{-2}$. The dependence of the persistence length on $\kappa$ has been reexamined theoretically in detail [147]. The salt-dependent renormalization of the persistence length can modify the predicted $\kappa$ dependence of $\sigma_c$ at high salt concentrations, thus providing slopes closer to those observed experimentally of about 1–1.8.

We do not attempt here a quantitative comparison with the experimental data because our model of a single sphere complexed by a flexible polyelectrolyte is too simple for this purposes and it neglects some important structural features of colloids and polyelectrolytes. Instead, the complexation of semiflexible polyelectrolytes with a sphere needs to be considered, which is a challenging problem that so far has remained untouched.

Complex formation of polyelectrolytes with some globular proteins (e.g., serum albumin, lysozyme), which possess nonhomogeneous charge distributions, has also been studied in experiments [124, 132, 137, 173]. Some additional interesting effects were detected. For instance, it was shown that polyelectrolyte–protein binding can occur on the wrong side of the isoelectric point. Moreover, the negatively charged polyelectrolytes were shown to bind to net negatively charged proteins due to polyelectrolyte electrostatic attraction to positive charge patches on the protein surface [124]. In some cases, the strength of polyelectrolyte–protein binding was shown to reach a maximum or a plateau at 10–30 mM of simple salt in solution. It was suggested that the corresponding Debye screening lengths are on the order of the protein size or of the typical separation of negatively and positively charged domains on the protein surface. Then, at such values of $\kappa$ the electrostatic attraction of polyelectrolytes to positively charged protein domains is substantial, whereas the repulsion from negatively charged regions is already screened [131, 173] (short-range attraction and long-range repulsion paradigm).

Further theoretical studies are required to include this charge patchiness in the model of electrostatic complexation of polyelectrolytes with oppositely charged objects, with the ultimate model example being the adsorption of polyelectrolytes onto Janus-like net-neutral particles with oppositely charged hemispheres [174]. Moreover, in order to clarify the appearance of polyelectrolyte-induced bridging attraction between two spherical particles [175–177], the influence of the length of a polymer and its charge density on the properties of the (onset of) aggregation process and the structure of the resulting coacervates can be studied in experiments.

## 6 Strong Adsorption: Theoretical Model

In the limit of strong adsorption, the polyelectrolyte adsorption energy is large compared to the thermal fluctuations of the polymer chain. Hence, the structural properties of adsorbed chains are essentially governed by maximization of polyelectrolyte–surface electrostatic interactions and minimization of polyelectrolyte–polyelectrolyte repulsion [59]. Therefore, we consider a polyelectrolyte chain

as an infinitely thin uniformly charged string, which assumes a definite conformation on the adsorbing surface. For simplicity, no distribution of charges underneath the surface is considered, but only a uniformly charged surface. Moreover, the dielectric constant of the surface bulk material is the same as the dielectric constant of the solution (namely that of water, $\epsilon \approx 80$) to avoid complications emerging from the appearance of image charges underneath the surface [50]. No effects of charge fluctuations on the polymer and on the surface are taken into account and neither are charge–charge correlations (see [178, 179] for more results).

The total energy of an adsorbed polyelectrolyte comprises several contributions. The most important of these are the electrostatic energy $E_{\mathrm{el}}$ of the polyelectrolyte in the electrostatic potential of the surface $\phi$ and the bending energy $E_{\mathrm{b}}$ due to possible conformational changes. We will not explicitly take into account polyelectrolyte charge–charge or excluded-volume interactions; they are instead implicitly considered by specific charge distributions $\rho(\mathbf{r})$.

The electrostatic energy of a polyelectrolyte with the charge density $\rho(\mathbf{r})$ in the electrostatic potential $\phi(\mathbf{r})$ is given by:

$$E_{\mathrm{el}} = \frac{1}{2} \int \phi(\mathbf{r}) \rho(\mathbf{r}) \, \mathrm{d}^3 r. \tag{56}$$

The electrostatic potential above the surface follows from the Poisson–Boltzmann equation. We apply the linearized Poisson–Boltzmann equation:

$$\Delta \phi(\mathbf{r}) = \kappa^2 \phi(\mathbf{r}), \tag{57}$$

i.e., we consider the limit $|e\phi| \ll k_{\mathrm{B}} T$. This is not necessarily a contradiction of the assumption of strong adsorption because a polyelectrolyte chain is long and highly charged.

The mechanical bending energy is associated with the rigidity of the polyelectrolyte $l = 2l_{\mathrm{p}}$ and is therefore given by the Kratky–Porod energy [180]:

$$E_b = k_{\mathrm{B}} T \frac{l_{\mathrm{p}}}{2} \int \left( \frac{\partial^2 r(s)}{\partial s^2} \right)^2 \mathrm{d}s. \tag{58}$$

We will next address the adsorption of DNA-like molecules onto cylindrical and spherical surfaces. Figure 12 shows possible wrapping scenarios for a cylinder and a sphere.

## 6.1 Adsorption at a Cylindrical Surface

We consider an infinitely long cylinder of radius $a$ oriented along the $z$-axis of the Cartesian reference frame. It has a uniform charge density $\sigma(z, \phi) = -\sigma_{\mathrm{c}} > 0$.

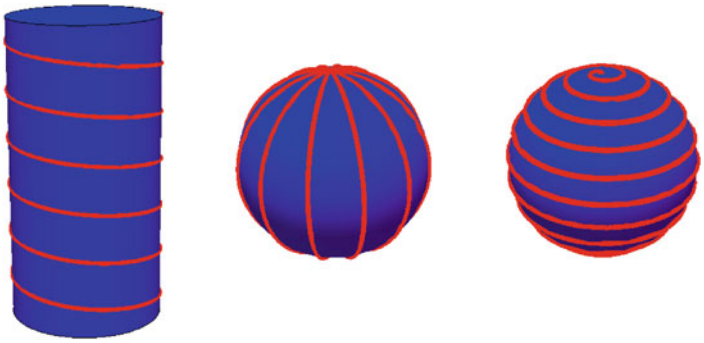

**Fig. 12** Wrapping of a polyelectrolyte around a uniformly charged cylinder and sphere. Various scenarios are possible: helices for cylinders (*left*) and, e.g., semi-circles (*middle*) or spirals (*right*) for spheres

Hence, the volume charge density $\rho$ is related to the surface charge density according to:

$$\rho(\mathbf{r}) = \rho(r, \varphi, z) = \delta(r - a)\sigma(z, \varphi). \tag{59}$$

The surface charge density is modulated by adsorbed polyelectrolytes.

### 6.1.1 Electrostatic Potential

In terms of cylindrical coordinates, the Poisson–Boltzmann equation (57) turns into [78]:

$$\frac{\partial^2\phi}{\partial r^2} + \frac{1}{r}\frac{\partial\phi}{\partial r} + \frac{1}{r^2}\frac{\partial^2\phi}{\partial\varphi^2} + \frac{\partial^2\phi}{\partial z^2} = \kappa^2\phi. \tag{60}$$

Applying the Fourier transformation of the potential:

$$\phi(r, \varphi, z) = \frac{1}{2\pi}\int_{-\infty}^{\infty} \mathrm{e}^{\mathrm{i}kz} \sum_{n=-\infty}^{\infty} \mathrm{e}^{\mathrm{i}n\varphi}\phi(r, n, k)\,\mathrm{d}k, \tag{61}$$

with:

$$\phi(r, n, k) = \frac{1}{2\pi}\int_{-\infty}^{\infty}\int_{0}^{2\pi} \mathrm{e}^{-\mathrm{i}kz}\,\mathrm{e}^{-\mathrm{i}n\varphi}\phi(r, \varphi, z)\,\mathrm{d}\varphi\,\mathrm{d}z, \tag{62}$$

the equation for the radial dependence:

$$\frac{\mathrm{d}^2\phi(r,n,k)}{\mathrm{d}(\kappa_k r)^2}+\frac{1}{\kappa_k r}\frac{\mathrm{d}\phi(r,n,k)}{\mathrm{d}(\kappa_k r)}-\left(\frac{n^2}{(\kappa_k r)^2}+1\right)\phi(r,n,k)=0 \tag{63}$$

is obtained, where $\kappa_k=\sqrt{k^2+\kappa^2}$ is the wave-length dependent screening parameter. With the boundary condition:

$$\left.\frac{\mathrm{d}\phi(r,n,k)}{\mathrm{d}r}\right|_{r=a}=-\frac{4\pi\sigma(k,n)}{\epsilon} \tag{64}$$

on the cylinder surface and a vanishing potential for $r\to\infty$, we find the potential:

$$\phi(r,n,k)=-\frac{4\pi\sigma(k,n)}{\epsilon}\frac{K_n(\kappa_k r)}{\kappa_k K_n'(\kappa_k a)}. \tag{65}$$

Here, $\sigma(k, n)$ is the Fourier transformed surface charge density $a(z,\varphi)$, the $K_n(r)$ are modified Bessel functions of the second kind [153], and the $K_n'(r)$ denote their derivatives.

The electrostatic energy (56) can be expressed by the potential $\phi\ (r, n, k)$ and the charge density $\sigma(k, n)$ according to:

$$E_{\mathrm{el}}=-(2\pi)^2 a\int_{-\infty}^{\infty}\sum_{n=-\infty}^{\infty}\frac{|\sigma(k,n)|^2}{\epsilon\kappa_k}\frac{K_n(\kappa_k a)}{K_n'(\kappa a)}\mathrm{d}k \tag{66}$$

### 6.1.2 Helical Charge Distributions

Double Helix

In a first step, we determine the potential of a charge distribution in the form of a double helix wrapped around a cylinder. The cylinder serves as a confining surface only, with cylinder–polyelectrolyte interactions being taken into account via the electrostatic self-energy of the complex.

We model the double helix by two negatively charged strings on the surface of an infinitely long cylinder. The helices are right-handed with the helical pitch $H>0$ and are separated by the distance $h$ along the axis of the cylinder. The charge density $\sigma(z, \varphi)$ of the strings is [78]:

$$\sigma(\varphi,z)=\pi\sigma_{\mathrm{p}}\sum_{n=-\infty}^{\infty}\left[\delta(\varphi+2\pi n-gz)+\delta(\varphi+2\pi n-g(z+h))\right] \tag{67}$$

with $g = 2\pi/H$. Here, $\sigma_p$ is the mean polymer surface charge density per pitch, i.e., $\int \sigma(\varphi, z) a \, d\varphi \, dz = Q = \sigma_p 2\pi a H$, where $Q$ is the total charge per pitch of the two strings of the double helix. Fourier transformation for this charge distribution yields:

$$\sigma(k, n) = \frac{\pi}{2} \sigma_p \delta(k + ng)[1 + e^{-ingh}]. \tag{68}$$

With the Fourier coefficients (65), the electrostatic potential is the sum of harmonics (see also [181]):

$$\phi(r, \varphi, z) = -\frac{2\sigma_p a}{\epsilon} \left\{ \frac{K_0(\kappa r)}{\kappa a K_1(\kappa a)} + \sum_{n-1}^{\infty} \frac{[\cos(n[\varphi - gz]) + \cos(n[\varphi - gz] + ngh)] K_n(\kappa_n r)}{\kappa_n a K_n'(\kappa_n a)} \right\}. \tag{69}$$

The renormalized reciprocal screening length for the $n$th harmonic is the combination of Debye screening length and "structural" screening length due to the charge periodicity:

$$\kappa_n = \sqrt{\kappa^2 + n^2 (2\pi/H)^2}. \tag{70}$$

The term $n = 0$ in (69) corresponds to the potential $\phi_0(r)$ of a uniformly charged cylinder. The terms with $n \neq 0$ are "corrections," which reflect the helicity of the charge distribution. These potential terms vary along the helix and may produce an accumulation of mobile cations in the vicinity of the negatively charged helical strings (see Fig. 13).

The electrostatic self-energy (66) per length (per pitch) of the helices becomes [78]:

$$E_{el} = \frac{2\pi\sigma_p^2 a^2}{\epsilon} \left[ \frac{K_0(\kappa a)}{\kappa a K_1(\kappa a)} - \sum_{n=1}^{\infty} \frac{[1 + \cos(ngh)] K_n(\kappa_n a)}{\kappa_n a K_n'(\kappa_n a)} \right] > 0. \tag{71}$$

The term with $n = 0$ corresponds to the self-energy of a uniformly charged cylinder with surface charge density $\sigma_p$. The terms with $n \neq 0$ are again corrections to this energy caused by the discrete, helical character of the charged strings. $E_{el}$ (71) has a minimum at $h = H/2$, where the electrostatic repulsion between the helical strings is minimal. When $H$ decreases, $\kappa_n$ increases and the electrostatic interaction becomes effectively better screened. Thus, the sum in (71) favors $H \to 0$. The value of each term in the sum decreases with $\kappa$ and $a$ because the function $K_n(\kappa a)/\left(-\kappa a K_n'(\kappa a)\right)$ decays with $\kappa a$.

In the limit $h \to 0$, we obtain the energy density for a single strand:

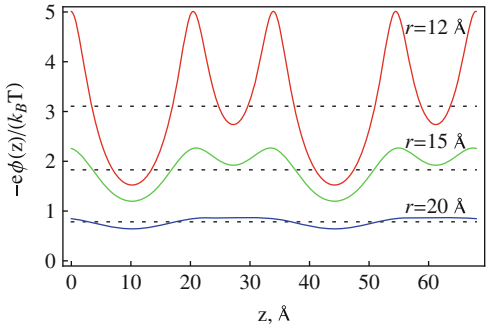


**Fig. 13** Electrostatic potential of a double helix with *B*-DNA parameters (with no adsorbed cations) according to (69) with $\varphi = 0$ at physical salt concentration [78]. The potential variation decreases for larger distances from the molecular axis. The *dotted lines* indicate the potentials of the corresponding uniformly charged cylinder

$$E_{\mathrm{el}} = \frac{2\pi\sigma_{\mathrm{p}}^2 a^2}{\epsilon}\left\{\frac{K_0(\kappa a)}{\kappa a K_1(\kappa a)} - 2\sum_{n=1}^{\infty}\frac{K_n(\kappa_n a)}{\kappa_n a K_n'(\kappa_n a)}\right\}. \tag{72}$$

This corresponds to the situation considered by Kunze and Netz [77]. The energy terms are, however, different. The authors find $E_{\mathrm{el}} \sim \tau_{\mathrm{p}}\eta(\eta - 1)$, where $\tau_{\mathrm{p}}$ is the linear charge density per pitch and $\eta = \sqrt{1 + (2\pi a/H)^2}$ [77], whereas our solution of the Poisson–Boltzmann equation yields $E_{\mathrm{el}} \sim \tau_{\mathrm{p}}\eta^2$. This difference has severe consequences on overcharging of cylinders, as we will discuss in the next section.

### Double-Stranded Jellium Helix

We now consider two negatively charged helical strings adsorbed on the surfaces of a positively charged cylinder. Because the cylinder charges are distributed homogeneously on its surface, we refer to this system as the "jellium" helix.

The charge density is now given by:

$$\sigma(\varphi, z) = -\sigma_{\mathrm{c}} + \pi\sigma_{\mathrm{p}}\sum_{n=-\infty}^{\infty}[\delta(\varphi + 2\pi n - gz) + \delta(\varphi + 2\pi n - g(z+h))], \tag{73}$$

where $\sigma_{\mathrm{c}}$ is the surface charge density. The corresponding electrostatic energy density is:

$$E_{\mathrm{el}} = \frac{2\pi\sigma_{\mathrm{c}}^2 a^2}{\epsilon}\left\{\frac{K_0(\kappa a)}{\kappa a K_1(\kappa a)}(1-\hat{\theta})^2 - \hat{\theta}^2\sum_{n=1}^{\infty}\frac{[1+\cos(ngh)]K_n(\kappa_n a)}{\kappa_n a K_n'(\kappa_n a)}\right\}, \tag{74}$$

where we introduced the ratio:

$$\hat{\theta} = \sigma_{\mathrm{p}}/\sigma_{\mathrm{c}}. \tag{75}$$

The repulsion between the strings does not favor full compensation of the cylinder charge by wrapped strings, and the complex is usually undercharged. In the limit $h \to 0$, the energy density of a single string is obtained. Finally, $E_{\mathrm{el}}$ decreases nearly exponentially with $\kappa$ at large $\kappa a$.

The molecule with the charge distribution (73) can be considered as a model for a *B*-DNA helix: charges on the strands represent the phosphates and the cylinder charge corresponds to adsorbed cations, smeared on the DNA surface (for *B*-DNA, $a \approx 10$ Å, $h \approx 0.4\ H$ [182]). Note that (74) could also be used for the description of electrostatically induced conformational changes of DNA, e.g., for the *B*- to *Z*-DNA transition at high salt concentrations [183]. Moreover, the exact theory of electrostatic interaction between two DNA duplexes predicts an attraction between them due to a correlated structure-driven zipper-like charge separation along the molecules [184].

### Multistranded Jellium Helix

The model for two strands can easily be extended to a situation with many adsorbed strands [78]. For $N_{\mathrm{s}}$ helical negatively charged strands, equally separated on the surface of a positively charged cylinder, the charge distribution is given by:

$$\sigma(z,\varphi) = -\sigma_{\mathrm{c}} + \pi\sigma_{\mathrm{p}} \sum_{m=-\infty}^{\infty} \sum_{s=0}^{N_s-1} \delta(\varphi + 2\pi m - g(z + sH/N_{\mathrm{s}})). \tag{76}$$

Here $\sigma_{\mathrm{p}}$ denotes the mean surface charge density for each string and $H/N_{\mathrm{s}}$ is the separation between the strings along the cylinder axis. If the total charge density of the strings $N_{\mathrm{s}}|\sigma_{\mathrm{p}}| = |\sigma_{\mathrm{c}}|$, they totally compensate the charge of the cylinder. The electrostatic energy density of the charge density (76) is given by:

$$E_{\mathrm{el}} = \frac{2\pi\sigma_{\mathrm{c}}^2 a^2}{\varepsilon} \left\{ \frac{K_0(\kappa a)}{\kappa a K_1(\kappa a)} (1-\hat{\theta})^2 - \hat{\theta}^2 \sum_{j=1}^{\infty} \frac{2K_j N_s(\kappa_j N_s a)}{\kappa_j N_s a K_j' N_s(\kappa_j N_s a)} \right\}. \tag{77}$$

The product $jN_{\mathrm{s}}$ gives the index of the functions $K_n(\kappa_n a)$. For $N_{\mathrm{s}} = 2$, the expression (77) turns into (74) [only the terms with even $n$ survive in (74) for $h = H/2$]. The energy density for a single string follows for $N_{\mathrm{s}} = 1$. This corresponds to the situation considered by Kunze and Netz [77]. However, the expressions for the energies are different, as mentioned in the last Sect. 6.1.2 (Double Helix).

The first term in (77) vanishes when the strings fully compensate the charge of the cylinder. Thus, this term favors a finite value of $H$, i.e., a helical conformation of the strings. The second term (the sum) represents the repulsive interaction between the strings. The sum is always negative, because $K_n'$ is negative. Hence, this term

will lead to a larger pitch than that given by the first term alone. As a consequence, the complex will at best be neutral or its effective charge $\sigma_{\text{eff}} = \sigma_c - \sigma_p$ will exhibit the same sign as the cylinder, in contrast to the findings of Kunze and Netz [77].

Bending Energy

The mechanical bending energy (58) associated with the rigidity of a string does not favors helical conformations. Larger persistence lengths $l_p$ and smaller cylinder radii result in a higher bending energy for the wrapped conformation. The parameterization $\mathbf{r}(s) = \{a\cos[2\pi s/(\eta H)],\ a\sin[2\pi s/(\eta H)],\ s/\eta\}^T$ of the contour vector $\mathbf{r}(s)$ along the helix yields for the bending-energy density for a cylinder with $N_s$ wrapped strings:

$$E_b(H) \approx \frac{l_p N_s k_B T}{2\eta H}\int_0^{\eta H}\left(\frac{\partial^2 \mathbf{r}(s)}{\partial s^2}\right)^2 \mathrm{d}s = \frac{l_p N_s k_B T}{2}\frac{(2\pi/H)^4 a^2}{\left[1+(2\pi a/H)^2\right]^{3/2}}. \tag{78}$$

### 6.1.3 Results for Helical Charge Distributions

The optimal helical pitch of the complex is found by minimizing the total energy:

$$E(\sigma_p, \sigma_c, \kappa, N_s, H, a) = E_{el}(\sigma_p, \sigma_c, \kappa, N_s, H, a) + E_b(H, a, l_p, N_s). \tag{79}$$

Figure 14 shows results for the optimal pitch for complexes of various string numbers $N_s$ in the case of constant surface charge density $\hat{\theta} = 1$ of the strings and of the cylinder. As expected, the optimal $H$ value increases with increasing chain stiffness. The optimal $H$ also increases with $N_s$ because of the higher total bending energy. For larger $\kappa$, the optimal pitch increases because the electrostatic interaction is more efficiently screened and the same bending energy leads to an energy minimum at larger $H$. Note that the calculation of the optimal number of strings $N_s$ and the part of the string attached to the cylinder, with cylinder and strings of finite size, requires the full free energy of charged semiflexible chains in solution, which is a more complicated task.

For constant linear charge densities $\tau_p$ and $\tau_c$ for weakly charged chains, where $\tau_p \ll \tau_c$, the electrostatic energy has a minimum at a finite value of $H$ and thus the helical conformation is favored for small $N_s$ values. Larger persistence lengths $l_p$ do not disfavor wrapping, as is evident from Fig. 15. Consequently, a smaller fraction of the cylinder charge $\hat{\theta} = \sigma_p/\sigma_c = \eta\tau_p/\tau_c$ is compensated by wrapped chains (see Fig. 15). The pitch increases with $N_s$ and with $l_p$, as shown in Fig. 15. For a given $\tau_p$ and $\tau_c$, beyond a certain number of adsorbed strings, the energy difference between a helical conformation and a conformation with straight rods is small. Hence, we may observe both kind of conformations, in particular when we

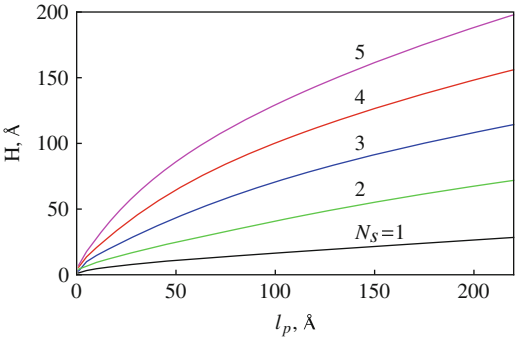


**Fig. 14** Optimal helical pitch of a complex with $N_s$ equidistant strings as a function of their persistence length for the parameters $\hat{\theta} = \sigma_p/\sigma_c = 1$, $a = 10$ Å, and $\sigma_c = \sigma_{B\text{-}DNA} = 16.8$ μC/cm$^2$ [(77) is used] [78]

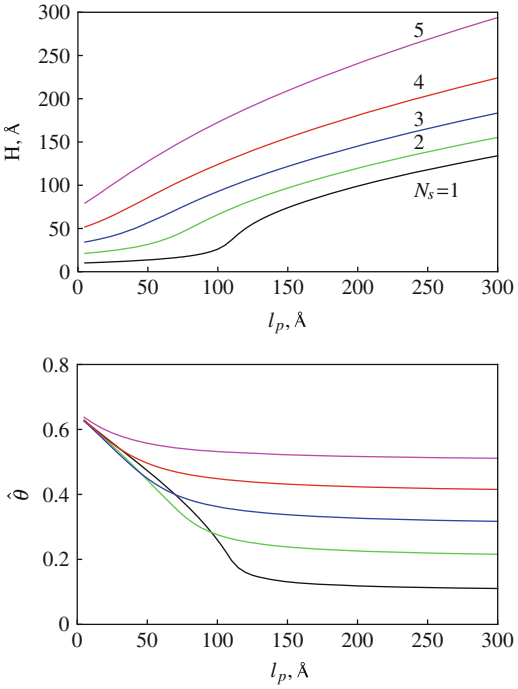


**Fig. 15** Optimal helical pitch (*top*) of a complex and its charge neutralization fraction $\hat{\theta} = \sigma_p/\sigma_c = \eta\tau_p/\tau_c$ (*bottom*), for constant $\tau_p$ and $\tau_c$ and for various strings [78]. Parameters: $a = 10$ Å, $\kappa = 1/[20$ Å$]$, $\tau_c = 1/$Å and $\tau_p = 0.1/$Å (the cylinder is ten times more strongly charged than each string)

take thermal fluctuations into account. This applies to the system with $N_s > 5$ in Fig. 15. Vice versa, for a given $N_s$ there is a threshold ratio $\tau_p/\tau_c$ above which the straight conformation is almost as favorable as the helical conformation and thermal fluctuation can induce transitions between these two states.

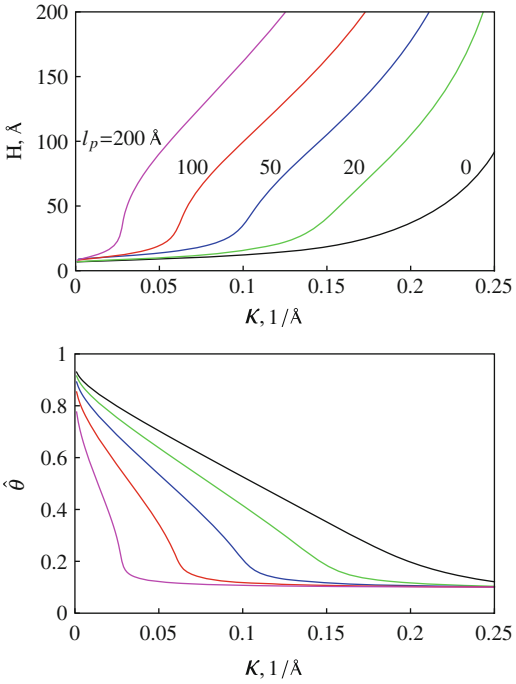


**Fig. 16** Optimal helical pitch (*top*) of a complex with a single adsorbed string ($N_s = 1$) and its charge neutralization fraction (*bottom*) as a function of $\kappa$ and for several values of the persistence length $l_p$ [78]. The other parameters are the same as for Fig. 15

With an increase in the cylinder radius, the corresponding electrostatic energy decreases for fixed linear charge densities. This can lead to higher values of the helical pitch (although $E_b$ decreases) and to a weaker charge neutralization of the cylinder by wrapped strings. With decreasing linear charge densities of polyelectrolyte strings, the value of the helical pitch increases more rapidly with the persistence length. Please note that in Fig. 15 such large $\tau_p$ and $\tau_c$ values are used that the linear Poisson–Boltzmann theory is no longer strictly applicable. But, it can provide an estimation of the features following from the full theory. With increasing salt concentration, the value of the optimal helical pitch increases for weakly charged chains (Fig. 16). At small $\kappa$, the electrostatic interaction is strong enough to compensate a large portion of the cylinder charge, whereas with increasing $\kappa$ the neutralization fraction $\hat{\theta}$ decreases rapidly. Figure 16 shows this dependence for $N_s = 1$ and for several values of the persistence length. The cylinder compensation parameter $\hat{\theta}$ never exceeds unity because such states are prohibited by the electrostatic self-energy penalty, which scales quadratically with the excess charge of the complex.

Our theory agrees with experiments on DNA–dendrimer well-ordered helical complexes, which display an increase in the pitch with decreasing dendrimer charge density [185]. Theoretical predictions of [77] indicate that the straight conformation of a single string adsorbed on an oppositely charged cylinder becomes favorable at

high salt concentrations. Our model also shows that, for a fixed number of strings $N_s$, the optimal $H$ increases when $\kappa$ increases (see Fig. 16) because $E_{el}$ decreases and the energy minimum shifts to larger $H$. In experiments, the pitch of DNA wrapped around dendrimers indeed increases with $\kappa$ for spherical [186] dendrimers, but it decreases for cylindrical dendrimers [187]. The helical pitch in salt-free solution of DNA wrapped around a cylindrical dendrimer was reported to be about $23 \pm 3$ Å [185]. This is smaller than the pitch of DNA in a nucleosome, $H \approx 24$–$27$ Å [13, 182], which is close to the equilibrium DNA–DNA separation in hexagonal aggregates [188, 189] and in two-dimensional DNA lattices [190, 191]. Note that in the region of interaxial separations (approximately 20–25 Å) a very strong DNA–DNA repulsion is detected [188]. The pitch of DNA–dendrimer complexes was reported to further decrease at higher salt concentrations [187]. An accompanying swelling of the dendrimers at high salt, however, complicates calculation of the real fraction of the neutralized dendrimer charge by wrapped DNA by our theory.

One might argue that the DNA persistence length decreases at high salt concentrations because the electrostatic persistence length $l_p^{el} \sim \kappa^{-2}$ decreases [164, 165]. The DNA could then wrap more densely around the cylinder. However, such effects should occur for spherical complexes also, but have not been observed in experiments. For colloids much larger than the DNA persistence length, nearly neutral complexes are often detected as a result of wrapping. For smaller colloids with dimensions $a \approx l_p$, when polymer bending severely impairs wrapping, strongly undercharged complexes have been detected, consistent with our predictions. This is illustrated in the article by Zinchenko et al. (see Fig. 3 in [192]).

Another unresolved issue is the charge of DNA–dendrimer complexes. Preferentially neutral complexes of DNA with spherical dendrimers were observed [186, 193], in contrast to a pronounced (up to a factor of 2) overcharging of cylindrical dendrimers by wrapped DNA [185]. The adsorption/attraction of a cylindrical complex onto a positively charged silica surface was used as evidence for overcharging. To have this attraction, however, the overcharging might not be required because the negative DNA charges are closer to the silica surface than the positive charges of the dendrimer and the net charge of the complex is not so relevant. Hence, advanced experiments are required to understand the nature of a possible overcharging of cylindrical DNA–dendrimer complexes.

## 6.2 *Adsorption at a Spherical Surface*

As mentioned in the Introduction, strongly adsorbed polyelectrolytes are able to form various patterns on spherical surfaces. We will limit our presentation to meridian-type polymer strings as shown in Fig. 12 (middle diagram), which cross at two points – the north and south poles [59]. Other charge patterns can also be

considered, but evaluation of the resulting energy expressions may be rather cumbersome.

For the considered spherical geometry, the charge density is of the general form:

$$\rho(r,\varphi,\vartheta) = \delta(r-a)\sigma(\varphi,\vartheta) \tag{80}$$

and depends on the spherical angles $\varphi$, $\vartheta$ only.

### 6.2.1 Electrostatic Potential

To solve the Poisson–Boltzmann equation (57) for the spherical geometry, we use the well-known expansion [194]:

$$\phi(r,\varphi,\vartheta) = \sum_{l,m} R_l(r) Y_{lm}(\varphi,\vartheta) \tag{81}$$

of the electrostatic potential in terms of spherical harmonics:

$$Y_{lm}(\varphi,\vartheta) = \sqrt{\frac{(2l+1)}{4\pi}\frac{(l-m)!}{(l+m)!}}\, P_l^m(\cos\ \vartheta)\, \mathrm{e}^{\mathrm{i}m\varphi}, \tag{82}$$

with $P_l^m(x)$ the associated Legendre polynomials ($l = 0, 1,\ldots; m = 0, \pm 1, \ldots, \pm l$) [153]. This leads to the equation:

$$\left[\frac{\mathrm{d}^2}{\mathrm{d}r^2} + \frac{2}{r}\frac{\mathrm{d}}{\mathrm{d}r} - \kappa^2 - \frac{l(l+1)}{r^2}\right] R_l(r) = 0 \tag{83}$$

for the radial function $R_l(r)$. The solution of the equation is:

$$R_l(r) \sim \frac{1}{\sqrt{\kappa r}} K_{l+1/2}(\kappa r) \tag{84}$$

for the boundary condition $R_l = 0$ in the limit $r \to \infty$ [153]. Hence, we obtain the potential [59]:

$$\phi(r,\varphi,\vartheta) = \sum_{l=0}^{\infty}\sum_{m=-l}^{l} C_{lm} Y_{lm}(\varphi,\vartheta)\frac{K_{l+1/2}(\kappa r)}{\sqrt{\kappa r}}. \tag{85}$$

The coefficients $C_{lm}$ are determined by the boundary condition at the sphere surface, which yields:

$$C_{lm} = -\frac{4\pi}{\epsilon k_l} \int_0^{2\pi} \int_0^{\pi} \sigma(\varphi, \vartheta) Y_{lm}^*(\varphi, \vartheta) \sin\vartheta \, \mathrm{d}\vartheta \, \mathrm{d}\varphi, \tag{86}$$

with the abbreviation:

$$k_l(a) = \frac{2\kappa a K'_{l+1/2}(\kappa a) - K_{l+1/2}(\kappa a)}{2a\sqrt{\kappa a}}.$$

$K'_{l+1/2}(x)$ is the derivative of $K_{l+1/2}(x)$ and $Y_{lm}^*$ is the complex conjugate of $Y_{lm}$.

The potential of the uniformly charged sphere $\phi_0(r)$ with the charge density $\sigma$ depends on $r$ only, i.e., only the term with $l = m = 0$ is relevant. Because $K_{1/2}(\kappa r) = \sqrt{\pi/2}\, \mathrm{e}^{-\kappa r}/\sqrt{\kappa r}$, one obtains from (85) the Debye–Hückel expression ($r > a$):

$$\phi_0(r) = \frac{4\pi a^2 \sigma}{\epsilon(1 + \kappa a)} \frac{\mathrm{e}^{-\kappa(r-a)}}{r}, \tag{87}$$

and:

$$E_0 = \frac{8\pi^2 a^3 \sigma^2}{\epsilon(1 + \kappa a)} \tag{88}$$

for the sphere electrostatic energy.

### 6.2.2 "Meridian" Charge Distribution

For a positively charged surface covered by $N_\mathrm{s}$ equally spaced negatively charged semicircles meeting at the north and south poles (see Fig. 12), $\sigma(\varphi, \vartheta)$ is given by [59]:

$$\sigma(\varphi, \vartheta) = -\sigma_\mathrm{s} + 2\pi\sigma_\mathrm{s}\hat{\theta} \sum_{s=0}^{N_s - 1} \delta\left(\varphi - \frac{2\pi s}{N_\mathrm{s}}\right), \tag{89}$$

i.e., the azimuthal angle of the $s$th semicircle is $\varphi = 2\pi s/N_\mathrm{s}$. $\hat{\theta}$ is the magnitude of the ratio of the total charge of the adsorbed polyelectrolyte and the surface charge. This charge density yields the electrostatic potential:

$$\phi(r, \varphi, \vartheta) = \phi_0(r)(1 - \hat{\theta}) + \frac{16\pi^2 \sigma_\mathrm{s} \hat{\theta}}{\epsilon} \sum_{l=0}^{\infty} \sum_{m=0}^{l} \frac{\delta_{m,jN_s}}{k_l} J_{lm} \frac{(2l+1)}{4\pi} \frac{(l-m)!}{(l+m)!} \times P_l^m(\cos\vartheta) \cos(m\varphi) \frac{K_{l+1/2}(\kappa r)}{\sqrt{\kappa r}}. \tag{90}$$

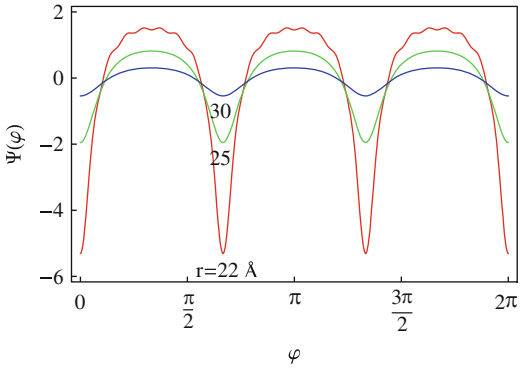


**Fig. 17** The "latitude" variation of the electrostatic potential of a spherical complex. Parameters: $a = 20$ Å, $\hat{\theta} = 1$, $\sigma_s = e_0/300$ Å$^2$, $\kappa^{-1} = 7$ Å, $N_c = 3$, $\vartheta = \pi/2$, $r = 22$, 25, and 30 Å (the potential variation is more pronounced close to the complex) [59]

The prime at the second sum indicates that the terms with $m = 0$ have to be multiplied by 1/2 and the term with $m = l = 0$ is not counted in the sum because it is included in the uniform part of the potential [59]. In the sum over $m$, only terms with $m = jN_s$ contribute, where $j$ is an integer. $J_{lm}$ is given by:

$$J_{lm} = \int_{-1}^{1} P_l^m(x)\, dx, \tag{91}$$

which can be expressed in terms of gamma functions and generalized hypergeometric functions [59, 153].

With (56), we obtain the electrostatic energy:

$$E_{el} = E_0(1-\hat{\theta})^2 - \frac{16\pi^3 a^2 \sigma_s^2 \hat{\theta}^2}{\epsilon} \sum_{l=0}^{\infty} {\sum_{m=0}^{l}}' \frac{\delta_{m,jN_s}}{k_l} J_{lm}^2 \frac{(2l+1)}{4\pi} \frac{(l-m)!}{(l+m)!} \frac{K_{l+1/2}(\kappa a)}{\sqrt{\kappa a}}. \tag{92}$$

The electrostatic potential (90) is the sum of the bare potential (87) and corrections due to the discreteness of the charge pattern. The dependence of the dimensionless potential $\Psi = e\phi/(k_B T)$ on the angles $\varphi$ and $\vartheta$ is depicted in Fig. 17. The magnitude of the potential variation decreases in the regions close to the "poles," i.e., when $\vartheta = 0, \pi$. The potential variations rapidly decrease as we move radially outward from the sphere and decreases with increasing number of circles. Note that although $\phi$ can be larger than unity for large values of $|\sigma_s|$, we expect our linear electrostatic model to grasp the potential variations qualitatively correctly.

Similarly, the energy of the complex consists of two terms. The first term is the energy of the sphere and of the uniformly smeared charge of the wrapped polyelectrolyte; this term favors electrically neutral complexes. The energy corrections from the

adsorbed polyelectrolyte circles (the second terms with the double sum) decrease in magnitude when the number of circles increases (provided that the total charge of the wrapped polymer is kept constant). Hence, within this model the adsorbed polyelectrolytes cannot overcharge the sphere. This result is similar to that discussed in the previous section for polyelectrolyte adsorption on an oppositely charged cylinder.

The mechanical bending energy follows from (58) by parametrization in terms of spherical coordinates. The contour $s$ of a circle is related to its angle via $s = a\vartheta$. Hence, we obtain for $N_s$ semicircles:

$$E_b = \frac{l_p \pi N_s k_B T}{2a}. \tag{93}$$

### 6.2.3 Results

The inevitable chain bending of polyelectrolytes with a rather large persistence length during adsorption on a spherical surface does not favor polyelectrolyte wrapping and shifts the equilibrium towards undercharged complexes. With the linear charge density $e/l_0$, the neutralization fraction:

$$\hat{\theta} = \left|\frac{e}{\sigma_s}\right| \frac{N_s}{4al_0} \tag{94}$$

decreases as the adsorbed polyelectrolyte becomes stiffer, as displayed in Fig. 18. With increasing number of circles, the energy corrections due to discreteness decrease in magnitude, i.e., the uniform energy term proportional to $(1-\hat{\theta})^2$ dominates, resulting in $\hat{\theta}$ values close to unity. According to (94), the optimal number of wrapped polyelectrolyte circles exhibits a similar persistence length dependence as $\hat{\theta}(l_p)$. For the parameters of Fig. 18, the maximal value of $N_s$ ($l_p \to 0$) is 27. Because $N_s$ is an integer number by definition, a staircase-like behavior for the optimal $\hat{\theta}$ is observed; with increasing $l_p$, the value of $N_s$ drops like $\hat{\theta}$ from 27 to 0 (94). For a weaker screening of the polyelectrolyte–sphere electrostatic attraction, more persistent polymers can be wrapped around the sphere (see Fig. 18). Similarly to Fig. 15 for the polyelectrolyte–cylinder charge compensation, Fig. 18 illustrates that the polyelectrolyte–sphere compensation fraction never exceeds unity, even for highly flexible chains and strong attraction conditions (realized at small $\kappa$ values).

At some critical value of $l_p$, the polyelectrolyte bending energy penalty exceeds the electrostatic attraction energy and $\hat{\theta}$ drops abruptly to zero, which corresponds to polyelectrolyte unwrapping, in complete analogy to the adsorption–desorption transition in the weak adsorption case. In the current model of strong adsorption of polyelectrolyte semicircles, the wrapping–unwrapping transition is of first order, in

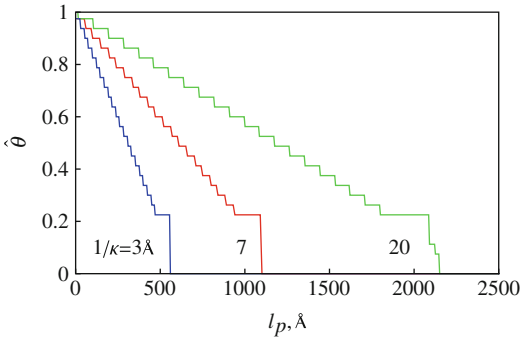


**Fig. 18** Dependence of the neutralization fraction $\hat{\theta}$ of polyelectrolyte complexes on the persistence length $l_p$. Parameters: $\sigma_s = e_0/30$ Å$^2$, $a = 20$ Å, $l_0 = 10$ Å, $1/\kappa = 3$, 7, and 20 Å [59]

contrast to the weak adsorption scenarios considered in Sects. 2–4 where the adsorption-deporption transition is rather continuous.

In general, adsorption of a polyelectrolyte directly onto a sphere surface occurs only if $l_p$ is smaller than a critical value, namely, when the energy gain upon adsorption exceeds the elastic energy cost of chain bending around the sphere. This condition is based on chain persistence and it results in two simple predictions for the adsorption–desorption equilibrium. For $\kappa a \gg 1$ adsorption occurs for $l_p < 2Zl_B/(l_0\kappa)$, where $Z = 4\pi a^2|\sigma_s/e|$ is the number of sphere charges. Thus, the sphere charge density scales like $|\sigma_s| \sim \kappa$ in this regime. In the limit of small $\kappa$, the electrostatic contribution to the persistence length has to be accounted for [164, 165], which leads to the inequality $Z > (8al_0\kappa^2)^{-1}$, i.e., we get $|\sigma_s| \sim \kappa^{-2}$. These scaling regimes were obtained after numerical minimization of the Debye–Hückel polyelectrolyte–sphere and the polyelectrolyte–polyelectrolyte interactions [71]. Such simple consideration can, however, result in a (unrealistically) high degree of sphere overcharging by wrapped polyelectrolytes – for instance, up to 30-fold overcharging for a complex mimicking a DNA–histone complex [71]. Another idea about overcharging of weakly charged spheres was suggested for the situation in which polyelectrolyte chains are in excess in the solution [76].

A strong overcharging of spherical particles covered by adsorbed strongly oppositely charged polyelectrolytes was predicted by Shklovskii and coworkers, who treated the problem by an approach reaching beyond the mean-field theory [83, 178, 195]. Their analysis was based on the image-charge attraction by additional polyelectrolytes at the adsorbing surface and on the picture of a strongly correlated liquid of polyelectrolytes on the substrate (Wigner crystal) [83, 178, 195]. The charge inversion, driven by repulsive correlations of polyelectrolytes on the macro-ion surface, was shown to become more pronounced with increasing salt concentration in the solution; it can reach up to 200–300% for solenoid-like complexes [83]. Although in our model the pattern of adsorbed polyelectrolytes also reveals strong correlations, they are treated within the mean-field Poisson–Boltzmann theory and thus isoelectric complexes are always favored energetically. Note also that, for polyelectrolytes of finite thickness, an asymmetric charge neutralization upon

polymer adsorption onto the sphere can result in overcharging of the complex, even in the mean-field description that might have relevance to overcharging of histone proteins by DNA in nucleosome core particles, as discussed previously [79].

Other scenarios, such as tennis-ball-like [83–85], rosette-like [73, 79], and equator-wrapping [192, 196] structures, are also possible candidates of ordered (Wigner-crystal-like) structures that minimize the electrostatic energy (see Figs. 2 and 12). For all these structures, in the strong adsorption limit, we expect to see nearly neutral or undercharged complexes within our model. At finite temperatures, the chain fluctuations are expected to diminish the amount of adsorbed polyelectrolytes. Inherently, the adsorption of a neutral fluctuating semiflexible polymer onto a spherical surface is a nontrivial problem [197, 198], and the presence of charges further complicates the behavior of the adsorbed polymer chain. However, we would like to point out that for uncharged polymers with large persistence lengths $4l_p > a$, the optimal conformation obtained by Spakowitz and Wang [197] is similar to the conformation treated in this section.

### 6.2.4 Experimental Results: DNA and Nucleosome

Our results on the formation of stable helical and solenoidal structures on cylinders and spheres in the strong adsorption limit are applicable in a wide range of physical systems. They include, e.g., the separation of carbon nanotubes by helical sequence-specific wrapping of single-stranded DNA molecules, which has been studied experimentally [199–203], theoretically [200, 204–208], and by computer simulations [209–211], as well as in helical patterning of charged interfaces [80–82, 212].

Specifically, the discussed wrapping scenario mimics certain properties of DNA–histone complexes in the nucleosome core particle (NCP), although various important details are neglected in the present analysis. However, if realistic charge patterns on the DNA, on the basic histone proteins, and on the highly charged histone tails are considered, then an exact treatment of the electrostatic interactions of an NCP becomes a complicated task, which is only likely to be solvable numerically [213–217]. Moreover, our results can be applied to complexation of DNA with synthetic colloidal oppositely charged nanoparticles, reminiscent of DNA–histone complexation in chromatin. For instance, DNA complexed with silica polylysine-coated nanospheres of charge density $\rho \approx e/\mathrm{nm}^2$ and with a diameter of 10–100 nm has been studied recently [192, 196]. DNA was shown to wrap around a nanoparticle from a few times up to about 40 times, depending on the sphere size and charge density. For a small number of turns, DNA is wrapped on the sphere equator, where the curvature is the smallest. The formation of large aggregates of DNA–nanoparticle complexes with 5–50 spheres per T4-phage DNA has been observed [192, 196]. As the nanoparticle concentration in solution increases, the aggregate becomes more and more compact. In the fully compacted state, the ratio between the total charge of the nanoparticles and the DNA charge depends on the particle size. Aggregates of small nanoparticles are strongly undercharged by wrapped DNA, whereas for the largest nanospheres at intermediate ionic strengths a small overcharging of the aggregates has been detected. Most efficient compaction has been achieved at nearly

physiological ionic strength, which is reminiscent of DNA–histone complexation in nucleosomes [218]. For salt concentrations above 1.5 M, when the electrostatic interactions are well screened, no DNA–nanosphere electrostatically-driven compaction could be achieved, whereas for low salt concentrations, when the electrostatic contribution to the DNA persistence length grows, compaction is suppressed by the bending energy penalty.

Note that typically electro-neutral aggregates are also observed in other dense self-assembled DNA nanostructures, e.g., DNA sandwich-like lamellar complexes with cationic lipids [191, 219–221], where complexation is suggested to be driven by the release of condensed counterions of DNA and of lipid head groups [222].

In general, electrostatic interactions in spherical complexes with arbitrary polyelectrolyte wrapping patterns and for arbitrary orientations of the complexes in space, pose a complicated mathematical problem. One can expect that the modulations of the electrostatic potential emerging in a solution near the complexes due to nonhomogeneous charge distributions will modify a DLVO-like pure repulsion between effective like-charged spheres [242]. Correlation-induced electrostatic attraction between complexes can occur when these potential modulations on the complexes are in phase: the potential patches of different sign face each other near the contact of the two complexes, forming an electrostatic zipper. The effective screening length of this electrostatic attraction $\sim (\kappa^2 + (2\pi/P)^2)^{-1/2}$ is a combination of $\kappa$ and of a typical period $P$ of alternating positive–negative patches on the surfaces. It is shorter than the decay length $1/\kappa$ of repulsive interactions between uniformly charged spheres. Thus, in order to overcome the net charge repulsion, the complexes should be neutralized to a large extent by the adsorbed polyelectrolytes $(\hat{\theta} \leq 1)$ and their separation should be smaller than $P$ (short-range attraction and long-range repulsion).

Such zipper-like electrostatic attraction could be one of the reasons for condensation of DNA molecules and of nucleosome core particles in solutions of some multivalent counterions (for a discussion see [25, 223]). Another possibility is internucleosomal attraction mediated by bridging interactions of flexible polypeptide histone tails [213, 224, 225]. The theoretical basis for such attraction driven by sharing of polyelectrolyte chains adsorbed simultaneously on two nucleosomes/macroions has been developed in [46, 175, 226, 227].

## 7 Limitations and Further Studies

The described theoretical concepts are certainly limited in their predictive power by the various underlying approximations that are adopted to derive analytical solutions. The following aspects apply (more or less) to weak and strong adsorption.

*Uniformly Charged Surface and Polymer Chain*—The implications of charge nonuniformities on surfaces and charge discreteness of adsorbing polyelectrolytes are not evident. Muthukumar studied the influence of surface-charge patchiness on

critical adsorption conditions within the variational trial function approach [228] (see also [52]). The main conclusion is that the critical surface charge density grows with decreasing size of the adsorption patch; however, it always remains larger than that for a uniformly charged surface and approaches this limit for larger enough charged patches. The effect of patterns on the adsorbing polyelectrolyte, and some degree of commensurability with the patchiness on the surface, are interesting issues for investigation in the future. Moreover, our model does not account for possible charge regulation effects on adsorbing surfaces and on polymer chains themselves caused by an approaching polyelectrolyte. Such effects are discussed for the adsorption of polyelectrolytes onto a titratable spherical particle [98]. Other effects such as a physical roughness of the adsorbing surface might also nontrivially alter the position of the adsorption–desorption threshold [229].

*Decoupling of Surface Potential and Polymer Surface Density*—This does not allow us to predict the amount of adsorbed polymer or the degree of surface charge compensation by the weakly adsorbed polyelectrolytes. In a more realistic model, the amount of already adsorbed polyelectrolyte should limit the adsorption of subsequent segments of the chain. Namely, the effective surface charge density of the adsorbing surface is renormalized by the adsorbed part of the polymer and thus the critical adsorption parameter has to grow in order to adsorb the entire chain. The corresponding eigenvalue equation is then, however, only amenable to a numerical solution [152, 226]. In the current model, the adsorbed polyelectrolyte layer effectively overcharges the surface because the charge density on the interface prior to the polyion adsorption is exactly balanced by small mobile counter- and co-ions from the electrolyte and the ionic distributions stay unchanged upon polyelectrolyte adsorption.

*Polymer Length*—We restrict ourselves to consideration of the ground state for the adsorption problem. For polymers shorter than a dozen Kuhn segments, the contributions of excited states to the Green function have to be taken into account. The value of the critical surface charge density is then expected to grow.

*Linear Versus Nonlinear Theory*—We apply the linear Debye–Huckel model to compute the electrostatic potential emerging near a charged surface. It is known, however, particularly at low salt concentrations, that the surface potential for the planar and curved interfaces can exceed the 25 mV allowed by this theory. In this limit, the full nonlinear Poisson–Boltzmann theory must be implemented, both for the surface [154, 230] and for the polyelectrolyte [231, 232]. Remarkably and quite unfortunately, the changes in scaling for the critical surface charge density predicted by our adsorption model occur in this limit of low salt. The electrostatic potentials in this limit are expected to be high and polyelectrolyte adsorption is therefore rather strong. Also, in the model the polyelectrolytes are treated as weakly charged, with the linear charge density below Manning's counterion condensation threshold.

*Low-Dielectric Interfaces*—The presence of a low-dielectric material beneath the adsorbing boundary has considerable implications for adsorption. In particular, in the proximity of such an interface the polyelectrolyte experiences a repulsive force from the image charges that effectively displace the polymer from the interfacial region of a high attractive potential. This image repulsion grows

quadratically with the polymer charge density. To compensate for this repulsion and to still trigger adsorption, higher critical adsorption parameters and surface charge densities are necessary, as we have shown recently [50]. Notably, for the planar interface in the limit of low salt $\kappa a \ll 1$, the scaling of $\sigma_c(\kappa)$ is also modified from the canonical cubical to a weaker quadratic dependence on $\kappa$. A contrary example of polyelectrolyte adsorption onto high-dielectric interfaces has been presented [233].

*Reversibility of Adsorption*—The employed model of weak adsorption implies reversible and equilibrium adsorption under all studied conditions. This assumption can be violated, particularly at low salt concentrations, when stronger and virtually irreversible adsorption of polyelectrolytes is expected to take place. There has to be a critical solution salinity below which the assumption of "weak" adsorption is no longer valid. The chains are likely to be adsorbed irreversibly (on experimentally relevant time-scales) by strong polyelectrolyte–surface attraction. Likewise, above some critical salinity and for well-shielded surface potentials, the kinetics of adsorption might be extremely slow on experimentally relevant timescales. The physical reason is that the polymer chains diffusing in solution are only rarely captured by a Debye-length-thin layer of attractive potential near the adsorbing boundary. In this review, we thus avoid many interesting issues regarding the kinetics of polyelectrolyte adsorption as a function of solution salinity and chain length, focusing instead on equilibrium properties and critical adsorption characteristics.

*Criterion for Adsorption*—A related issue is an experimentally relevant criterion for polyelectrolyte adsorption. The scaling relations presented above for critical adsorption are determined by the condition of a zero eigenvalue $\lambda_0$. This is certainly inaccessible in experiments. Often, the criterion for adsorption is chosen such that the chain is near the surface most of the time, say $>90\%$. Such a requirement will give rise to higher critical surface charge densities and to potentially different scaling relations.

*Possible Nonmonotonic Effect of Salt*—Our simple model neglects inter- and intrachain electrostatic interactions. The latter can be incorporated into the final result via an effective salt-dependent persistence length, whereas the former requires more elaborate adsorption models to be implemented. It has been found experimentally for adsorption of some polyelectrolytes [234] that the addition of salt has two major effects. The first effect, the standard screening of chain-surface attraction at higher salt, is captured in our model. The second effect is connected to the changes in polyelectrolyte stiffness. Namely, in the low-salt limit if the amount of salt is increased, the chain persistence length is reduced and the interchain electrostatic repulsions in the adsorbed layer are diminished. Both effects, neglected in our model, can facilitate polyelectrolyte adsorption at low-to-intermediate salt concentrations. This is in contrast to the progressively weaker adsorption at higher salt predicted by our model and caused by pure screening of polymer surface attraction [66]. More results are presented in a recent publication [235]. A nonuniform dependence of the amount of adsorbed polyelectrolyte on salt concentration, or screening-enhanced adsorption, which has been observed for a number of

polymers experimentally [236], is often a consequence of short-range nonelectrostatic chain–surface attraction.

*Nearly Gaussian Chains*—For weak adsorption, The conformational properties of adsorbing chains are assumed to be only weakly perturbed upon adsorption. This might not be true well above the adsorption threshold, when quite dense polymer layers are formed next to the interface. For critical adsorption conditions, however, this approximation is expected to be valid.

*Strong Adsorption Limit*—Similarly to the weak adsorption limit, the inherent limitations of the linearized electrostatic theory are to be remembered. Here, the limitations might be even more severe because some well-defined polyelectrolyte patterns are assumed in the model of polyelectrolyte–cylinder and polyelectrolyte–sphere complex formation, which require a strong polyelectrolyte–surface attraction. Although the adopted approach does not predict overcharging in these cases, dropping the assumption of an infinitely thin polyelectrolyte and including an asymmetric charge neutralization along the DNA–sphere contact [237, 238] reproduces the extent of nucleosome overcharging quite well [79]. In applications to DNA–histone wrapping, our model of a uniformly bendable nonstretchable worm-like chain should be severely modified [239, 240], if we are interested in the precise energetics of DNA wrapping, with site-specific DNA–histone interactions, sequence-specific curvature effects [241], and possible kinks in the structure.

## 8 Conclusions

In this review, we have summarized theoretical concepts and recent advances for the adsorption of linear polyelectrolyte molecules onto curved surfaces in the weak and strong adsorption limit. A mean-field description is adopted, and the interaction potentials between the polyelectrolyte and the surfaces are derived from the linearized Poisson–Boltzmann equation for the corresponding geometries (planes, cylinders, and spheres). The derivation of an exact analytical solution of the adsorption problem for curved surfaces is a major challenge and is yet unsolved.

In the weak adsorption limit, we provide an exact analytical solution for polyelectrolyte–sphere adsorption by replacing the Debye–Hückel potential by the Hulthén potential. Other geometries require different approaches. As a generic concept, we propose application of the WKB method of quantum mechanics, which we adopted to electrostatic polyelectrolyte adsorption problems. We have demonstrate that this description provides valuable analytical solutions and resolves a long-standing puzzle about the scaling properties of critical polyelectrolyte adsorption in curved geometries.

We have shown that the scaling behavior of the critical adsorption parameters indeed changes dramatically in the limit of low salinity or large curvature of the surface, e.g., for the critical surface charge density from $|\sigma_c| \sim \kappa^3$ for a plane to $|\sigma_c| \sim (\kappa a)^2$ for a cylinder and to $|\sigma_c| \sim (\kappa a)^1$ for the spherical surface. Maximal entropic penalty for polyelectrolyte confinement near a sphere and, concurrently, minimal energetic benefit from polyelectrolyte–surface attraction yield much larger

critical surface charge densities and weaker $\kappa a$ scaling in the low-salt limit. This consistent geometry-mediated decline in the scaling exponent for cylindrical and spherical surfaces is fully consistent with experimental data on polyelectrolyte complexation [129]. The data provide clear evidence that the planar Wiegel-like solution [40] does not reproduce the critical scaling behavior detected for instance in a series of experiments of the Dubin group. We hope that this fact, as well as the novel description of the underlying physics, will find a proper appreciation among experimentalists.

The issue of critical polyelectrolyte adsorption is intimately coupled to the polymer-mediated bridging attraction between oppositely charged macro-ions immersed in a polymer solution. Moreover, electrostatically driven self-assembly of single-stranded RNA molecules on the interior of positively charged capsids, as it occurs in many spherical and rod-like single-stranded viruses, offers another field for potential applications of our theoretical results. The WKB method developed above has recently been implemented to weak polyelectrolyte adsorption under confined conditions [49] and to adsorption onto low-dielectric interfaces [50]. The power of the WKB approach can even be extended to more complicated adsorption situations, such as patchy surfaces, specific charged patterns on concave and convex interfaces, Janus particles, etc., and other (nearly arbitrary) potentials of polyelectrolyte–surface interactions. This might open an avenue to approach more realistic situations of polyelectrolyte adsorption and to quantitatively reproduce experimental results in the future.

In the limit of strong adsorption, we analyzed the energetics of highly stable complexes of thin polyelectrolyte worm-like chains with cylindrical and spherical particles of opposite charge. An important conclusion here is that overcharging of complexes is penalized by the electrostatic Born self-energy term, rendering nearly neutral and undercharged complexed most abundant, in agreement with outcomes from a number of complexation experiments [192]. For a cylindrical surface, the applications of our results include a description of the phase transitions in DNA duplexes, wrapping of single-stranded DNAs onto carbon nanotubes, DNA wrapping on cylindrical dendrimer molecules, etc. For a spherical colloid, the wrapping of polyelectrolytes mimics in particular DNA complexation with the histone core proteins in nucleosomes. Moreover, the theoretical description of helical charge patterns of adsorbed polyelectrolytes on a cylinder and solenoidal wrapping of polyelectrolytes on a sphere offer a framework for addressing DNA–DNA and nucleosome–nucleosome electrostatic interactions [25].

The various concepts applied above are extremely useful and provide valuable insight into polyelectrolyte adsorption. Comparison with experimental results confirms a variety of predicted dependencies and provides a deeper understanding of the underlying physical phenomena. On the other hand, there are still a number of effects that cannot be accounted for by the current theoretical description. Here, further extensions and refinements of the models are necessary.

**Acknowledgements** We thank J.-F. Berret, P. Dubin, G. Manning, M. Muthukumar, H. Schiessel, S. Stoll, and M. Ullner for many insightful discussions and correspondence. Special thanks go to S. Stoll for providing us the snapshots presented in Figs. 1 and 2. The work was supported by the German Research Foundation, DFG grant CH 707/5-1 to AGC.

## References


1. Chakroborty AK, Golumbfskie AJ (2001) Annu Rev Phys Chem 52:537
2. O'Shaughnessy B, Vavylonis D (2005) J Phys Condens Matter 17(R63)
3. Takahashi A, Kawaguchi M (1982) Adv Polym Sci 46:1
4. Patel SS, Tirrell M (1989) Annu Rev Phys Chem 40:597
5. Lindström T (1991) In: Roberts JC (ed) Paper chemistry. Blackie, London, p 25
6. Tanaka H (1998) Paper. Dekker, New York, p 389 (Chap. 19)
7. Wågberg L, Forsberg S, Johansson A, Juntti P (2002) J Pulp Paper Sci 28:222
8. Netz RR, Andelman D (2003) Phys Rep 308:1
9. Dobrynin AV, Rubinstein M (2005) Prog Polym Sci 30:1049
10. Dobrynin AV (2008) Curr Opin Colloid Interface Sci 13:376
11. Boroudjerdi H, Kim Y, Naji A, Netz RR, Schlagberger X, Serr A (2005) Phys Rep 416:129
12. Wong C (2006) Curr Opin Colloid Interface Sci 11:310
13. Luger K, Mäder AW, Richmond RK, Sargent DF, Richmond TJ (1997) Nature 389:251
14. White CL, Suto RK, Luger K (2001) EMBO J 20:5207
15. Davey CA, Richmond TJ (2002) Proc Natl Acad Sci USA 99:1196
16. Ong MS, Richmond TJ, Davey CA (2007) J Mol Biol 368:1067
17. Vasudevan D, Chua EYD, Davey CA (2010) J Mol Biol 403:1
18. Tang S, Davey CA (2011) Curr Opin Struct Biol 21:128
19. Schiessel H (2003) Macromolecules 36:3424
20. Cherstvy AG (2009) J Phys Chem B 113:4242
21. Belyi VA, Muthukumar M (2006) Proc Natl Acad Sci USA 103:17174
22. Forrey C, Muthukumar M (2009) J Chem Phys 131:105101
23. Angelescu DG, Linse P, Nguyen TT, Bruinsma RF (2008) Eur Phys J E Soft Matter 25:323
24. Elrad OM, Hagan MF (2010) Phys Biol 7:045003
25. Cherstvy AG (2011) Phys Chem Chem Phys 13:9942
26. Wang J, Muthukumar M (2011) J Chem Phys 135:194901
27. Šiber A, Podgornik R (2008) Phys Rev E Stat Nonlin Soft Matter Phys 78:051915
28. Šiber A, Zandi R, Podgornik R (2010) Phys Rev E Stat Nonlin Soft Matter Phys 81:051915
29. Šiber A, Lošdorfer Božič A, Podgornik R (2012) Phys Chem Chem Phys 14:3746
30. Caruso F, Lichtenfeld H, Donath E, Möhwald H (1999) Macromolecules 32:2317
31. Skirtach AG, Yashchenok AM, Möhwald H (2011) Chem Commun 47:12736
32. Lyklema J (1995) Fundamentals of interface and colloid science: solid–liquid interface. Academic, London
33. Fleer GJ, Cohen Stuart MA, Scheutjens J, Cosgrove T, Vincent B (1993) Polymers at interfaces. Chapman & Hall, London
34. Cohen Stuart M, Cosgrove T, Vincent B (1985) Adv Colloid Interface Sci 24:143
35. Chodanowski P, Stoll S (2001) J Chem Phys 115:4951
36. Cohen Stuart MA (1988) J Phys (France) 49:1001
37. de Gennes PG (1981) Macromolecules 14:1637
38. Birshtein TM, Borisov OV (1991) Polymer 32:916
39. Birshtein TM, Borisov OV (1991) Polymer 32:923
40. Wiegel FW (1977) J Phys A: Math Gen 10:299
41. Muthukumar M (1987) J Chem Phys 86:7230
42. Baumgaertner A, Muthukumar M (1991) J Chem Phys 94:4062
43. Dubin PL, The SS, McQuigg DW, Chew CH, Gan LM (1989) Langmuir 5:89
44. Zhang H, Ohbu K, Dubin PL (2000) Langmuir 16:9082
45. Man X, Yan D (2010) Macromolecules 43:2582
46. Tong C, Zhu Y, Zhang H, Qiu F, Tang P, Yang Y (2011) J Phys Chem B 115:11307
47. Wang Z, Li B, Ding D, Wang Q (2011) Macromolecules 44:8607
48. Cherstvy AG, Winkler RG (2011) Phys Chem Chem Phys 13:11686
49. Cherstvy AG (2012) Biopolymers 97:311

50. Cherstvy AG, Winkler RG (2012) J Phys Chem B 116:9838
51. Ulrich S, Seijo M, Stoll S (2006) Curr Opin Colloid Interface Sci 11:268
52. Hoda N, Kumar S (2008) J Chem Phys 118:124907
53. Man X, Yang S, Yan D, Shi A (2008) Macromolecules 41:5451
54. Chervanyov AI, Heinrich G (2009) J Chem Phys 131:104905
55. Odijk T (1980) Macromolecules 13:1542
56. van Goeler F, Muthukumar M (1994) J Chem Phys 100:7796
57. Haronska P, Vilgis TA, Grottenmüller R, Schmidt M (1998) Macromol Theory Simul 7:241
58. Winkler RG, Cherstvy AG (2006) Phys Rev Lett 96:066103
59. Cherstvy AG, Winkler RG (2006) J Chem Phys 125:064904
60. Winkler RG, Cherstvy AG (2007) J Phys Chem B 111:8486
61. Wentzel G (1926) Z Phys 38:518
62. Kramers HA (1926) Z Phys 39:828
63. Brillouin L (1926) C R Acad Sci 183:24
64. Langer RE (1937) Phys Rev 51:669
65. Linse P (1996) Macromolecules 29:326
66. Shubin V, Linse P (1997) Macromolecules 30:5944
67. van der Schee HA, Lyklema J (1984) J Phys Chem 88:6661
68. van de Steeg HGM, Cohen Stuart MA, de Keizer A, Bijsterbosch BH (1992) Langmuir 8:8
69. Borisov OV, Zhulina EB, Birshtein TM (1994) J Phys II 4:913
70. Dobrynin AV, Deshkovski A, Rubinstein M (2001) Macromolecules 34:3421
71. Kunze KK, Netz RR (2000) Phys Rev Lett 85:4389
72. Boroudjerdi H, Netz RR (2005) J Phys Condens Matter 17(S1137)
73. Schiessel H, Rudnick J, Bruinsma R, Gelbart WM (2000) Europhys Lett 51:237
74. Schiessel H (2003) J Phys Condens Matter 15:R699
75. Marky NL, Manning GS (1991) Biopolymers 31:1543
76. Netz RR, Joanny JF (1999) Macromolecules 32:9013
77. Kunze KK, Netz RR (2002) Europhys Lett 58:299
78. Cherstvy AG, Winkler RG (2004) J Chem Phys 120:9394
79. Cherstvy AG, Winkler RG (2005) J Phys Chem B 109:2962
80. Kohlstedt KL, Solis F, Vernizzi G, Olvera de la Cruz M (2007) Phys Rev Lett 99:030602
81. Kohlstedt K, Vernizzi G, Olvera de la Cruz M (2009) J Phys Condens Matter 21:424114
82. Solis FL, Vernizzi G, Olvera de la Cruz M (2011) Soft Matter 7:1456
83. Ngyuen TT, Shklovskii BI (2001) J Chem Phys 114:5905
84. Ngyuen TT, Shklovskii BI (2001) J Chem Phys 115:7298
85. Ngyuen TT, Shklovskii BI (2001) Physica A 291:324
86. Allen RJ, Warren PB (2004) Langmuir 20:1997
87. Park SY, Bruinsma RF, Gelbert WM (1999) Europhys Lett 46:454
88. Mateescu EM, Jeppesen C (1999) Europhys Lett 46:493
89. Gurovitch E, Sens P (1999) Phys Rev Lett 82:339
90. Golestanian R (1999) Phys Rev Lett 83:2473
91. Schiessel H, Bruinsma RF, Gelbart WM (2001) J Chem Phys 115:7245
92. Ulrich S, Laguecir A, Stoll S (2005) Macromolecules 38:8939
93. Arcesi L, La Penna G, Perico A (2007) Biopolymers 86:127
94. Cametti C, Truzzolillo D (2011) J Phys Chem B 115:7248
95. Stoll S, Chodanowski P (2002) Macromolecules 35:9556
96. Lyulin SV, Darinskii AA, Lyulin AV (2005) Macromolecules 38:3990
97. de Carvalho SJ (2010) Europhys Lett 92:18001
98. Carnal F, Stoll S (2011) J Phys Chem B 115:12007
99. Carrillo J, Dobrynin AV (2007) Langmuir 23:2472
100. Cao Q, Zuo C, Ma Y, Li L, Zhang Z (2011) Soft Matter 7:506
101. Su CJ, Chen CY, Lin MC, Chen HL, Iwase H, Koizumi S, Hashimoto T (2012) Macromolecules 45:5208

102. Wallin T, Linse P (1996) Langmuir 12:305
103. Wallin T, Linse P (1996) J Phys Chem 100:17873
104. Wallin T, Linse P (1997) J Phys Chem B 101:5506
105. Akinchina A, Linse P (2002) Macromolecules 35:5183
106. Laguecir A, Stoll S (2005) Polymer 46:1359
107. Kong CY, Muthukumar M (1998) J Chem Phys 109:1522
108. Messina R, Holm C, Kremer K (2001) Phys Rev E Stat Nonlin Soft Matter Phys 65:041895
109. Messina R, Holm C, Kremer K (2002) J Chem Phys 117:2947
110. Messina R (2009) J Phys Condens Matter 21:113102
111. Yamakov V, Milchev A, Borisov O, Dünweg B (1999) J Phys Condens Matter 11:9907
112. Ellis M, Kong CY, Muthukumar M (2000) J Chem Phys 112:8723
113. Messina R (2004) Phys Rev E Stat Nonlin Soft Matter Phys 70:051802
114. Messina R (2006) Phys Rev E Stat Nonlin Soft Matter Phys 74:049906
115. Stevens MJ, Kremer K (1993) Phys Rev Lett 71:2228
116. Winkler RG, Gold M, Reineker P (1998) Phys Rev Lett 80:3731
117. Liu S, Muthukumar M (2002) J Chem Phys 116:9975
118. Netz RR (2003) Phys Rev Lett 90:128104
119. Frank S, Winkler RG (2008) Europhys Lett 83:38004
120. Frank S, Winkler RG (2009) J Chem Phys 131:234905
121. McQuigg DW, Kaplan JI, Dubin PL (1992) J Phys Chem 96:1973
122. Dubin P, Bock J, Davis R, Schulz DN, Thies C (eds) (1994) Macromolecular complexes in chemistry and biology. Springer, Berlin
123. Li Y, Dubin PL, Spindler R, Tomalia DA (1995) Macromolecules 28:8426
124. Mattison KW, Dubin PL, Brittain IJ (1998) J Phys Chem B 102:3830
125. Xia JL, Dubin PL, Kokufuta E, Havel H, Muhoberac BB (1999) Biopolymers 50:7128
126. Miura N, Dubin PL, Moorefield CN, Newkome GR (1999) Langmuir 15:4245
127. Zhang H, Dubin PL, Ray J, Manning GS, Moorefield CN, Newkome GR (1999) J Phys Chem B 103:2347
128. Feng XH, Dubin PL, Zhang HW, Kirton GF, Bahadur P, Parotte J (2001) Macromolecules 34:6373
129. Wang Y, Dubin PL, Zhang H (2001) Langmuir 17:1670
130. Kayitmazer AB, Seyrek E, Dubin PL, Staggemeier BA (2003) J Phys Chem B 107:8158
131. de Vries R, Weinbreck F, de Kruif CG (2003) J Chem Phys 118:4648
132. Cooper CL, Goulding A, Kayitmazer AB, Ulrich S, Stoll S, Turksen S, Yusa S, Kumar A, Dubin PL (2006) Biomacromolecules 7:1025
133. Mishael YG, Dubin PL, de Vries R, Kayitmazer AB (2007) Langmuir 23:2510
134. Fresnais J, Lavelle C, Berret JF (2009) J Phys Chem C 113:16371
135. Kayitmazer AB, Quinn B, Kimura K, Ryan GL, Tate AJ, Pink DA, Dubin PL (2010) Biomacromolecules 11:3325
136. Antonov M, Mazzawi M, Dubin PL (2010) Biomacromolecules 11:51
137. Kizilay E, Kayitmazer AB, Dubin PL (2011) Adv Colloid Interface Sci 167:24
138. Sennato S, Truzzolillo D, Bordi F (2012) Soft Matter 8:9384
139. Hesselink FT (1977) J Colloid Interface Sci 60:448
140. Decher G, Hong JD, Schmitt J (1992) Thin Solid Films 210/211:831
141. Lvov Y, Decher G, Haas H, Mohwald H, Kalachev A (1994) Physica B 198:89
142. Decher G (1997) Science 277:1232
143. Boudou T, Crouzier T, Ren K, Blin G, Picart C (2009) Adv Mater 21:1
144. Lindholm S, Cohen Stuart MA (2013) Relaxation phenomena during polyelectrolyte complex formation. Adv Polym Sci. doi:10.1007/12_2012_XXX
145. Barrat JL, Joanny JF (1993) Europhys Lett 24:333
146. Ullner M, Woodward CE (2002) Macromolecules 35:1437
147. Everaers R, Milchev A, Yamakov V (2002) Eur Phys J E Soft Matter 8:3
148. Ullner M (2003) J Phys Chem B 107:8097

149. Hofmann T, Winkler RG, Reineker P (2003) J Chem Phys 118:6624
150. Doi M, Edwards SF (1986) The theory of polymer dynamics. Oxford University, Oxford
151. Podgornik R (1992) J Phys Chem 96:884
152. Borukhov I, Andelmann D, Orland H (1999) J Phys Chem B 103:5042
153. Gradshteyn IS, Ryzhik IM (1980) Table of integrals, series, and products. Academic, San Diego
154. Andelmann D (1995) Electrostatic properties of membranes: the Poisson-Boltzmann theory. In: Lipowsky R, Sackmann E (eds) Handbook of biological physics, vol 1. Elsevier, Washington, DC, p 603
155. Hulthén L (1942) Arkiv Mat Astron Fysik 28A(5)
156. Lam CS, Varshni YP (1971) Phys Rev A 4:1875
157. Gil A, Koepf W, Segura J (2004) Numerical Algorithms 36:113
158. Dobrynin A (2005) Macromolecules 38:9304
159. Guo Z, Taubes CH, Oh JE, Maher LJ III, Mohanty U (2008) J Phys Chem B 112:16163
160. Savelyev A, Materese CK, Papoian GA (2011) J Am Chem Soc 133:19290
161. Barrat JL, Joanny JF (1996) Adv Chem Phys 94:1
162. Nguyen TT, Shklovskii BI (2002) Phys Rev E Stat Nonlin Soft Matter Phys 66:021801
163. Holm C, Joanny JF, Kremer K, Netz RR, Reineker P, Seidel C, Vilgis TA, Winkler RG (2004) Adv Polym Sci 166:3
164. Odijk T (1977) J Polym Sci Polym Phys Ed 15:477
165. Skolnick J, Fixman M (1977) Macromolecules 10:944
166. Shafir A, Andelman D, Netz RR (2003) J Chem Phys 119:2355
167. Muthukumar M (2012) Adv Chem Phys 149:129
168. Parsegian VA (1973) Annu Rev Biophys Bioeng 2:221
169. Manning GS (1978) Q Rev Biophys 11:179
170. Manning GS (2001) Macromolecules 34:4650
171. Manning GS (2007) J Phys Chem B 111:8554
172. Reed WF, Ghosh S, Medjahdi G, Francois J (1991) Macromolecules 24:6189
173. Seyrek E, Dubin PL, Tribet C, Gamble EA (2003) Biomacromolecules 4:273
174. Cherstvy AG (in preparation)
175. Podgornik R (2003) J Chem Phys 118:11286
176. Licer M, Podgornik R (2020) J Phys Condens Matter 22:414102
177. Truzzolillo D, Bordi F, Sciortino F, Sennato S (2010) J Chem Phys 133:024901
178. Grosberg AY, Nguyen TT, Shklovskii BI (2002) Rev Mod Phys 74:329
179. Teif VB, Bohinc K (2011) Prog Biophys Mol Biol 105:208
180. Kratky O, Porod G (1949) Recl Trav Chim Pays Bas 68:1106
181. Kornyshev AA, Lee DJ, Leikin S, Wynveen A (2007) Rev Mod Phys 79:943
182. Saenger W (1984) Principles of nucleic acid structure. Springer, New York
183. Cherstvy AG (2005) J Chem Phys 123:116101
184. Kornyshev AA, Leikin S (1999) Phys Rev Lett 82:4138
185. Gössl I, Shu L, Schlüter D, Rabe JP (2002) J Am Chem Soc 124:6860
186. Chen W, Turro NJ, Tomalia DA (2000) Langmuir 16:15
187. Gössl I, Shu L, Schlüter D, Rabe JP (2002) Single Mol 3:315
188. Rau DC, Parsegian VA (1992) Biophys J 61:260
189. Cherstvy AG, Kornyshev AA, Leikin S (2002) J Phys Chem B 106:13362
190. Rädler JO, Koltover I, Salditt T, Safinya CR (1997) Science 275:810
191. Koltover I, Wagner K, Safinya CR (2000) Proc Natl Acad Sci USA 97:14046
192. Zinchenko AA, Yoshikawa K, Baigl D (2005) Phys Rev Lett 95:228101
193. Kabanov VA, Sergeyev VG, Pyshkina OA, Zinchenko AA, Zezin AB, Joosten JGH, Brackman J, Yoshikawa K (2000) Macromolecules 33:9587
194. Jackson JD (1962) Electrodynamics. Wiley, New York
195. Ngyuen TT, Grosberg AY, Shklovskii BI (2000) J Chem Phys 113:1110
196. Zinchenko AA, Chen A (2006) J Phys Condens Matter 18:R453

197. Spakowitz AJ, Wang ZG (2003) Phys Rev Lett 91:166102
198. Mondescu RP, Muthukumar M (1998) Phys Rev Lett 57:4411
199. Zheng M, Jagota A, Strano MS, Santos AP, Barone P, Chou SG, Diner BA, Dresselhaus MS, Mclean RS, Onoa GB, Samsonidze GG, Semke ED, Usrey M, Walls DJ (2003) Science 302:1545
200. Lustig SR, Jagota A, Khripin C, Zheng M (2005) J Phys Chem B 109:2559
201. Tu X, Manohar S, Jagota A, Zheng M (2009) Nature 460:250
202. Yarotski DA, Kilina SV, Talin AA, Tretiak S, Prezhdo OV, Balatsky AV, Taylor AJ (2009) Nano Lett 9:12
203. Rotkin SV (2010) Annu Rev Phys Chem 61:241
204. Manohar A, Tang T, Jagota A (2007) J Phys Chem C 111:17835
205. Enyashin AN, Gemming S, Seifert G (2007) Nanotechnology 18:245702
206. Gurevitch I, Srebnik S (2008) J Chem Phys 128:144901
207. Khripin CY, Manohar S, Zheng M, Jagota A (2009) J Phys Chem C 113:13616
208. Srebnik S, Douglas JF (2011) Soft Matter 7:6897
209. Johnson RR, Johnson ATC, Klein ML (2008) Nano Lett 8:69
210. Johnson RR, Kohlmeyer A, Johnson ATC, Klein ML (2009) Nano Lett 9:537
211. Roxbury D, Manohar S, Jagota A (2010) J Phys Chem C 114:13267
212. Vernizzi G, Kohlstedt K, Olvera de la Cruz M (2009) Soft Matter 5:736
213. Korolev N, Lyubartsev AP, Nordenskiöld L (2006) Biophys J 90:4305
214. Kepper N, Foethke D, Stehr R, Wedemann G, Rippe K (2008) Biophys J 95:3692
215. Borourjerdi H, Naji A, Netz RR (2011) Eur Phys J E 72:151
216. Korolev N, Fan Y, Lyubartsev AP, Nordenskiöld L (2012) Curr Opin Struct Biol 22:151
217. Voltz K, Trylska J, Calimet N, Smith JC, Langowski J (2012) Biophys J 102:849
218. Yager TD, McMurray CT, van Holde KE (1989) Biochemistry 28:2271
219. Farago O, Grønbech-Jensen N, Pincus P (2006) Phys Rev Lett 96:018102
220. Cherstvy AG (2007) J Phys Chem B 111:7914
221. Farago O, Grønbech-Jensen N (2011) Soft Matter 7:4302
222. Wagner K, Harries D, May S, Kahl V, Rädler JO, Ben-Shaul A (2000) Langmuir 16:303
223. Cherstvy AG, Everaers R (2006) J Phys Condens Matter 18:11429
224. de Frutos M, Raspaud E, Leforestier A, Livolant F (2001) Biophys J 81:1127
225. Raspaud E, Chaperon I, Leforestier A, Livolant F (1999) Biophys J 77:1547
226. Podgornik R (2004) J Polym Sci B 42:3539
227. Podgornik R, Licer M (2006) Curr Opin Coll Interf Sci 11:273
228. Muthukumar M (1995) J Chem Phys 103:4723
229. Sung W, Sung J, Lee SK (2005) Phys Rev E 71:031805
230. Verwey E, Overbeek J (1948) Theory of the stability of lyophobic colloids. Dover, Mineola
231. Hansen PL, Podgornik R, Parsegian VA (2001) Phys Rev E 64:021907
232. Tuinier R (2003) J Colloid Interface Sci 258:45
233. Cheng CH, Lai PY (2004) Phys Rev E 70:061805
234. Hansupalak N, Santore MM (2003) Langmuir 19:7423
235. Forsman J (2012) Langmuir 28:5138
236. Briones XG, Encinas MV, Petri DFS, Pavez JE, Tapia RA, Yazdani-Pedram M, Urzua MD (2011) Langmuir 27:13524
237. Mirzabekov AD, Rich A (1979) Proc Natl Acad Sci USA 76:1118
238. Manning GS (2003) J Am Chem Soc 125:15087
239. Wiggins PA, Nelson PC (2006) Phys Rev E 73:031906
240. Becker NB, Everaers R (2009) Structure 17:579
241. Zakrzewska K, Lavery R (2012) Curr Opin Struct Biol 22:160
242. de Graaf J, Boon N, Dijkstra M, van Roij R (2012) J Chem Phys 137:104910

Adv Polym Sci (2014) 255: 57–96
DOI: 10.1007/12_2012_171

Published online: 8 August 2013

# Aggregation of Charged Colloidal Particles

**Nikolai I. Lebovka**

**Abstract** This chapter reviews the recent progress in aggregation of colloidal particles with long-range interactions, including simple colloids and polyelectrolytes. The relevant interactions between colloidal particles, including Born repulsion, van der Waals, electrostatic, structural solvation, hydrophobic hydrodynamic interactions and attraction between like-charge colloids, charge nonuniformity, and adsorbed polymer, are analyzed. The main types of computer models used for simulation of cluster morphology and aggregation kinetics of the different interacting species (similarly and oppositely charged particles and polyelectrolytes) are reviewed. The main scaling laws for different aggregating kernels that describe diffusion-limited, reaction-limited, gelling, and retarded aggregations are also presented and analyzed.

**Keywords** Aggregation · Charged particles · Colloids · Kinetics · Morphology · Polyelectrolyte complex (PEC)

## Contents



N.I. Lebovka (✉)
Institute of Biocolloidal Chemistry Named After F.D. Ovcharenko, NAS of Ukraine,
42, blvr. Vernadskogo, 03142 Kiev, Ukraine
e-mail: lebovka@gmail.com

## 1 Introduction

Polymeric nanoparticles are colloidal particles consisting of macromolecular compounds. Among these materials the polyelectrolyte complex (PEC) nanoparticles are of particular interest. These particles with integrated drugs, proteins, vaccines, or diagnostic agents can be used as carriers in different pharmaceutical and biomedical applications [1]. The benefits of their use include controlled drug release and limited toxicity. Moreover, water-soluble and biodegradable PEC nanoparticles may be used as drug delivery systems in humans [2, 3].

PEC nanoparticles are prepared by mixing of two oppositely charged polyanions and polycations. Formation of PEC nanoparticles is controlled by the structure of the polycation/polyanion components, concentration, mixing order, mixing ratio, ionic strength, pH, temperature, and other factors [4]. Key factors determining successful applications of PEC nanoparticles are related to good reproducibility of the formation process, monomodality, and the possibility of obtaining particles with determined and graded sizes.

The process of PEC nanoparticle formation usually includes the initial diffusion stage of mutual entanglement between polymers and formation of primary particles and the further stage of their aggregation and rearrangement of the already formed aggregates [2, 4]. The macroscopically homogeneous systems containing very small primary PEC nanoparticles (approximately 5–20 nm) were developed using special preparation techniques [5]. The process of aggregation of the primary PEC nanoparticles may result in formation of larger nanoparticles. As a result, a turbid colloidal, or two-phase system of supernatant liquid and precipitated PEC nanoparticles is formed [6]. Using of consecutive centrifugation and separation steps allows significant decrease in the polydispersity of the colloidal system, elimination of the primary PEC nanoparticles, and, finally, prevailing of the secondary nanoparticles with radii of about 100–200 nm in dispersion [4]. The secondary PEC nanoparticles have many particular advantages for applications in

biomedicine [7]. Formation of the secondary PEC aggregates and their final size, stability, and polydispersity are controlled by Coulomb interactions between charged primary PEC nanoparticles. Computer simulation techniques can be particularly useful for study of such processes.

This chapter is organized as follows: Section 2 reviews the main equations describing important interactions between dissimilar colloidal particles. The contributions of Born repulsion, van der Waals, electrostatic, structural solvation, and hydrophobic hydrodynamic interactions, as well as the effects of attraction between like-charge colloids, charge nonuniformity, and adsorbed polymer are analyzed. Section 3 presents the main types of computer models used for simulation of cluster morphology and results for different interacting species (similarly and oppositely charged particles and polyelectrolytes) and different models (DLA-like, Eden-like). Section 4 considers the classical Smoluchowski model, the theoretical approach of population balance equations (PBE), classification of kernels, and the main types of scaling in aggregation behavior. The recent data on aggregations kinetics of charged PEC particles are also presented.

## 2 Interactions Between Colloidal Particles

The Derjaguin–Landau–Verwey–Overbeek (DLVO) theory is commonly used to describe interactions of charged surfaces across liquids [8, 9]. The DLVO theory models the interparticle interactions by superposing van der Waals attractions and electrostatic double layer repulsion forces. The direct force measurements have confirmed this theory down to surface separations of few nanometers [10].

The important characteristic of electrolytes are the Bjerrum length, $\lambda_B$, and Debye length, $\lambda_D$, defined as:

$$\lambda_B = \frac{e^2}{4\pi\varepsilon\varepsilon_0 k_B T}, \tag{1}$$

$$\lambda_D = \sqrt{\frac{\varepsilon\varepsilon_0 k_B T}{2\rho e^2}}. \tag{2}$$

Here, $\varepsilon$ and $\varepsilon_0$ are the dielectric constants of the medium and vacuum, respectively, $k_B$ is the Boltzmann constant, $T$ is the absolute temperature, $\rho$ is the number density of the added salt, $e$ is the charge of an electron, and $\lambda_D = \left(\sqrt{8\pi\lambda_B\rho}\right)^{-1}$.

The value of $\lambda_B$ is defined as the distance at which the interaction between two elementary charges equals $k_B T$. At room temperature in water, $T = 298$ K and $\lambda_B = 56/\varepsilon \approx 0.7$ nm. At this condition, the dissociation energy of the ionic pair with a distance $R \cong 0.7$ nm between the opposite charges $u_d = k_B T\lambda_B/R$ is of order

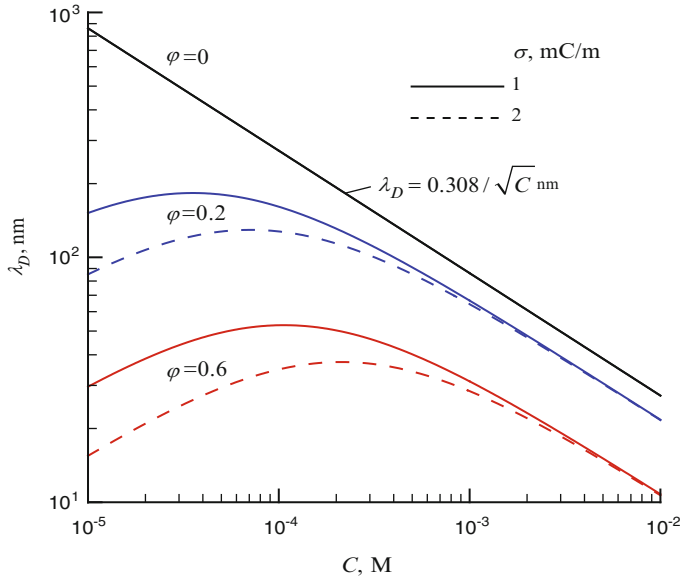


**Fig. 1** Debye screening length, $\lambda_D$, versus the molar concentration of salt, $C$, at different volume fractions $\varphi$ and surface charge densities $\sigma$ of colloidal particles. The radius of particles, $r$, was 85 nm

of $k_BT$ and the ionic pair is unstable. However, such an ionic pair may be stable in less polar solvent.

The Debye length, $\lambda_D$, at room temperature may be estimated as $\lambda_D = 0.308/\sqrt{C}$ nm, where $C$ is the molar concentration of salt (1 M $= 10^3$ mol m$^{-3}$). Note that when the volume fraction of colloidal particles $\varphi$ is not low, the Debye length $\lambda_D$ becomes dependent on $\varphi$, colloidal particle radius, $r$, and colloidal particle surface charge density, $\sigma$ [11]:

$$\lambda_D(\varphi) = \lambda_D(0)\sqrt{\frac{1-\varphi}{1+1.5\sigma\varphi/(e\rho r)}}. \tag{3}$$

The $\lambda_D(\varphi)$ dependence becomes important when the volume fraction of particles, $\varphi$, is large, or the concentration of salt $C$ is very low. Moreover, the value of $\lambda_D$ passes through a maximum with increase in $C$ (Fig. 1).

## *2.1 van der Waals Interactions*

According to the Derjaguin approximation [12], the energy of van der Waals interactions between spherical particles of radii $r_i$ and $r_j$ is:

**Table 1** Examples of Hamaker constants for different materials [13]

| Medium | Hamaker constant, $A$ (J/$10^{-20}$) |
|---|---|
| Polystyrene | 7.8 |
| Poly(methyl methacrylate) | 7.1 |
| Silica | 6.5 |
| Quartz | 11.0–18.6 |
| Water | 3.3–6.4 |
| Pentane | 3.8 |
| Ethanol | 4.2 |
| Cyclohexane | 5.2 |

$$u_{\mathrm{w}}(h) = -\frac{A}{6}\left(\frac{2r_i r_j}{R^2-\left(r_i+r_j\right)^2}+\frac{2r_i r_j}{R^2-\left(r_i-r_j\right)^2}+\ln\left[\frac{R^2-\left(r_i+r_j\right)^2}{R^2-\left(r_i-r_j\right)^2}\right]\right)$$
$$= -\frac{A}{6}\left(\frac{2}{S^2+4Sx}+\frac{2}{S^2+4Sx+4}+\ln\left[\frac{S^2+4Sx}{S^2+4Sx+4}\right]\right), \tag{4}$$

where $h$ is the surface-to-surface separation distance, $R = h + r_i + r_j$ is the distance between the centers of particles, $A$ is the Hamaker constant, $S = h/\bar{r}_{\mathrm{g}}$, $\bar{r}_{\mathrm{g}} = \sqrt{r_i r_j}$ is the mean geometrical radius, and $x = \bar{r}/\bar{r}_{\mathrm{g}}$, $\bar{r} = \left(r_i + r_j\right)/2$ is the mean radius.

At small separation distance, i.e., at $h \ll \bar{r}_{\mathrm{g}}$, the energy of van der Waals interactions is inversely proportional to the surface-to-surface separation distance:

$$u_{\mathrm{w}}(h) \approx -\frac{A}{6}\frac{r*}{h}, \tag{5}$$

where $r^* = 2r_i r_j/\left(r_i + r_j\right)$.

The value of $A$ corresponds to the effective Hamaker constant for the interaction between particles $i$ and $j$ in the dispersion medium. The values of the Hamaker constant are presented for different materials in Table 1.

The effective value of $A_{123}$ is related to Hamaker constants of individual materials $A_{11}$, $A_{22}$, and $A_{33}$ and can be estimated as [14]:

$$A_{123} = \left(\sqrt{A_{11}}-\sqrt{A_{33}}\right)\left(\sqrt{A_{22}}-\sqrt{A_{33}}\right). \tag{6}$$

For similar particles, i.e., at $A_{11} \approx A_{22}$, the value of $A_{33}$ has a positive sign that corresponds to the attractive van der Waals interactions. However, when the value of $A_{33}$ is intermediate between those of $A_{11}$ and $A_{22}$, it has a negative sign that corresponds to the repulsive van der Waals interactions.

In fact, the Hamaker constant $A_{131}$ is not constant but depends on the concentration of electrolyte and on retardation [15]:

$$A_{123} = A_0(1-2h/\lambda_{\mathrm{D}})\exp(-2h/\lambda_{\mathrm{D}}) + A_1 F_{\mathrm{R}}(h), \tag{7}$$

where $A_0$ and $A_1$ are the zero-frequency and high-frequency contributions, respectively, and $F_R$ is the retardation function [16]. The zero-frequency contribution represents the net effect of orientation and induction interactions, and the high frequency term arises from London dispersion interactions. Note that the retardation effect can be ignored for a small distance between the particle surfaces (<5–10 nm).

In recent years, many investigators, in order to overcome difficulties with simulations, have used the simplified forms of attraction potentials, e.g., the Morse potential [17]:

$$u_M(h) = u_M^0 \exp(-h/\lambda)(\exp(-h/\lambda) - 2), \tag{8}$$

where $\lambda$ is the range parameter and $u_M^0$ is the potential well depth.

## 2.2 Electrostatic Interactions

The most popular potential that captures the essential behavior of electrostatic interactions between two equal spherical colloids of charge $Ze$ is the Yukawa potential:

$$u_Y(R) = \pm u_Y^\alpha \exp\left(-\frac{R-r}{\lambda_D}\right)\frac{r}{R}, \tag{9}$$

where the sign is positive for equally charged particles and negative for oppositely charged particles, $R = h + 2r$ is the distance between the centers of the particles, and:

$$u_Y^0 = \frac{(Ze)^2 r \exp(r/\lambda_D)}{4\pi\varepsilon\varepsilon_0}. \tag{10}$$

### 2.2.1 DLVO Approximation

The same form of potential follows from Derjaguin, Landau [8], Verwey and Overbeek [9] (DLVO) theory that invokes the Debye–Hückel approximation to linearize the Poisson–Boltzmann equation:

$$\begin{aligned} u_Y(h) &= \pm\frac{(Ze)^2}{4\pi\varepsilon\varepsilon_0 R}\frac{\exp(-h/\lambda_D)}{(1+r/\lambda_D)^2} \\ &= \pm\frac{(Ze)^2 g^2}{4\pi\varepsilon\varepsilon_0 R}\exp(-R/\lambda_D), \end{aligned} \tag{11}$$

where $g = \exp(r\lambda_D)/(1 + r\lambda_D)$ is the geometric factor that reflects the absence of screening inside the particle exclusion region.

Equation 11 is only valid in the weak Coulomb coupling regime. For highly charged colloidal particles, strong electrostatic coupling between colloidal particles and ions results in additional screening of $Ze$. In a general case, the functional dependence of effective charge $Z^*e$ on real charge $Ze$ may be rather complex [18] and can be determined by geometry of particles, distribution of charges on their surface, and concentration of ions.

The extension of the Derjaguin approximation for electrostatic interaction energy between two dissimilarly charged spheres of radii $r_i$ and $r_j$ was introduced by Hogg, Healy, and Feurstenau (HHF) [19]. Two expressions that are valid under both constant charge, $\sigma$, and constant potential, $\psi$, conditions were proposed:

$$u_e(h)^{\psi} = u_e^0 \left\{ -2\ln\left[\frac{1 + e^{-h/\lambda_D}}{1 - e^{-h/\lambda_D}}\right] + \frac{\left(\zeta_i^2 + \zeta_j^2\right)}{\zeta_i\zeta_j}\ln\left(1 - e^{-2h/\lambda_D}\right)\right\} \tag{12}$$

$$u_e(h)^{\psi} = u_e^0 \left\{ +2\ln\left[\frac{1 + e^{-h/\lambda_D}}{1 - e^{-h/\lambda_D}}\right] + \frac{\left(\zeta_i^2 + \zeta_j^2\right)}{\zeta_i\zeta_j}\ln\left(1 - e^{-2h/\lambda_D}\right)\right\}, \tag{13}$$

where $u_e^0 = \pi\varepsilon\varepsilon_0 r * \zeta_i\zeta_j$, $r* = 2r_ir_j/\left(r_i + r_j\right)$, $\zeta$ is the zeta-potential, and $h$ is the surface-to-surface separation distance.

Approximations for electrostatic repulsion in Eqs. 12, 13 are valid for $h \ll r^*$, relatively small values of $\zeta$, $\zeta/z < kT_B/e \cong 25$ mV, and $r^*/\lambda_D > 10$. Corrections to the fourth and sixth powers of surface potentials in the HHF formulas have been made in [20]. Other more general formulas can be found in the literature [21].

### 2.2.2 Attraction Between Like-Charge Colloids

Many experimental works have shown that unusual long-range attractive interactions, which cannot be explained by the DLVO theory [22–25], may exist for similarly and highly charged colloidal particles. It is interesting that these interactions were observed only in the presence of charged walls.

The theoretical explanations of this effect are rather controversial [26–28]. A highly charged colloidal particle of charge $Ze$ captures $N$ oppositely charged counterions of charge $ze$, which form a very thin shell around the charged colloidal particle surface, resulting in a very strong screening. Under certain conditions, the counterions may totally neutralize or even overcharge the colloidal particle [29]. The charge neutrality is fulfilled when the colloidal particle captures $N = N_n = Z/z$ counterions. In the ground state (i.e. at $T = 0$), the spherical colloidal particle can capture even more positionally correlated counterions and the effective charge of

colloidal particle $Z^*e$ gains the same sign as that of counterions [26, 30]. Estimations have shown that at $Z \gg z$ [30]:

$$N \approx N_n + 0.8265\sqrt{Z/z}, \tag{14}$$

and the maximally possible value of $Z^*$ is:

$$Z^* = (N - N_n)z \propto \sqrt{Zz}. \tag{15}$$

The estimation based on Debye, Huckel, and Bjerrum theory predicts that in the strong Coulomb coupling regime the counterion correlations can give rise to attractions at short separations between particles [31, 32]. The analytical calculations predict that the effective long-range interactions between like-charge colloids immersed in a confined electrolyte are repulsive [33]. However, the possibility of long-range attractions arising from charge fluctuations was theoretically predicted [34]. Recent extensive theoretical and computer simulations have shown the important role of counterion correlations [32, 35] and charge fluctuations of either colloidal particles [36], or condensed counterions [37].

The experimentally observed attractive interactions between like-charged colloidal spheres [25] were explained by a nonequilibrium hydrodynamic effect [38]. A mechanism was also proposed based on formation of the depletion zone of counterions between nearly touching like-charged colloidal particles [39].

According to Manning's theory [40], the rodlike polyelectrolyte can capture $N$ oppositely charged counterions:

$$N = (1 - 1z\xi)Z/z, \tag{16}$$

where $\zeta = \lambda_B/b$ is the coupling strength.

The theory predicts that attraction is possible only in the presence of multivalent counterions and if the number of counterions condensed on polyions exceeds [41]:

$$N > N_n/2 = Z/2z \gg 1. \tag{17}$$

So, attraction is possible only for polyelectrolytes with a high coupling strength, $\zeta > 2/z$.

Taking into account the many-body interactions between highly charged colloids and counterions, Tokuyama proposed the following equation for effective attractive potential [42, 43]:

$$u_T(R) = u_T^0\Big\{(Z/z)^3 F(\lambda_m/R) - F(\lambda/R)\Big\}, \tag{18}$$

where $u_T^0 = 0.5k_BT(Zz\lambda_B/\lambda_D)^2$, $R = h + 2r$ is the distance between the centers of particles, $Ze$ and $ze$ correspond to the bare charges of colloid particles and counterions, respectively, $\lambda_m = \lambda_B\sqrt{z/Z}$, and $F(x) = (x-1)x\exp(-x) - \int_x^\infty y^{-1}\exp -y dy$.

Note that this type of potential was used in Brownian-dynamics simulations of charged colloidal suspensions, where gas, liquid-droplet, and crystal-droplet phases were identified [44].

### 2.2.3 Effect of Charge Nonuniformity

The charge nonuniformity on the surface of colloidal particles may also significantly contribute to the electrostatic interactions. It can arise from selective ion adsorption on the surface of colloidal particles and distribution of $\zeta$ potential [45, 46]. The surface charge nonuniformity can lead to attractive electrostatic and hydrophobic interactions between particles and cause suspension instability [47–49]. An extension of the HHF model for the randomly charged surfaces gives the following Velegol–Thwar potential [46]:

$$u_{\mathrm{V}}(h)^{\psi} = u_{\mathrm{e}}^{0}\left\{2\ln\left[\frac{1+e^{-h/\lambda_{\mathrm{D}}}}{1-e^{-h/\lambda_{\mathrm{D}}}}\right] + \frac{\left(\zeta_i^2+\zeta_j^2+\sigma_i^2+\sigma_j^2\right)}{\zeta_i\zeta_j}\ln\left(1-e^{-2h/\lambda_{\mathrm{D}}}\right)\right\}, \quad (19)$$

where $u_{\mathrm{e}}^{0} = \pi\varepsilon\varepsilon_{\mathrm{o}}r^{*}\,\zeta_i\zeta_j,$ and $\sigma$ is the variance of the surface $\zeta$ potential.

## 2.3 Born Repulsion

Short-ranged repulsion between the cores of colloidal particles (assuming that the particles cannot interpenetrate) may be approximated by the Born potential [50]:

$$u_{\mathrm{B}}(h) = -\frac{u_{\mathrm{B}}^{0}}{R^{*}}\left(\frac{R^{*2}-14R^{*}+54}{\left(R^{*}-2\right)^{7}} + \frac{-2R^{*2}+60}{R^{*7}} + \frac{R^{*2}+14*R^{*}+54}{\left(R^{*}+2\right)^{7}}\right), \quad (20)$$

where $R^{*} = R/2r$, $R$ is the distance between the centers of the particles, and value of $u_{\mathrm{B}}^{0}$ determines the primary minimum of potential.

## 2.4 Structural Solvation Interactions

Direct measurement using atomic force microscopy has shown the presence of short-range repulsion or attraction solvation forces between colloidal particles. These forces reflect the finite size of the solvent molecules and are important only at certain values of pH and electrolyte concentrations. The distance

dependence of the structural solvation potential may be approximated as was first described by Marcelja and Radic [13, 51]:

$$u_s(h) = u_s^0 \exp(-h/\lambda_s), \tag{21}$$

where $u_s^0 = rp_s\lambda_s^2$, $p_s$ is the structural pressure constant, and $\lambda_s$ (approximately 0.2–2 nm) is the solvation decay length. Usually, the monotonic exponential decay superimposes on an oscillatory profile.

## 2.5 Hydrophobic Interactions

Hydrophobic interactions are rather typical for organic colloidal particles (e.g., the particles of latex) dissolved in water. They produce a net attractive contribution. The hydrophobic potential for two equal spherical colloidal particles is expressed as [13]:

$$u_h(h) = -u_h^0 \exp(-h/\lambda_h), \tag{22}$$

where $u_h^0 = 2\pi r\gamma\lambda_h$, $\gamma(\sim 10 - 50\,\mathrm{mJ/m^2})$ and $\lambda_h(\sim 1 - 2\,\mathrm{nm})$ are empirical parameters.

This contribution is rather short-ranged and reduces only the height of the DLVO potential barrier without modifying the depth of the secondary minimum [52].

## 2.6 Effect of Polymers

### 2.6.1 Adsorbing Polymer

Polymer adsorption may result in bridging attraction or steric repulsion between two particles. The scaling theory of polymer adsorption that accounts for the interaction between the polymer and the surface and for variation of polymer concentration near the surface [53, 54] was used for derivation of the interaction potential between two spherical colloidal particles coated by polymer [55–57]:

$$u_p^a(h) = u_p^0\left[-\ln(2\delta/h) + \sqrt{2}\Gamma^{5/4}\left(\left(\lambda_p/h\right)^{1/4} - \left(\lambda_p/2\delta\right)\right)^{1/4}\right], \tag{23}$$

where $u_p^0 rvk_BT/\left(a_m^3\right)16\varphi_p^{9/4}\lambda_p^2\Gamma$, $v$ is the numerical constant, $a_m$ is the effective monomer size, $\varphi_p$ is the polymer volume fraction at a single surface, $\Gamma$ is the degree of surface saturation by the adsorbed polymer (fractional polymer surface coverage), $\delta$ is the thickness of the adsorbed polymer layer, and $\lambda_p$ is the scaling length, which is a measure of the segment surface interactions.

The first term within the square brackets in Eq. 23 corresponds to the short-range bridging attraction and the second term is for steric (excluded volume) repulsion.

### 2.6.2 Non-adsorbing Polymer

Depletion of attraction caused by the presence of a non-adsorbing polymer may be calculated as [10]:

$$u_{\mathrm{p}}^{\mathrm{n}}(h) = -u_{\mathrm{p}}^{0}\left(1 - 3t/4 + t^{3}/16\right), \tag{24}$$

where $u_{\mathrm{p}}^{0} = 4\pi p_0 (r+\delta)^3/3$, $p_0$ is the osmotic pressure in the bulk, $\delta$ is the exclusion thickness, and $t = (2r + h)/(a + \delta)$.

## 2.7 *Hydrodynamic Interactions*

Hydrodynamic interaction mediated by the solvent originates from the movement of particles and occurs when particles are close to each other. It is determined by the viscous drag dependence on interparticle distance [16, 58] and results in a decrease in the particle diffusion coefficient by the factor $\beta$, i.e., $D = D_0\beta$ [59, 60]. Here, $D_0$ is the diffusion coefficient of a particle in the infinitely diluted solution. For motion along the line of the particle centers, the exact expression for $\beta$ was obtained by Brenner [61] and was approximated by the following rational function [62]:

$$\beta(h/r) \simeq \frac{6(h/r)^2 + 13(h/r) + 1}{6(h/r)^2 + 4(h/r)}. \tag{25}$$

Formally, hydrodynamic repulsion energy $u_{\mathrm{hd}}$ may be expressed as the following correction to the total energy:

$$u_{\mathrm{hd}}(h) = k_{\mathrm{B}}T \ln \beta(h/r). \tag{26}$$

The effect of hydrodynamic interactions on aggregation of colloidal particles may be rather essential and simulation results show that they constrain the growth of aggregates [63]. Computational simulation predicts that many-body hydrodynamic interactions between colloidal particle are able to reduce the solid fraction required for percolation or gelation [64, 65]. The merging of clusters into condensed aggregate was observed at particle volume fracture $\varphi$ as low as 0.06–0.12 [64].

In concentrated suspensions of charged colloidal particles, the strong Coulomb interaction prevents the particles from moving freely and leads to an effective screening of hydrodynamic interaction [66]. Such a screening may be particularly

important in polyelectrolyte solutions with strong coupling of electrostatic and hydrodynamic interactions between the polymer chains [67, 68].

### 2.8 Interaction Between Colloidal Aggregates

Until recently, there was no clear conception about interaction between two aggregates consisting of many individual particles. Practically all efforts were devoted to studies of interactions between single particles with an idealized shape, e.g., spheres, cylinders, and ellipsoids.

The general schema of calculation of the van der Waals interaction energy between irregularly shaped molecular aggregates was developed in 1998 [69]. More recently, the calculations of van der Waals and double layer interactions between colloidal aggregates were performed [70, 71]. The direct numerical calculations of the van der Waals interaction between fractal aggregates of colloidal particles (based on a pairwise summation of interaction energies between all particles) have shown that they can be fairly well approximated by the energy of interaction between the closest pair of primary particles [70]. However, it was noted that the surface distance between two aggregates is governed by the morphology of clusters and there may be an apparent impact on the van der Waals interaction. Similar estimations were done for the double layer interactions between fractal or hexagonal closed-packed aggregates with considerable overlapping of double layer inside the aggregates and between two interacting aggregates [71]. It was shown that for the relatively thin double layer ($\lambda_D \leq 0.2r$ for closed-packed aggregates and $\lambda_D \leq r$ for aggregates with a small fractal dimension), the interaction of aggregates is close to the interaction of the nearest pair of the primary particles. However, in thick double layers ($\lambda_D > r$), the overlapping of the double layer inside the aggregate was noticeable and formation of a spheroidal double layer around the aggregate was observed.

## 3 Simulation of Cluster Morphology

A number of theoretical models and computer simulation approaches were developed for description of the cluster morphology [72], reaction kinetics, and time dependence of the cluster-size distributions [73].

### 3.1 Main Types of Computer Models

The cluster morphology may depend on details of colloidal particle interactions, mechanism of particle attachment to the cluster, and dimensionality of the problem. The existing models for cluster morphology simulation account for the trajectory of

the moving particles (diffusion limited aggregation, DLA; reaction limited aggregation, RLA; ballistic aggregation, BA; and Eden-like aggregation) [74].

In the DLA model, the individual particles or clusters stochastically diffuse via Brownian trajectories towards one another and every collision between them results in formation of a larger cluster [75]. The clusters formed display a fractal morphology that depends upon the space dimension in the DLA model. In the RLA model, the probability of attachment is small and only a small fraction of collisions between clusters leads to formation of larger clusters. Traditionally, DLA and RLA are called rapid and slow aggregations, respectively.

A similar mechanism of aggregation is used in the BA model; however, here the trajectories of moving particles are assumed to be linear [76–78]. In the Eden-like aggregation model, new single particles attach to the cluster at its perimeter [79]. The type of diffusion motion strongly affects the cluster morphology, e.g., Brownian motion generates typical fractal DLA clusters, linear trajectories lead to compact structures, and Levy-flight trajectories allow continuous changes of the cluster morphology [80].

The above models are irreversible. Finally, it is expected that clusters grow and merge until formation of a single connected cluster. However, the experimental studies show that some systems can display the presence of reversible aggregation. In a rapid aggregation process, the clusters with loose structure arise initially, and after a certain time they can restructure to more compact clusters with higher fractal dimensionality [81, 82]. The process of thermal restructuring of fractal polymer clusters dispersed in water was experimentally observed using small-angle light scattering [83].

In the absence of aggregation, restructuring resulted in an increase in the fractal dimension. A simple model of the restructuring kinetics, based on coalescence theory of liquid droplets, was developed [83]. Reversible-growth models were also built. These models allow unbinding of particles and imply that later on, during the restructuring, the ramified clusters become compact [84, 85]. The details of cluster morphology strongly depend on the interparticle interaction, the presence of restructuring, and external fields [86]. Impact of interactions on the intrastructure of colloidal clusters was recently studied by Brownian dynamics simulations [17]. It was shown that an increase in density of suspension results in stronger intercluster interactions that affect the intrastructure of clusters. However, perturbation of the intrastructure of clusters was shown to be low in diluted suspension.

## *3.2 Similarly Charged Particles*

For colloidal suspensions, the influence of the combination of short-range attractions and long-range repulsions on clustering phenomena [87] is extremely interesting. It is expected for charged particles that cluster accumulates net charge and may reject association of additional particles at a certain critical size.

The long-range repulsion may result in limitation of the cluster size [87, 88]. Coulomb repulsion tries to break charged spherical clusters or introduce an ellipsoidal deformation [89, 90]. In 1935, Weizsacker studied the stability of the atomic nucleus by analyzing the potential energy of the charged spherical cluster $u_t$ [91]. In the case when the cluster is filled by $N$ primary particles with radius $r$ and charge $Ze$, the value of $u_t$ includes the volume $u_v$, surface $u_s$, and electrostatic $u_e$, terms:

$$u_t(N) = u_v + u_s + u_e = -u_0 N + aN^{2/3} + bN^{5/3}, \tag{27}$$

where $u_0$ is the binding energy per particle, $a = 4\pi\gamma r^2 \phi^{-2/3}$ is the surface tension parameter, $b = 3k_B T \lambda_B \varphi^{1/3}/5r$ is the electrostatic repulsion parameter, $\gamma$ is the surface tension at the interface between the aggregate and solvent, $\varphi$ is the volume fraction of particles in the aggregate, and $\lambda_B = (Ze)^2/(4\pi\varepsilon\varepsilon_0 k_B T)$ is the Bjerrum length for primary particles in the aggregate.

The radius of a spherical cluster may be calculated as:

$$r^c = r(N/\varphi)^{1/3}. \tag{28}$$

Figure 2 shows examples of dimensionless total potential energy of a spherical cluster, $u_t/u_0$, versus the number of primary particles, $N$, at a fixed value of $a$ ($a/u_0 = 2$) and different values of $b/u_0$. The clusters are definitely stable at $u_t < 0$. At relatively small charge $Z$ of the primary particles, the curve $u_t$ goes through the maximum (see, inset in Fig. 2) at:

$$N_1^{\max} = \left(\frac{2a}{3u_0}\right)^3 \left(1 + \frac{20a^3 b}{9u_0^3}\right), \tag{29}$$

and bigger clusters are stable (i.e. $u_t < 0$) in the certain range of $N$ values.

A noticeable change in the shape of the $u_t$ curve is observed for a charged cluster (Fig. 2), e.g., at $a = 0$, i.e. in absence of surface tension, the $u_t$ function curve goes through the minimum and has two zeros at $N = 0$ and at:

$$N = N_2^{\max} = (1/b)^{3/2} = \left(\frac{5}{3\varphi^{1/3}} \frac{r}{\lambda_B} \frac{u_0}{k_B T}\right)^{3/2}. \tag{30}$$

Note that the critical size $N_2^{\max}$ corresponds to the physical situation when the next primary particle cannot attach to the compact spherical cluster. In principle, the cluster grown may continue through formation of noncompact branching morphology structures with smaller value of $\varphi$. Thus, the critical size $N_2^{\max}$ corresponds to development of morphological instability.

Stability analysis with respect to ellipsoidal deformation has shown that even bigger clusters (initially formed and then becoming charged) may lose stability and dissociate on smaller clusters (Fig. 2) at certain critical size:

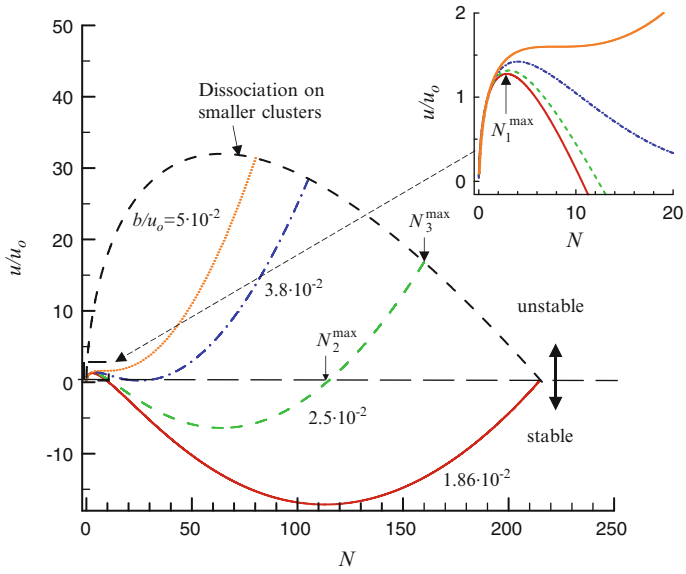


**Fig. 2** Dimensionless total potential energy of a spherical cluster, $u_t/u_0$, versus the number of primary particles, $N$, at $a/u_0 = 2$ and at different values of $b/u_0$. *Inset* shows the enlarged part of this figure at small values of $u_t/u_0$ and $N$

$$N = N_3^{\max} \approx 2a/b = \frac{10}{3\varphi}\,\frac{r}{\lambda_B}\,\frac{4\pi\gamma r^2}{k_B T} \tag{31}$$

that corresponds to development of dissociative instability.

In both Eqs. 30 and 31, the larger cluster corresponds to the larger ratio of $r/\lambda_B$ and smaller value of $\varphi$. The stable growth regime is expected for zero value of $\lambda_B$ ($b = 0$), which corresponds to formation of an infinite cluster or gel-like phase. However, the completely unstable growth regime is expected when $\lambda_B$ exceeds some critical value. In this case, the value of $u_t$ is positive at any value of $N > 0$ (see, e.g., the case of $b/u_0 = 3.8\times10^{-2}$ in Fig. 2). Energetically, the critical sizes $N_1^{\max}, N_2^{\max}$ and $N_3^{\max}$ are controlled by ratios $u_s/u_0$, $u_e/u_e$ and $u_s/u_0$, respectively (Fig. 3).

Figure 4 compares $N_2^{\max}$ and $N_3^{\max}$ versus ratio $2a/b$ behavior for fixed values of $a$ (surface tension parameter). The slightly charged clusters (small values of $\lambda_D$) can grow to larger size and the values of $N_3^{\max}$ and $N_2^{\max}$ coincide. In this unstable grown regime, the morphological and dissociative instabilities develop simultaneously. For highly charged clusters (large values of $\lambda_D$), the value of $N_3^{\max}$ may noticeably exceed the value of $N_3^{\max}$ at certain critical $\lambda_D$.

In principle, these general considerations are consistent with recent experimental and computer simulation results. The finite-size clusters were experimentally realized in suspensions of colloidal particles with interactions induced by a non-adsorbing polymer [92, 93]. Cluster morphology was dependent on the range of the

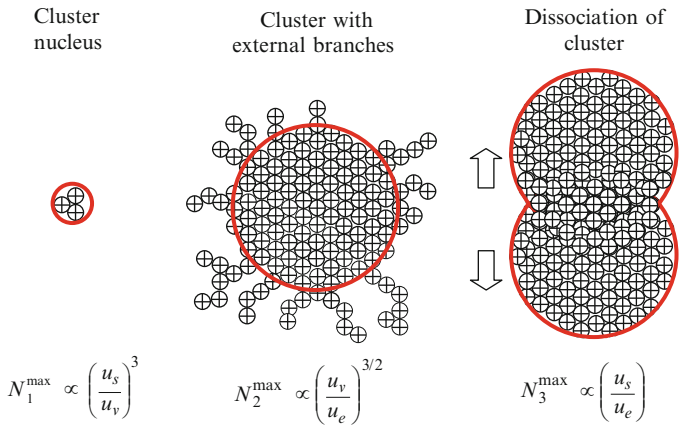


**Fig. 3** The critical sizes of charged cluster $N_1^{max}$, $N_2^{max}$ and $N_3^{max}$. The values of $N_1^{max}$, $N_2^{max}$ and $N_3^{max}$, correspond to the formation of initial nucleus, growth of external branches, and dissociation of charged droplets, respectively

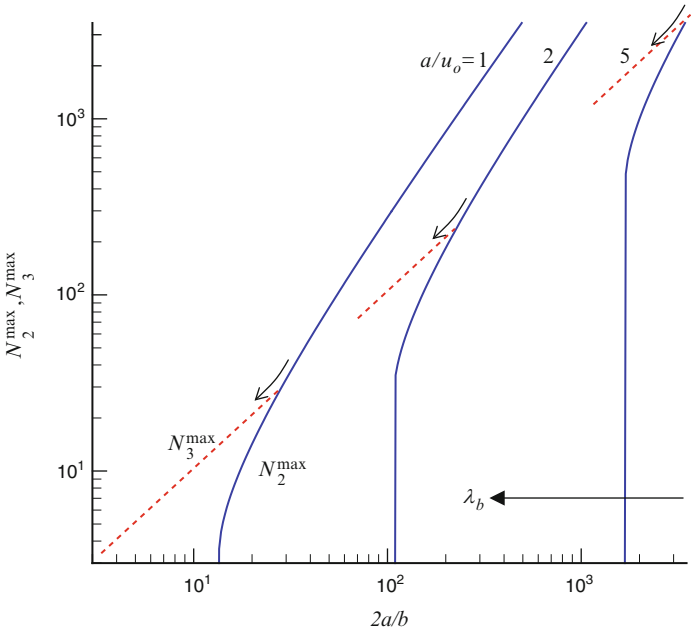


**Fig. 4** Maximum cluster sizes $N_2^{max}$ and $N_3^{max}$ versus ratio $2a/b$ at fixed values of $a/u_0 = 1$, 2, and 5

interaction and was becoming more compact for longer range interactions. The origin of such behavior is not completely clear so far.

The large charged clusters may be unstable with respect to formation of elongated or linear structures. The theory predicts formation of near-linear chains with

small fractal dimension, $d_f \sim 1$, in polyelectrolytes in the limit of high electrostatic interactions ($\lambda_B \sim 0.1$ nm) [94]. Formation of linear structures was observed also in Monte Carlo simulations of a short polyelectrolyte with various numbers of beads, $N = 8$–$80$ [95]. The value of $d_f$ was noticeably increasing as Bjerrum length $\lambda_B$ decreased.

The effect of the range of interactions on the structural and kinetic properties of a computer-simulated two-dimensional aggregating colloidal system was studied using the repulsive Yukawa potential [96] (Eq. 9). The increase in $\lambda_D$ or $u_0$ provokes arrangement of aggregates into linear structures. The repulsive interactions also have a strong influence on the kinetic behavior of the coagulation process. The structure of small clusters composed of up to 80 particles interacting simultaneously via attractive and repulsive forces was recently simulated [97]. A short-range attraction was simulated by generalization of the Lennard–Jones potential and a long-range repulsion was simulated by the screened electrostatic Yukawa potential. The competition between attraction and repulsion resulted in formation of stable clusters, and the ground-state clusters were preferentially growing almost in one dimension. The extensive numerical simulations were done for suspended charged colloidal particles at a screening length comparable to the particle radius [98]. It was shown that at low temperature, particles organize into quasi one-dimensional aggregates connecting via branching mechanism into a percolating gel structure. Note that experimental data indicate a more elongated and open morphology of the fractal-like aerosol agglomerates at larger charge [99].

### 3.2.1 DLA-Like Model

The impact of long-range interactions on cluster morphology has been intensively studied for different variants of the DLA model [100–103]. It was shown using a quasi-deterministic two-dimensional (2D) particle–cluster growth model with attractive cluster–particle forces proportional to $R^{-\alpha}$ that the growing cluster was dendritic. Moreover, strong reduction of the fractal dimension, $d_f$, with increase in $\alpha$ was observed [100]. The 2D DLA model with the power-like potential, $u(R) = u_0 R^{-\alpha}$, was also studied [101, 104]. Here, $u_0$ and $\alpha$ are parameters. Note that this model is equivalent to the ordinary DLA in the limits of short range interactions, $\alpha \to \infty$, or $u_0 = 0$. In this problem, the aggregates were grown on a triangular lattice and the effects of anisotropy were important.

The detailed structure of clusters was strongly dependent on $\alpha$, or $u_0$, e.g., in the case of attractive interactions at large $|u_0|$ and long-range interaction (i.e., for small $\alpha$), the clusters grew with stable tips and were of dendritic shape. The observed effects reflected the anisotropy induced by the underlying lattice that stabilized the tips of the growing arms. In the limit of small $|u_0|$ and large $\alpha$, the transition from dendritic to tip-split aggregates was observed. At fixed value of $u_0$, the estimated fractal dimension $d_f$ increased with increase in $\alpha$, which reflected tip destabilization [101].

The similar cluster–cluster variants of DLA aggregation with either attractive or repulsive interactions were also studied [102, 103]. These simulations were done

using off-lattice models both for 2D [103] and three dimensional (3D) [102] systems. The interaction energy $u_{ij}$ of two non-overlapping clusters including $i$ and $j$ particles was approximated by the power law:

$$u_{ij} = u_0 \sum_{k=1}^{i} \sum_{i=1}^{j} R_{kl}^{-\alpha}, \tag{32}$$

where $R_{kl}$ is the distance between the $k$th particle in the cluster $i$ and $l$th particle in the cluster $j$.

Both the theory and simulation results gave the following estimates for fractal dimensionality $d_f$ versus parameter $\alpha$ dependence:

$$d_f = \begin{cases} d_0, \alpha > 2d_0 \\ d_0(\alpha + 2)/(2(d_0 + 1)), 1 < \alpha \leq 2d_0, \end{cases} \tag{33}$$

where $d_0$ is the fractal dimensionality in the cluster–cluster aggregation model without interactions. It equals $d_0 \sim 1.6$ and $d_0 \sim 2.1$ for 2D and 3D systems, respectively.

Figure 5 presents $d_f$ versus $\alpha$ dependencies for 2D and 3D systems. The figure shows that short range interactions ($\alpha > 2d_0$) do not change the value of $d_f$, but long range ($1 < \alpha \leq; 2d_0$) interactions lead to substantial changes in $d_f$. Moreover, long range interactions can have an important effect on the local structure of clusters [102, 103]. The shape and size of the aggregates may be sensitively dependent on the balance between attraction and repulsion interactions [98].

### 3.2.2 Eden-Like Model

The stochastic Eden-like model of aggregation of the charged particles in 2D systems was developed [105, 106]. In this model, the particles overcome the electrostatic repulsive barrier created by the aggregate and stick to it due to the existence of short-range attractions.

By variation of two model parameters, the screening length, $\lambda$, and the attractive binding energy per particle, $u_0$, formation of the aggregates with the following morphologies was studied: linear or near-linear, linear with bending, worm-like, dense-branching or dense-branching with a core, and compact Eden-like aggregates. Figure 6 presents an example of a cluster with a charged core and external branches. The regions of finite and infinite growth of clusters with different morphologies are presented in the form of a diagram as $\lambda$ versus $u_0$. The structure and fractal properties of the ramified clusters were studied. It was found that the clusters did not reveal the fractal properties at any values of $\lambda$ and $u_0$ and a sharp transition between linear ($d_f = 1$) and dense-branching ($d_f = 2$) morphologies was observed.

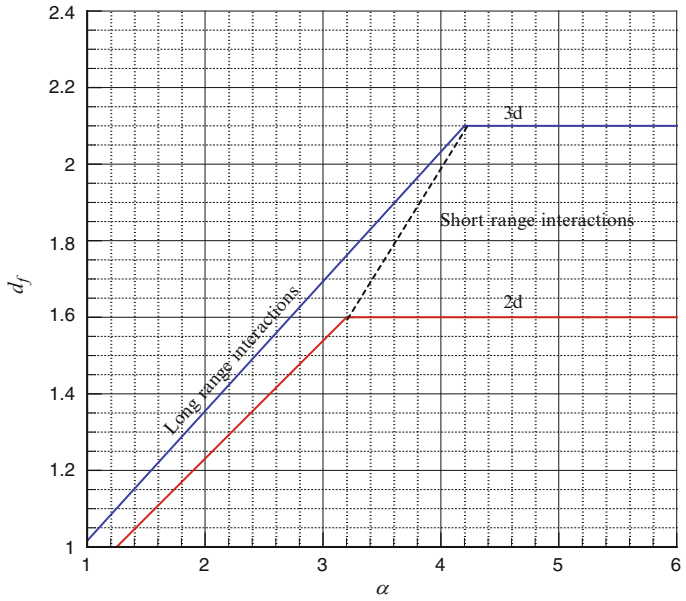


**Fig. 5** Fractal dimensionality $d_f$ versus power exponent $\alpha$ for 2D and 3D cluster–cluster DLA model

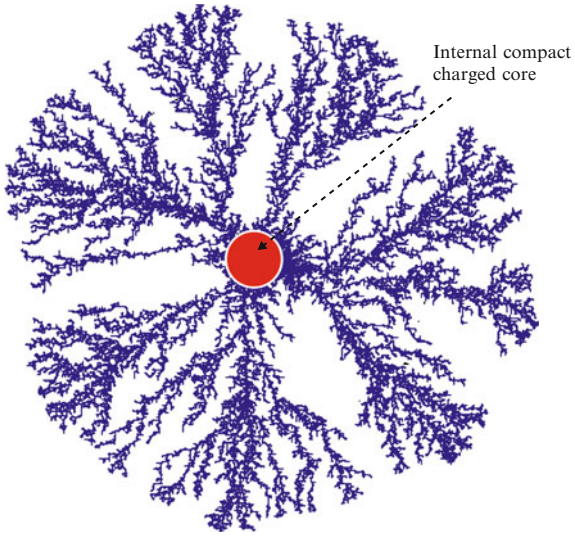


**Fig. 6** Internal structure of cluster obtained using Eden-like model of aggregation of charged particles ($\lambda = 1$, $u_0 = 60$). The cluster includes a core (central dense charged part) and external branches [105]

## 3.3 Oppositely Charged Particles

### 3.3.1 Simple Colloids

The particles of a mixture of oppositely charged nanoparticles form charged aggregates (complexes), in which each charged particle is screened by a shell of oppositely charged particles [107, 108]. The stable core-and-shell aggregates were confirmed in experiments with the mixtures of oppositely charged metal nanoparticles [107] When the net charges of positive and negative species are equal, the aggregates are neutral and condense into a macroscopic drop, i.e., the system becomes unstable. The theory developed in [109] predicts a possibility of enhanced aggregation of larger charged particles induced by the small polyions of the opposite charge. This phenomenon may reflect the partial "condensation" of the small particles and reduction of the strong electrostatic repulsion between screened (larger) colloidal particles.

The Brownian dynamic simulation of aggregation between the oppositely charged particles has shown that heteroaggregation produces more branched aggregates than the usual diffusive aggregation [110]. Moreover, the cluster discrimination was observed at the late stages of aggregation, when neutral clusters were disappearing faster than charged ones [111].

The presence of linear chaining with particle charge alternating down a chain in aggregates of the oppositely charged polystyrene spheres was revealed by different experimental techniques and was supported by Brownian dynamics simulation [112]. It was shown that branching of an aggregate composed of oppositely charged particles may be varied from a linear chain structure ($d_f \sim 1.2$) to a structure of diffusion-limited aggregates ($d_f \sim 1.7$) by an increase in concentration of the background electrolyte. Formation of linear chains was explained by the short-range attraction between the oppositely charged particles and long-range repulsion between the identical particles. The experiments and the Brownian dynamics simulations of heteroaggregation between the oppositely charged particles [113–115] has shown that small silica (diameter ~ 25 nm, negatively charged) particles covered the surface of large alumina (diameter ~ 400 nm, positively charged) particles. For small amounts of silica particles, agglomeration of the silica-covered alumina particles was observed, and it was demonstrated that the agglomerates were of elongated shape.

### 3.3.2 Polymers

Behavior of solutions of oppositely charged polymers is rather similar to that of solutions of oppositely charged colloids. However, higher flexibility of the polymer chains results in a less ordered structure of the polyion solutions. Pairing of the oppositely charged polyions, their aggregation, and complexation of anionic and

cationic polyelectrolytes have been intensively studied in many theoretical [116–121] and experimental [122–124] works.

The phase diagram of asymmetric positively and negatively charged chains in an oppositely charged polyelectrolyte was theoretically obtained [125]. It was shown that cylindrical and lamellar cluster structures with nonzero net charge were formed at high polymer concentration. Nonuniform distribution of charge along the annealed polyelectrolyte chains was observed [116, 121]. The theoretical predictions and Monte Carlo simulations show that charges accumulate at the ends of chains. [116]. The cluster size distribution functions of the oppositely charged macroions in solution were studied using the Monte Carlo simulations [120]. It was demonstrated that increasing electrostatic coupling results in formation of larger clusters, and a single cluster comprising all the macroions forms at the strongest coupling. The structure of symmetric polycation–polyanion mixtures without salt in good solvents was studied using the Langevin sampling simulation technique and field-theoretic simulation methods [119, 126]. The obtained results allowed explanation of the phenomenon of complex coacervation, a type of phase separation in which dense liquid precipitates coexist with supernatant solvent.

Brownian dynamics computer simulations have shown that variation in electrostatic interactions changed the size, shape, and local density distribution of the complexes formed by terminally charged hyperbranched polymers and oppositely charged neutralizing linear polyelectrolytes [127]. The ultrasoft core model of interpenetrating polycations and polyanions was proposed for investigation of the polyelectrolyte aggregation using different theoretical approaches and molecular dynamic simulations [117]. The clustering and segregation of the oppositely charged species was observed. At sufficiently low temperatures and densities, the oppositely charged polyions tend to form weakly interacting neutral pairs. The break-up of ion pairs was observed with increase in temperature. This was followed by the percolation transition from low temperature dielectric (insulator) state to high temperature ionic (conductor) state [117].

The Monte Carlo simulations were applied to study the complexation, phase separation, and redissolution of polyelectrolyte–macroion solutions [128]. It was shown that introduction of the oppositely charged polyelectrolytes into a stable macroion solution with repelling macroions resulted in a decrease in the solution stability. The system was unstable at macromolecular charge equivalence when a large and loose cluster of macroions and polyelectrolytes was forming. Finally, redissolution of macroions occurred in the excess of polyelectrolyte.

The complexation between a polyampholyte and a charged particle was studied using Monte Carlo simulations [129, 130]. The increasing charge density and particle size resulted in change of configuration of the polyampholyte chain adsorbed on the particle surface. At large charge density and particle size, collapse of the polyampholyte chain on the particle surface was observed [129]. The effects of different model parameters (polyampholyte contour length, nanoparticle surface charge, pH of solvent, ionic concentration, etc.) on possible polyampholyte conformations at the nanoparticle surface were investigated [130].

The process of aggregation of the oppositely charged polyions (positively charged liposomes and negatively charged polyelectrolyte sodium polyacrylate) was studied by means of Monte Carlo simulation [131]. The model accounted for heterogeneous charge distribution at the particle surface, related with the correlated polyion adsorption [46]. Formation of long-living clusters of polyelectrolyte-decorated particles was demonstrated. Molecular dynamics simulations were performed to study the polyampholyte–polyelectrolyte complexes in solutions [124, 132]. It was demonstrated that polyampholyte chain binds to a polyelectrolyte in a way optimizing electrostatic interactions between the ionic groups in both polymeric chains. Formation of the micellar complex by anionic polyelectrolyte and cationic surfactants (in monomeric and dimeric forms) was investigated by molecular dynamics simulation [133]. Results have shown that the dimeric form interacts more strongly with the polyanion and the size of the micellar complex becomes larger with an increase in the surfactant concentration.

### *3.4 Effect of Dipolar Interactions*

The effects of dipolar interactions on DLA processes were studied in details for 2D and 3D off-lattice models [134–137]. The fractal dimensionality $d_f$ was a monotonically increasing function of the temperature (or decreasing function of dipolar forces). For example, it varied continuously from about 1.78 for small dipolar interactions to about 1.35 for large dipolar interactions (3D model) [134, 135]. Therefore, the structure of clusters formed at low temperatures or strong dipolar forces was less branched and more open ($d_f \sim 1$) than in free DLA with no interactions. On increase in temperature or decrease in dipolar forces, the value of $d_f$ reached the limit value of free DLA [136, 137]. The values $d_f = 1.13 \pm 0.01$ and $d_f = 1.37 \pm 0.03$ were obtained in the limit of zero temperature for 2D and 3D systems, respectively. Transitions between an ordered, or quasi-ordered, and a disordered phase were also observed for high values of the reduced temperature [138]. The long range correlations between the dipoles were revealed in the low-temperature ordered phase.

## 4 Kinetics of Aggregation

Kinetics of aggregation, coalescence, and annihilation or fragmentation are important in many physical, chemical and biological processes [21, 80, 139–141]. The popular mean field Smoluchowski approach [73] gives good description of simple aggregation systems. However, in the presence of restructuring, long range interactions, and formation of clusters with fractal geometry, more complicated approaches based on computer simulation methods are useful.

## 4.1 Aggregation as a Second-Order Reaction

In the simplest case, only primary particles are present at initial time, $t = 0$, with initial number density of $\rho_0$ and volume fraction of $\varphi = 4\pi r^2\rho_0/3$. It can be supposed that in very diluted systems ($\leq$1% vol) only two particle collisions are important. The regime of "fast" aggregation is assumed, i.e., two primary particles form an aggregate when they "touch" at the distance of $2r$ between their centers. The disappearance of primary particles can be considered as a second-order reaction [73]:

$$\frac{\mathrm{d}n_1}{\mathrm{d}t} = -k^{\mathrm{f}} n_1^2, \tag{34}$$

where $n_1$ is the dimensionless concentration of the primary particles, i.e. $n_1 = \rho_1/\rho_0$, and $k^{\mathrm{f}}$ ($\mathrm{s}^{-1}$) is the fast aggregation rate constant. Note that $k^{\mathrm{f}} = 1/\tau_{\mathrm{a}}$, where $\tau_{\mathrm{a}}$ is the half-aggregation time corresponding to $n_1 = 1/2$.

The integration of Eq. 34 gives:

$$n_1 = (1 + t/\tau_{\mathrm{a}})^{-1}. \tag{35}$$

Estimations show [73]:

$$k^{\mathrm{f}} = 8\pi Dr = \frac{4k_{\mathrm{B}}T\rho_0}{3\eta}, \tag{36}$$

where $D = \frac{k_{\mathrm{B}}T}{6\pi r\eta}$ is the diffusion coefficient, and $\eta$ is the viscosity of solvent.

The half-aggregation time of colloidal dispersion, $\tau_{\mathrm{a}}$, may be estimated as:

$$\tau_{\mathrm{a}} = 1/k^{\mathrm{f}} = \tau_{\mathrm{B}}/\varphi = \frac{3\eta}{4k_{\mathrm{B}}T\rho_0}, \tag{37}$$

where $\tau_{\mathrm{B}} = r^2/(6D)$ is the Brownian time. During the Brownian time, the length of diffusion is equal to the radius of the primary particle, $r$.

For example, the Brownian time, $\tau_{\mathrm{B}}$, of 10 nm particles ($\eta \sim 0.001$ Pa s) in water at room temperature ($T = 298$ K) is equal to $0.76 \times 10^{-6}$ s. Figure 7 presents plots of $\tau_{\mathrm{a}}$ versus $r$ at different values of the volume fraction of particles, $\varphi$.

In the presence of repulsive interactions, the sticking probability becomes smaller than 1 and the so-called "slow" aggregation regime may be realized. The slow aggregation rate constant, $k^{\mathrm{s}}$ may be estimated as:

$$k_{ij}^{\mathrm{s}} = k^{\mathrm{f}} w_{ij}, \tag{38}$$

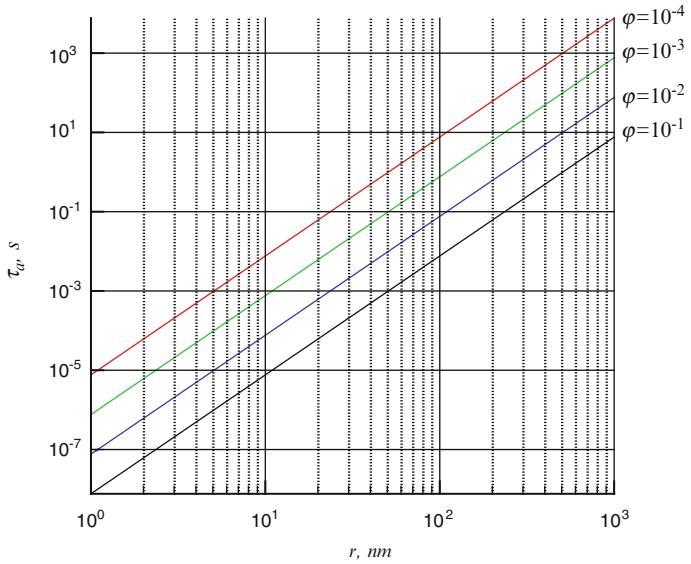


**Fig. 7** Half-aggregation time $\tau_a$, versus radius of particle $r$ at different values of the volume fraction of particles, $\varphi$. The estimation was done using Eq. 37 for suspension of particles in water, $T = 298$ K and $\eta \sim 0.001$ Pa s

where $W_{ij}$ ($\geq 1$) is the dimensionless Fuchs stability ratio, which can be considered as the inverse sticking probability [142]:

$$w_{ij} = \int_0^\infty \frac{\exp(u_t(x)/k_B T)}{(x+2)^2} \mathrm{d}x. \tag{39}$$

Here, $x = h/\overline{r_{ij}}, \overline{r_{ij}} = \left(r_i + r_j\right)/2,$ and $u_t$ is the total energy, i.e., the sum of the attractive, $u_a$, and repulsive, $u_r$, parts.

It was shown that the value of $W_{ij}$ is mainly determined by the height of the energy barrier $u_t^{max}$ located at $h \cong \lambda_D$ and the following approximate relation was obtained for equal sized particles, $r = r_i = r_j$, [143]:

$$W_{ij} = \frac{\lambda_D}{2r} \exp\left(u_t^{max}/k_B T\right). \tag{40}$$

Usually, it is assumed that fast and slow aggregations are controlled by attractive and total interactions, respectively, and the equation used for estimation of $W_{ij}$ is more complicated:

$$W_{ij} = \frac{\int_0^\infty \mathrm{d}x \, \exp(u_t/k_B T)/(x+2)^2}{\int_0^\infty \mathrm{d}x \, \exp(u_a/k_B T)/(x+2)^2}. \tag{41}$$

## 4.2 Population Balance Equations

In order to account for formation of dimers, trimers, and larger aggregates, von Smoluchowski proposed in his pioneering work [73] the following system of population balance equations (PBE):

$$\frac{\mathrm{d}n_m}{\mathrm{d}t^*} = \frac{1}{2}\sum_{i=1}^{m-1} k_{i,m-i} n_i(t) n_{m-j}(t) - n_m(t)\sum_{i=1}^{\infty} k_{m,i} n_i(t), \tag{42}$$

where $n_m$ is the dimensionless concentration of the clusters of size $m$, $k_{i,m-i}$ are dimensionless reaction constants, or kernels, and $t^* = k^{\mathrm{f}}t = t/\tau_{\mathrm{a}}$ is the normalized time.

At initial moment of time, $t = 0$, all clusters are assumed to be monomeric and $n_1 = 1$. The first term ("birth" term) in Eq. 42 corresponds to the collision between two clusters ($i$-mers and $m - i$-mers) and formation of $m$-mers. In first summation, each collision is accounted for twice; hence, a factor of 1/2 is included. The second summation corresponds to the decrease in concentration of $m$-mers through aggregation with other clusters.

In fact, the PBE approximation is a mean field approximation valid for dilute systems. Moreover, this approximation does not account for internal structure and differences in the spatial configuration of clusters. For the known functional dependence of $k_{m,i}$, time evolution of the cluster population $n_m(t)$ can be calculated from Eq. 42.

During the aggregation the total mass of clusters:

$$\sum_{i\geq 1} i n_i(t) = 1, \tag{43}$$

is conserved.

The important characteristics of the cluster distributions are dimensionless total number of clusters $n$:

$$n(t) = \sum_{i\geq 1} n_i(t) \tag{44}$$

and mean cluster size (mass), $s(t)$:

$$s(t) = \sum_{i\geq 1} i^2 n_i(t). \tag{45}$$

**Table 2** Analytical solutions of PBE for constant, sum, and product kernels

| Kernel, $k_{i,j}$ | Concentration of clusters of size $m$, $n_m$ | Number of clusters, $n$ | Size of clusters, $s$ |
|---|---|---|---|
| 2 | $\frac{t^*(m-1)}{(1+t^*)^{(m+1)}}$ | $\frac{1}{1+t^*}$ | $1 + 2t^{*z}$, $z = 1$ |
| $i + j$ | $\frac{(ma)^{m-1}\exp(-ma-t^*)}{m!}$, $a = 1 - \exp(-t^*)$ | $\exp(-t^*)$ | $\exp(\alpha t^*)$, $\alpha = 2$ |
| $2ij$, at $t^* \leq 0.5$ | $\frac{(2mt^*)^{m-1}\exp(-2mt^*)}{mm!}$ | $1 - t^*$ | $\left(1 - t^*/t_g^*\right)^{-\beta}$, $\beta = 1$ |
| $2ij$, at $t^* > 0.5$ | $\frac{(m)^{m-1}\exp(-m)}{2\,mm!t^*}$ | $1/(4t^*)$ | $\infty$, gel |

Here, $t^* = t/\tau_a$ is the dimensionless aggregation time [73, 144–146]

## 4.3 Popular Kernels

The analytical solutions of PBE were obtained for some functional forms of kernels, e.g., for constant $k_{ij} = 2$, sum $k_{ij} = i + j$, and product $k_{ij} = i + j$ kernels (Table 2). An exact solution exists also for linear combination of these three kernels:

$$k_{ij} = A + B(i + j) + Cij, \tag{46}$$

where $A$, $B$, and $C$ are the arbitrary constants, as well as for $q$-sum kernel:

$$k_{ij} = 4 - q^i - q^j, \tag{47}$$

where $0 < q < 1$, and for many other kernels (for a review see, [144]).

Figure 8 shows examples of distribution functions $f(m) = mn_m/(mn_m)_{\max}$ obtained from analytical solutions presented in Table 2 for constant ($k_{ij} = 2$), sum ($k_{ij} = i + j$), and product ($k_{ij} = 2ij$) kernels at different moments in time. It is interesting that at long times the distribution function for the constant kernel has a bell-like shape, whereas for sum and product kernels they monotonically decay with increasing $m$.

The case of constant kernel is similar to the situation that was analyzed in Sect. 4.1. The fast aggregation problem with the constant kernel was exactly solved by Smoluchowski in 1917 [73]. This model is based on the more complicated kernel for 3D Brownian aggregation:

$$k_{ij}^{B} \simeq \frac{1}{2}\left(i^{-1/3} + j^{-1/3}\right)\left(i^{1/3} + j^{1/3}\right) = 1 + (i/j)^{1/3} + (j/i)^{1/3}. \tag{48}$$

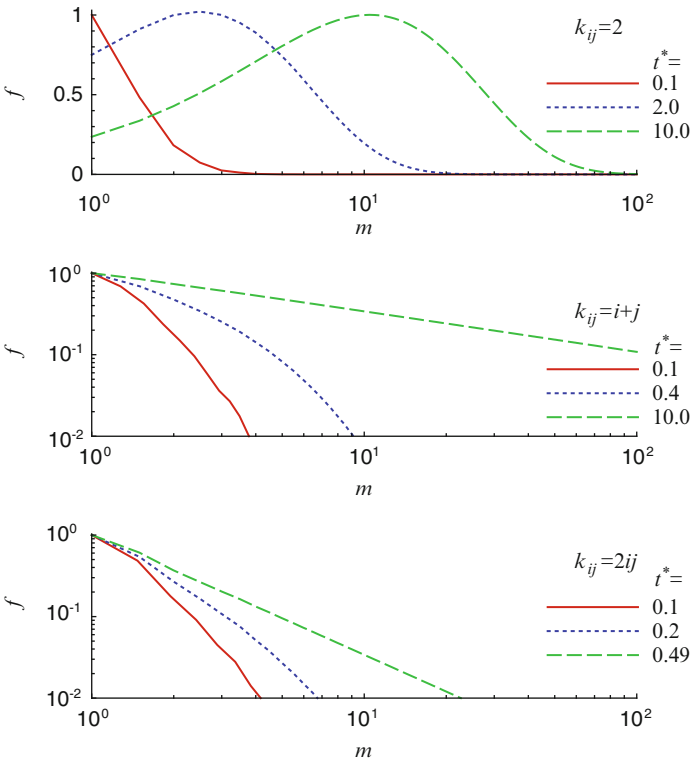


**Fig. 8** Normalized cluster distribution functions $f(m) = mn_m/(mn_m)_{\max}$ for constant ($k_{ij} = 2$), sum ($k_{ij} = i + j$), and product ($k_{ij} = 2ij$) kernels at different dimensionless times $t^* = t/\tau_a$

Note that Brownian kernel $k_{ij}^{B}$ has a constant value of about 2 when $i \approx j$. The kernels for Brownian $(k_{ijf}^{B})$ or ballistic $(k_{ijf}^{b})$ aggregation of fractal particles are [147]:

$$k_{ijf}^{B} \simeq \frac{1}{2}\left(i^{-1/d_f} + j^{-1/d_f}\right)\left(i^{1/d_f} + j^{1/d_f}\right), \tag{49}$$

$$k_{ijf}^{b} \simeq \frac{1}{2}\left(i^{-1} + j^{-1}\right)^{1/2}\left(i^{1/d_f} + j^{1/d_f}\right), \tag{50}$$

where $d_f$ is the fractal dimension of the cluster.

The exact analytical solutions of PBE for Brownian and ballistic kernels have not yet been obtained. In slow aggregation regime, these kernel may be estimated as:

$$k_{ij}^{s,B(b)} = k_{ij}^{B(b)}/W_{ij}. \tag{51}$$

Note that the constant kernel kinetics is the slowest as compared to kinetics of the sum and product kernels. It is interesting to note that formation of the infinite

**Table 3** Classification of kernels among three different classes (I, II, III) and gelling (G) or non-gelling (N) behavior

| Kernel, $k_{i,j}$ | Type of kernel | Homogeneity parameter, $\lambda$ | Type of cluster union, $\mu$ | Class, behavior |
|---|---|---|---|---|
| 2 | Constant | 0 | 0 | II, N |
| $i + j$ | Sum | $\lambda$ | 0 | II, N |
| $2ij$ | Product | 2 | 1 | I, G |
| $1 + \left(\frac{i}{j}\right)^{1/3} + \left(\frac{j}{i}\right)^{1/3}$ | Brownian | $-1/3$ | 0 | III, N |
| $1 + \left(\frac{i}{j}\right)^{1/d_f} + \left(\frac{j}{i}\right)^{1/d_f}$ | Fractal Brownian | $-1/d_f$ | 0 | III, N |
| $\frac{1}{2}\left(\frac{1}{i} + \frac{1}{j}\right)^{1/2}\left(i^{1/d_f} + j^{1/d_f}\right)$ | Fractal ballistic | $1/d_f - 1/2$ | $-1/2$ | III, N |
| – | DLA | 0 | $\geq 0$ | I, N |
| – | RLA | 1 | $\geq -1$ | I, N |

See Fig. 9 for the relationship between $\lambda$ and $\mu$ and the behavior and class of kernel, respectively

cluster takes place for the product kernel within the finite time at $t_g = 0.5\tau_s$. It corresponds to the sol–gel transition. At time exceeding $t_g$, the particles belong to two different populations in the finite (sol phase) and infinite (gel phase) clusters [145].

## 4.4 Classification of Kernels

For simple aggregation models, the kernel $k_{ij}$ is usually a homogeneous function:

$$k_{ai,aj} = a^{\lambda} k_{ij}, \tag{52}$$

where $a$ is a positive constant and may be presented for large-size clusters as the product of powers $i^{\mu}$ and $j^{\nu}$ [148]:

$$k_{i,j} \simeq i^{\mu} j^{\nu}. \tag{53}$$

Here, $\mu$ and $\nu$ are exponents, $\nu = \lambda - \mu$, $i \ll j$, and $i \gg 1$, and kernels with $\lambda > 2$ and $\lambda > 1 + \mu$ are unphysical. The values of $\lambda$ and $\mu$ for different types of kernels are presented in Table 3.

Figure 9 shows the $\lambda$ versus $\mu$ diagram for different types of kernels. The class of the kernel is determined by the sign of the $\mu$ exponent. The big + big and big + small unions of particles form within the class I ($\mu > 0$) and class III ($\mu < 0$),

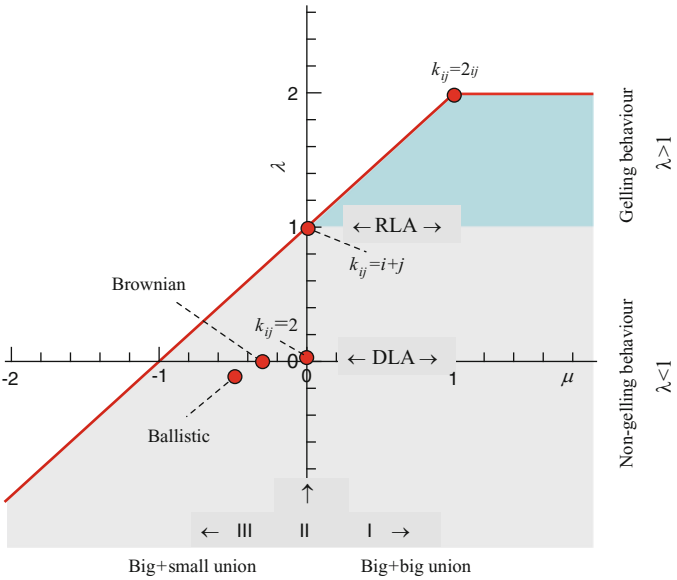


**Fig. 9** Classification of kernels. $\lambda$ versus $\mu$ diagram is presented. The *shaded area* corresponds to the physically plausible limit for $\lambda$ ($\leq 2$) and $\mu$ ($\leq \lambda - 1$)

respectively. For class II ($\mu = 0$), any type of union is probable. The kernels with $\lambda > 1$ and $\lambda \leq 1$ correspond to the gelling and non-gelling behavior, respectively. Finally, the well-known regimes of DLA and RSA aggregations correspond to the constant values of $\lambda = 0$ and $\lambda = 1$, respectively. The Brownian aggregation belongs to the DLA-type of aggregation and the sum kernel aggregation belongs to the RLA-type of aggregation. The simple product kernel $k_{ij} = 2ij$ corresponds to the gelling behavior at the limiting high value of $\lambda = 2$.

## 4.5 Dynamic Scaling

It was found in many experimental and theoretical studies of dynamic scaling that the time dependence of cluster distribution for long times, large $m$, and non-gelling system can be expressed as [149]:

$$n_m(t) \propto s(t)^{-2} f(m/s(t)), \tag{54}$$

where $f(x)$ is a scaling function that depends on the sign of $\mu$. The $f(x)$ decreases monotonically for kernels with $\mu \geq 0$ (I and II class), whereas it is a bell-shaped function for $\mu > 0$.

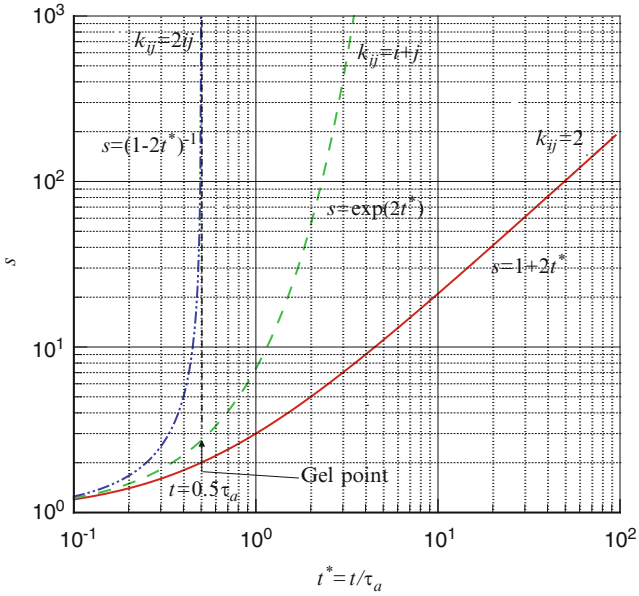


**Fig. 10** Mean cluster size $s(t)$ versus dimensionless time $t^* = t/\tau_a$ for different types of kernels. *Arrow* shows the gelling time, $t_g = 0.5\tau_a$ for the product kernel, $k_{ij} = 2ij$

The time dependence of mean cluster size $s(t)$ at $\lambda < 1$ follows:

$$s(t) \propto t^z, \tag{55}$$

at $\lambda = 1$, it follows:

$$s(t) \propto \exp(\alpha t), \tag{56}$$

and for gelling systems:

$$s(t) \propto (1 - t/t_g)^{\beta}. \tag{57}$$

Here, $\alpha$ and $\beta$ are constants and the following is a dynamic exponent:

$$z = 1/(1 - \lambda). \tag{58}$$

Note that continuous transition from $z = 1$ ($\lambda = 0$) to $z = \infty$ ($\lambda = 1$) corresponds to the transition from DLA to RLA model [150].

Figure 10 shows the examples of $s$ versus $t/\tau_a$ obtained from analytical solutions presented in Table 2 for constant ($k_{ij} = 2$), sum ($k_{ij} = i + j$), and product ($k_{ij} = 2ij$) kernels. It is important that the three basic kernels can be used for an approximate description of the main features of DLA (Eq. 55), RLA (Eq. 56), and gelling (Eq. 57) models.

Finally, both theory and experiments have shown a universal long-term behavior of the cluster-size distribution $n_m(t)$ for non-gelling systems, $\lambda < 1$ [148, 149]:

$$\begin{aligned} n_m(t)/n_1(t) &\to \infty, \quad \mu < 1 \\ n_m(t) &\sim t^{-w} m^{-\tau}, \quad \mu < 0, w > 1, \tau < \lambda + 1 \\ n_m(t) &\sim t^{-w} m^{-\tau}, \quad \mu > 1, w = 1, \tau = \lambda + 1 \end{aligned} \tag{59}$$

where $w$ and $\tau$ are the scaling exponents.

To date, the dynamic scaling in heteroaggregation within the PBE approach was mainly tested for the simplified kernels. Practical applications of Eq. 51 for kernel estimation is restricted because of the absence of detailed relations for interactions of real particles with the fractal structure or rough surface.

The realistic kernels of different types were tested for a description of RLA aggregation [151–153]. The following two types of kernels:

$$k_{ij} = \frac{k_{ij}^{\mathrm{B}} f}{W_{ij}} (ij)^{\lambda} \tag{60}$$

and:

$$k_{ij} = \frac{k_{ij}^{\mathrm{B}} f}{W_{ij}} \frac{(ij)^{\lambda}}{1 + \left[(ij)^{\lambda} - 1\right]/W_{ij}}, \tag{61}$$

were used for comparison of the theory and experiments [151]. Here, $k_{ij}^{\mathrm{B}} f$ is the Brownian kernel of fractal particles and $W_{ij}$ is the stability ratio.

It was assumed that the stability ratio is constant in the course of aggregation, $W_{ij} \approx W^{\mathrm{in}}$. The initial value, $W^{\mathrm{in}}$, was experimentally determined for polymer latex particles in aqueous suspensions. The aggregation rate was measured at the very initial stage, where the presence of triplets was negligible [151]. The kernels in Eqs. 60, 62 were found to be appropriate for simulation of experimental results subject to proper tuning of the exponent $\lambda$. Moreover, the kernels in Eq. 62 were suitable for description of the continuous transition from DLA-like aggregation at $W = 1$ to RLA-like aggregation at $W \to \infty$ [152].

The Brownian dynamic simulations of aggregation between the oppositely charged particles were made using classical DLVO potential [111]. The results were compared with theoretical calculations using a twofold homogeneous kernel, $k_{ij} \propto (i + j)^{\lambda}$, where $\lambda$ ($\leq 0$) is the homogeneity parameter. The exponent $z$ (see, Eq. 58) obtained from simulation was an increasing function of $r/\lambda_{\mathrm{D}}$. The continuous transition from ballistic-like aggregation, at low $r/\lambda_{\mathrm{D}}$ ($z < 1$), to DLA-like aggregation, at high $r/\lambda_{\mathrm{D}}$ ($z = 1$), was observed. Most of the features of charge heteroaggregation kinetics obtained using Brownian dynamic simulation were well described by the PBE theory with dynamic exponent $z$ estimated as $\simeq 1/(1 - \lambda)$.

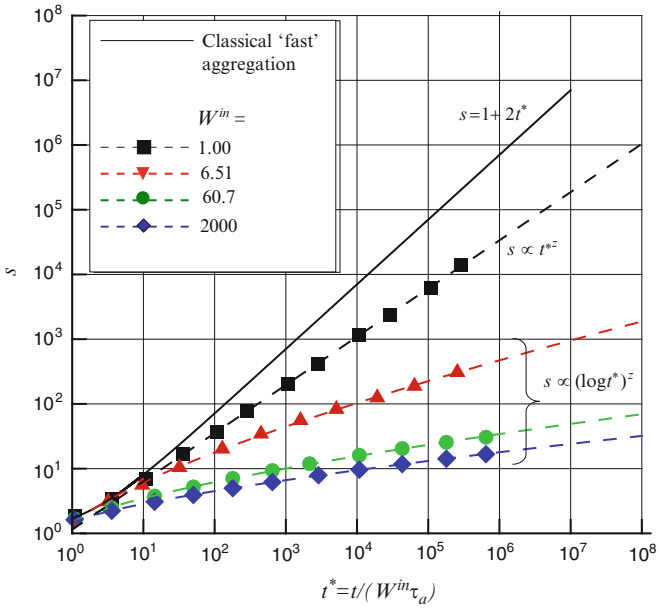


**Fig. 11** Mean particle size $s$ versus dimensionless time $t^* = t/W^{in}\tau_a$ for different initial values of stability ratios $W^{in} = 1$, $W^{in} = 6.51$ ($\lambda_D = 1$ nm), $W^{in} = 60.7$ ($\lambda_D = 2$ nm), and $W^{in} = 2{,}000$ ($\lambda_D = 9$ nm). The *solid line* corresponds to the classical model of fast aggregation, where size dependence of the aggregate diffusion coefficient is neglected. *Dashed lines* are results of approximation by the power law ($s \propto t^{*z}$, $W^{in} = 1$), or logarithmic power law ($s \propto (\log t^*)^z$, $W^{in} > 1$) The simulations were done assuming $A = 10^{-20}$ J and $\zeta = 40$ mV. Compiled from published data [154]

Recently, computer simulations of the aggregation process of PEC nanoparticles were carried out [154]. The aggregation kinetics was studied accounting for the size dependence of the aggregate diffusion coefficient, classical DLVO potential for interactions between two unequal particles, and Fuchs stability ratio with hydrodynamic corrections. It was assumed that the value of stability factor $W_{ij}$ is not constant and depends upon the size and charge of aggregating species. Figure 11 presents the calculated time dependencies of mean particle size $s$ for different initial values of the stability ratio $W^{in} = W_{ij}(t = 0)$. The classical constant rate approximation results in overestimation of the mean size of a particle compared to the non-classical model of fast aggregation ($W_{ij} = 1$) with the size-dependent diffusion coefficient. Note that both models follow the power law $s(t)$ dependence (Eq. 55), but with different dynamic exponents, $z = 1$ and $z = 0.745 \pm 0.005$, for the classical and non-classical models of fast aggregation, respectively (Fig. 11). The simulated data show a noticeable deviation of $s(t)$ curves for slow aggregation ($W^{in} > 1$) from the same curves for fast aggregation ($W^{in} = 1$).

Moreover, analysis of data presented by Starchenko et al. [154] have shown that the universal logarithmic scaling:

$$s(t) \propto (\log t)^z, \tag{62}$$

with the same exponent $z = 0.70 \pm 0.01$ was observed for all the studied values of $W^{\text{in}}$ (>1).

This result reflects a noticeable increase in $W_{ij}$ stability ratios in the course of aggregation compared to the initial value $W^{\text{in}}$. The data demonstrate also that enhancement of the electrostatic repulsion, related to the increase in the Debye length $\lambda_{\text{D}}$ or $\zeta$ potential, results in a retardation of the growth. Good correspondence between theory and experiment was observed at small Debye length, $\lambda_{\text{D}} < 3$–5 nm, in the so-called colloid regime. However, the effect of electrolyte on the PEC conformation became important at larger $\lambda_{\text{D}}$ and simulation failed to describe experiments [154].

## 5 Conclusion

The study of aggregation has been intensively developed during the last 100 years and is relatively mature. However, aggregation is a very complex problem and this field still remains an open research area. Colloid stability is basically defined by interparticle forces of different origin and interaction length. The exact analytical expressions have not yet been obtained for many important contributions. Moreover, in suspensions of charged particles, the long-range and many-body effects, collective correlations between charges, and the effects of charges heterogeneously distributed on the surface of particles (so-called patchy surfaces [155]) may be particularly important. For polymeric systems, the emphasis should be directed towards the interaction between core–shell particles containing a compact core and covered by a charged soft shell. The theory and experiments show realization of the different morphologies of the aggregates, including compact, linear-like, branched, fractal, and mixed morphologies. However, the advantages of computer simulations are still restricted by relatively small and closed systems and, as a rule, the use of very primitive models for interparticle potentials. The theoretical understanding of aggregation kinetics is mainly based on original Smoluchowski theory (1917) and oversimplified assumptions about the size dependence of both the cluster diffusion coefficient and sticking probability. More complex analysis is required to account for the restructuring of aggregates, which can be particularly important for clusters with fractal morphology [156]. Finally, the aggregation processes in PEC nanoparticles are still far from being fully understood. For these systems, which behave as suspensions of core–shell particles, the impact of polyelectrolyte conformations on the final size of nanoparticles was revealed [154]. Future progress needs the range of experimentally studied types of polyions to be broadened and the development of more sophisticated theories in order to prepare aggregates of PEC particles with desired size and properties.

**Acknowledgements** The author appreciates the financial support from the National Academy of Sciences of Ukraine and Dr. N. S. Pivovarova for her help with the preparation of the manuscript.

## References

1. Mohanraj VYC (2006) Nanoparticles a review. Trop J Pharm Res 5(1):561–573
2. Hartig S, Greene R, Dikov M, Prokop A, Davidson J (2007) Multifunctional nanoparticulate polyelectrolyte complexes. Pharmaceut Res 24:2353–2369. doi:10.1007/s11095-007-9459-1
3. Lankalapalli S, Kolapalli VRM (2009) Polyelectrolyte complexes: a review of their applicability in drug delivery technology. Indian J Pharm Sci 71(5):481–487. doi:10.4103/0250-474X.58165
4. Muller M, Kesler B, Frohlich J, Poeschla S, Torger B (2011) Polyelectrolyte complex nanoparticles of poly(ethyleneimine) and poly(acrylic acid): preparation and applications. Polymer 3(2):762–778. doi:10.3390/polym3020762
5. Müller M, Reihs T, Ouyang W (2005) Preparation of monomodal polyelectrolyte complex nanoparticles of pdadmac/poly(maleic acid-alt-alpha-methylstyrene) by consecutive centrifugation. Langmuir 21(1):465–469
6. Dautzenberg H (2000) Light scattering studies on polyelectrolyte complexes. Macromol Symp 162:1–21
7. Panyam P, Labhasetwar V (2003) Biodegradable nanoparticles for drug and gene delivery to cells and tissue. Adv Drug Deliv Rev 55:329–347
8. Derjaguin BV, Landau L (1941) Theory of the stability of strongly charged lyophobic sols and of the adhesion of strongly charged particles in solutions of electrolytes. Acta Phys Chim USSR 14:633–662
9. Verwey EJW, Overbeek JTG (1948) Theory of the stability of lyophobic colloids. Elsevier, Amsterdam
10. Quemada D, Berli C (2002) Energy of interaction in colloids and its implications in rheological modeling. Adv Colloid Interface Sci 98(1):51–85. doi:10.1016/S0001-8686(01)00093-8
11. Eastman J (2010) Stability of charge-stabilised colloids. In: Colloid science: principles, methods and applications, 2nd edn. Wiley-Blackwell
12. Derjaguin BV (1934) Untersuchungen ueber die reibung und adhaesion IV. Theorie des anhaften kleiner teilchen. Kolloid Z 69:155–164
13. Israelachvili J (1991) Intermolecular and surface forces. Academic, New York
14. Shaw DJ (1992) Introduction to colloid and surface chemistry. Butterworth-Heinemann, Oxford
15. Mahanty J, Ninham B (1976) Dispersion forces. Academic, New York
16. Russel WB, Saville DA, Schowalter WR (1989) Colloidal dispersions. Cambridge University Press, New York
17. Malins A, Williams SR, Eggers J, Tanaka H, Royall CP (2011) The effect of inter-cluster interactions on the structure of colloidal clusters. J Non-Cryst Solids 357(2):760–766. doi:10.1016/j.jnoncrysol.2010.08.021
18. dos Santos AP, Diehl A, Levin Y (2009) Electrostatic correlations in colloidal suspensions: density profiles and effective charges beyond the Poisson-Boltzmann theory. J Chem Phys 130:124110
19. Hogg R, Healy TW, Fuerstenau DW (1966) Mutual coagulation of colloidal dispersions. Trans Faraday Soc 62:1638–1651. doi:10.1039/TF9666201638
20. Ohshima H, Healy TW, White LR (1982) Improvement on the Hogg-Healy-Fuerstenau formulas for the interaction of dissimilar double layers: I. Second and third approximations for moderate potentials. J Colloid Interface Sci 89(2):484–493. doi:10.1016/0021-9797(82)90199-0

21. Elimelech M, Gregory J, Jia XWR (1995) Particle deposition and aggregation – measurement, modelling and simulation. Elsevier, Amsterdam
22. Boroudjerdi H, Kim YW, Naji A, Netz R, Schlagberger X, Serr A (2005) Statics and dynamics of strongly charged soft matter. Phys Rep 416(3–4):129–199. doi:10.1016/j.physrep. 2005.06.006
23. Kékicheff P, Spalla O (1995) Long-range electrostatic attraction between similar, charge-neutral walls. Phys Rev Lett 75:1851–1854. doi:10.1103/PhysRevLett.75.1851
24. Kjellander R (1996) Ion-ion correlations and effective charges in electrolyte and macroion systems. Ber Bunsen Phys Chem 100(6):894–904. doi:10.1002/bbpc.19961000635
25. Larsen AE, Grier DG (1997) Like-charge attractions in metastable colloidal crystallites. Nature 385:230–233
26. Levin Y (2002) Electrostatic correlations: from plasma to biology. Rep Prog Phys 65:1577–1632
27. Bohinc K, Zelko J, Sunil Kumar PB, Iglic A, Kralj-Iglic V (2009) Attraction of like-charged surfaces mediated by spheroidal nanoparticles with spatially distributed electric charge: theory and simulation. In: Advances in planar lipid bilayers and liposomes, vol 9. Academic, Burlington
28. Vlachy V (1999) Ionic effects beyond Poisson-Boltzmann theory. Annu Rev Phys Chem 50:145–165
29. Shklovskii BI (1999) Screening of a macroion by multivalent ions: correlation-induced inversion of charge. Phys Rev E 60:5802–5811. doi:10.1103/PhysRevE.60.5802
30. Patra M, Patriarca M, Karttunen M (2003) Stability of charge inversion, thomson problem, and application to electrophoresis. Phys Rev E 67:031402. doi:10.1103/PhysRevE.67.031402
31. Levin Y (1999) When do like charges attract? Physica A 432:432–439
32. Levin Y (2005) Strange electrostatics in physics, chemistry, and biology. Physica A 352(1): 43–52. doi:10.1016/j.physa.2004.12.033
33. Trizac E, Raimbault JL (1999) Long-range electrostatic interactions between like-charged colloids: steric and confinement effects. Phys Rev 60:6530–6533
34. Kirkwood JG, Shumaker JB (1952) Forces between protein molecules in solution arising from fluctuations in proton charge and configuration. Proc Natl Acad Sci USA 38:863–871
35. Grønbech-Jensen N, Mashl RJ, Bruinsma RF, Gelbart WM (1997) Counterion-induced attraction between rigid polyelectrolytes. Phys Rev Lett 78:2477–2480. doi:10.1103/PhysRevLett.78.2477
36. Belloni L, Spalla O (1997) Attraction of electrostatic origin between colloids. J Chem Phys 107(2):465–480. doi:10.1063/1.474408
37. Podgornik R, Parsegian VA (1998) Charge-fluctuation forces between rodlike polyelectrolytes: pairwise summability reexamined. Phys Rev Lett 80:1560–1563. doi:10.1103/PhysRevLett.80.1560
38. Squires TM, Brenner MP (2000) Like-charge attraction and hydrodynamic interaction. Phys Rev Lett 85:4976–4979. doi:10.1103/PhysRevLett.85.4976
39. Allahyarov E, D'Amico I, Löwen H (1998) Attraction between like-charged macroions by coulomb depletion. Phys Rev Lett 81:1334–1337. doi:10.1103/PhysRevLett.81.1334
40. Manning GS (1969) Limiting laws and counterion condensation in polyelectrolyte solutions I. Colligative properties. J Chem Phys 51(3):924–933. doi:10.1063/1.1672157
41. Arenzon J, Stilck J, Levin Y (1999) Simple model for attraction between like-charged polyions. Eur Phys J B 12:79–82
42. Tokuyama M (1998) Theory of slow dynamics in highly charged colloidal suspensions. Phys Rev E 58:R2729–R2732. doi:10.1103/PhysRevE.58.R2729
43. Tokuyama M (1999) Effective forces between macroions in highly charged colloidal suspensions. Phys Rev E 59:R2550–R2553. doi:10.1103/PhysRevE.59.R2550
44. Terada Y, Tokuyama M (2004) Novel liquid- and crystal-droplet phases on highly charged colloidal suspensions. Physica A 334(3–4):327–334. doi:10.1016/j.physa.2003.10.078
45. Fitch RM (1997) Polymer colloids. Academic, New York

46. Velegol D, Thwar PK (2001) Analytical model for the effect of surface charge nonuniformity on colloidal interactions. Langmuir 17:7687–7693. doi:10.1021/la010634z
47. Czarnecki J (1985) The effects of surface inhomogeneities on the interactions in colloidal systems and colloid stability. Adv Colloid Interface Sci 24:283–319. doi:10.1016/0001-8686(85)80035-X
48. Grant M, Saville D (1995) Electrostatic interactions between a nonuniformly charged sphere and a charged surface. J Colloid Interface Sci 171(1):35–45. doi:10.1006/jcis.1995.1148
49. Stankovich J, Carnie SL (1999) Interactions between two spherical particles with nonuniform surface potentials: the linearized poissonboltzmann theory. J Colloid Interface Sci 216 (2):329–347. doi:10.1006/jcis.1999.6326
50. Schowalter WR, Eidsath AB (2001) Brownian flocculation of polymer colloids in the presence of a secondary minimum. Proc Natl Acad Sci USA 98:3644–3651. doi:10.1073/pnas.061028498
51. Podgornik R, Harries D, DeRouchey J, Strey HH, Parsegian VA (2008) Interactions in macromolecular complexes used as nonviral vectors for gene delivery. In: Gene and cell therapy: therapeutic mechanisms and strategies. CRC, Burlington
52. Morales V, Anta JA, Lago S (2003) Integral equation prediction of reversible coagulation in charged colloidal suspensions. Langmuir 19:475–482
53. de Gennes P (1981) Polymer solutions near an interface. 1. Adsorption and depletion layers. Macromolecules 14:1637–1644
54. de Gennes P (1982) Polymer solutions near an interface. 2. Interaction between two plates carrying adsorbed polymer layers. Macromolecules 15:492–500
55. Runkana V, Somasundaran P (2007) Mathematical modeling of coagulation and flocculation of colloidal suspensions incorporating the influence of surface forces. In: Colloid stability and application in pharmacy. Colloid and interface science series, vol 3. Wiley-VCH, Weinheim
56. Runkana V, Somasundaran P, Kapur P (2006) A population balance model for flocculation of colloidal suspensions by polymer bridging. Chem Eng Sci 61:182–191
57. Somasundaran P, Runkana V (2009) Aggregation of colloids: recent developments in population balance modeling. In: Highlights in colloid science. Wiley-VCH, Weinheim
58. Grier DG, Behrens SH (2001) Interactions in colloidal suspensions: electrostatics, hydrodynamics and their interplay. In: Electrostatic effects in biophysics and soft matter. Kluwer, Dordrecht
59. Derjaguin B, Muller V (1967) Slow coagulation of hydrophobic colloids. Dokl Akad Nauk SSSR 176:738–741
60. Spielman LA (1970) Viscous interactions in brownian coagulation. J Colloid Interface Sci 33(4):562–571. doi:10.1016/0021-9797(70)90008-1
61. Brenner H (1961) The slow motion of a sphere through a viscous fluid towards a plane surface. Chem Eng Sci 16(34):242–251. doi:10.1016/0009-2509(61)80035-3
62. Honig E, Roebersen G, Wiersema P (1971) Effect of hydrodynamic interaction on the coagulation rate of hydrophobic colloids. J Colloid Interface Sci 36(1):97–109. doi:10.1016/0021-9797(71)90245-1
63. Kovalchuk N, Starov V (2011) Aggregation in colloidal suspensions: effect of colloidal forces and hydrodynamic interactions. Adv Colloid Interface Sci. doi:10.1016/j.cis.2011.05.009
64. Cao X, Cummins H, Morris J (2012) Hydrodynamic and interparticle potential effects on aggregation of colloidal particles. J Colloid Interface Sci 368(1):86–96. doi:10.1016/j.jcis.2011.11.050
65. Furukawa A, Tanaka H (2010) Key role of hydrodynamic interactions in colloidal gelation. Phys Rev Lett 104:245702. doi:10.1103/PhysRevLett. 104.245702
66. Riese DO, Wegdam GH, Vos WL, Sprik R, Fenistein D, Bongaerts JH, Grübel G (2000) Effective screening of hydrodynamic interactions in charged colloidal suspensions. Phys Rev Lett 85(25):5460–5464

67. Muthukumar M (1997) Dynamics of polyelectrolyte solutions. J Chem Phys 107 (7):2619–2635. doi:10.1063/1.474573
68. Muthukumar M (2005) Polyelectrolyte dynamics. In: Rice SA (ed) Advances in chemical physics, vol 131. Wiley, Hoboken
69. Arunachalam V, Marlow WH, Lu JX (1998) Development of a picture of the van der Waals interaction energy between clusters of nanometer-range particles. Phys Rev E 58:3451–3457
70. Babick F, Schiel K, Stintz M (2011) Van-der-Waals interaction between two fractal aggregates. Adv Powder Technol 22(2):220–225. doi:10.1016/j.apt.2010.11.014
71. Schiesl K, Babick F, Stintz M (2012) Calculation of double layer interaction between colloidal aggregates. Adv Powder Technol 23(2):139–147. doi:10.1016/j.apt.2011.01.005
72. Vicsek T (1992) Fractal growth phenomena. Word Scientific, Singapore
73. Smoluchowski M (1917) Uber brownsche molekularbewegung unter einwirkung auserer kruafte und deren zusammenhang mit der verallgemeinerten diffusions- gleichung. Ann Phys-Leipzig 48:1103–1112
74. Meakin P (1999) A historical introduction to computer models for fractal aggregates. J Sol–gel Sci Technol 15:97–117
75. Witten TA, Sander LM (1981) Diffusion-limited aggregation, a kinetic critical phenomenon. Phys Rev Lett 47:1400–1403
76. Sutherland D (1966) Comment on Vold's simulation of floc formation. J Colloid Interface Sci 22:300
77. Sutherland DN (1967) A theoretical model of floc structure. J Colloid Interface Sci 25:373–380
78. Vold M (1963) Computer simulation of floe formation in a colloidal suspension. J Colloid Sci 18:684–695
79. Eden M (1961) A two-dimensional growth process. In: Proceedings of the Fourth Berkeley Symposium on Mathematics, Statistics and Probability, vol 4: Biology and Problems of Health. University of California Press, Berkeley
80. Jullien R, Botet R (1987) Aggregation and fractal aggregation. World Scientific, Singapore
81. Aubert C, Cannell DS (1986) Restructuring of colloidal silica aggregates. Phys Rev Lett 56:738–741. doi:10.1103/PhysRevLett.56.738
82. Liu J, Shih WY, Sarikaya M, Aksay IA (1990) Fractal colloidal aggregates with finite interparticle interactions: energy dependence of the fractal dimension. Phys Rev A 41:3206–3213. doi:10.1103/PhysRevA.41.3206
83. Jia Z, Wu H, Morbidelli M (2007) Thermal restructuring of fractal clusters: the case of a strawberry-like core-shell polymer colloid. Langmuir 23:5713–5721. doi:10.1021/la063254s
84. Jullien R, Meakin P (1989) Simple models for the restructuring of three-dimensional ballistic aggregates. J Colloid Interface Sci 127(1):265–272. doi:10.1016/0021-9797(89)90027-1
85. Shih WY, Aksay IA, Kikuchi R (1987) Reversible-growth model: cluster-cluster aggregation with finite binding energies. Phys Rev A 36:5015–5019. doi:10.1103/PhysRevA.36.5015
86. Rioux C, Slobodrian RJ (2012) Experimental discrimination of electrostatic and magnetic forces in particle-particle aggregation. Adv Space Res 49(10):1408–1414
87. Groenewold J, Kegel WK (2004) Colloidal cluster phases, gelation and nuclear matter. J Phys Condens Matter 16:S4877–S4886
88. Sciortino F, Mossa S, Zaccarelli E, Tartaglia P (2004) Equilibrium cluster phases and low-density arrested disordered states: the role of short-range attraction and long-range repulsion. Phys Rev Lett 93:055701
89. Rayleigh L (1882) On the equilibrium of liquid conducting masses charged with electricity. Philos Mag 14:184–186
90. Smirnov BM (2006) Cluster processes in gases and plasmas. Distributions, structures, phenomena, kinetics of atomic systems. Wiley-VCH, Weinheim
91. Weizsacker CFV (1935) Zur theorie der kernmassen. Z Phys 96:431–458
92. Lu PJ, Conrad JC, Wyss HM, Schofield AB, Weitz DA (2006) Fluids of clusters in attractive colloids. Phys Rev Lett 96:028306. doi:10.1103/PhysRevLett.96.028306

93. Lu PJ, Zaccarelli E, Ciulla F, Schofield AB, Sciortino F, Weitz DA (2008) Gelation of particles with short-range attraction. Nature 453:499–503. doi:10.1038/nature06931
94. de Gennes P, Pincus P, Velasco R, Brochard F (1976) Remarks on polyelectrolyte conformation. J Phys-Paris 37(12):1461–1473
95. Brender C, Danino M, Shatz S (1999) Fractals in Monte Carlo simulations of a short polyelectrolyte. J Phys A Math Gen 32(2):235
96. Fernandez-Toledano JC, Moncho-Jorda A, Martinez-Lopez F, Gonzalez AE, Hidalgo-Alvarez R (2007) Two-dimensional colloidal aggregation mediated by the range of repulsive interactions. Phys Rev E 75:041408. doi:10.1103/PhysRevE.75.041408
97. Mossa S, Sciortino F, Tartaglia P, Zaccarelli E (2004) Ground-state clusters for short-range attractive and long-range repulsive potentials. Langmuir 20(24):10756–10763. doi:10.1021/la048554t
98. Sciortino F, Tartaglia P, Zaccarelli E (2005) One-dimensional cluster growth and branching gels in colloidal systems with short-range depletion attraction and screened electrostatic repulsion. J Phys Chem B 109(46):21942–21953. doi:10.1021/jp052683g
99. Chakrabarty RK, Moosmuller H, Garro MA, Arnott WP, Slowik JG, Cross ES, Jeong-Ho Han PD, Onasch TB, Worsnop DR (2008) Morphology based particle segregation by electrostatic charge. J Aerosol Sci 39(9):785–792
100. Block A, van Blah W, Schellnhuber HJ (1991) Aggregation by attractive particle-cluster interaction. J Phys A Math Gen 24:L1037–L1044
101. Indiveri G, Scalas E, Levi A, Gliozzi A (1999) Morphologies in two-dimensional growth with attractive long-range interactions. Physica A 273(3–4):217–230. doi:10.1016/S0378-4371(99)00231-9
102. Meakin P (1990) The effects of attractive and repulsive interactions on three-dimensional reaction-limited aggregation. J Colloid Interface Sci 134(1):235–244. doi:10.1016/0021-9797(90)90271-O
103. Meakin P, Muthukumar M (1989) The effects of attractive and repulsive interaction on two-dimensional reaction-limited aggregation. J Chem Phys 91(5):3212–3221. doi:10.1063/1.456942
104. Indiveri G, Levi A, Gliozzi A, Scalas E (1996) Cluster growth with long-range interactions. Thin Solid Films 284–285:106–109
105. Ivanenko Y, Lebovka N, Vygornitskii N (1999) Eden growth model for aggregation of charged particles. Eur Phys J B 11:469–480
106. Lebovka NI, Ivanenko YV, Vygornitskii NV (1998) Deterministic eden model of charged-particles aggregation. Europhys Lett 41(1):19
107. Pinchuk AO, Kalsin AM, Kowalczyk B, Schatz GC, Grzybowski BA (2007) Modeling of electrodynamic interactions between metal nanoparticles aggregated by electrostatic interactions into closely-packed clusters. J Phys Chem C 111(32):11816–11822. doi:10.1021/jp073403v
108. Zhang R, Shklovskii B (2005) Phase diagram of solution of oppositely charged polyelectrolytes. Physica A 352(1):216–238. doi:10.1016/j.physa.2004.12.037
109. Harnau L, Hansen JP (2002) Colloid aggregation induced by oppositely charged polyions. J Chem Phys 116(20):9051–9057. doi:10.1063/1.1471550
110. Puertas A, Fernandez-Barbero A, De las Nieves F (2000) Aggregation between oppositely charged colloidal particles. In: Buckin V (ed) Trends in colloid and interface science XIV. Progress in colloid and polymer science, vol 115. Springer, Berlin, pp 55–58
111. Puertas A, Fernandez-Barbero A, de las Nieves F (2002) Kinetics of colloidal heteroaggregation. Physica A 304(34):340–354. doi:10.1016/S0378-4371(01)00564-7
112. Kim AY, Hauch KD, Berg JC, Martin JE, Anderson RA (2003) Linear chains and chain-like fractals from electrostatic heteroaggregation. J Colloid Interface Sci 260(1):149–159. doi:10.1016/S0021-9797(03)00033-X

113. Cerbelaud M, Videcoq A, Abelard P, Pagnoux C, Rossignol F, Ferrando R (2008) Heteroaggregation between $Al_2O_3$ submicrometer particles and $SiO_2$ nanoparticles: experiment and simulation. Langmuir 24(7):3001–3008. doi:10.1021/la702104u
114. Cerbelaud M, Videcoq A, Abelard P, Ferrando R (2009) Simulation of the heteroagglomeration between highly size-asymmetric ceramic particles. J Colloid Interface Sci 332 (2):360–365. doi:10.1016/j.jcis.2008.11.063
115. Piechowiak MA, Videcoq A, Ferrando R, Bochicchio D, Pagnoux C, Rossignol F (2012) Aggregation kinetics and gel formation in modestly concentrated suspensions of oppositely charged model ceramic colloids: a numerical study. Phys Chem Chem Phys 14:1431–1439. doi:10.1039/C1CP22980J
116. Castelnovo M, Sens P, Joanny JF (2000) Charge distribution on annealed polyelectrolytes. Eur Phys J E 1:115–125
117. Coslovich D, Hansen J, Kahl G (2011) Ultrasoft primitive model of polyionic solutions: structure, aggregation, and dynamics. J Chem Phys 134(24):244514 (15 pages), www.scopus.com
118. Coslovich D, Hansen JP, Kahl G (2011) Clustering, conductor-insulator transition and phase separation of an ultrasoft model of electrolytes. Soft Matter 7:1690–1693. doi:10.1039/C0SM01090A
119. Lee J, Popov YO, Fredrickson GH (2008) Complex coacervation: a field theoretic simulation study of polyelectrolyte complexation. J Chem Phys 128(22):224908. doi:10.1063/1.2936834
120. Rydén J, Ullner M, Linse P (2005) Monte Carlo simulations of oppositely charged macroions in solution. J Chem Phys 123(3):034909. doi:10.1063/1.1949191
121. Zito T, Seidela C (2002) Equilibrium charge distribution on annealed polyelectrolytes. Eur Phys J E 8:339–346
122. Buchhammer HM, Mende M, Oelmann M (2003) Formation of mono-sized polyelectrolyte complex dispersions: effects of polymer structure, concentration and mixing conditions. Colloids Surf A 218(1):151–159. doi:10.1016/S0927-7757(02)00582-4
123. Buchhammer HM, Mende M, Oelmann M (2004) Preparation of monodisperse polyelectrolyte complex nanoparticles in dilute aqueous solution. In: Tauer K (ed) Aqueous polymer dispersions. Progress in colloid and polymer science, vol 124. Springer, Berlin, pp 98–102
124. Dobrynin AV (2008) Theory and simulations of charged polymers: from solution properties to polymeric nanomaterials. Curr Opin Colloid Interface Sci 13(6):376–388. doi:10.1016/j.cocis.2008.03.006
125. Oskolkov NN, Potemkin II (2007) Complexation in asymmetric solutions of oppositely charged polyelectrolytes:phase diagram. Macromolecules 40(23):8423–8429. doi:10.1021/ma0709304
126. Popov YO, Lee J, Fredrickson G (2007) Field-theoretic simulations of polyelectrolyte complexation. J Polym Sci Pol Phys 45:3223–3230
127. Dalakoglou G, Karatasos K, Lyulin S, Lyulin A (2008) Brownian dynamics simulations of complexes of hyperbranched polymers with linear polyelectrolytes: effects of the strength of electrostatic interactions on static properties. Mat Sci Eng B-Solid 152(1–3):114–118. doi:10.1016/j.mseb.2008.06.012
128. Skepo M, Linse P (2003) Complexation, phase separation, and redissolution in polyelectrolytemacroion solutions. Macromolecules 36:508–519
129. Feng J, Ruckenstein E (2003) Monte Carlo simulation of polyampholyte-nanoparticle complexation. Polymer 44(10):3141–3150. doi:10.1016/S0032-3861(03)00208-8
130. Ulrich S, Seijo M, Carnal F, Stoll S (2011) Formation of complexes between nanoparticles and weak polyampholyte chains. Monte Carlo simulations. Macromolecules 44:1661–1670
131. Sennato S, Truzzolillo D, Bordi F, Sciortino F, Cametti C (2009) Colloidal particle aggregates induced by particle surface charge heterogeneity. Colloids Surf A 343 (1–3):34–42. doi:10.1016/j.colsurfa.2009.01.026
132. Jeon J, Dobrynin AV (2005) Molecular dynamics simulations of polyampholyte-polyelectrolyte complexes in solutions. Macromolecules 38:5300–5312

133. Xu Y, Feng J, Liu H, Hu Y, Jiang J (2007) Molecular dynamics simulation of polyelectrolyte with oppositely charged monomeric and dimeric surfactants. Mol Simul 33(3):261–268. doi:10.1080/08927020601158679
134. Jullien R, Botet R, Mors PM (1987) Computer simulations of cluster-cluster aggregation. Faraday Discuss Chem Soc 83:125–137. doi:10.1039/DC9878300125
135. Mors PM, Botet R, Jullien R (1987) Cluster-cluster aggregation with dipolar interactions. J Phys A Math Gen 20:L975
136. Pastor-Satorras R, Rubi JM (1995) Particle-cluster aggregation with dipolar interactions. Phys Rev E 51:5994–6003
137. Pastor-Satorras R, Rubi R (1998) Fractal properties of cluster of colloidal magnetic particles. Prog Colloid Polym Sci 110:29–33
138. Pastor-Satorras R, Rubi J (2000) Dipolar interactions induced order in assemblies of magnetic particles. J Magn Magn Mater 221:124–131
139. Family F (1985) Kinetics of aggregation and gelation. Elsevier, Amsterdam
140. Meakin P (1992) Aggregation kinetics. Phys Scripta 46(4):295
141. Meakin P (1998) Fractals, scaling and growth far from equilibrium. Cambridge University Press, Cambridge
142. Fuchs N (1934) Ueber die stabilitat und aufladung der aerosole. Z Phys 89:736–743
143. Reerink H, Overbeek JTG (1954) The rate of coagulation as a measure of the stability of silver iodide sols. Faraday Discuss Chem Soc 18:74–84
144. Leyvraz F (2003) Scaling theory and exactly solved models in the kinetics of irreversible aggregation. Phys Rep 383:95–212
145. McLeod JB (1962) On an infinite set of non-linear differential equations. Q J Math 13:119–128
146. Melzak ZA (1953) The effects of coalescence in certain collision processes. Q J Mech Appl Math 11:231–234
147. Gmachowski L (2000) Estimation of the dynamic size of fractal aggregates. Colloids Surf A 170(23):209–216. doi:10.1016/S0927-7757(99)00532-4
148. Zift RM, McGrady ED, Meakin P (1985) On the validity of Smoluchowski's equation for cluster-cluster aggregation kinetics. J Chem Phys 82:5269–5274
149. Fernandez-Barbero A, Cabrerizo-Vilchez M, Martinez-Garcia R, Hidalgo-Alvarez R (1996) Effect of the particle surface charge density on the colloidal aggregation mechanism. Phys Rev E 53:4981–4989. doi:10.1103/PhysRevE.53.4981
150. Asnaghi D, Carpineti M, Giglio M, Sozzi M (1992) Coagulation kinetics and aggregate morphology in the intermediate regimes between diffusion-limited and reaction-limited cluster aggregation. Phys Rev A 45:1018–1023. doi:10.1103/PhysRevA.45.1018
151. Lattuada M, Sandkuhler P, Wu H, Sefcik J, Morbidelli M (2003) Aggregation kinetics of polymer colloids in reaction limited regime: experiments and simulations. Adv Colloid Interface Sci 103:33–56
152. Odriozola G, Moncho-Jorda A, Schmitt A, Callejas-Fernandez J, Martinez-Garcia R, Hidalgo-Alvarez R (2001) A probabilistic aggregation kernel for the computer-simulated transition from DLCA to RLCA. Europhys Lett 53:797803
153. Runkana V, Somasundaran P, Kapur PC (2005) Reaction-limited aggregation in presence of short-range structural forces. AICHE J 51:1233–1245
154. Starchenko V, Muller M, Lebovka N (2008) Growth of polyelectrolyte complex nanoparticles: computer simulations and experiments. J Phys Chem C 112:8863–8869
155. Bianchi E, Blaak R, Likos CN (2011) Patchy colloids: state of the art and perspectives. Phys Chem Chem Phys 13:6397–6410. doi:10.1039/C0CP02296A
156. Gruy F (2011) Population balance for aggregation coupled with morphology changes. Colloids Surf A 374(13):69–76. doi:10.1016/j.colsurfa.2010.11.010

Adv Polym Sci (2014) 255: 97–138
DOI: 10.1007/12_2012_203

Published online: 15 June 2013

# Ion Conduction in Solid Polyelectrolyte Complex Materials

**Cornelia Cramer and Monika Schönhoff**

**Abstract** This chapter describes the progress made in understanding the mechanisms of ion conduction in polyelectrolyte complexes (PEC). Understanding of ion dynamics is based on frequency-dependent conductivity data obtained by impedance spectroscopy as a function of temperature, hydration, and composition. In most of the work, strong polyelectrolytes such as poly(alkali 4-styrene sulfonate) (AlkaliPSS) and poly(diallyldimethyl ammoniumchloride) (PDADMAC) are employed, forming complexes of type $x$AlkaliPSS · $(1 - x)$ PDADMAC. The dc conductivity is always determined by the alkali ions, which exhibit a size-dependent mobility. This holds even in PEC with an excess of PDADMAC. The ion dynamics and transport mechanisms are different in PDADMAC-rich and in NaPSS-rich PEC. We review the treatment of the frequency-dependent shape of conductivity spectra by scaling concepts and by models involving forward–backward hopping motions of small ions as well as localized motions of charges. Thus, many quantitative concepts established in other disordered ion conductors can be transferred to PEC. In addition to the well-known time–temperature superposition principle (TTSP), the novel concept of time–humidity superposition (THSP) was established for PEC and describes the dependence of ion dynamics on water content.

**Keywords** Dielectric spectroscopy · Electrolyte · Impedance spectroscopy · Ion conductor · Ion dynamics · Polyelectrolyte complex

## Contents



C. Cramer and M. Schönhoff (✉)
Institute of Physical Chemistry, University of Muenster, Correnstraße 28/30, 48149 Münster, Germany
e-mail: cramerc@uni-muenster.de; schonhoff@uni-muenster.de

## 1 Introduction

The unusual properties of polymer networks formed by the complexation of oppositely charged polyions has already been the subject of very early research, following the initial work of Bungenberg de Jong et al. [1]. In these early days, polyelectrolyte complexes (PEC) had already been proposed as novel solid materials for a range of applications such as membranes for filtration or in fuel cells, as battery separators, as conductive coatings and so forth, as reviewed by Michaels [2]. Nevertheless, research on polyelectrolyte complexes as a solid material was sparse in the following decades. With the seminal work on the dielectric properties of *solid* complexes by Michaels [3–5] almost forgotten, a lot of research during the following years focused on *soluble* complexes in aqueous solution, and various structural models were discussed on the basis of scattering and other experiments. An overview is given by several review articles [6–8].

A major breakthrough was achieved with the advent of polyelectrolyte multilayers (PEM), the layered analogue to PEC, formed by the so-called layer-by-layer deposition of polyions with alternating sign of charge [9]. The process is predominantly driven by multiple electrostatic interactions and is therefore very versatile with respect to the different charged building blocks that can be employed in multilayer formation. External parameters such as salt concentration [10], pH value [11] or temperature [12] provide control of the layer thickness, which typically lies in the range of 1 nm per layer. Research in the field of PEM has vastly expanded in the past two decades, and there are numerous potential applications such as containers, sensors, drug delivery, etc. Various review articles provide information about structural aspects and summarize the properties of PEM [13–16].

With these developments, new interest arose in PEC as a solid material, partly due to the similarity to PEM concerning the local molecular structure so that they could act as reference material. The structural similarity was shown by solid state NMR, where the interatomic distances of the complexed monomers were found to be identical in PEC and in PEM [17]. Furthermore, employing regions of stability in dependence on electrolyte conditions, the phase diagrams of PEC and PEM systems are comparable to each other [18, 19]. The newer work on PEC was recently reviewed [20].

Renewed interest in solid PEC was, however, also strongly triggered by the rising demand for novel materials with tailored properties for electrochemical applications. Both types of competing devices, i.e. fuel cells and Li ion batteries require suitable materials acting as the polymer electrolyte membrane, which separates the electrodes and is required to exhibit a high ionic ($Li^+$ or protons, respectively) and negligible electronic conductivity. At the same time, the material has to allow thin film processing and exhibit high mechanical and chemical stability. In fuel cells, Nafion has long been the benchmark material, as it shows a microphase separation into hydrophobic, stabilizing domains and hydrated channels, where the interface (carrying free sulfate groups) provides the proton conduction properties [21]. In Li ion batteries, the classical state-of-the-art polymeric materials is poly(ethyleneoxide) (PEO) and many modifications thereof attempt to achieve a compromise between high mechanical stability and high ionic conductivity. One example is to apply salt-in-polymer electrolytes made from comb-shaped copolymers, which exhibit short oligoether side chains that can solubilize and transport the ions [22–24], while the backbone can be crosslinked to provide mechanical stability. Typically, such bulk polymers are then prepared as a thin membrane with a thickness in the micrometer range.

Aiming at applications in electrochemical energy devices, PEM fulfill two of the three main requirements because of their generic material properties: firstly, PEM layer thickness can be tuned in the nano- to micrometer range. A low film thickness is of advantage to yield low overall resistance and fast loading. Secondly, in spite of the low thickness, PEM are tremendously stable, which is an effect of the multiple electrostatic interactions between subsequent layers. Their mechanical properties have been extensively investigated in free-standing geometries, and Young's moduli of the order of gigapascal (GPa) have been found [25, 26].

A challenge remains, however, to fulfill the third requirement, which is to achieve large ionic conductivities in these films. In several publications, dc conductivities of PEM ranging from $10^{-12}$ S cm$^{-1}$ to $10^{-5}$ S cm$^{-1}$ have been reported [27–30]. Studies of the conductivities of PEM started with the seminal work by Durstock and Rubner who investigated films of PSS/PAH and PAA/PAH, where PAA denotes poly(acrylic acid), PSS is poly(styrene sulfonate sodium salt), and PAH is poly(allylamine hydrochloride). They found dc conductivities, $\sigma_{dc}$, in the range of $10^{-12}$ to $10^{-7}$ S cm$^{-1}$ [27], where the maximum of $10^{-7}$ S cm$^{-1}$ was achieved only at strong hydration. Further studies of conductivities in PEM suggested them as potential ion conductive materials for battery applications [28, 29]. When employing poly(2-acrylamido-2-methyl-1-propansulfonic acid)

(PAMPS) as a polyanion, at high humidity a dc conductivity of $\sigma_{dc} \approx 10^{-5}$ S cm$^{-1}$ was achieved, which is in a realistic range for applications [28]. Different polyelectrolyte pairs tested for their conductivity even involved polymers known as ion conductors in their bulk form, such as Nafion as an established proton conductor [28], PEO as a classical polymer electrolyte [29] or polyphosphazene, an optimized polymer electrolyte providing flexible main chains [30, 31].

However, despite these studies on conductivities of different types of PEM, a fundamental understanding of ion transport properties in PEM is not yet in sight. A major problem in the interpretation of conductivity data is the lack of knowledge about the composition of the films. Because PEM are formed by self-assembly, the compensation of surface charges upon chain adsorption controls the stoichiometry of the films. The excess charges of an outermost polyelectrolyte layer might become fully compensated by the oppositely charged segments of the subsequent layer ("intrinsic charge compensation"), or, if this is sterically not favorable, small counterions might incorporate into the film in order to compensate the polyion charges ("extrinsic charge compensation"). Thus, PEM are a material of unknown stoichiometry. Though in first approximation the gain of translational entropy of the small counterions would always lead to intrinsic charge compensation being favored, in a number of polyion combinations a deviation from a 1:1 stoichiometry of the polyions has been found and a substantial degree of extrinsic charge compensation by small counterions was concluded [32–34].

In hydrated multilayers, even protons can contribute to the conductivity. Several authors employ Nafion in multilayer formation and discuss protons as the dominating charge carriers in the dc conductivity [35–38]. The contribution of other ions was found to be negligible in hydrated PEM [39]. Indeed, the hydration state of the layer assembly has a strong influence on the conductivity, as shown when films are compared in the dry and the completely hydrated state [27, 28, 35]. A review of the activities up to 2007 is given by Lutkenhaus and Hammond [38]. It is generally argued that protons carry the current; however, an analysis of the contributions of other small counterions suffers from the lack of systematic knowledge about the composition of PEM.

Therefore, PEC act as a model material with the same local molecular structure of the complex, but have the advantage of a variable stoichiometry and known ion content. In PEC, the content of small cations and anions is known because it depends on the mixing ratio of the polyions. Furthermore, systems with mainly one type of counterion can be prepared if excess salt is removed by dialysis. In this way, conductivity data in dependence of the composition can be related to the conductivity contribution of a single type of charge carrier [40, 41]. For this purpose, solid PEC complexes have to be prepared from complexes formed in aqueous solution. The broad composition range includes both water-soluble as well as insoluble complexes, i.e. complex coacervates. Both can be treated by drying and subsequently pressing the polymer material to form a dense solid [40].

In this article we review the knowledge gained from impedance spectroscopy on such solid PEC materials. Dry and humidified complexes are investigated, the latter in systematic dependence of the relative humidity (RH), both as a function of composition and of temperature.

On the one hand, the simple dc conductivity provides information for discussion of the relevance of the contributions of different ionic species, such as the alkali cations, anions, or protons to the conductivity. The activation of ionic mobility by temperature or by increasing RH shows interesting analogies, such that humidity is considered as an activation parameter.

On the other hand, special focus is put on the shape of conductivity spectra. Modeling of different contributions to the spectra in the framework of concepts established in other well-characterized ion conductors sheds more light on the transport processes in PEC, especially on shorter time scales (see Sect. 3.4). Furthermore, in recent years general scaling concepts such as the time–temperature superposition principle (TTSP) have been applied to polyelectrolyte complexes. Their power in giving a generalized description of ionic transport processes is tremendous. In particular, a novel time–humidity superposition principle (THSP) was established (see Sect. 5.3). This review therefore also focuses on the basics and implications of ion transport models and scaling concepts.

## 2 Conductivity Spectra: Concepts and Initial Findings

### *2.1 Basic Concepts of Conductivity Spectroscopy*

Conductivity spectroscopy is a unique tool for studying the dynamics of ions in condensed matter. In many disordered ion-conducting materials, the motion of ions occurs via hopping processes where ions leave their sites and jump into vacant neighboring sites. Frequency-dependent conductivities have the advantage of providing information about ion dynamics on different time scales, the latter being given by the inverse angular frequency, $\omega$. Therefore, conductivity spectroscopy can be considered as a "microscope in time" [42]. Wide-range conductivity spectra probe the transition from elementary steps of the ionic movement to macroscopic transport. Applying linear response theory, the complex conductivity $\hat{\sigma}(\omega)$ is proportional to the Fourier transform of the current density autocorrelation function $\langle \mathbf{i}(0) \cdot \mathbf{i}(t) \rangle$:

$$\hat{\sigma}(\omega) = \frac{V}{3k_{\mathrm{B}}T} \cdot \int_0^\infty \langle \mathbf{i}(0) \cdot \mathbf{i}(t) \rangle \cdot \exp(-i\omega t) \mathrm{d}t, \tag{1}$$

where $T$ is the temperature and $k_{\mathrm{B}}$ is the Boltzmann constant. The current density can be expressed as a summation over all $N$ charge carriers:

$$\mathbf{i}(t) = \frac{1}{V} \cdot \sum_0^N q_i \cdot \mathbf{v}_i(t) \tag{2}$$

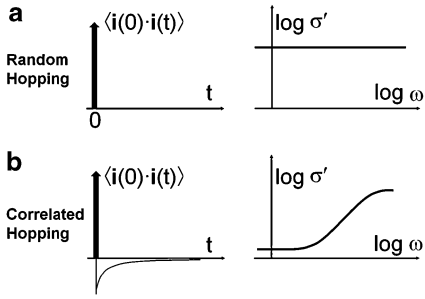


**Fig. 1** Random versus correlated jump diffusion: velocity autocorrelation functions and corresponding real parts of the complex conductivity [42]

with their charges and velocities denoted by $q_i$ and $v_i$, respectively. $V$ is the volume of the sample. Both $i(t)$ and its autocorrelation function are functions of time $t$. In the case that there is only one type of mobile charge carrier and if cross-correlations between movements of different ions $i$ and $j$ can be neglected (single particle approximation), the complex conductivity is simply expressed by the velocity autocorrelation function $\langle v(0) \cdot v(t) \rangle$:

$$\hat{\sigma}(\omega) = \frac{Nq^2}{3Vk_BT} \cdot \int_0^\infty \langle v(0) \cdot v(t) \rangle \cdot \exp(-i\omega t) \mathrm{d}t. \tag{3}$$

The complex conductivity $\hat{\sigma}(\omega)$ consists of a real part, denoted as $\sigma'(\omega)$ and an imaginary part denoted as $\sigma''(\omega)$:

$$\hat{\sigma}(\omega) = \sigma'(\omega) + \mathrm{i}\sigma''(\omega). \tag{4}$$

Similar to many complex physical quantities, the real and the imaginary part of the complex conductivity are interconnected via Kramers–Kronig-relations. This implies that $\sigma'(\omega)$ and $\sigma''(\omega)$ contain the same information and can be transformed into each other, provided that the complete experimental spectrum is known. In the work described in this review, both the real and the imaginary part of the complex conductivity were experimentally determined, but the discussion will focus on the real part of the conductivity. The dc conductivity is defined as the conductivity of the ion conducting material, which one would measure in the limit $\omega \rightarrow 0$ under conditions where the interface to the electrodes does not block ion transport ("non-blocking" electrodes).

The simplest approach to describe the ion dynamics in disordered materials is to assume completely uncorrelated, random ion movements [42]. In this case, the jump of an ion moving in a forward direction is only correlated to itself, thus the velocity autocorrelation function is proportional to a Dirac Delta function at $t = 0$ (see Fig. 1a). The complex conductivity obtained by Fourier transform is then independent of frequency. This means that the real part of the conductivity shows no dispersion and *at all frequencies* the ac conductivity $\sigma'(\omega)$ can be identified with the dc conductivity. By contrast, conductivity spectra of most ion-conducting materials show that $\sigma'(\omega)$ varies with frequency. This is schematically illustrated

in Fig. 1b, which has been redrawn from Funke et al. [42]. At low frequencies, a dc plateau is typically observed, but at higher frequencies $\sigma'(\omega)$ is found to increase with frequency. According to Fig. 1b, at even higher frequencies the conductivity should again reach another plateau region. The velocity autocorrelation function corresponding to the spectrum of Fig. 1b consists of a Dirac Delta function at $t = 0$, but also of a negative contribution that approaches zero at longer times. Such a negative autocorrelation has been termed backward correlation of ionic motion. It can be understood by using the general concept of the MIGRATION model developed by Funke and coworkers for commonly studied ion conductors such as inorganic glasses or crystals, polymeric materials, and ionic liquids [42–44]. The central idea of this model is that because of their mutual repulsive Coulomb interactions, equally charged mobile ions tend to stay apart from each other. If a mobile ion leaves its site by hopping into a vacant neighboring site, mismatch is created. The system then tends to reduce the mismatch, which can be done either by a correlated backward hop of the ion itself or by a rearrangement of its neighboring ions. In the first case, which forms the backward correlation effect on short time scales, the previous forward jump of the ion under consideration turns out to be unsuccessful, whereas in the second case the ion successfully moves to a new site. Successful hops are the basis for long-range ion transport.

With the MIGRATION concept in mind, one can easily understand the frequency dependence of $\sigma'(\omega)$ as presented in Fig. 1b. At small frequencies, the corresponding time window $\Delta t = 1/\omega$ is large enough to count only successful hops contributing to the long-range ion transport. In the conductivity spectrum, this corresponds to a dc conductivity plateau probed at low frequencies (see Fig. 1b). With increasing frequency, however, the time window of observation becomes small enough to also count forward jumps, which – on a longer time scale – will be cancelled by a backward hop. The dynamic conductivity therefore registers all jumps not proven unsuccessful within the given time window and the conductivity increases monotonously with frequency. When the time-window is so small that each ionic jump contributes to the conductivity, the latter should become constant again (high-frequency plateau) (see Fig. 1b). The existence of such a high-frequency plateaus has indeed been reported for experimental conductivity spectra of some crystalline ion-conductors, but these plateaus occur at frequencies much higher (typically in the gigahertz to terahertz regime); see for example [42] and references given therein.

## 2.2 *Early Dielectric and Conductivity Spectra of PEC*

As already mentioned in the Introduction, pioneering work on solid PEC dates back to the 1960s, when Michaels and coworkers published systematic studies on the frequency dependence of the complex permittivity [2, 3]. They investigated the influence of the RH and the concentration of dopant salt like NaBr, respectively, on the complex permittivity of PEC. The complexes were made of poly (vinyl benzyl trimethyl ammonium chloride) (PVBTAC) and sodium poly(styrene sulfonate) (NaPSS).

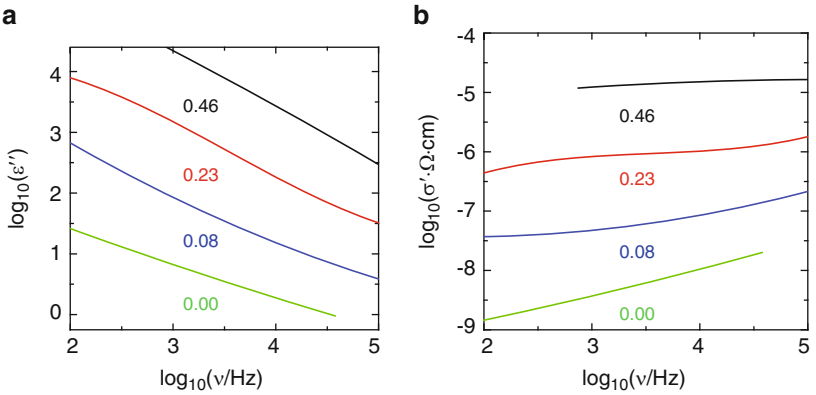


**Fig. 2** (**a**) Influence of the NaBr content on the dielectric loss factor $\varepsilon''$ of NaPSS/VBTAC complexes at 27.5 °C; data redrawn from Fig. 5 of [2]. (**b**) The corresponding conductivity spectra have been calculated from $\varepsilon''$ using the relation $\sigma'(\nu) = 2\pi\nu\varepsilon_0\varepsilon''(\nu)$. The concentration of the dopant NaBr is defined as equivalents per equivalent of neutral polysalt

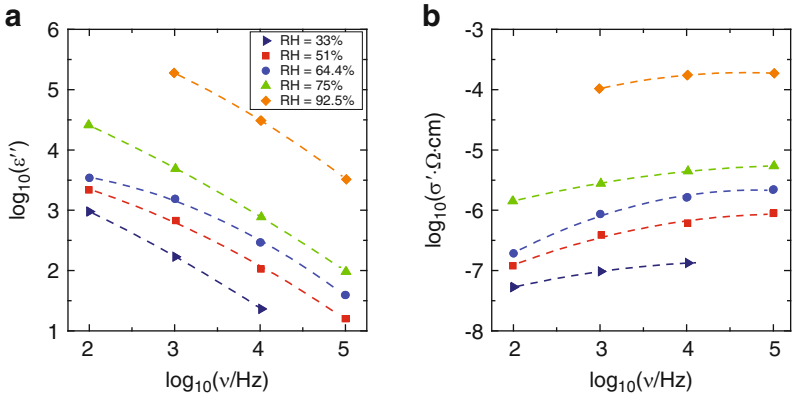


**Fig. 3** (**a**) Influence of the relative humidity on the dielectric loss factor $\varepsilon''$ of NaPSS/ VBTAC complexes at 27.8 °C; data were redrawn from Fig. 9 of [3]. (**b**) The corresponding conductivity spectra have been calculated from $\varepsilon''$

The complex permittivity $\hat{\varepsilon}(\nu) = \varepsilon'(\nu) - i\varepsilon''(\nu)$ is related with the complex conductivity via $\hat{\sigma}(\nu) = i2\pi\nu\varepsilon_0\hat{\varepsilon}(\nu)$, where $\varepsilon_0$ is the permittivity of vacuum. Therefore, the imaginary part of the permittivity (dielectric loss), $\varepsilon''$, is proportional to the real part of the conductivity: $\sigma'(\nu) = 2\pi\nu\varepsilon_0\varepsilon''(\nu)$. For comparison with newer results presented in the next paragraphs we transformed some of the published $\varepsilon''$ spectra into $\sigma'(\nu)$ (see Figs. 2, 3, and 4). Here and in the following, $\nu$ always stands for the experimental frequency which is connected to the angular frequency via $\nu = \omega/(2\pi)$.

Michaels et al. [2, 3] found that the stoichiometric NaPSS/VBTAC complex, when completely free of extraneous electrolytes, exhibits a high dc resistivity (approximately $10^{10}$ Ω cm). The value of $\varepsilon'$ measured at 100 Hz changes from 50 to 5 (for water-saturated PEC) and from about 5 to 3 (for dried PEC) at 0.1 MHz. When doped with simple electrolytes like NaBr, the absolute values of the complex permittivity as well as the dependence of $\varepsilon'$ and $\varepsilon''$ on frequency change significantly. Figure 2 shows the influence of the dopant salt [2].

In the investigated frequency range, the dielectric loss as well as the corresponding conductivity $\sigma'$ increase with dopant concentration by several oders of magnitude. For undoped PEC, the conductivity spectrum only shows a dispersive regime. With higher dopant concentration, a dc plateau becomes visible. The spectra show strong similarity with those of Fig. 1b. Though not stated by the authors, the superimposed slight decay of $\sigma'$ towards smaller frequencies seen for 0.23 and 0.46 is propably due to polarization effects, which can never be avoided when blocking electrodes are used.

Michaels et al. also determined the influence of the RH on the permittivity of polyelectrolyte complexes (see Fig. 3). The data points of Fig. 3a have been taken from Fig. 9 of [3]; the dashed lines as well as the real part of the conductivity have been calculated for this review. The data show that the dc conductivity increases significantly with RH. Also here, polarization effects are detectable at low frequencies.

Michaels et al. concluded from their results that the permittivity spectra mostly arise from minor displacements of the ionic side groups of the macromolecules. Traces of small ions, which are also present in nominally intrinsically compensated complexes, are claimed to be also involved in these local motions, but their long-range mobility is rather small. Water “loosens” the structure and facilitates ion motion.

## 2.3 *The Structural Analogue: Polyelectrolyte Multilayers and Their Conductivity*

After the very early work by Michaels et al., the next frequency-dependent permittivity spectra of solid polyelectrolyte materials were only published in 2001 by Durstock and Rubner, who studied PEM prepared by the layer-by-layer technique [27]. The investigated PEM were made of the polycation poly(allylamine hydrochloride) (PAH) and the polyanions PAA or PSS. The authors investigated very systematically the influences of parameters like pH, temperature, salt content, and RH (wet and dry PEM) on the real and imaginary part of the permittivity.

In Fig. 4, we see how temperature influences the shape and the values of the dielectric loss and the corresponding conductivity spectra of PAH/PSS PEM. At a given frequency, the conductivity increases with temperature. One also sees that the transition into the dispersive regime shifts to higher frequencies when the temperature is raised. Electrode polarization effects are visible at the lowest frequencies.

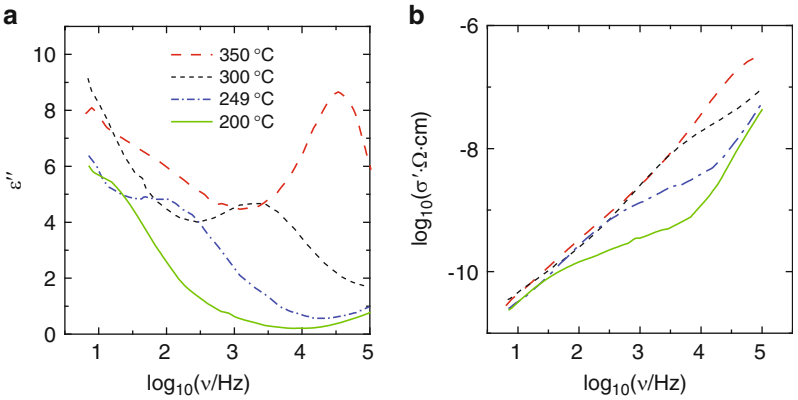


**Fig. 4** (**a**) Influence of the temperature on the dielectric loss factor $\varepsilon''$ for PEM made of PAH/PSS (pH 3.5 and no salt in either of the two polyelectrolyte solutions). The data have been redrawn from Fig. 6 of [27]. (**b**) The corresponding conductivity spectra have been calculated from $\varepsilon''$ in this work

Such effects are known to be more strongly prounced the thinner the film and/or the higher the conductivity.

Durstock and Rubner arrived at the conclusion that PEM contain small mobile ions, although their concentration is very low. The temperature dependence of the PAH/PSS PEM is less pronounced than that of PAH/PAA PEM. This finding is explained by the fact that the matrix of the PAH/PSS PEM is more rigid. The strongest impact on the conductivity of polyelectrolyte multilayers is, however, the RH of the environment. The dc conductivity is found to increase by 4–5 orders of magnitude when comparing a dry PEM with a wet PEM (RH = 85–90%). Durstock and Rubner therefore concluded that the mobility and the number density of mobile ions increase with RH due to a solvation effect [27].

Further work by DeLongchamp and Hammond on other PEM materials confirmed the strong influence of humidity on the dc conductivity [28, 29]. These authors reached dc conducitivities up $10^{-5}$ S cm$^{-1}$ at room temperature if the PEM were exposed to a RH of 100%. They concluded that at high humidities the ionic mobility is governed by the polyelectrolyte matrix and that it is strongly coupled to motions of the polylelectrolyte segments and will therefore depend on the connectivity of the matrix.

What all of the work described so far has in common is that ratio of polycation to polyanion did not vary significantly in the investigated materials. In PEM materials this ratio cannot be tuned, because in multilayer formation the polyelectrolyte stoichiometry is controlled by self-assembly. The work of Michaels on PEC was devoted to 1:1 complexes, which are almost completely intrinsically charge-compensated. In the following sections we will review recent systematic studies on conductivity spectra of PEC, where the composition was varied. We will present the influences of PEC composition, type of alkali ions present in the PEC, temperature and RH on the dynamic conductivity of solid PEC. Based on the presented analysis, we will be able to arrive at further conclusions about how the microscopic ion dynamics in PEC can be visualized and how it is influenced by different parameters. With the help

of scaling relations, the separate influences of number density and ionic mobility on the ion conductivity will be discussed.

## 3 Conductivity Spectra of Dried PEC: Dependence on Temperature

### *3.1 Isothermal Conductivity Spectra of PEC*

This part focuses on the properties of PEC materials in the completely dry state. Typically, these complexes are dialyzed, dried, and compressed into solid pellets of roughly 1 mm thickness prior to impedance experiments. PEC with $x \geq 0.5$ are cotton-like, white homogeneous solid substances. For PDADMAC-rich complexes ($x < 0.5$) we can distinguish two phases: one phase is cotton-like (similar to that of the PSS-rich compositions) and the second is a hard salt-like phase. The two-phase PEC materials were thoroughly milled and mixed before use [40]. DSC results showed no indication for phase separation in any of the PEC, but confirmed the glassy character of the investigated samples. This implies that the second phase present in the PDADMAC-rich complexes does not undergo any phase transition within the investigated temperature range. Solid-state NMR studies on dried AlkaliPSS-rich PEC (with $0.53 \leq x < 1$) clearly showed that the alkali ions are randomly distributed in the PSS-rich PEC, indicating a non-segregated structure [45]. The finding that dried PSS-rich PEC are homogeneous, whereas PDADMAC-rich are not, corresponds to results obtained by Carrière et al. for hydrated complexes. From the asymmetric behavior of the osmotic coefficient of hydrated PEC in dependence of mixing ratio, $x$, it was concluded that polyanion-rich PEC are homogeneous, whereas polycation-rich PEC undergo a microphase separation of neutral from anion-rich regions [46]. More experimental details on sample preparation, characterization and experimental procedures are given in the literature [40].

As a typical example, Fig. 5 shows data of $x$NaPSS $\cdot$ $(1 - x)$ PDADMAC for $x = 0.40$ and 0.60 [40]. The low-frequency part of each spectrum is determined by a frequency regime where the conductivity is independent of frequency. The corresponding conductivity value of each isotherm can be identified with the dc conductivity; the values will be discussed in detail in Sect. 3.2.

With increasing temperature, $T$, the conductivity values increase and the onset of conductivity dispersion shifts to higher frequency. The latter effect can be detected in the PEM spectra of Fig. 4b and it is well known to also exist in other ion-conducting materials. In Fig. 5, the common definition $\sigma'(\nu^*) = 2\sigma_{dc}$ is used for the onset frequency, $\nu^*$, which characterizes the transition from the dc into the dispersive regime. In both PEC materials, the onset points are on a straight line, but their slope differs. For $x = 0.40$, the slope is smaller than one, for $x = 0.60$ it exceeds one. This is one of the marked differences between the spectra of PEC that are rich in PDADMAC and those that are rich in NaPSS. The implications of this difference will be further discussed in Sect. 5.2 in the context of scaling principles.

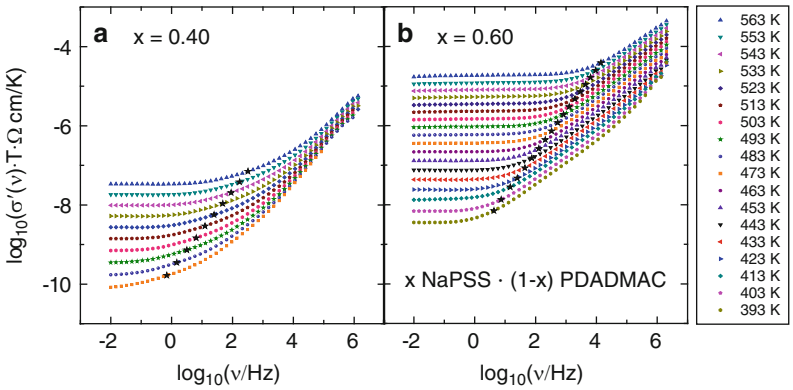


**Fig. 5** Representative spectra of the real part of the conductivity of PEC with $x = 0.40$ (**a**) and $x = 0.60$ (**b**). The *stars* mark the onset frequencies defined as $\sigma'(\nu^*) = 2\sigma_{dc}$ [40]

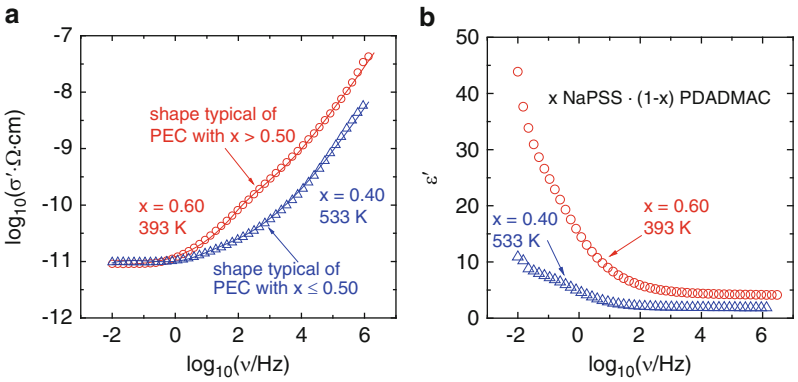


**Fig. 6** Spectral shape of (**a**) the real part of the conductivity and (**b**) the real part of the permittivity for $x$NaPSS·$(1 - x)$PDADMAC complexes with $x = 0.40$ and $x = 0.60$ [47]

It is also visible in Fig. 5 that the conductivity increases with NaPSS content. At constant temperature, the conductivity for PEC with $x = 0.60$ exceeds the conductivity of PEC with $x = 0.40$ by more than two orders of magnitude. The difference between isothermal conductivities of different PEC is most pronounced in the dc regime.

Whereas at first sight the spectral shape in the dispersive regime of the conductivity spectra of both materials displayed in Fig. 5 seems to be in accordance with the conductivity spectra of other ion-conducting materials, there are, however, differences. These differences are twofold. Depending on composition, PEC spectral shapes differ from each other and all of them differ from those of most other ion-conducting materials [47]. The first finding is visible in Fig. 6a, which shows two isotherms of PEC with $x = 0.40$ and 0.60, which have almost the same dc conductivity. Figure 6b displays the corresponding values of the real part of the

permittivity, $\varepsilon'$, which is connected to the imaginary part of the complex conductivity $\sigma''$ via $\varepsilon'(\nu) = \sigma''(\nu)/(2\pi\nu\varepsilon_0)$.

It was shown that the shape of the complex conductivity spectra of the investigated PEC systems can be divided into two classes: those with $x > 0.50$ and those with $x \leq 0.50$ [47]. In Fig. 6a it is obvious that, for comparable dc conductivities, the dispersive regime begins earlier on the frequency scale for PEC with $x > 0.50$ than for the other PEC. In all materials with $x > 0.50$, a "shoulder" occurs in the conductivity spectra, roughly between 0.1 kHz and 10 kHz. An analogous behavior is hardly detectable for $x \leq 0.50$. The real part of the permittivity shows higher values, and $\varepsilon'$ decays more rapidly with increasing frequency, for $x > 0.50$ than for $x \leq 0.50$. An analysis of the exact shape of the real part of the dynamic conductivity will be described in Sect. 3.4.

## *3.2 Temperature Dependence of the DC Conductivity of PEC*

The dc conductivities can be extracted from Nyquist plots of the complex impedance by fitting parameters of a model equivalent circuit to the data. The equivalent circuit always consists of a parallel connection of an Ohmic resistance and a constant phase element [40]. The same dc values are also obtained by identifying the conductivity values of the low-frequency plateau with the dc conductivity. This extraction of dc conductivities from the spectra of dried PEC is straightforward because electrode polarization effects are almost absent.

In a typical experimental procedure, conductivity spectra were measured during two subsequent heating and cooling cycles. In the first cycle, the sample was cooled down to about −90°C. After that the temperature was increased up to 200°C in steps of 10°C. Then, the samples were kept at 200°C for about 3 h and cooled down stepwise by 10°C to the lowest temperature at which the conductivity could still be determined. These measurements are termed "first measurement series." In a second measurement series, the sample was first heated to 300°C and, after a prolonged isothermal heat treatment of more than 6 h, the temperature dependence of the complex conductivity was measured by decreasing the temperature stepwise by 10°C. Arrhenius plots of the ionic conductivity of a PEC with $x = 0.70$ obtained from both series are shown in Fig. 7. The upper straight line shown in this figure corresponds to the conductivity before annealing the sample at high temperatures and it obeys the Arrhenius law. Strong deviations from Arrhenius behavior start above 25°C. This temperature is consistent with DSC data obtained for a first heating, which were interpreted as a loss of water [40]. The loss of water continues until 200°C is reached.

The conductivity observed during cooling down from 200°C is also Arrhenius-type; however, it is three orders of magnitude lower than the conductivity of the samples before drying. In passing, one notes that in contrast to the huge discrepancy of the ionic conductivity values of "humid" and "dried" NaPSS/PDADMAC PEC, the activation enthalpy of the conductivity is almost identical. The latter finding is

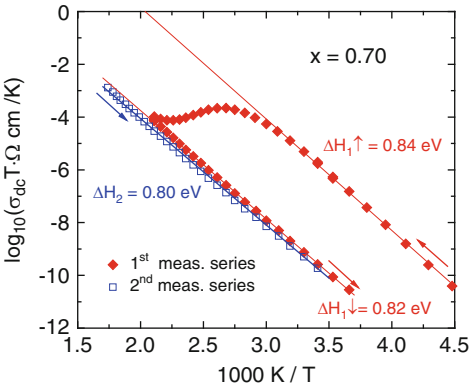


**Fig. 7** First (*full diamonds*) and second (*open squares*) measurement series of the dc conductivity as a function of reciprocal temperature for PEC with $x = 0.70$. The *upper line* corresponds to the conductivity before, the lower line to the conductivity after annealing the sample at high temperatures [40]

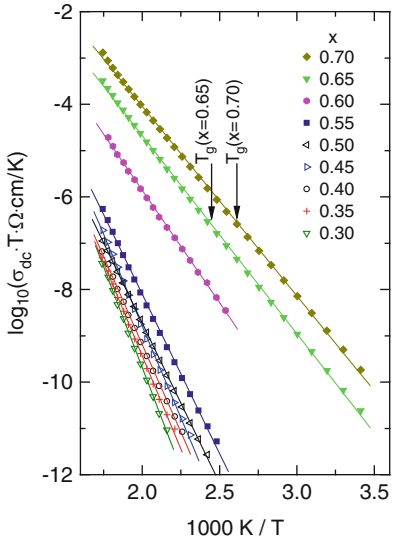


**Fig. 8** Arrhenius plot of the ionic dc conductivities of various $x$NaPSS·$(1 - x)$ PDADMAC dried PEC samples [40]

in contrast to analogous PEC materials in which LiPSS or CsPSS are used instead of NaPSS [48]. This will be discussed in more detail in Sect. 3.3.

The dc conductivities determined on dried PEC materials after annealing at 300°C are presented in Fig. 8. The dc conductivities of all investigated PEC show Arrhenius behavior [40]. The values of the glass transition temperature ($T_g$), as obtained by DSC, are indicated. In all other PEC of Fig. 8, where $T_g$ is not indicated by an arrow, the presented data refer to the status above $T_g$. It is remarkable that in those PEC for which measurements could be performed at temperatures both above and below the calorimetric $T_g$, there is no change in the temperature dependence of $\sigma_{dc}T$ when passing through the glass transition. This implies that PEC materials are "strong" glasses. This finding of an Arrhenius dependence is in contrast to many other polymer electrolyte systems, where the temperature dependence of the conductivity follows a Vogel–Tammann–Fulcher equation.

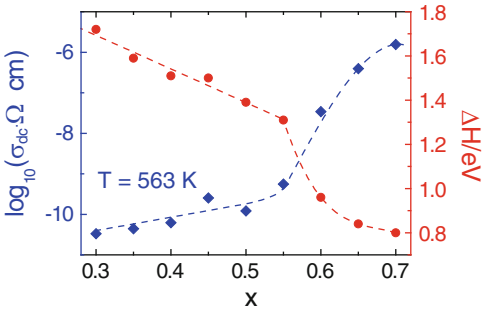


**Fig. 9** Activation enthalpy (*circles*, right *y*-axis) and dc conductivity (*squares*, left *y*-axis) of dry *x*NaPSS·(1 − *x*)PDADMAC PEC, the latter being taken at 563 K as a function of composition [40]

Figure 8 shows a strong compositional dependence of both the absolute conductivity values at a given temperature as well as the activation enthalpy (derived from the slope of the presented lines). The values of the activation enthalpy $\Delta H_{dc}$ of the dc conductivity as well as of the pre-exponential factors of the Arrhenius law: $\sigma_{dc}T = A_{dc}\exp[-\Delta H_{dc}/(k_BT)]$ are summarized in table III of [40].

Figure 9 shows the activation enthalpies along with the isothermal dc conductivity at 563 K for all investigated PEC as a function of composition. From $x = 0.30$ up to roughly $x = 0.55$, the dc conductivity increases and the activation enthalpy decreases almost linearly. Above $x = 0.55$, the increase in NaPSS content is then accompanied by a much stronger increase in $\sigma_{dc}$ and decrease in $\Delta H_{dc}$. The strong increase in $\sigma_{dc}$ with $x$ is reminiscent of inorganic glasses in which the dc conductivity increases with the number density of mobile ions in a power-law fashion [49, 50]. The latter finding is attributed to a strong increase in ion mobility [49].

The dependence of the dc conductivities and the parameters derived thereof show that there are distinct differences between the ion dynamics in PDADMAC-rich and PSS-rich PEC. In both cases, however, the Arrhenius dependence of $\sigma_{dc}T$ clearly shows that the ion dynamics in PEC materials is determined by the thermally activated hopping processes of the mobile ions. The fact that the isothermal dc conductivity increases continuously with NaPSS content indicates that the chloride ions do not dominate the ion transport, even in PEC materials with an excess of polycations and thus $Cl^-$ as the most abundant mobile charge carrier. Otherwise, $\sigma_{dc}$ as a function of $x$ should pass through a minimum, which is obviously not seen experimentally. The conductivity measured for PEC with $x \leq 0.50$ could therefore be either due to residual $Na^+$ ions or protons. To shed more light on this aspect, PEC in which the sodium ions were replaced by lithium or cesium ions were studied. These results are discussed in the following section.

## 3.3 *Temperature-Dependent Ionic Conductivity as a Function of the Type of Alkali Ion*

Conductivity measurements with temperature cycling (analogous to the procedure described in Sect. 3.2, Fig. 7) were performed on different types of AlkaliPSS/PDADMAC of various compositions [48].

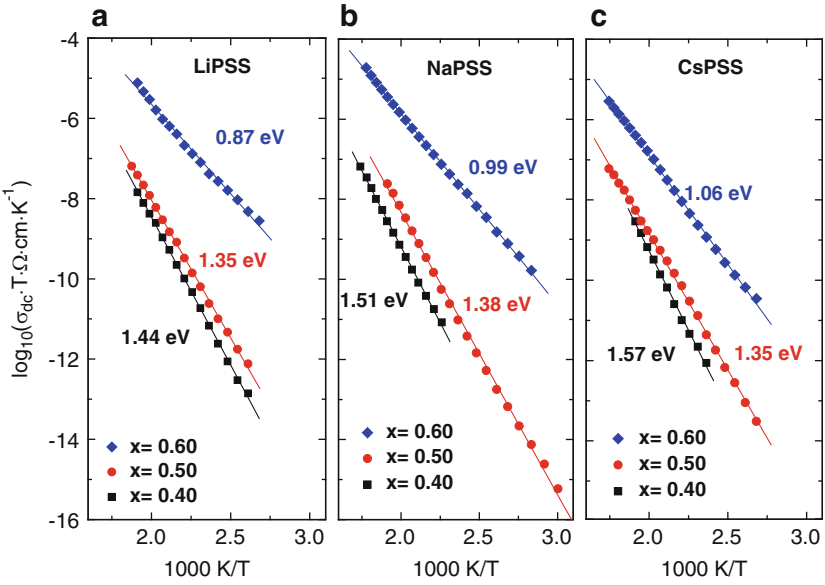


**Fig. 10** (**a**–**c**) Temperature-dependent conductivity of dried PEC samples of composition $x$(Li, Na, or Cs)PSS·(1 − $x$)PDADMAC [48]

Because conductivity values and activation enthalpies derived from the first measurement series do not show any systematic dependence on composition nor on the kind of alkali cation, they seem to be determined by an arbitrary amount of residual water. In contrast, the dc conductivity and enthalpy values determined for dried PEC remain unaffected by further heating or cooling processes and show clear trends. The loss of water generally lowers the ionic conductivity of dried PEC by several orders of magnitude compared to as-prepared PEC. In addition to cations or anions, protons or hydronium ions might contribute to the dc conductivity of the non-annealed PEC samples determined in the first heating run.

For all types of alkali PEC, the residual water appears to have a large effect on the charge carrier mobility, enhancing it by several orders of magnitude. In accordance with this, the activation enthalpy is lower for water-containing PEC. An explanation for both effects and a detailed picture of the influence of water on ion transport is given in Sect. 4, where systematic studies at controlled RH are described.

Figure 10 shows the temperature-dependent dc conductivity data obtained for dried complexes taken during a second measurement series. For PEC with $x = 0.5$, there is a slight difference in the conductivity values for Li, Na or Cs as counterions, occurring in the order $\sigma_{dc}$(LiPSS) > $\sigma_{dc}$(NaPSS) > $\sigma_{dc}$(CsPSS). This implies that the dc conductivities are correlated to the size of the alkali cation present in the PEC. Furthermore, the activation enthalpies of ion migration all lie in the range between 1.35 and 1.38 eV and do, therefore, agree within experimental error. Ideally, 0.5 PSS · 0.5 PDADMAC PEC would be completely intrinsically charge-

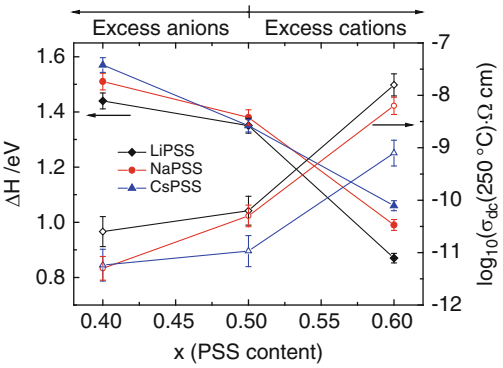


**Fig. 11** Activation enthalpy (*full symbols*, left *y*-axis) and dc conductivity at 200°C (*open symbols*, right *y*-axis) as a function of composition. The *solid lines* are guides for the eye [48]

compensated and would not contain any kind of conducting species in the matrix. Therefore, such PEC should not be ion-conducting at all. However, it is evident from the experimental data that PEC of composition 0.5 PSS (Li, Na and Cs) · 0.5 PDADMAC are not perfectly intrinsically compensated, but still have a small amount of mobile ions. In such PEC, which consist of strongly crosslinked polyions and are diluted with respect to small ions, the nature of the alkali PSS (LiPSS, NaPSS and CsPSS) does not seem to play a significant role as far as the activation enthalpy is concerned.

Turning now to non-stoichiometric complexes with a large charge carrier density, the conductivities of PSS-rich complexes with $x = 0.6$, compared at a fixed temperature, are smaller, the larger the ionic radius of the alkali ion. Conductivity values determined at 200°C are plotted in Fig. 11 along with the activation enthalpies derived from the Arrhenius equation. Accordingly, activation enthalpy values are found to increase with cation radius. Although in dried PEC the finding of a size-dependent ionic mobility is new, such effects are well known for other amorphous ion-conducting materials. In inorganic borate glasses with 30 mol% alkali oxide, for example, the activation enthalpy was found to change from 0.78 to 0.87 eV when $Li_2O$ was replaced by $K_2O$ [51].

In general, the dc conductivity can be expressed as:

$$\sigma_{dc} = q \cdot N_V \cdot \mu, \tag{5}$$

where $q$, $N_V$ and $\mu$ stand for the ion charge, the number density of mobile ions and the ionic mobility, respectively. With increasing ion content, a linearly increasing $\sigma_{dc}$ would thus be expected. The very strong increase in $\sigma_{dc}$ with PSS content when changing $x$ from 0.5 to 0.6, seen for all three types of PSS, cannot be explained by a simple increase in the charge carrier number density; there must also be an enhancement of the charge carrier mobility. This is evident from the detailed $x$-dependence of $\sigma_{dc}$ in Na-PEC (see Fig. 9), being rather exponential than linear. The same behavior is seen here for the Cs- and Li-PEC. It was shown by Bunde, Ingram, and Maass that the strong increase in the ionic dc conductivity in an inorganic glass occurring upon a relatively small increase in the number density

of ions results from a significant increase in the ion mobility. The mobility increase goes along with a decrease in the activation enthalpy connected with the long-range ion transport [49]. Although the simulations of Bunde, Ingram, and Maass refer to inorganic glassy conductors, the concept can be transferred to PSS-rich PEC. Ion transport results if ions move into vacant sites that were recently vacated by other ions. The higher the ion content, the more of such just-vacated sites exist and therefore the ion mobility increases. This means that the number density of mobile ions strongly influences the energy landscape in which ions move. This change is also reflected in the activation enthalpy as a parameter characterizing the long-range ion transport. One should not misinterpret $\Delta H$ as a simple activation barrier between two different ion sites; this enthalpy is connected with successful ionic hopping processes causing long-range transport. Therefore, $\Delta H$ reflects thermally activated movements of initially hopping ions as well as correlated movements of neighboring surrounding ions.

The three different alkali types of PSS-rich PEC just discussed bear some similarity to inorganic cation-conducting glassy materials. The $x$-dependence of $\sigma_{dc}$ and $\Delta H$ for a given type of alkali ion is itself a strong indication that the alkali ions are the most mobile species in dried PSS-rich PEC. This conclusion is also strongly supported by the dependence of $\sigma_{dc}$ and $\Delta H$ on the type of cation for different alkali PEC with constant $x$. The fact that these quantities correlate so well with the ionic radius clearly shows that PSS-rich PEC are alkali cation-conducting materials.

In PDAMAC-rich PEC, the situation differs. For a given alkali PEC-system, the conductivity increases and the activation enthalpy decreases when changing $x$ from 0.40 to 0.50. Although these changes are less pronounced than those resulting from a change of $x$ from0.50 to 0.60, they still indicate conduction of residual cations rather than conduction of chloride ions. If $Cl^-$ ions were the most mobile species, one would expect the conductivity of PEC with $x = 0.40$ to be higher than that of $x = 0.50$, which is not the case. Instead, the conductivity monotonously increases with PSS content. Thus, two conclusions are obtained: (1) The mobility of the $Cl^-$ ions is negligible and for all compositions the conductivity is dominated by the contribution of the alkali cations. (2) The number of residual alkali ions in PEC with $x \leq 0.5$ slightly increases with PSS content and, as a result, the conductivity increases and the activation enthalpy decreases slightly with increasing $x$.

The presented results, however, shed even more light on the type of charge carriers in chloride-rich PEC: even for $x \leq 0.50$, the dc conductivity depends on the type of alkali ion. This can be taken as a direct proof that in PEC, where $Cl^-$ ions should be the majority extrinsic charge carriers, residual alkali ions indeed provide the major contribution to the overall conductivity due to their much higher mobility. One open question is why the activation enthalpy values of PEC with $x = 0.50$ do not show any systematic variation with the type of alkali ion, whereas they do differ for PEC that deviate from $x = 0.50$. One reason for this could be that the exact composition is hardest to control for $x = 0.50$. Theoretically, it should be perfectly intrinsically charge-compensated. In practice, however, the number of crosslinks between the polyions might change slightly from sample to sample. In other words,

the deviation from the theoretical stoichiometry will be higher than for all other compositions with a larger number of small excess ions. In addition, the network of complexes with $x = 0.5$ deviates from the networks of all other compositions where extrinsic compensation is not just a defect, but defined by the excess ions.

In addition to the obvious, differing structural properties of PSS-rich and PDADMAC-rich PEC explained in Sect. 3.1, the differences in shape of the conductivity spectra for PSS-rich and PDADAC-rich PEC (see Fig. 6) also imply structural differences between both types of PEC. As a consequence, the energy landscape in which ions can move and thus contribute to the long-range transport probed by the dc conductivity will also differ. If we assume no connectivity of anion-rich regions in a phase-separated PDADMAC-rich PEC, the anion transport will be drastically decreased. In addition to the large size of the $Cl^-$ ions, such structural differences might be a reason for the low $Cl^-$ mobility.

Having discussed the long-range ion transport, as probed by the dc conductivity in the different types of PEC, the next section discusses ion dynamics in the different PEC on a more local scale, i.e., at higher frequencies.

## *3.4 Modeling of Conductivity Spectra*

There are many different models describing the overall shape of the frequency-dependent conductivity, which cannot all be summarized here. Most of the models have been developed to describe inorganic disordered ion-conducting materials such as glasses. PEC, forming polymeric glasses with mobile charge carriers, can in many respects, be described by the same models. One successful approach uses computer simulations for treating the ion motions in static energy landscapes within a random barrier model [52–54]. The random barrier model takes disorder into account by choosing an energy landscape with randomly distributed barriers of different heights. In most of these simulations, Coulomb interactions between the moving ions are neglected. In some works, however, the influence of Coulomb interactions on the scaling properties of conductivity spectra is discussed [52].

Other successful models describing the overall shape of frequency-dependent conductivity spectra are the counterion model and the dipolar model of Dieterich and coworkers [55] Here, Monte Carlo simulations are used to describe the hopping motions of small ions. All Coulomb interactions between mobile ions and their immobile counterions are taken into account. Disorder is introduced by randomly placing fixed counterions into the center of cubes forming a lattice. In the counterion model, long range transport of the mobile cations is possible; however, the dipolar model only considers local motions of the mobile ions in the vicinity of their immobile neighboring counterions (dipoles). Interactions between fluctuating dipoles are taken into account.

As a further development, the MIGRATION model considers microscopic ion hopping in an energy landscape that changes with time [42]. A distribution of barriers in the energy landscape is not taken into account. Instead, the model

focuses on the time dependence of the energy landscape occurring when mobile ions leave their site. This model has one big advantage over the other models because it yields a set of analytic equations with fitting parameters. These equations allow calculation of conductivity spectra that are in agreement with experimental spectra, where the exact spectral shape differs slightly from system to system. For this reason, the MIGRATION model was chosen for performing fits to PEC spectra and will described in more detail.

The acronym MIGRATION stands for MIsmatch Generated Relaxation for the Accommodation and Transport of IONs. The model considers in a detailed way backward correlations between the successive jumps of a mobile ion. As already outlined in Sect. 2.1, these backward correlations give rise to the negative part in the velocity autocorrelation function and thereby to dispersion of the conductivity. The model distinguishes between the "single particle route" and the "many particle route". Both can reduce mismatch, which is created when a charged particle leaves its site. In the first case, the previous forward jump of the ion under consideration is cancelled out by a correlated backward jump, whereas in the second case the ion has successfully moved to a new site with a rearrangement of charges in the environment causing relaxation of the mismatch. Successful hops result in long-range ion transport. The rate of relaxation on the many-particle route is related to single-particle functions such as the velocity autocorrelation function, from which the complex conductivity can be derived via Eq. (3). Local mismatch is, however, not only reduced by the rearrangement of the neighboring ions, but at the same time also progressively shielded. An empirical parameter $K$ is introduced to quantify the time dependence of the shielding effect. More details are given in [42] and references therein. The parameter $K$ turns out to modify the shape of the conductivity spectra, increasing values of $K$ resulting in a more gradual onset of the dispersion. In most single cation glasses and also in many crystals, the value of $K$ is found to be close to 2.0. The parameter $K$ appears to be related to the effective number density of mobile ions. The smaller the number density, the higher is the value of $K$. Accordingly, materials with small concentrations of mobile cations are reproduced by model spectra with larger $K$ values than those with high cation contents. Large values of $K$ have also been reported for mixed cation glasses and for materials with a low dimensionality of the pathways for the ion transport [42, 56].

The main focus in reviewing modeling approaches in PEC is here on the NaPSS-rich compositions with $x > 0.50$, where a phase separation can be excluded. The following discussion will analyze the ion transport mechanism on a microscopic scale by looking at the shape of the conductivity spectra. The corresponding conductivity spectra are representative for all compositions with $x > 0.50$ (see also Fig. 6). Figure 12 shows one conductivity spectrum of 0.60 NaPSS · 0.40 PDADMAC taken at 393 K. The dashed line was obtained on the basis of the MIGRATION concept with the model parameter $K = 2.4$ [57].

Whereas the model curve describes the experimental spectrum very well at low and at high experimental frequencies, one sees variations in the intermediate frequency range. These deviations remain, even if the value of the parameter $K$ is varied.

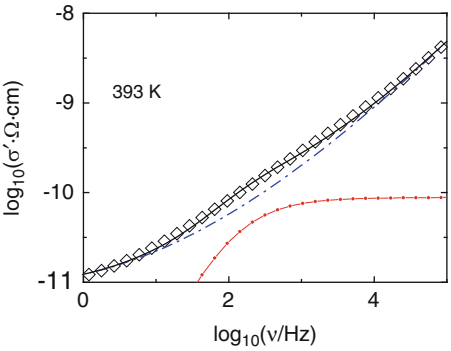


**Fig. 12** Experimental conductivity spectrum (*open symbols*) of dry 0.60 NaPSS·0.40 PDADMAC PEC taken at 393 K. The *dashed blue line* shows a model curve from the MIGRATION concept ($K = 2.4$). The *black solid line* results from a superposition of the MIGRATION curve and the *red spectrum*, which results from localized hopping [47]

The deviations between the MIGRATION curve resulting from correlated forward–backward hopping motions of the ions and the experimental spectrum indicate that additional movements of charged particles or groups do contribute to the conductivity in the dispersive regime. The total spectrum displayed by the symbols in Fig. 12, can, however, be described very well if an additional contribution to the conductivity is considered (red line in Fig. 12). The red line in Fig. 12 was obtained by the following equation:

$$\sigma'_{\mathrm{loc}}(\omega) = \sigma'_{\mathrm{loc}}(\infty) \cdot \left[1 + (\omega t_1)^{-1}\right]^{-q} \quad \text{with} \quad q > 1 \tag{6}$$

the exponent being 1.7. This type of equation was introduced for describing the high frequency conductivity spectra of ion-conducting glasses [58, 59]. The index "loc" characterizes localized motions. $\sigma_{\mathrm{loc}}(\infty)$ is a high-frequency-plateau value and $t_1$ marks the crossover from the $q$-power-law dependence into the plateau $\sigma_{\mathrm{loc}}(\infty)$. For inorganic glasses, the reported exponents ranged from 1.1 to 1.3, being closer to 1 than to 2. Nevertheless, we can transfer the concept of localized ionic motions [58, 59], which is somewhere between the two scenarios of a Debye process on the one hand and localized hopping of interacting particles leading to a nearly-constant-loss-behavior (NCL) on the other hand. An exponent of 2 in Eq. (3) would correspond to a Debye-type process, where a non-interacting dipole moves locally [60]. In such a Debye case one can envisage an ion hopping in a double minimum potential that it cannot leave, even at longer times. The environment is rigid and the potential energy landscape does therefore not change with time. The real part of the conductivity corresponding to a Debye process shows a $\sigma'_{\mathrm{Debye}}(\omega) \propto \omega^2$ frequency dependence at sufficiently low frequencies and then turns into a high-frequency plateau regime.

The other scenario that can be considered is that many dipoles strongly interact with each other. This was independently shown by Funke et al. within an extended

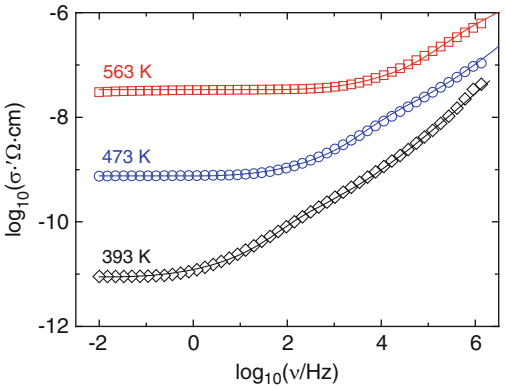


**Fig. 13** Experimental conductivity spectra (*symbols*) of PEC with $x = 0.6$ taken at different temperatures. The *solid lines* result from a fit described in the text [47]

version of the MIGRATION concept [42, 61] and by Dieterich et al. within their dipolar version of the counterion model [55] that such processes lead to the well-known "nearly constant loss (NCL) behavior". The NCL behavior implies that the imaginary part of the permittivity becomes almost independent of frequency, which corresponds to a $\sigma'_{\mathrm{NCL}}(\omega) \propto \omega$ dependence in the real part of the conductivity. Conductivity spectra obtained on the basis of the two models given above indeed show the proportionality of $\sigma' \propto \nu$ over wide ranges in frequency. At very low frequencies, the model spectra bend over into a $\omega^2$ dependence, and at high frequencies into a high-frequency plateau. As shown earlier [58], power laws with $q > 1$ imply that the corresponding mean square displacement of the mobile ions will always merge into a plateau regime at sufficiently long times, indicating that the motion under consideration is strictly localized. In contrast to a pure Debye-type process, however, the environment of the considered ion is not completely frozen. If an ion performs a jump within its double minimum potential, neighboring ions will react to this hop and move very slightly, inducing a time dependence of the potential energy. So, there is some interaction between the ion hopping locally and its environment, but the interaction is not as pronounced as in the dipolar model of Dieterich [62, 63] or in the extended version of the MIGRATION model of Funke [42, 61]. The presence of a contribution as described by Eq. (3) in the investigated PEC materials implies that localized motions of ions in not completely rigid environments should also be considered in PEC materials.

Figure 13 shows different conductivity isotherms, which can all be well described by a superposition of a MIGRATION-type curve and another curve resulting from Eq. (3). The MIGRATION curve represents ion transport that involves correlated forward–backward ion hopping sequences that lead to long-range transport at sufficiently long times. The other contribution is characterized by the $\sigma_{\mathrm{q}}$ frequency dependence, which merges into a plateau regime within the experimental frequency window, and represents localized ionic movements. In Sect. 5, it will be shown that all parts of the conductivity isotherms (including the shoulder) follow the same scaling relation in dependence on temperature. This fact implies that both type of processes, potentially successful and localized hops, probably involve the same kinds

of ions, i.e., $Na^+$ ions. Spectra of $x \leq 0.50$ can be fitted in a similar way. The component describing the localized motions of charged particles is still necessary to describe the spectra, but its contribution to the total spectra is much less pronounced than in the case of PSS-rich PEC (see also Fig. 6). In passing, we note that the conductivity spectra of PEM can also be described by a superposition of a MIGRATION-type contribution and a contribution that reflects strictly localized movements. Also, in the case of PEM, the $q$-values are close to 2, but the bending into the $\sigma_{loc}(\infty)$ plateau regime is not visible at the measured frequencies [47].

## 4 RH-Dependent Spectra

The work by Michaels [2, 3] and Durstock and Rubner[27], described in the previous section showed that permittivity (and therefore also conductivity) spectra of PEC and PEM strongly differ for dried and hydrated materials. The reason is that these materials take up water when exposed to a humid atmosphere. In order to relate humidity and water content, several studies have dealt with the water uptake of multilayers, employing reflectivity techniques, [64, 65] or of complexes, employing gravimetric analysis [66].

To investigate the RH-dependent conductivity, studies on PEC [66, 67] and PEM [30, 39] were performed. In this work, the composition and the type or amount of alkali ions were varied and samples were equilibrated at different RH. Here, we discuss the RH dependence for the two PEC systems $x$NaPSS·$(1 - x)$ PDADMAC and $x$CsPSS·$(1 - x)$ PDADMAC [66]. The results refer to compositions $x \geq 0.50$, i.e., for systems that are either stoichiometric or have an excess of alkali ions. As outlined before, such PEC can be considered as homogenous materials.

### *4.1 Conductivity Spectra of PEC at Constant RH*

Figure 14a,b shows a log–log plot of the real part of the conductivity spectra $\sigma'$ against experimental frequency $\nu$ of NaPEC and CsPEC, taken after equilibration at different RH values. At low RH (29% and 46%) no appreciable electrode polarization effects are seen. However, with increasing RH, polarization effects move into the experimental frequency window.

For both kinds of complexes (NaPEC and CsPEC) and over the entire humidity regime, a well-defined low-frequency plateau is observed, where the conductivity is independent of frequency and can be identified with the dc conductivity. With increasing RH, the dc plateau moves towards higher conductivity values. At frequencies higher than those of the dc regime, the conductivity increases monotonously with frequency at all RH. Moreover, the onset of this dispersion shifts towards higher frequency with increasing humidity. The onset of dispersion is characterized by the onset frequency $\nu^*$ (shown as star symbols in Fig. 14). These

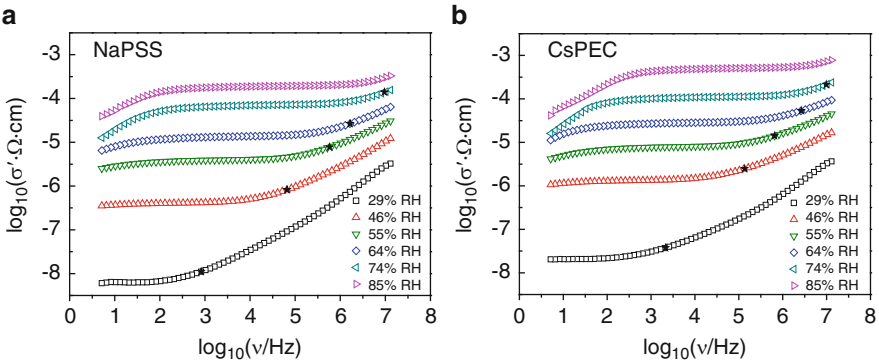


**Fig. 14** Conductivity spectra of (**a**) NaPEC with $x = 0.60$ and (**b**) CsPEC with $x = 0.60$ after equilibration at different RH as given in the legend. The corresponding onset frequencies $\nu^*$ are marked by *stars* [66]

results demonstrate the systematic trends in the differences between dry and hydrated materials that were already visible in the early literature data of Michaels et al. (Fig. 3b) and in the PEM data of Rubner and Durstock (Fig. 4b).

Though the sets of conductivity spectra of NaPEC and CsPEC show qualitatively the same dependence on frequency and on humidity, a major difference is that (in contrast to the dry PEC described above) the conductivities are generally greater for CsPEC. Impedance spectra were taken in a similar way for a range of compositions, $x = 0.50$–$0.75$, and all of them show qualitatively the same shapes and dependences on frequency and humidity. A possible explanation of the higher conductivity in CsPEC could be that the water content in CsPEC of a given composition is higher than in the respective NaPEC. However, gravimetric analysis showed that over the entire humidity range the water content in PEC increases almost linearly with humidity and that the water content in NaPEC is higher compared to CsPEC for similar composition. So, the fact that the conductivity of CsPEC at a given composition is higher than that of the respective NaPEC cannot be traced back to a higher water content in CsPEC [66].

## *4.2 RH Dependence of the DC Conductivity of PEC*

Figure 15 shows $\log(\sigma_{dc})$ as a function of the RH for NaPEC and CsPEC for different compositions. For all compositions $x$, a strong dependence of $\sigma_{dc}$ on RH is observed, and the variation extends about four orders of magnitude. Moreover, $\log(\sigma_{dc})$ generally increases almost linearly with RH for NaPEC as well as for CsPEC for all compositions. This dependence can be described by the linear relation $\log(\sigma_{dc}) = \text{aRH} + \text{constant}$. The straight lines in Fig. 15 are obtained by linear regression. A linear increase in $\log(\sigma_{dc})$ indeed shows a strong influence of the humidity on the ion transport. Because studies of the amount of water show that it scales roughly linearly with the RH, it implies that a merely linear increase in

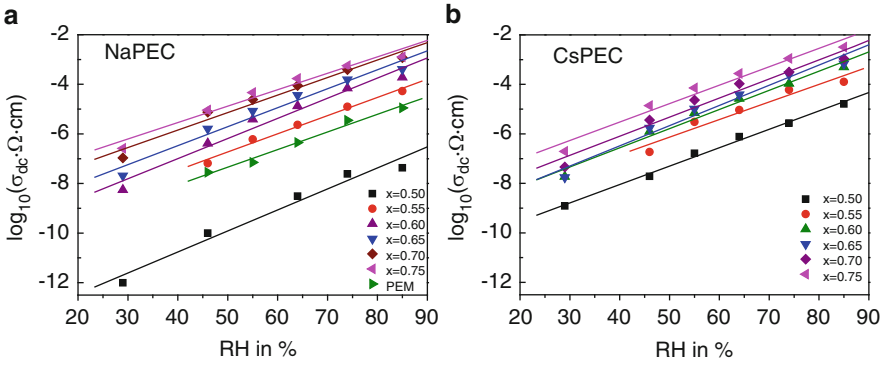


**Fig. 15** Plots of logarithm of $\sigma_{dc}$ versus RH for (**a**) NaPEC and (**b**) CsPEC [66]. The *lines* are obtained by linear regression. Additionally, in (**a**), the conductivity of PEM composed of the same polymers is given for comparison; these values are taken from [30]

the amount of water causes an exponential increase in the ionic mobility. This behavior, observed in [66] for the first time in PEC, had previously been observed in different types of PEM [30, 39].

## *4.3 Influence of the Alkali Ion Size in Hydrated PEC*

As already mentioned in context with Fig. 14, in hydrated PEC a larger alkali ion causes a greater conductivity. In Fig. 16, data for similar compositions of NaPEC and CsPEC are systematically compared, employing the data of Fig. 15. The slope of the plot of $\log(\sigma_{dc})$ versus RH for different composition is $0.08 \pm 0.01$ and does not depend on the composition or the type of alkali cation. The slope values are in the range of the slope found for PEM composed of the same material as reported by Akgöl et al., which was $0.075 \pm 0.015$ [39]. In PEM, the value of the slope differed for PEM made from different polyelectrolyte components and was attributed to the degree of swelling of different types of PEM [39]. It showed, however, no dependence on the types of counterions involved in multilayer formation.

Similarly, the values of the slope in Fig. 15 indicate that conductivities of both NaPEC and CsPEC have the same dependence on humidity. In the case of PEC with $x = 0.50$, the $\sigma_{dc}$ of CsPEC, at a particular humidity, is almost three orders of magnitude higher than the $\sigma_{dc}$ of NaPEC (see Fig. 16, top left). However, the difference decreases as one goes towards more PSS-rich compositions. At low PSS content, $\sigma_{dc}$ for CsPEC is always higher over the entire humidity regime. For more PSS-rich compositions ($x \geq 0.65$), the conductivity of CsPEC and NaPEC are equal, within the error limit.

As already reported in context with the temperature-dependent measurements, here we see again that $\sigma_{dc}$ does not scale linearly with ion concentration. For example, the dc conductivity of NaPEC with $x = 0.70$ is about two orders of

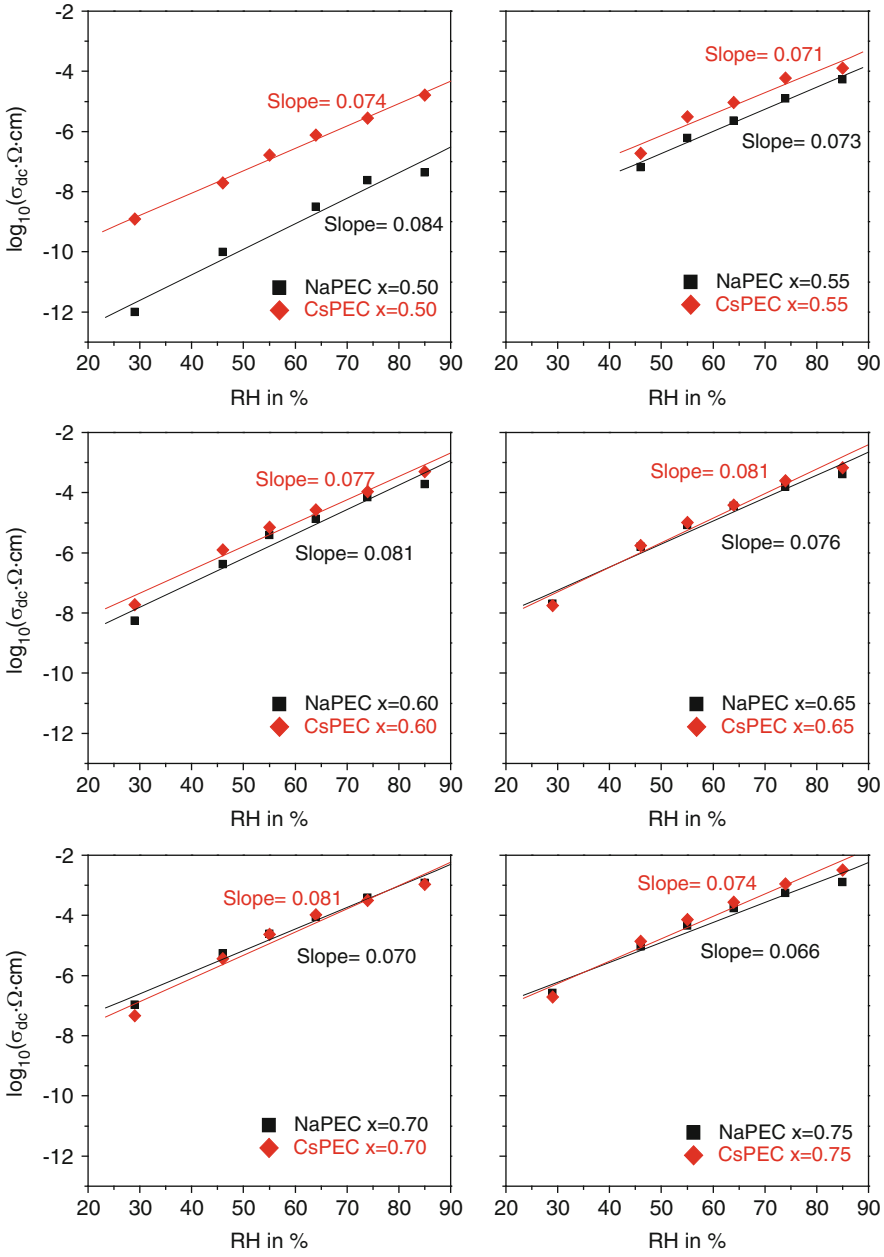


**Fig. 16** Plots of logarithm of $\sigma_{dc}$ versus RH for similar compositions of NaPEC and CsPEC [66]

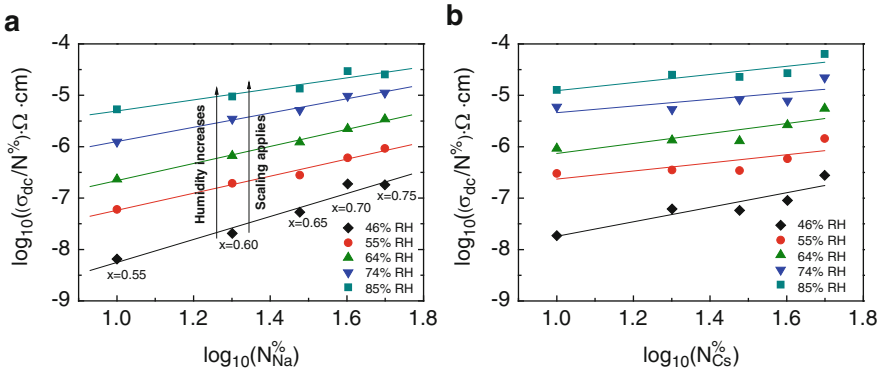


**Fig. 17** Plots of logarithm of $\sigma_{dc}/N^{\%}$ versus excess of counter ions ($N^{\%}$) for (**a**) NaPEC and (**b**) CsPEC. The *lines* are obtained by linear regression [66]

magnitude higher as compared to NaPEC with $x = 0.55$. Again, such an increase in conductivity with ion concentration cannot be explained by the increase in the charge carrier concentration itself, but by a concentration-dependent mobility. As in other glassy materials, the change of mobility with charge density follows a power law [49, 50]. Next, we describe investigations into the variation of the mobility with the number density at a particular RH. A log–log type plot of ($\sigma_{dc}/N_V$) versus the number density $N_V$ shows the dependence of the ion mobility. It is assumed that in the studied PSS-rich PEC the number density of mobile ions is proportional to $N^{\%}$, where $N^{\%}$ is the fraction of polyion charges that is not intrinsically compensated by oppositely charged polyion groups, but by an excess counterion. This is a valid assumption because the PEC density is almost independent of composition. In NaPEC with $x = 0.60$, 80% of the total number of polyion charges undergo electrostatic crosslinking and 20% are compensated by small counterions, which we denote as $N^{\%} = 20\%$. For $x = 0.65$ we get $N^{\%} = 30\%$ and so on. Figure 17 shows the variation of $\sigma_{dc}/N^{\%}$ as a function of $N^{\%}$. The variation of $\log(\sigma_{dc}/N^{\%})$ with the counterion excess is linear, irrespective of humidity, for both NaPEC (Fig. 17a) as well as CsPEC (Fig. 17b). This suggests that the mobility of the ions follows a power law in dependence on their density.

The three main observations obtained on the basis of this systematic investigation of impedance spectra for PEC with different amounts of incorporated ions and different counterions are: (1) Over the entire humidity range, the water content in PEC increases almost linearly with humidity and the water content in NaPEC is higher compared to CsPEC for similar composition. (2) The conductivity of CsPEC is higher than that of NaPEC at a given RH value for PEC with low or moderate ion content. However, at high ion contents both CsPEC and NaPEC show the same conductivity values, within the error limits. (3) The dc conductivity of all studied PEC increases exponentially with humidity and follows the linear dependence log ($\sigma_{dc}$) = a·RH + constant. As discussed before [67], and in Sect. 4, the influence of RH on the conductivity is so strong that it cannot be simply traced back to a slight

softening of the PEC matrix caused by the absorption of water. Instead, the mobile cations and their local environment also have to be considered. What implications do the above observations have concerning the ion transport mechanisms in humidified PEC? What are the charged species governing the ion transport? In the case of dry PEC, alkali ions are the major conducting species [41, 47].

By contrast, for humidified PEM it was shown that the dominant conducting species are protons [39]. This might be due to the low salt ion concentration in PEM as compared to PEC, or due to a very high mobility of protons in hydrated samples. Thus, in the humidified PEC investigated here, the charge carriers could either be protons as well, or small cations, or a combination of both.

In PEC with $x = 0.50$, the number of incorporated small ions should be theoretically zero, but small values close to zero are difficult to control. In PEC compositions with $x \neq 0.50$, the amount of alkali ions involved in extrinsic charge compensation is well defined and determined by the ratio of polycations to polyanions. The number of $Na^+$ or $Cs^+$ ions is therefore known and $N^{\%}$ ranges between 10% in the case of $x = 0.55$ and 50% in the case of $x = 0.75$. From this, it follows that if protons were the dominant conducting species in humidified PEC, differences in conductivity between NaPEC and CsPEC with the same composition $x$ would have to arise from differences in the water content. However, the water content in NaPEC is generally greater, wheres the conductivity (see Fig. 14) is lower than or similar to the conductivity of CsPEC. These observations are an indication against proton conduction in humidified PEC. It is thus evident that, even in strongly hydrated PEC, alkali ions are the charge carriers dominating the conductivity. Here, however, the mobility of the larger alkali ion, $Cs^+$, is higher than that of $Na^+$. This indicates that, in contrast to dry PEC, it is not the size of the bare ion itself, but the size of the hydration shell, being larger for $Na^+$ than for $Cs^+$, that controls the mobility.

More information on the conducting species in humdified PEC and the influences of number density and mobility of ions on the conductivity can be obtained on the basis of new scaling relations, which are described in the following section.

## 5 Scaling of Conductivity Spectra

In the last section, the shapes of PEC conductivity spectra taken at a constant composition, but at different external parameters, i.e., temperature [41] and RH [67] were reviewed. In addition to modeling, further information is accessible from scaling relations that holds for conductivity spectra. Before going into details, basic scaling concepts for ion-conducting materials will be briefly summarized.

## 5.1 Principle of Scaling

The conductivity spectra of many materials possess a temperature-independent shape and can, therefore, be superimposed to a so-called "mastercurve" [68]. This is commonly termed "TTSP" (time-temperature superposition principle). Validity of the TTSP implies that an enhancement of temperature causes a general acceleration of all dynamic processes in the material and thus a shift on the time axis, or, more relevant for conductivity spectra, on the frequency axis. The validity of the TTSP for the real part of the complex conductivity $\sigma'/\sigma_{dc}$ can be expressed by a function $\sigma'/\sigma_{dc} = F(\nu/\nu_0)$, where $\nu_0$ is an individual scaling parameter for each conductivity isotherm. The scaling function, $F$, is independent of temperature. An appropriate choice of $\nu_0$ for each curve is necessary to superimpose spectra measured at different temperatues to a master curve. A straightforward approach is to assign $\nu_0$ to the onset frequency of the conductivity dispersion, $\nu^*$, which can be defined in various manners. In almost all studies, the definition $\sigma'(\nu^*) = 2\sigma_{dc}$ is used (see the stars in Fig. 5). TTSP then means that all conductivity spectra, for example from Fig. 5, do exactly overlap to form one master curve when the spectra are shifted along the $\log(\nu)$ and the $\log(\sigma' T)$ axis in order to make the onset points overlap.

The special case of Summerfield scaling [69, 70] is fulfilled if $\sigma_{dc}T$ and $\nu^*$ are proportional to each other. Connecting the onset frequencies in a plot of $\log(\sigma' T)$ versus $\log(\nu)$ yields a straight line of slope 1. Summerfield scaling can be expressed by:

$$\frac{\sigma'(\nu)}{\sigma_{dc}} = F\left(\frac{\nu}{\sigma_{dc} \cdot T}\right) \tag{7}$$

and it describes the straightforward case where the temperature enhancement causes the acceleration of all dynamic processes without affecting structural properties such as the number density of charges or pathways of ion transport. Then, the temperature influence on conductivity spectra can be described by a shift along a line of slope 1 in the $\log(\sigma' T)$ versus $\log(\nu)$ diagram.

Deviations from this simple form of scaling may imply that the shape of the spectra is changing with temperature. In this case, TTSP is not valid any more. On the other hand, deviations from Eq. (7) might imply that the spectral shape remains identical, but the shift along either axis required to produce the master curve differs, i.e., the simple proportionality between $\sigma_{dc}T$ and $\nu^*$ is not valid anymore. This was also found for some materials [71, 72]. In the case that the slope of the line connecting the onset frequencies exceeds one, $\sigma_{dc}T$ increases more strongly with $T$ than does $\nu^*$. One way to describe this type of deviation from Summerfield scaling is to include an additional scaling factor for the frequency scale, which itself depends on temperature: $\frac{\sigma'(\nu)}{\sigma_{dc}} = F\left(\frac{\nu}{\sigma_{dc} \cdot T} \cdot f(T)\right)$. With $f(T)$ included, all spectra taken at different temperatures can then be scaled on a master curve. The scaling relation:

$$\frac{\sigma'(\nu)}{\sigma_{dc}} = F\left(\frac{\nu}{\sigma_{dc} \cdot T} \cdot T^{\alpha}\right) \tag{8}$$

has been reported on the basis of theoretical calculations by Baranovskii and Cordes [73] and found to fit experimental data by Murugavel and Roling [71, 72]. But, whereas Baranovskii and Cordes [73] and also other authors doing simulation work [52, 53] reported negative $\alpha$-values, the experimentally determined $\alpha$-values by Roling et al. were always positive [71, 72]. A positive $\alpha$-value means that the temperature dependence of $\nu^*$ is less pronounced than that of $\sigma_{dc}T$ and it implies that the characteristic mean square displacement of the mobile ions at a time given by $t^* = 1/(2\pi\nu^*), \langle r^2(t^*)\rangle$, increases with temperature. There are two possible reasons for this [71, 72]. Either the number density of mobile ions increases or the number of available pathways for the ions decreases with increasing temperature. In the latter case, the ions have to travel longer distances until they can finally leave their initial site, resulting in an increase in the characteristic mean square displacement with temperature. Although not outlined in the references cited before, one should keep in mind that a possible proportionality of the scaling factor $f(T)$ to $T^{\alpha}$, as implied by the Baranovskii and Cordes scaling function, can hardly be distinguished from an exponential type of dependence $f(T) \propto \exp(-1/T)$ if the temperature range under investigation is small and not varying by several orders of magnitude. The latter proportionality would be consistent with an assumption that the formation of additional charge carriers contributing to the conductivity was thermally activated in an Arrhenius fashion. This could explain why the number density of mobile ions increases with temperature yielding a temperature dependence of the conductivity spectra, where the slope of the straight line connecting the onset frequencies is larger than one.

These concepts, established for describing ion transport in inorganic materials, were recently employed to test the validity of the scaling properties in polyelectrolyte materials, as outlined in the next section.

## 5.2 The Time–Temperature Superposition Principle in PEC

This section deals with the scaling properties of PEC conductivity spectra with respect to their temperature dependence. On the one hand, it is shown that the TTSP is valid for each investigated PEC composition, indicating that the shape of the conductivity spectra does not change with temperature for a given composition. In addition, scaling factors as a function of composition are discussed. The temperature dependence of the onset frequencies $\nu^*$ for four compositions is shown in Fig. 18 (open symbols and right $y$-axis), where it is compared with the respective temperature dependence of $\sigma_{dc}T$ (full symbols and left $y$-axis). In each case, the Arrhenius law is overall valid for the considered quantity. Very slight deviations are only seen at high temperatures. If Summerfield scaling with $\sigma_{dc}T \propto \nu^*$ was valid, the

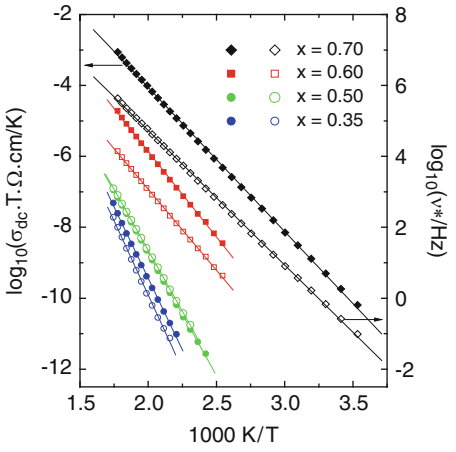


**Fig. 18** Temperature dependence of $\sigma_{dc}T$ (*full symbols* referring to left *y*-axis) and $\nu^*$ (*open symbols* referring to right *y*-axis). Note that the left *y*-axis is shifted by a factor of $10^{-10}$ relative to the right *y*-axis

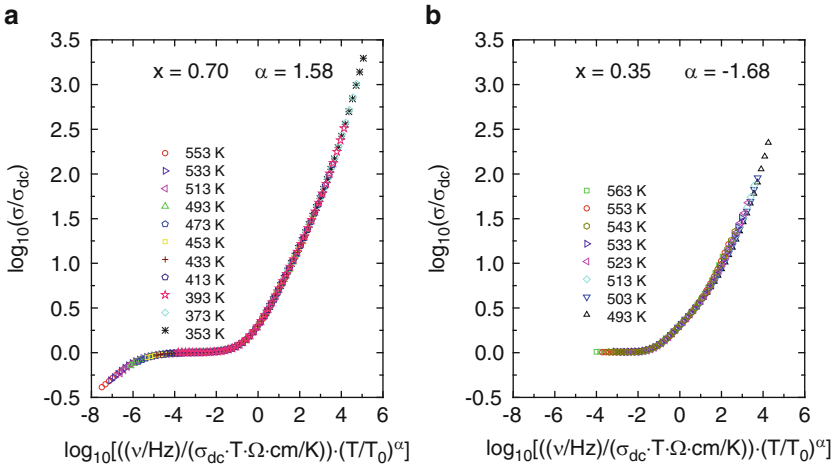


**Fig. 19** Baranovski and Cordes scaling (**a**) with $\alpha = 1.58$ for $x = 0.70$ and (**b**) with $\alpha = -1.68$ for $x = 0.35$ [41]

straight lines of $\log(\sigma_{dc}T)$ and of $\log(\nu^*)$ versus $1/T$ of a given composition should be parallel. This is obviously not the case for PEC with $x = 0.35$ nor for those with $x = 0.60$ and $x = 0.70$. For the latter two, PEC we find that $\log(\sigma_{dc}T)$ decreases stronger with increasing $1/T$ than does $\log(\nu^*)$. This is also true for all other compositions with $x > 0.50$. For $x = 0.50$, the deviation in the $1/T$ dependence between $\log(\sigma_{dc}T)$ and of $\log(\nu^*)$ is not very pronounced, but quantitative analysis shows that $\log(\sigma_{dc}T)$ decreases a bit more strongly with increasing $1/T$ than $\log(\nu^*)$. An opposite trend is seen for the complex with $x = 0.35$. Here, the decrease in $\log(\sigma_{dc}T)$ with increasing $1/T$ is less pronounced than the decrease in $\log(\nu^*)$.

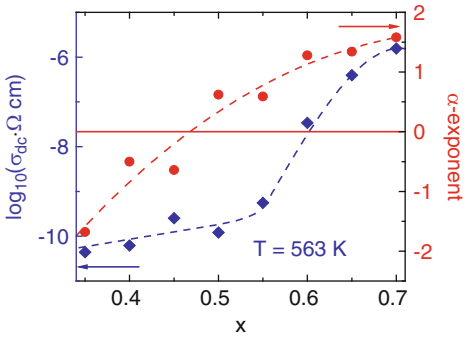


**Fig. 20** $\alpha$-exponent (*circles*, right $y$-axis) and $\sigma_{dc}(T)$ at 563 K (*squares* left $y$-axis) as a function of PSS content $x$. The *dashed lines* are for eye guidance [41]

The temperature dependence of the onset frequencies $\nu^*$ for all complex compositions can be described by the Baranovski–Cordes scaling function, which means that $\nu* \propto \sigma_{dc} \cdot T \cdot T^{-\alpha} = \sigma_{dc} \cdot T^{1-\alpha}$, but the sign and the absolute values of $\alpha$ differ strongly with composition.

Figure 19 shows two examples for sets of conductivity spectra of PEC, which have been scaled according to Baranovskii and Cordes [73], each set with a different $\alpha$-value. The spectra for $x = 0.70$ can, indeed, be nicely superimposed to a master curve (see Fig. 19a); the TTSP is very well fulfilled. For $x = 0.35$, the superimposed spectra of Fig. 19b show slight deviations at very high normalized frequencies, but the spectral shape is independent of temperature for several decades on the frequency scale, even far above the onset of dispersion.

From these and other results [41], it is concluded that the TTSP is valid in the complete measured frequency/temperature range for $x > 0.50$ and in a limited frequency range for $x < 0.50$. However, $\sigma_{dc}T$ and $\nu^*$ have distinct temperature dependences. The $\alpha$-exponent values were obtained from linear regression of $\log(\nu^*/\sigma_{dc})$ versus $\log(T)$ for all investigated PEC and are plotted in Fig. 20. An increasing trend of $\alpha$ from $-1.68$ to 1.58 if $x$ changes from 0.35 to 0.70 can be identified. $\alpha = 0$ in $\dfrac{\sigma'(\nu)}{\sigma_{dc}} = F\left(\dfrac{\nu}{\sigma_{dc} \cdot T} \cdot T^{\alpha}\right)$ is equivalent to Summerfield scaling. Considering the dashed line in Fig. 20, the $\alpha = 0$ crossover occurs at $x \approx 0.47$. Thus, a sample close to the 1:1 PSS/PDADMAC composition should best obey Summerfield scaling. Here, $\alpha$ changes its sign from negative values for all PDADMAC-rich samples to positive values for all PSS-rich samples and the PEC samples with $x = 0.50$. Positive $\alpha$-values correspond to the composition regime where the dc conductivity increases very strongly with $x$, i.e., the NaPSS-rich regime.

As discussed above, measurements with dried PEC with different alkali ions clearly showed that alkali ions govern the ionic transport in PSS-rich samples. Chloride ions might also be present in the PSS-rich complexes, but their concentration and their mobility will be much lower than the mobility of the smaller alkali ions. As $\alpha$ is always larger than zero in NaPSS-rich complexes, the $Na^+$ ion number density increases and/or the number of available pathways decreases with

temperature and the effect is more pronounced with higher the PSS content. If the number density of mobile ions was thermally activated, then more and more $Na^+$ ions would become mobile with increasing temperature and thus contribute to the long-range transport. This argument is reminiscent of the "weak electrolyte model" put forward by Ravaine and Souquet [74] for explaining the ion transport in inorganic glasses. On the other hand, the density of available pathways for the ion transport could decrease if the chain conformation of the polyelectrolyte network changed with temperature. Structural rearrangements and a higher local mobility of chain segments could block the ways for the $Na^+$ ions, leading to an increase in the characteristic mean square displacement.

PDADAMAC-rich PEC behave differently. In analogy to the arguments given above, a negative $\alpha$-value means that either the number density of mobile ions decreases or the number of available pathways for the ions increases with increasing temperature. Summerfield scaling of conductivity spectra retained for $\alpha = 0$ can therefore be considered as a special case where neither the number density of mobile ions nor the number of available ion pathways depend on temperature, or both effects are present, but cancel out.

In Fig. 6, the spectral shape of PSS- and PDADMAC-rich PEC was shown to differ significantly. The differences in the $\alpha$-values found here are a further indication for the existence of different structures in different kinds of PEC. One possible explanation is that in PDADMAC-rich PEC the large $Cl^-$ ions, being the dominant species of small counterions, have to be hosted in the matrix. This will lead to larger voids in the polyelectrolyte matrix in which the $Cl^-$ ions are embedded. The pathways for the ion transport of the diluted $Na^+$ ions will be therefore completely different than in PSS-rich PEC, where $Cl^-$ will be of very minor importance. In the latter, PEC $Na^+$ ions might find a network of connected pathways. A consistent picture about the ion transport arises with the assumption that in all dried PEC alkali ions always govern the ion transport. In addition, we assume for PDADMAC-rich PEC that all $Na^+$ ions are "dissociated" from their counter charges (similar to a dilute solution of a weak electrolyte), implying that they all contribute to the ion transport. As the number density of the $Na^+$ is low in PDADMAC-rich PEC, the conductivity is very low. With increasing temperature, however, more pathways become accessible for the sodium ions. The higher the $Na^+$ concentration in the PSS-rich samples becomes, the more we have to consider that the number density of mobile charge carries is thermally activated. The release of more mobile $Na^+$ with increasing temperature then governs the temperature dependence of the onset of conductivity dispersion.

## *5.3 The Time–Humidity Superposition Principle in PEC*

Figures 14 and 21 show that an increase in RH has a similar effect on conductivity spectra as an increase in temperature: the dc conductivity increases with RH and the onset of dispersion is characterized by $\nu^*$ shifts to higher frequencies. In contrast,

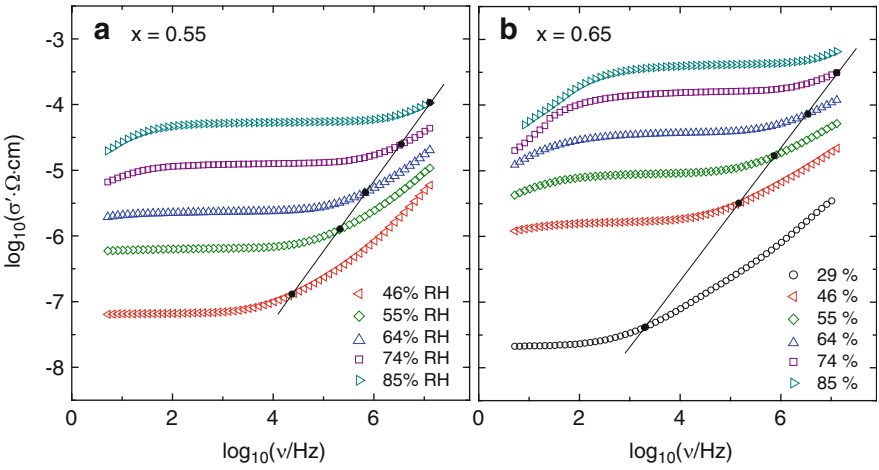


**Fig. 21** Representative spectra of $\sigma'(\nu)$ of $x$NaPSS $(1-x)$PDADMAC complexes with (**a**) $x = 0.55$ and (**b**) $x = 0.65$ taken at different RH. The *solid symbols* mark the onset frequencies defined by $\sigma'(\nu^*) = 2\sigma_{dc}$

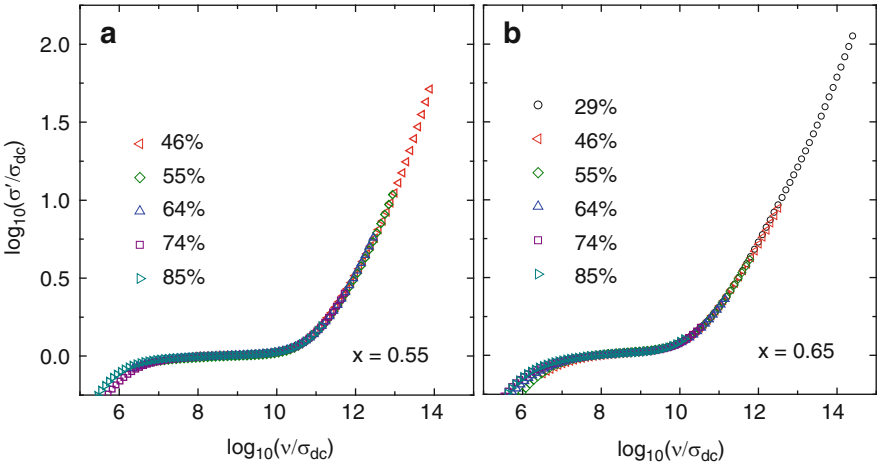


**Fig. 22** Scaled conductivity spectra of $x$NaPSS $(1-x)$PDADMAC complexes with (**a**) $x = 0.55$ and (**b**) $x = 0.65$ obtained from the corresponding spectra of Fig. 21

the slope of the straight lines connecting the onset frequencies is here equal to one, showing a direct proportionality between $\sigma_{dc}$ and $\nu^*$.

In order to test whether the shape of the spectra shows any variation with humidity, it was tried to superimpose the different spectra by shifting them along the straight line connecting the onset frequencies, completely analogous to the treatment of temperature-dependent spectra. The results are displayed in Fig. 22, where the $y$- and $x$-axes are normalized in analogy to temperature-dependent

conductivity spectra, i.e., by plotting $\log(\sigma'/\sigma_{dc})$ against $\log(\nu/\sigma_{dc})$. It should be noted that a division of the experimental frequency $\nu$ by $\sigma_{dc}$ (instead of $\sigma_{dc}T$) is completely sufficient here, because the temperature is not varied in the RH-dependent experiments.

The results in Fig. 22 show that the RH-dependent spectra of a given PEC, can, indeed, be superimposed to a master curve. The agreement between the curves is excellent in all parts of the spectra except at low frequencies, where electrode polarization effects dominate; however, these do not describe material properties. We can therefore claim that for the presented polyelectrolyte materials there is a time–humidity superposition-principle (THSP) in analogy to the well-established TTSP. Moreover, the special case of Summerfield-type scaling is fulfilled. The same holds true for other investigated PEC compositions not presented here.

We note that a similar concept of generalized dynamics has been found in PEC in rheological spectra, for which the salt concentration is the parameter causing a general enhancement of the dynamics; thus, it was termed time–salt superposition [75].

What can be concluded from the above observation of a time–humidity superposition in conductivity spectra? First, the strong exponential increase in the conductivity with RH shows that its influence on the ion dynamics is much stronger than expected for a slight softening of the PEC matrix induced by the absorption of water. The ion dynamics is therefore strongly decoupled from the polyion network dynamics, a property already previously discussed [40, 47, 67]. The dispersive conductivity reflects the ion dynamics occurring in a time window, $1/(2\pi\nu)$, and thus probes ionic hopping occurring on short time and length scales. The long-time limit of the dynamics is probed by the dc conductivity reflecting macroscopic ion transport. The THSP implies that the increase in RH of the environment does not change the basic principle of the ion conduction mechanism, but only leads to the same enhancement of the ion dynamics on all time and length scales. The reason for this is that with increasing RH water is absorbed into the PEC, which changes the energy landscape for the moving ions in such a way that ion long-range transport as well as local ion motions are strongly facilitated. This can be visualized if the temperature and the humidity dependence of the dc conductivity are combined in one equation. Dried polyelectrolyte complexes of type $x$NaPSS·$(1-x)$ PDADMAC behave like strong glass-formers: the dc conductivity is Arrhenius-activated below and even above the glass transition temperature with the same activation enthalpy. Temperature-dependent measurements show that at constant elevated humidity the complexes also follow the Arrhenius law, which will be subject of a forthcoming paper from this laboratory (De et al., unpublished results). The experimental results can be empirically combined into the following equation:

$$\sigma_{dc}(T, \mathrm{RH}) \propto (1/T) \cdot \exp(-\Delta H_{dc}/(k_B T)) \cdot \exp(B \cdot \mathrm{RH}). \tag{9}$$

In Eq. (9), $\Delta H_{dc}$ is the activation enthalpy of the dc conductivity as derived from an Arrhenius plot of the dried samples, and $B$ is a parameter determined from the slope of the straight line representing $\ln(\sigma_{dc})$ as a function of RH. Rewriting of Eq. (9) yields:

$$\sigma_{dc}(T,\mathrm{RH}) \propto (1/T)\cdot\exp(-(\Delta H_{dc} - B^{\#}\cdot\mathrm{RH})/(k_B T)) \quad \text{with} \quad B^{\#} = Bk_B T. \quad (10)$$

Equation (10) clearly shows that $B^{\#}$RH reduces the activation enthalpy of the dc conductivity determined for dried samples. The microscopic origin for this is that the presence of water absorbed by the complexes at elevated RH lowers the activation barriers for the ion transport. For constant temperature but varying humidity, as in the present case, this lowering effect is more pronounced the higher the RH. For constant RH but varying temperature, the term exp($B$RH) simply turns into a constant pre-exponential factor resulting in the familiar Arrhenius law, where the conductivity increases with temperature.

The validity of the THSP for the RH-dependent conductivity spectra shows that the lowering of the activation barriers for the ion transport not only influences the long-range transport probed by the dc conductivity, but also the ion transport occurring on shorter time and length scales.

Secondly, the fact that not only the THSP, but also the special type of Summerfield-analogue scaling is fulfilled in humidified PEC, has even more implications about the underlying ion transport mechanism. This can be seen when again considering the established temperature-dependent behavior. Because the dynamic conductivity is determined by the ion dynamics occurring in a time window $1/(2\pi\nu)$, the onset frequency $\nu^*$ can be taken as a measure for the time scale in which local dynamics (measured in the dispersive regime) turn into long-range transport (measured in the dc regime). The corresponding time $t^*$ is determined by the ion mobility. The higher the ion mobility, the shorter the time needed for the ion transport to become long-range transport. The inverse onset-frequency $\nu^*(T)$ is therefore proportional to $\mu(T)$, which shows the same activation enthalpy. In the Summerfield case, where $\sigma_{dc}$ is also proportional to $\nu^*(T)$, the number density $N_v$ of mobile ions therefore has to be constant. One might even look at other characteristic points on each conductivity isotherm. If conductivity isotherms in a plot of $\log(\sigma(\nu, T))$ versus $\log(\nu)$ are considered and if characteristic points on each isotherm, in analogy to the onset points, are defined via $\sigma'(\nu_n,T) = n\sigma_{dc}(T)$ (with $n$ being a real number $> 0$), then the straight line connecting these characteristic points will always have a slope of one. This means that no matter how the characteristic points are defined, $\sigma'(\nu_n,T)$ and therefore $\mu(\nu_n,T)$ will always be proportional to the onset frequency $\nu^*(T)$ and therefore activated with the same activation enthalpy. Thus, in the Summerfield case, it is in fact exclusively the ion mobility that is thermally activated and shows the same enhancement on short as well as long time scales and we can write:

$$\sigma(\nu,T) = N_v\cdot\mu(\nu,T)\cdot q. \quad (11)$$

On the other hand, if $N_v$ depends on temperature and $\mu$ still is the quantity that has the same activation energy as $\nu^*$, then, due to the change of $N_v$ with temperature, $\sigma_{dc}(T)$ will no longer be proportional to the onset frequency $\nu^*(T)$. If the number density of mobile ions increases with temperature, $\sigma_{dc}(T)$ will increase

more strongly as $\nu^*(T)$. Considering a log–log plot of the normalized conductivity versus normalized frequency, the straight line connecting the onset frequencies will then have a slope exceeding one. The same holds true for all other straight lines connecting other characteristic points defined via $\sigma'(\nu_n,T) = n\sigma_{dc}(T)$. This behavior has been discussed above for the temperature-dependent spectra of dried $x$NaPSS $(1 - x)$ PDADMAC PEC with an excess of NaPSS.

These principles derived for temperature-dependent conductivity spectra will now be transferred to the humidity-dependent scaling of $\sigma(\nu,\mathrm{RH})$. Here, the conductivity can be written very generally as:

$$\sigma(\nu, \mathrm{RH}) = N_v(\mathrm{RH}) \cdot \mu(\nu, \mathrm{RH}) \cdot q. \tag{12}$$

Assuming that, like in the temperature case, the mobility at short and long time scales, $\mu(\nu_n,\mathrm{RH})$, is "activated" in the same way as the onset frequencies, then the Summerfield-type of scaling found experimentally implies that the number density of mobile ions does not depend on RH. In analogy to the temperature-dependent conductivity spectra of other ion-conducting materials showing Summerfield scaling, the only effect of humidity is to increase the ionic mobility. The finding of a constant number density in the RH-dependent conductivity spectra as deduced above is in contrast to the temperature dependence of similar NaPSS/PDADAMAC complexes with an excess of NaPSS, where the number density of mobile $Na^+$ ions seems to increase with temperature [41, 47]. This means that although there are strong similarities between the influence of temperature and RH on the ion dynamics, these influences are not completely identical. In completely dry polyelectrolyte complexes, some bound $Na^+$ ions are released to take part in the conduction process when the temperature is raised [41]. By contrast, an increase in humidity does not change the number density of mobile ions. The reason for this could be that even at a RH of 29%, the lowest value employed, the complexes have already absorbed an amount of water sufficient for hydrating all $Na^+$ ions, which can then contribute to the ion transport. During long-range transport, the hydrated $Na^+$ ions (which stay in the vicinity of not intrinsically compensated polyanion charges) move to other negative counter sites that are temporally accessible, while always avoiding other $Na^+$ ions of same charge. This thermally activated process is speeded up with increasing water content according to Eq. (10), while the number of mobile cations remains the same.

However, this special type of Summerfield-type RH-dependence in ion-conducting materials is not necessarily a general finding. It is well known that some materials have conductivity spectra that obey the TTSP with temperature -independent spectral shapes of the conductivity, but nevertheless deviate from Summerfield scaling [41, 44, 71, 76, 77]. In these materials, the shape of the conductivity spectra is found to be independent of temperature (TTSP fulfilled), but the slope of the line connecting the onset frequencies in a plot of log $(\sigma' T)$ versus log$(\nu)$ differs from one, in most cases exceeding one. As explained in [41, 71], the latter effect can be explained by a number density of mobile ions that increases with temperature. Analagous deductions can also be made on the basis of the

RH-dependent scaling procedure proposed here. In materials where THSP, but not humidity-dependent Summerfield scaling, applies the scaling procedure proposed here could, therefore, be used to quantify the increase in mobile ions resulting from the absorption of water. This would allow a distinction between the increase in mobility and number density of the mobile ions with RH, which is impossible from $\sigma_{dc}$ alone. In summary, the newly found THSP for frequency-dependent conductivities can help in identifying the extent to which the increase in conductivity with RH is due to an increase in mobility and/or to an increase in the number density of mobile ions.

## 6 Summary and Outlook

We have presented here the state of the art in impedance spectroscopy performed on PEC materials and the implications for ion dynamics and transport as concluded from such data. The major findings include identification of the main contribution to charge transport, which is the cationic counterion for both cation-rich and anion-rich PEC. In dry PEC, the mobility of smaller alkali cations is greater, whereas in humidified PEC the hydration shell causes larger alkali cations to exhibit a greater mobility, an indication that transport involves the hydration shell.

Furthermore, scaling concepts such as time–temperature and time–humidity superposition describe the frequency-dependent dynamics in PEC. From these concepts, conclusions about the dependence of charge carrier concentration on temperature and humidity can be drawn. The overall picture arising from the work reviewed here is consistent with PEC forming a dense polymeric glass with very low matrix mobility, but with fairly mobile charge carriers, the mobility of which (and also the activation energy of ionic motion) is dependent on their size. Thus, ion motion takes place in a rather static potential energy landscape by Arrhenius-activated jumps of the ions. Model approaches to describe such jump contributions to the conductivity spectrum could be successfully transferred from other disordered ion-conducting materials.

So far, impedance spectroscopy has been applied to only a few PEC materials. Mostly, studies have been performed on the standard polyelectrolytes also employed in layer-by-layer formation, such as PSS, PDADMAC and only a few more. Therefore, how far the properties depend on the molecular structures involved is still an open question.

Another interesting aspect is the crossover between cation-dominated conductivity and proton-dominated conductivity that should occur with increasing water content for PEC. So far, only PEM with their intrinsically low concentration of residual counterions were identified as proton conductors. However, for strongly humidified stoichiometric PEC with nominally no residual counterions, a similarly dominating proton contribution to the conductivity can be expected. Such knowledge is relevant for potential applications of PEM either as proton or as $Li^+$ conductors, in particular

for the question of how far conductivity contributions of protonic or cationic charge carriers can be tuned by the polyelectrolyte composition or by external parameters.

## References


1. Bungenberg de Jong HG (1949) In: Kruyt HR (ed) Colloid science. Elsevier, Amsterdam, pp 232–55, 59–330, 5–429 and 33–80
2. Michaels AS (1965) Polyelectrolyte complexes. J Ind Eng Chem 57:32–40
3. Michaels AS, Falkenstein GL, Schneider NS (1965) Dielectric properties of polyanion–polycation complexes. J Phys Chem 69:1456–1465
4. Michaels AS, Miekka RG (1961) Polycation–polyanion complexes: preparation and properties of poly(vinylbenzyltrimethylammonium styrenesulfonate). J Phys Chem 65:1765–1773
5. Michaels AS, Mir L, Schneider NS (1965) A conductometric study of polycation–polyanion reactions in dilute aqueous solution. J Phys Chem 69:1447–1455
6. Philipp B, Dautzenberg H, Linow KJ, Koetz J, Dawydoff W (1989) Polyelectrolyte complexes – recent developments and open problems. Prog Polym Sci 14:91–172
7. Dautzenberg H (2000) Light scattering studies on polyelectrolyte complexes. Macromol Symp 162:1–21
8. Thünemann AF, Müller M, Dautzenberg H, Joanny JF, Löwen H (2004) Polyelectrolyte complexes. In: Schmidt M (ed) Polyelectrolytes with defined molecular architechture II. Advances in Polymer Science, vol. 166. Springer, Berlin, pp 113–171
9. Decher G, Hong JD (1991) Buildup of ultrathin multilayer films by a self-assembly process. 2. Consecutive adsorption of anionic and cationic bipolar amphiphiles and polyelectrolytes on charged surfaces. Ber Bunsen Ges Phys Chem 95:1430–1434
10. Decher G, Hong JD, Schmitt J (1992) Buildup of ultrathin multilayer films by a self-assembly process. 3. Consecutively alternating adsorption of anionic and cationic polyelectrolytes on charged surfaces. Thin Solid Films 210:831–835
11. Bieker P, Schönhoff M (2010) Linear and exponential growth regimes of multilayers of weak polyelectrolytes in dependence on pH. Macromolecules 43:5052–5059
12. Büscher K, Graf K, Ahrens H, Helm CA (2002) Influence of adsorption conditions on the structure of polyelectrolyte multilayers. Langmuir 18:3585–3591
13. Decher G (1997) Fuzzy nanoassemblies: toward layered polymeric multicomposites. Science 277:1232–1237
14. Bertrand P, Jonas A, Laschewsky A, Legras R (2000) Ultrathin polymer coatings by complexation of polyelectrolytes at interfaces: suitable materials, structure and properties. Macromol Rapid Commun 21:319–348
15. Schönhoff M (2003) Layered polyelectrolyte complexes: physics of formation and molecular properties. J Phys Condens Matter 15:R1781–R1808
16. Sukhishvili SA (2005) Responsive polymer films and capsules via layer-by-layer assembly. Curr Opin Colloid Interface Sci 10:37–44
17. Rodriguez LNJ, De Paul SM, Barrett CJ, Reven L, Spiess HW (2000) Fast magic-angle spinning and double-quantum H-1 solid-state NMR spectroscopy of polyelectrolyte multilayers. Adv Mater 12:1934–1938
18. Kovacevic D, van der Burgh S, de Keizer A, Stuart MAC (2002) Kinetics of formation and dissolution of weak polyelectrolyte multilayers: role of salt and free polyions. Langmuir 18:5607–5612
19. Sukhishvili SA, Kharlampieva E, Izumrudov V (2006) Where polyelectrolyte multilayers and polyelectrolyte complexes meet. Macromolecules 39:8873–8881
20. van der Gucht J, Spruijt E, Lemmers M, Stuart MAC (2011) Polyelectrolyte complexes: bulk phases and colloidal systems. J Colloid Interfae Sci 361:407–422

21. Kreuer KD (2001) On the development of proton conducting polymer membranes for hydrogen and methanol fuel cells. J Membr Sci 185:29–39
22. Cui MZ, Li ZY, Zhang J, Feng SY (2008) Siloxane-based polymer electrolytes. Prog Chem 20:1987–1997
23. Karatas Y, Kaskhedikar N, Burjanadze M, Wiemhofer HD (2006) Synthesis of cross-linked comb polysiloxane for polymer electrolyte membranes. Macromol Chem Phys 207:419–425
24. Kunze M, Karatas Y, Wiemhöfer HD, Eckert H, Schönhoff M (2010) Activation of transport and local dynamics in polysiloxane-based salt-in-polymer electrolytes: a multinuclear NMR study. Phys Chem Chem Phys 12:6844–6851
25. Dubreuil F, Elsner N, Fery A (2003) Elastic properties of polyelectrolyte capsules studied by atomic-force microscopy and RICM. Eur Phys J E Soft Matter Biol Phys 12:215–221
26. Picart C, Senger B, Sengupta K, Dubreuil F, Fery A (2007) Measuring mechanical properties of polyelectrolyte multilayer thin films: novel methods based on AFM and optical techniques. Colloids Surf A 303:30–36
27. Durstock MF, Rubner MF (2001) Dielectric properties of polyelectrolyte multilayers. Langmuir 17:7865–7872
28. DeLongchamp DM, Hammond PT (2003) Fast ion conduction in layer-by-layer polymer films. Chem Mater 15:1165–1173
29. DeLongchamp DM, Hammond PT (2004) Highly ion conductive poly(ethylene oxide)-based solid polymer electrolytes from hydrogen bonding layer-by-layer assembly. Langmuir 20:5403–5411
30. Akgöl Y, Hofmann C, Karatas Y, Cramer C, Wiemhöfer HD, Schönhoff M (2007) Conductivity spectra of polyphosphazene-based polyelectrolyte multilayers. J Phys Chem B 111:8532–8539
31. Argun AA, Ashcraft JN, Herring MK, Lee DKY, Allcock HR, Hammond PT (2010) Ion conduction and water transport in polyphosphazene-based multilayers. Chem Mater 22:226–232
32. Hoogeveen N, Stuart M, Fleer G, Böhmer M (1996) Formation and stability of multilayers of polyelectrolytes. Langmuir 12:3675–3681
33. Jaber JA, Schlenoff JB (2007) Counterions and water in polyelectrolyte multilayers: a tale of two polycations. Langmuir 23:896–901
34. Crouzier T, Picart C (2009) Ion pairing and hydration in polyelectrolyte multilayer films containing polysaccharides. Biomacromolecules 10:433–442
35. Daiko Y, Katagiri K, Matsuda A (2008) Proton conduction in thickness-controlled ultrathin polycation/nafion multilayers prepared via layer-by-layer assembly. Chem Mater 20:6405–6409
36. Xi JY, Wu ZH, Teng XG, Zhao YT, Chen LQ, Qiu XP (2008) Self-assembled polyelectrolyte multilayer modified nafion membrane with suppressed vanadium ion crossover for vanadium redox flow batteries. J Mater Chem 18:1232–1238
37. Jiang SP, Liu ZC, Tian ZQ (2006) Layer-by-layer self-assembly of composite polyelectrolyte-nafion membranes for direct methanol fuel cells. Adv Mater 18:1068–1072
38. Lutkenhaus JL, Hammond PT (2007) Electrochemically enabled polyelectrolyte multilayer devices: from fuel cells to sensors. Soft Matter 3:804–816
39. Akgöl Y, Cramer C, Hofmann C, Karatas Y, Wiemhöfer HD, Schönhoff M (2010) Humidity-dependent dc conductivity of polyelectrolyte multilayers: protons or other small ions as charge carriers? Macromolecules 43:7282–7287
40. Imre ÁW, Schönhoff M, Cramer C (2008) A conductivity study and calorimetric analysis of dried poly(sodium 4-styrene sulfonate)/poly(diallyldimethylammonium chloride) polyelectrolyte complexes. J Chem Phys 128:134905
41. Imre ÁW, Schönhoff M, Cramer C (2009) Unconventional scaling of electrical conductivity spectra for PSS-PDADMAC polyelectrolyte complexes. Phys Rev Lett 102:255901
42. Funke K, Cramer C, Wilmer D (2005) Concept of mismatch and relaxation for self-diffusion and conduction in ionic materials with disordered structures. In: Kärger J, Heitjans P (eds) Diffusion in condensed matter. Springer, Berlin, pp 857–893

43. Pas SJ, Banhatti RD, Funke K (2006) Conductivity spectra and ion dynamics of a salt-in-polymer electrolyte. Solid State Ionics 177:3135–3139
44. Santic A, Wrobel W, Mutke M, Banhatti RD, Funke K (2009) Frequency-dependent fluidity and conductivity of an ionic liquid. Phys Chem Chem Phys 11:5930–5934
45. Causemann S, Schönhoff M, Eckert H (2011) Local environment and distribution of alkali ions in polyelectrolyte complexes studied by solid-state NMR. Phys Chem Chem Phys 13:8967–8976
46. Carrière D, Dubois M, Schönhoff M, Zemb T, Möhwald H (2006) Counter-ion activity and microstructure in polyelectrolyte complexes as determined by osmotic pressure measurements. Phys Chem Chem Phys 8:3141–3146
47. Schönhoff M, Imre ÁW, Bhide A, Cramer C (2010) Mechanisms of ion conduction in polyelectrolyte multilayers and complexes. Z Phys Chem 224:1555–1589
48. Bhide A, Schönhoff M, Cramer C (2012) Cation conductivity in dried poly(4-styrene sulfonate) poly(diallydimethylammonium chloride) based polyelectrolyte complexes. Solid State Ionics 214:13–18
49. Bunde A, Ingram MD, Maass P (1994) The dynamic structure model for ion transport in glasses. J Non-Cryst Solids 172:1222–1236
50. Imre ÁW, Berkemeier F, Mehrer H, Gao Y, Cramer C, Ingram MD (2008) Transition from a single-ion to a collective diffusion mechanism in alkali borate glasses. J Non-Cryst Solids 354:328–332
51. Gao Y, Cramer C (2005) Mixed cation effects in glasses with three types of alkali ions. Solid State Ionics 176:2279–2284
52. Roling B (2001) Modeling of ion transport processes in disordered solids: Monte Carlo simulations of the low-temperature particle dynamics in the random barrier model. Phys Chem Chem Phys 3:5093–5098
53. Schrøder TB, Dyre JC (2000) Scaling and universality of ac conduction in disordered solids. Phys Rev Lett 84:310–313
54. Maass P, Rinn B, Schirmacher W (1999) Hopping dynamics in random energy landscapes: an effective medium approach. Philos Mag B 79:1915–1922
55. Dieterich W, Maass P (2002) Non-Debye relaxations in disordered ionic solids. Chem Phys 284:439–467
56. Cramer C, Brunklaus S, Gao Y, Funke K (2003) Dynamics of mobile ions in single- and mixed-cation glasses. J Phys Condens Matter 15:S2309–S2321
57. Cramer C, Akgöl Y, Imre ÁW, Bhide A, Schönhoff M (2009) Ion dynamics in solid polyelectrolyte materials. Z Phys Chem 223:1171–1185
58. Cramer C, Funke K (1992) Observatio of 2 relaxatio processes in an ion conducting glass yields new structural information. Ber Bunsen Ges Phys Chem 96:1725–1727
59. Cramer C, Funke K, Saatkamp T, Wilmer D, Ingram MD (1995) High frequency conductivity plateau and ionic hopping processes in a ternary lithium borate glass. Z Naturforsch A Phys Sci 50:613–623
60. Funke K, Maue T, Wilmer D, Cramer C, Saatkamp T (1994) Different kinds of localized hopping in solid electrolytes. In: Ramanarayanan TA, Worrell WL, Tuller HL (eds) Ionic and mixed conducting ceramics. The Electrochemical Society Softbound Proceedings, Pennington, pp 564–573
61. Laughman DM, Banhatti RD, Funke K (2009) Nearly constant loss effects in borate glasses. Phys Chem Chem Phys 11:3158–3167
62. Rinn B, Dieterich W, Maass P (1998) Stochastic modelling of ion dynamics in complex systems: dipolar effects. Philos Mag B 77:1283–1292
63. Knödler D, Dieterich W, Petersen J (1992) Coulombic traps and ion conduction in glassy electrolytes. Solid State Ionics 53:1135–1140
64. Köhler R, Dönch I, Ott P, Laschewsky A, Fery A, Krastev R (2009) Neutron reflectometry study of swelling of polyelectrolyte multilayers in water vapors: influence of charge density of the polycation. Langmuir 25:11576–11585

65. Kügler R, Schmitt J, Knoll W (2002) The swelling behavior of polyelectrolyte multilayers in air of different relative humidity and in water. Macromol Chem Phys 203:413–419
66. De S, Cramer C, Schönhoff M (2011) Humidity dependence of the ionic conductivity of polyelectrolyte complexes. Macromolecules 44:8936–8943
67. Cramer C, De S, Schönhoff M (2011) Time-humidity-superposition principle in electrical conductivity spectra of ion-conducting polymers. Phys Rev Lett 107:028301
68. Dyre JC, Maass P, Roling B, Sidebottom DL (2009) Fundamental questions relating to ion conduction in disordered solids. Rep Prog Phys 72: 046501
69. Summerfield S (1985) Universal low-frequency behavior in the ac hopping conductivity of dispersed systems. Philos Mag B 52:9–22
70. Summerfield S, Butcher PN (1985) Universal behavior of ac hopping conductivity of disordered systems. J Non-Cryst Solids 77–8:135–138
71. Murugavel S, Roling B (2002) Ac conductivity spectra of alkali tellurite glasses: composition-dependent deviations from the Summerfield scaling. Phys Rev Lett 89:195902
72. Murugavel S, Roling B (2004) Ionic transport in glassy networks with high electronic polarizabilities: conductivity spectroscopic results indicating a vacancy-type transport mechanism. J Phys Chem B 108:2564–2567
73. Baranovskii SD, Cordes H (1999) On the conduction mechanism in ionic glasses. J Chem Phys 111:7546–7557
74. Ravaine D, Souquet JL (1977) Thermodynamic approachto ionic conductivity in oxide glasses. 1. Correlation of ionic conductivity with chemical potential of alkali oxide in oxide glasses. Phys Chem Glasses 18:27–31
75. Spruijt E, Sprakel J, Lemmers M, Stuart MAC, van der Gucht J (2010) Relaxation dynamics at different time scales in electrostatic complexes: time-salt superposition. Phys Rev Lett 105:208301
76. Imre ÁW, Voss S, Mehrer H (2002) Ionic transport in 0.2[XNa2O·(1-X)Rb2O]·0.8B2O3 mixed-alkali glasses. Phys Chem Chem Phys 4:3219–3224
77. Cramer C, Brückner S, Gao Y, Funke K (2002) Ion dynamics in mixed alkali glasses. Phys Chem Chem Phys 4:3214–3218

Adv Polym Sci (2014) 255: 139–172
DOI: 10.1007/12_2012_178

Published online: 16 September 2013

# Relaxation Phenomena During Polyelectrolyte Complex Formation

**Saskia Lindhoud and Martien A. Cohen Stuart**

**Abstract** Polyelectrolyte complex formation is a well-studied subject in colloid science. Several types of complex formation have been studied, including PEMs, macroscopic polyelectrolyte complexes, soluble complexes and polyelectrolyte complex micelles. The chemical nature of the complex-forming polyelectrolytes and the environmental conditions (e.g., pH, ionic strength and temperature) influence the final structural properties of these complexes. This chapter deals with the kinetics of polyelectrolyte complex formation and discusses how ionic strength, charge density and pH influence the dynamics of the complexes, which can range from glass-like (solid) precipitates to liquid-like phases. The switching between the glass-like and liquid-like phase as a function of the ionic strength has a strong analogy to the phase behaviour of polymer melts as function of temperature.

By performing calorimetry during complex formation it has been found that the enthalpy of complex formation of systems that form glass-like phases has an opposite sign to the enthalpy of systems that form liquid-like phases, i.e., the formation of glass-like phases is exothermic and the formation of liquid-like phases is endothermic. The free energy ($\Delta_f G$), enthalpy ($\Delta_f H$) and entropy ($\Delta_f S$) of polyelectrolyte complex formation and how they vary as a function of the ionic strength will be discussed.

Results from dynamic light scattering (DLS) titrations, Atomic Force Microscopy (AFM), surface force measurements and rheology will be used to illustrate how differences in kinetics show up in experiments on colloidal micellar systems.

S. Lindhoud (✉) and M.A. Cohen Stuart
Laboratory of Physical Chemistry and Colloid Science, Wageningen University,
Dreijenplein 6, 6703 HB Wageningen, The Netherlands
e-mail: saskia.lindhoud@gmail.com; martien.cohenstuart@wur.nl

In the section on DLS titrations, three-component systems containing two oppositely charged polyelectrolytes and protein molecules will be discussed. This chapter concludes with a section dedicated to the complex formation of oppositely charged protein molecules.

**Keywords** AFM • DLS • Kinetics • PEC • PEM • Relaxation time • Rheology

## Contents



## 1 Kinetics of Polyelectrolyte Complex Formation

When two oppositely charged polyelectrolytes are mixed at equal (stoichiometric) charge ratio, a neutral complex will form. This process is *schematically* depicted in Fig. 1, where one can see that before the reaction a negatively charged polymer with ten charges is accompanied by ten positively charged counterions, and that the positively charged polymer (also having ten charges) is accompanied by ten negatively charged counterions. Basically, polyelectrolyte complex formation can be regarded as an ion-exchange process where polymer–counterion pairs are replaced by polymer–polymer ion pairs [2]. The main driving force for this process at low salt concentrations is an increase in entropy. In Fig. 1 it can be seen that before the reaction there are two (compound) "particles" and after the reaction there are 21 particles: The increase in accessible volume to the $Na^+$ and $Cl^-$ ions is responsible for this.

Polyelectrolyte complexes consisting of linear polyelectrolytes will phase-separate into a dense polymeric phase and a dilute aqueous phase. Depending on the type of polyelectrolytes used and the ionic strength, one finds that this dense phase is either solid-like or liquid-like. The dynamic state of the complex phase gives clues about whether the complex is in equilibrium or whether it is likely to be in a kinetically quenched state.

The reversibility of polyelectrolyte complex formation influences the relaxation process, which consists of two steps. The first step is the formation of initial polyelectrolyte complexes, with the simultaneous release of the counterions.

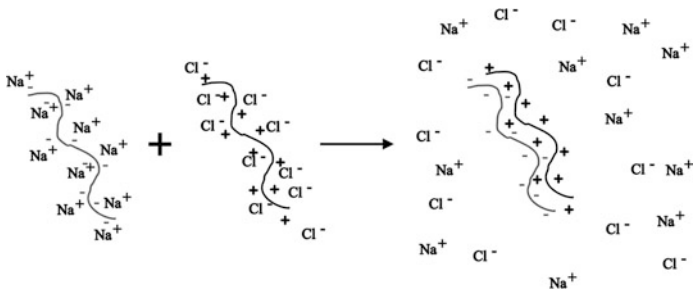


**Fig. 1** Polyelectrolyte complex formation [1]

This step is diffusion-controlled; it depends on the rate of collisions between the oppositely charged species. Factors influencing this step are the polyelectrolyte concentration and the temperature. The second step is rearrangement of these initial complexes towards their equilibrium state. These rearrangements occur via polyelectrolyte exchange reactions between the polymer chains within the complex or with free polymer chains in solution [3, 4].

The second step is not driven by the release of small ions and its driving force is therefore much smaller. Instead, this step is mainly driven by an increase in configurational entropy. The time needed for the polyelectrolyte exchange reactions to occur depends on the molecular properties of the polyelectrolytes (i.e., their hydrophobicity [5, 6]), whether the charges are pH-dependent, the charge density and the chain length. Solvent properties such as ionic strength and pH and the nature of the counterions may further influence the rate of rearrangement of the polyelectrolyte complexes towards their equilibrium state.

Broadly speaking, the following classification can be made in terms of system relaxation time ($\tau$) as compared to the experimental time ($\tau_{exp}$). The ratio of these times is often called the "Deborah number" ($De$). For $De < 1$, the relaxation time is shorter than the experimental timescale ($\tau < \tau_{exp}$); for $De \approx 1$, the relaxation behaviour is observed during the experiment; and for $De \gg 1$, the relaxation behaviour is quenched. Glass-like structures are typically found in the kinetically quenched regime. In the fast relaxing (equilibrium) regime, the formation of liquid-like phases is observed.

Liquid-like complexes, which are also called "complex coacervates" and were first described by Bungenberg de Jong [7], are mainly found at high ionic strengths or when two oppositely charged biomacromolecules with low charge densities (such as gum arabic and gelatin) are mixed [8–12]. This indicates that charge density and ionic strength are important parameters that influence the relaxation behaviour of polyelectrolyte complexes. Monovalent ions weaken the complex, and the complex will dissolve when the salt ions have weakened the complex to such an extent that the translational entropy of the polymer chains takes over. The salt concentration at which this happens will be referred to as the "critical salt concentration" [13]. At this salt concentration, the concentration of polymers in the dense phase is equal to that in the dilute phase.

Binodal compositions of polyelectrolyte complexes as a function of the ionic strength have been studied by Spruijt et al. [13]. They used fluorescently labelled polyacrylic acid (PAA) and poly(*N*,*N*-dimethylaminoethyl methacrylate) (PDMAEMA) with different chain lengths. The dilute and dense polymeric phases were separated. The dense phase was weighed and dried and weighed again to determine the amount of water. The composition of the dilute phase was measured using a densiometer; the concentration of fluorescently labelled PAA was determined using UV–visible spectrometry. A phase diagram could be constructed. It was found that the water content of the complex is independent of the polymer chain length, far from the critical salt concentration, and that it increases upon increasing the ionic strength.

The first theory of polyelectrolyte complex formation was proposed by Voorn and Overbeek [14, 15]. This mean field model was used to describe the binodal compositions, the water content and the critical salt concentration as a function of the polymer chain length. This theoretical description uses the Debye–Hückel approximation; the approximations within the derivation of the electrostatic interaction free energy are therefore only valid at low charge densities. The correlation effects at high concentrations of salt and monomeric units are neglected, and ion pairing effects such as counterion condensation are not taken into account. Despite these limitations, the experimental results could be described reasonably well [13].

Over the years, the theory of polyelectrolyte complex formation has been further developed. The theory of Voorn and Overbeek was later extended by Nakajima and Sato, who included an interaction parameter $\chi$ to account for additional interactions such as hydrophobicity [16]. Correlation effects within the dense complex phase were included in the theory by Castelnovo and Joanny, which enables prediction of a critical salt concentration [17]. Kramarenko and Khokhlov included specific ion-pairing energies, but their theory ignores the formation of ion pairs between polyelectrolytes and monovalent counterions; hence, they do not present a salt dependence of the complex formation [18]. Heterogenous cell models can be used to describe experimental data on polyelectrolyte complex formation. These models take the spatial structure of the complex into account [19]. In Sect. 3 on protein–protein complexation we discuss how such a model can be used to describe experimental data.

## *1.1 Strongly and Weakly Charged Polyelectrolytes*

The previous section described how the relaxation rate of polyelectrolyte complex formation may depend on the nature of the charges on the polyelectrolytes. The polyelectrolytes in Fig. 1 are strongly charged polyelectrolytes, i.e., their charge is independent of the pH of the system. However, there are many polyelectrolytes that are weak (e.g., with carbonyl or amine groups), many of natural origin, and their number of charges is dependent on the pH of the system. Figure 2 shows the charge of these weakly charged polyelectrolytes as function of the pH *schematically*.

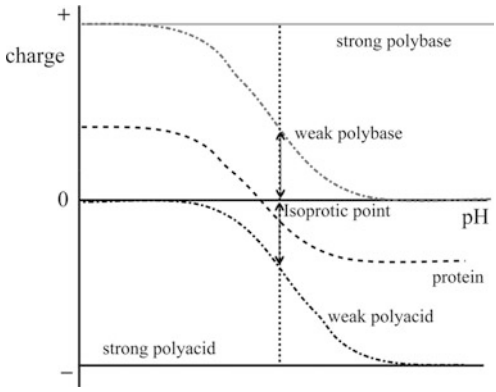


**Fig. 2** Charge of weak and strong polyelectrolytes, and of proteins as function of the pH [1]

A weak polybase is fully charged at low pH and uncharged at high pH, whereas weak polyacids are fully charged at high pH and uncharged at low pH. The exact pH at which weak polyelectrolytes become fully charged of course depends on the chemical nature of the polymer.

Protein molecules are very special weak polyelectrolytes; they not only have a charge that is dependent on the pH, but they are usually ampholytic, carrying both acidic and basic groups so that the sign of their charge is dependent on the pH. This means that at a certain pH they are electroneutral (isoelectric). Generally, the number of charges on fully charged protein molecules is much lower than on synthetic polyelectrolytes, so the charge density of protein molecules is rather low. Complex formation between two oppositely charged protein molecules will be discussed at the end of this chapter.

## *1.2 Polyelectrolyte Multilayer Formation*

A widely studied class of polyelectrolyte complexes are polyelectrolyte multilayers (PEMs). These structures form on charged surfaces exposed, in an alternate fashion, to a solution containing polyanions and to a solution containing polycations or vice versa. Because of the ease of preparation, several aspects of PEMs have been studied. The differences between polyelectrolyte complex formation from two strong polyelectrolytes and from two weak polyelectrolytes will be discussed. Examples of polyelectrolyte complex formation discussed in this section mainly come from PEM formation.

Polyelectrolyte complex formation in salt-free systems, between two strong polyelectrolytes, was first studied by Fuoss and coworkers. Upon mixing solutions containing oppositely charged polyelectrolytes, they observed the rapid formation of colloidal particles with stoichiometric composition [20]. Stoichiometric

complexes were also found by Michaels [21]. It was found that the composition of the colloidal precipitate was independent of the relative proportions in which the polyelectrolytes were mixed, and independent of the order of addition. The same phenomenon is found in multilayers consisting of two strongly charged polyelectrolytes. Within the multilayers stoichiometry is obeyed; only the surface bears a considerable excess charge and the charges on the polymers balance each other without the requirement for additional counterions [22].

A certain minimum charge density is needed for PEM formation to occur. Four different regimes can be identified when one fully charged polyelectrolyte is used and the charge density of the oppositely charged polyelectrolyte is varied [2, 23–25]. First, when the charge density is very low, no PEMs will form. The second regime is where interactions other than electrostatic interactions (such as hydrogen bonding, hydrophobic interactions and van der Waals interactions) cause the formation of PEMs; typically these "PEMs" are thin. The ionic strength does not influence the formation of these multilayers, nor its thickness or surface roughness [25, 26]. The third regime is roughly found between a charge density of 50% and 75%. In this regime, thicker PEMs are found because the uncharged patches of the polyelectrolytes require more space. Fourth, above a charge density of roughly 75%, thinner multilayers are formed. In this regime, the polyelectrolytes adsorb in a flat conformation, because repulsion between the charged groups on the polymer leads to stretching of the polymer backbone [2, 23, 24]. Also, linear growth of PEMs is observed.

For PEM formation, two growth regimes are found: exponential [27–29] and linear growth. Linear growth is typically observed when two strongly charged polyelectrolytes are used and for two weakly charged polyelectrolytes at a pH in between their p$K$s and at low ionic strength [30, 31]. During linear PEM growth, the thickness increment is constant for each polyelectrolyte addition.

Exponential multilayer growth is observed when the salt concentration is increased for weakly charged polyelectrolytes at a pH close to their isoprotic point, $\mathrm{pH} = \frac{1}{2}(\mathrm{p}K_{\mathrm{anion}} + \mathrm{p}K_{\mathrm{cation}})$ (see Fig. 2) [31]. In some cases, addition of salt to systems containing two strongly charged polyelectrolytes will also induce exponential growth. In other cases, the thickness increment may become a function of the ionic strength. Which scenario will apply when strongly charged polymers are used depends on the chemical nature of the polyelectrolytes. When exponential growth is observed, the thickness increment ($dh$) becomes proportional to the overall thickness $h$ ($dh \sim h$).

The differences between linearly and exponentially growing films have been explained by the inward and outward diffusion of polyelectrolytes [27, 32]; hence, it depends on the presence of a mobile polymeric component. When vertical diffusion of polyelectrolytes within a PEM was observed [33], a model was proposed based on this inward and outward diffusion throughout the film of at least one of the polyelectrolytes [28]. In these studies, fluorescently labelled polyelectrolytes were used and their diffusion through the polyelectrolyte multilayer was probed using confocal microscopy.

Another aspect that has been studied is the influence of polyelectrolyte chain length on PEM formation. Short polymer chains have a tendency to form polyelectrolyte complexes in solution rather than form PEMs. An explanation for this phenomenon is that the number of charged groups on a polyelectrolyte determines the number of counterions that can be released. At a certain chain length the entropy gain due to counterion release is approximately the same as the entropy of free chains or polyelectrolyte complexes in solution [34].

The complex formation between two weakly charged polyelectrolytes depends on the pH of the system. At both low and high pH one of the polyelectrolytes is uncharged (see Fig. 2) and no polyelectrolyte complex formation will occur. A complication is that the charge density also depends on charged objects in their vicinity: weakly charged polyelectrolytes are able to mutually influence their dissociation behaviour [30, 35–39]. This feature will later be discussed in more detail (see Sect. 2.1.1 on pH during light scattering titrations).

At low ionic strength and when the pH is fixed, three different growth regimes are observed for PEM formation [30]. At low and high pH, when one of the polyelectrolytes is fully charged and the other one is very weakly charged, multilayer formation may occur due to interactions other than electrostatic interactions. For instance, it is known that PAA forms hydrogen bonds at low pH [40]. This regime is similar to the first regime of PEM formation for strong polyelectrolytes with low charge densities. The second regime is observed at a pH where one polymer is almost fully charged and the other polymer is becoming charged. At this pH range, exponentially growing PEMs are often observed and thick PEMs are found [30]. In the third regime, thin linearly growing PEMs are found. Here the pH equals the average p$K$ of the two polyelectrolytes. This point at $\mathrm{pH} = \frac{1}{2}(\mathrm{p}K_{\mathrm{anion}} + \mathrm{p}K_{\mathrm{cation}})$ is called the isoprotic point and is indicated in Fig. 2. This regime is the most favourable for PEM formation [2, 30, 31].

The growth behaviour of PEMs can be controlled by mixing a weakly and a strongly charged polymer with the same charge (to form one layer). Two growth regimes are found using this procedure, namely initial exponential growth and later, from a certain number of layers on, linear growth. The growth rate in the linear regime is smaller than the growth rate of the exponentially growing regime. The proposed explanation for this phenomenon is that the number of chains diffusing in and out of the PEM during each cycle becomes constant [29].

A transition from exponential to linear growth was also observed during multilayer formation of two weakly charged polyelectrolytes [41, 42]. The observation of the exponential-to-linear transition resulted in a new model, the three-zone model, which is no longer based on diffusion of polyelectrolytes into and out of the PEM. The behaviour of the PEM in the first zone, the zone in closest contact to the substrate, is mainly determined by the properties of the surface. Above a certain number of layers the third zone is found, in which the multilayer grows exponentially. From a certain layer number on, the film undergoes a restructuring of the bottom layers of the third zone. The zone in which this restructuring occurs is referred to as the second zone. This zone hinders the diffusion process of polyelectrolytes within the film and the film starts growing linearly [41]. Diffusion of high

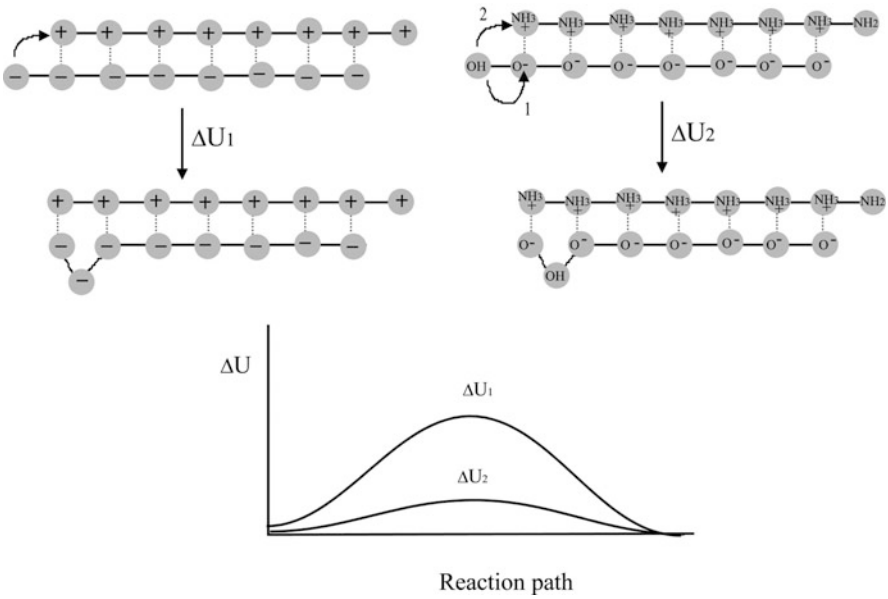


**Fig. 3** Difference in energy of breaking of polyelectrolyte exchange reactions of oppositely charged strong polyelectrolytes ($\Delta U_1$) and two oppositely charged weak polyelectrolytes ($\Delta U_2$) at low salt concentration [1]

molecular weight polymers is restricted to the upper part of the film, whereas polymers with lower molecular weights can diffuse into and through the entire film [41].

## *1.3 Influence of Ionic Strength on the Kinetics of Polyelectrolyte Complex Formation*

The ionic strength is a very important factor in determining the kinetics of polyelectrolyte complex formation. At low ionic strength, rearrangement of the initially formed aggregates towards their equilibrium structure for two strongly charged polyelectrolytes is much more hindered (in terms of activation energy) than for two weakly charged polyelectrolytes. A simple cartoon representing this process is sketched in Fig. 3. It can be seen that the energy barrier of breaking one ion pair for two strongly charged polyelectrolytes is much higher than for two weakly charged polyelectrolytes. This difference is due to the ability of protons to move from one polyelectrolyte to the other. The energy required for the rearrangement of the complex is constrained by the difference in p*K*s of the charged groups. For strong polyelectrolytes and the absence of counterions, rearrangement costs the full electrostatic energy.

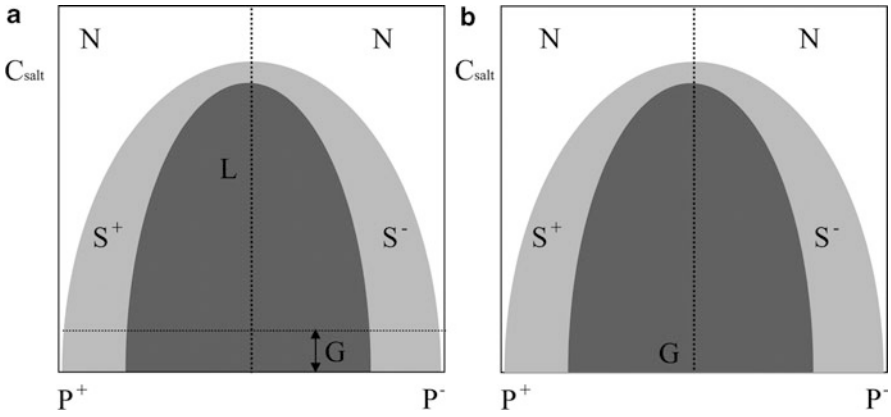


**Fig. 4** Stability diagram of polyelectrolyte complexes as a function of the ionic strength for systems where (a) $\tau \approx \tau_{exp}$ and (**b**) $\tau > \tau_{exp}$. On the *horizontal axis* is the composition of the mixture given. On the *vertical axis* is the salt concentration ($C_{salt}$). The *L* region indicates a liquid state, and the *G* region the glassy (quenched) state; *S* indicates soluble polyelectrolyte complexes. In the *N* region, no complexation occurs [1]. (**a**) is a slight modification of the diagram proposed by Kovacevic et al. [31]

Figure 4 shows schematic stability diagrams of polyelectrolyte complexes for systems where $\tau \approx \tau_{exp}$ (Fig. 4a) and systems where $\tau > \tau_{exp}$ (Fig. 4b), as function of the ionic strength. The main difference between these two stability diagrams is the appearance of a liquid phase (L). Whether a liquid phase is found in a system depends on the nature of the polyelectrolytes, i.e., weakly charged polyelectrolytes tend to form liquid-like complex phases as above a certain (low) salt concentration. In these systems, exponential growth is typically observed above a certain ionic strength. Systems containing strongly charged polyelectrolytes, which typically show linear PEM growth, form glass-like phases, although at very high salt concentration these glass-like complexes may again become liquid-like. Examples of both systems will be discussed in Sect. 2.1 on dynamic light scattering titration.

Small ions can help polyelectrolyte complexes to rearrange in the same manner as protons do (see Fig. 3) [43]. Increasing the ionic strength makes the breaking of an ion pair cheaper in terms of energy. For PEMs it has been observed that addition of salt to an existing PEM leads to more loop formation of the polyelectrolytes at the surface of the PEM, because of screening of the intermolecular repulsion in this upper layer [22]. An increase in the distance between the charged groups of the polyelectrolytes is observed, resulting in an increase in multilayer thickness at higher ionic strength. The internal structure of PEMs can be altered by increased external ionic strength. Due to the presence of additional charges at the upper layer in terms of salt, both perpendicular interdiffusion (for the absorbing polymer) and parallel interdiffusion (resulting in smoothing the surface) occurs at the multilayer surface [44].

One way to study the dynamical response of polyelectrolyte complexes and to obtain information about their relaxation time is to carry out rheological

measurements. Relaxation dynamics at different time scales have been studied by Spruijt et al. [43] on 1:1 PAA/PDMAEMA complexes with different chain lengths, the same polymers that were used to study the binodal compositions [13] (see Sect. 1 on the kinetics of polyelectrolyte complex formation). By studying the storage and loss moduli of these complexes as a function of frequency at different salt concentrations, curves having the familiar shape of a viscoelastic fluid (e.g., polymer melt or concentrated polymer solution) were obtained. In these curves, the storage and loss modulus cross at some typical frequency. At high salt concentrations, liquid-like behaviour is observed in the experimental frequency window; here, the deformations relax faster than they are typically applied. Soft-solid behaviour is observed at low salt concentrations; relaxation of the deformations occurs slower than they are typically applied. Interestingly, the salt concentration influences the absolute values of the moduli, but not the shape of the curves, which means that the rheological data can be superimposed using two salt-dependent shift-factors: the apparent relaxation time $\tau_c$ and the modulus $G_c$. Similar behaviour is found in polymer melts as function of temperature; here, the procedure of shifting the data in order to make them coincide is known as "time–temperature superposition". Hence, the polyelectrolyte complexes possess the property of "time–salt superposition". This finding suggests that the dynamics of electrostatic complexes is simple in nature. By choosing the shift factors in such a way that the rescaled frequency equals 1, the apparent relaxation time of polyelectrolyte complexes as function of the salt concentration and ionic strength can be estimated.

A decrease in salt concentration results in a slightly more than exponential increase in relaxation time. The two longest polymers show an even stronger increase in relaxation time at low salt concentration. For common polymers, the divergence of the relaxation time at low temperatures indicates the glass transition of the system. Polyelectrolyte complexes at low salt also undergo a glass transition (see Fig. 4) and become kinetically quenched.

## *1.4 Entropy, Enthalpy and Free Energy*

It has also been observed that certain systems show different growth behaviour as function of the temperature [45, 46]. Exponentially growing multilayers are more sensitive to changes in temperature than linearly growing systems. To gain more insight into this phenomenon, Laugel et al. [47] performed isothermic titration calorimetry (ITC) to study the entropy ($\Delta_f S$) and enthalpy ($\Delta_f H$) of polyelectrolyte complex formation. They made an important discovery: the sign of the enthalpy correlates with the growth behaviour of PEMs. A negative $\Delta_f H$, indicating an exothermic process, is found in cases of linear growth. Addition of salt results in a $\Delta_f H$ of around zero (slightly negative or positive). Endothermic processes (positive $\Delta_f H$) are observed for systems that typically show exponential growth, e.g., polyelectrolyte complex formation of two weakly charged polyelectrolytes above an ionic strength of 150 mM. Similar results were obtained by means of

differential scanning calorimetry [48]. Apparently, the ability of complexes to rearrange correlates strongly to the sign of $\Delta_f H$.

Also, simulations have been used to study the entropy and enthalpy of polyelectrolyte complex formation. Ou and Muthukumar used Langevin dynamics simulations to study the thermodynamic properties of polyelectrolyte complexation [49]. They studied both strongly and weakly interacting polyelectrolytes at low and high salt concentrations. As function of the ionic strength, they found that the enthalpy of polyelectrolyte complex formation is reduced due to screening of the charges within the system. The entropy of the counterion release also decreases in the presence of salt. This reduction in entropy is more significant for strongly interacting systems than for weakly interacting systems.

Let us now try to sketch the behaviour of the enthalpy, entropy and free energy ($\Delta_f G$) as a function of the salt concentration. Upon increasing the ionic strength, a change from exothermic to endothermic behaviour is observed. This means that at low ionic strength the complex formation is enthalpically favourable, but it becomes entropically driven when the salt concentration is increased. This may be explained considering the following reaction:

$$P^+P^- + A^+B^- \leftrightarrows P^+B^- + P^-A^+ \tag{1}$$

Here $P^+$ and $P^-$ refer to the different polyelectrolytes and $A^+$ and $B^-$ to the simple salt ions. Increasing numbers of simple ions in the system will screen the electrostatic repulsion between the polyelectrolyte layers, shifting the equilibrium to the right and resulting in a less compact structure [22]. Eventually, the result will be an increased mobility of the polyelectrolytes within the PEM or polyelectrolyte complexes.

In Fig. 5, a qualitative picture of the thermodynamic properties $\Delta_f H$, $\Delta_f G$ and $\Delta_f S$ of polyelectrolyte complex formation is sketched as a function of the salt concentration. As discussed before (see Fig. 1), at low ionic strength the counterion release leads to large positive $\Delta_f S$, and thus $-T\Delta_f S$ is strongly negative (where $T$ is temperature). With increasing ionic strength, the contribution to the entropy becomes smaller because of the presence of small ions in the system. In Fig. 5, $-T\Delta_f S$ is sketched for increasing salt concentration. Its contribution remains negative over the entire salt range.

The change in potential energy associated with interionic distances ($r_{ij}$) is reflected in $\Delta_f H$:

$$\Delta_f H = \Delta_f \left( \sum_{ij} \frac{e^2}{4\pi\varepsilon r_{ij}} \right) \tag{2}$$

Here, $e$ is the charge, $r_{ij}$ is the interionic distance between opposite charges and $\varepsilon$ is the dielectric constant. The value of $\Delta_f H$ is negative at low salt concentration due to the tightness of ion pairs within the complex and the large Debye length, which implies a loose counterion cloud around the original polyelectrolytes.

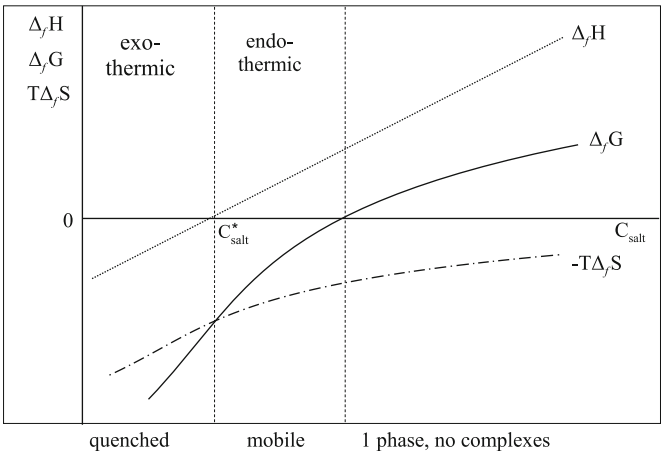


**Fig. 5** $\Delta_f H$, $\Delta_f G$ and $\Delta_f S$ of polyelectrolyte complex formation as functions of the salt concentration. Reprinted from [50] with permission. Copyright 2009, American Chemical Society

The ion pairs become less tight when the ionic strength is increased, due to screening of the charges, whereby the Debye length decreases and the counterion clouds become more compact. Both effects together cause $\Delta_f H$ to increase and eventually become positive. Hence, there is an athermal ionic strength, $C^*_{salt}$. Because $\Delta_f G = \Delta_f H - T\Delta_f S$, the trend of the free energy upon increasing ionic strength is also upward, crossing the zero axis at a salt concentration higher than the athermal point.

The influence of the pH on polyelectrolyte complex formation can be explained in a similar way, the only difference being that now protons fulfil the role of salt ions. In water, protons will be present and it is known that water is present in polyelectrolyte complexes [8, 51–56]. The reaction that occurs as function of the pH is:

$$PH^+ PO^- \leftrightarrows P + POH \tag{3}$$

where $PH^+$/P is the polybase pair and $PO^-$/POH is the polyacid pair.

It is difficult to make a simple sketch of the behaviour of $\Delta_f H$, $\Delta_f G$ and $\Delta_f S$ for weakly charged polyelectrolytes. At either low or high pH one of them will be fully charged (see Fig. 2). Moreover, weakly charged polyelectrolytes can mutually influence their dissociation behaviour (this will be explained in more detail in Sect. 2.1.1) and therefore their charge densities [30, 35–38].

The measurements by Laugel et al. on the complex formation between two weakly charged polyelectrolytes were performed at the isoprotic point [47]. It has already been discussed that under these conditions and at low ionic strength two weakly charged polyelectrolytes will act as two fully charged polyelectrolytes. At other pH values, it is difficult to predict the behaviour of $\Delta_f H$ and $\Delta_f S$ because they will be a function of the pH and a graphical representation of $\Delta_f H$, $\Delta_f G$ and $\Delta_f S$ would require an additional pH axis.

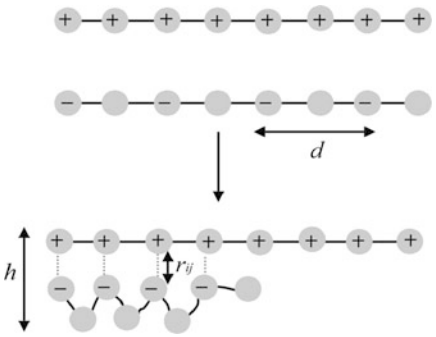


**Fig. 6** Distances that dictate the relaxation behaviour of polyelectrolyte complexes: $d$ is the distance between the charges on the polymer, $r_{ij}$ is the distance between the opposite charges on the two polyelectrolytes within the complex and $h$ is the total thickness of the stoichiometric polyelectrolyte complex [1]

There are three distances that are important for the ability of the polymers to rearrange within the complex. These distances are shown in Fig. 6. In this figure, $d$ indicates the distance between the like charges on the polymer (i.e. the charge density). For weakly charged polymers $d$ can be altered by changing the pH. $r_{ij}$ is the distance between the two oppositely charges within the complex. Both $d$ and $r_{ij}$ will affect the distance $h$, which indicates the density of the stoichiometric complex. When $d$ and $r_{ij}$ are small, $h$ is small and rearrangement of the polyelectrolytes within the complex becomes difficult. In this case, glass-like structures are likely be formed and $De \gg 1$. The enthalpy of complex formation ($\Delta_f H$) is negative, indicating an exothermic process. When the charge density is low and the distance between the opposite charges is large, $h$ is large and it becomes easier for the polyelectrolytes to rearrange. In this case, $De \approx 1$ and the polyelectrolyte complex formation is an endothermic process.

## 2 Experimental Techniques

### *2.1 Dynamic Light Scattering Titrations*

One way to study polyelectrolyte complex formation in solution is using dynamic light scattering (DLS) titrations on micelle-forming systems. Here, a solution of polyelectrolytes is titrated to a solution of oppositely charged polyelectrolytes, at least one of the polyelectrolytes should have a neutral hydrophilic block, and after every addition the intensity and hydrodynamic radius are measured. When a pH electrode is fitted into the measuring cell, the pH can be followed during the titration. In this titration, nanoparticles will be formed (instead of insoluble polyelectrolyte complexes) with a polyelectrolyte core and a neutral corona.

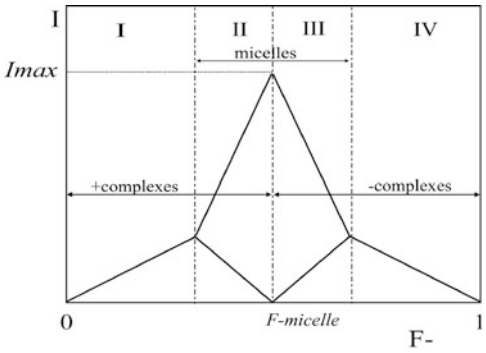


**Fig. 7** Light scattering intensity ($I$) as a function of the composition ($F^-$) for polyelectrolyte complex micelle formation. See text for a description of regions I–IV. Reprinted from [50] with permission. Copyright 2009, American Chemical Society

These particles are called by several names in literature: block ionomer complexes [57], polyion complex micelles [58], complex coacervate core micelles [59] and polyelectrolyte complex micelles. An extensive review of this type of micelle has been written by Voets et al. [60].

During a light scattering titration, the scattered intensity can be studied as function of the composition ($F^-$):

$$F^- = 1 - F^+ = \frac{[n_-]}{[n_-] + [n_+]} \tag{4}$$

Plots of light scattering intensity ($I/C$) versus $F^-$ (where $I/C$ is the light scattering normalised with respect to the polymer concentration) were first reported and discussed by Van der Burgh et al. [61]. For the systems they studied, a symmetrical pattern consisting of four regions (I–IV) was found. This is schematically shown in Fig. 7. Starting at $F^- = 0$ (having only positively charged polyelectrolytes in solution), a slight increase in intensity is seen first upon the addition of titrant (I). This increase is thought to reflect the formation of small soluble complexes having a positive charge.

At a certain composition the slope ($I/C$) becomes more pronounced. At this point, the polyelectrolyte complex micelles start to form (II). Their mass is considerably larger than that of the soluble complexes, with a more pronounced increase in scattering intensity as a result. A maximum in scattering intensity is found at $F^- \approx 0.5$, where the system is electroneutral and the mass of the particles is maximal. This composition will be referred to as $F^-_{\text{micelle}}$. Addition of more negatively charged macromolecules to the system leads to the disintegration of the polyelectrolyte complex micelles, giving a similar (but negative) slope on $I(F^-)$ as before the formation of the micelles (III). After disintegration of the micelles, the slope becomes less pronounced and the solution once again contains soluble complexes, now with negative charge (IV).

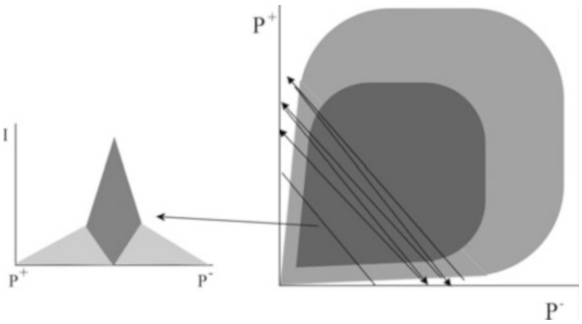


**Fig. 8** Phase diagram of polyelectrolyte complex formation (*right*) and its relation to an $I(F^-)$ plot (*left*). The *dark grey areas* indicate stoichiometric complexes; the *light grey areas* indicate soluble complexes. The *arrows* indicate "walking through" the phase diagram when multilayers are prepared (slightly exaggerated)

The main difference between light scattering composition titrations as shown here and PEM formation is the number of times a system goes through the phase diagram. This is schematically illustrated in Fig. 8. In Fig. 8, the phase diagram of two polyelectrolytes $P^+$ and $P^-$ is presented together with an $I(F^-)$ plot. During a light scattering titration, polymers with one charge are titrated to polymers with opposite charge and the system moves through the phase diagram once. In the case of multilayer formation, the surface is exposed to one type of polyelectrolyte, then the surface is rinsed with solvent to remove the excess material. Subsequently, the surface is exposed to a solution containing polyelectrolytes with the opposite charge. This process is repeated until the desired number of layers is achieved. So, during multilayer build-up the system passes through the phase diagram several times. Of course an important requirement for multilayer formation is that the relaxation time of the system is longer than the experimental time scale, otherwise the PEM will dissolve and soluble complexes in solution will form.

### 2.1.1 pH During Light Scattering Titrations

Figure 9 shows the results of a light scattering titration where a solution containing the positively charged homopolymer $PDMAEMA_{150}$ is titrated into a solution containing poly(acrylic acid)-*block*-poly(acryl amide) ($PAA_{42}$-$PAAm_{417}$). The plot of I versus $F^-$ presented in Fig. 9a is very similar to the scheme shown in Fig. 7. The hydrodynamic radius ($R_h$) as function of the composition $F^-$ is shown in Fig. 9b. This radius can only be measured in the composition range at which micelles are present in the system. No accurate measurements of the hydrodynamic radius of the soluble complexes can be made.

The pH as function of $F^-$ is presented in Fig. 9c. The pH is not constant during the titration, although it has the same value at $F^- = 0$, $F^- = F^-_{\text{micelle}}$, and $F^- = 1$. Between these points, the proton concentration changes during the titration.

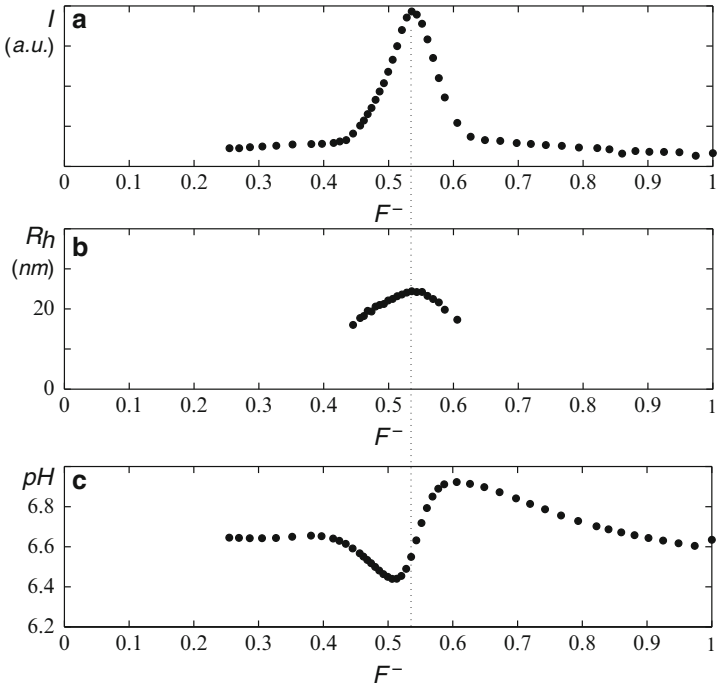


**Fig. 9** Light scattering titrations of complex coacervate core micelles made of diblock copolymer and homopolymer: (**a**) intensity versus composition, (**b**) hydrodynamic radius versus composition and (**c**) pH versus composition. Raw data were provided by Hofs et al. [48]. Reprinted from [62] with permission. Copyright 2007, American Chemical Society

This change is due to proton uptake or release by the macromolecules involved in the complexation process. This kind of curve will be found when the pH at which the complexation process is studied lies between the p$K$s of the different polyelectrolytes (i.e., in the isoprotic point, see Fig. 2).

In this system, the components are weak polyelectrolytes and have a charge that varies with pH. The degree of ionisation, $\alpha$, of these groups can be expressed [63] as:

$$\alpha_{\pm} = \frac{1}{1 + 10^{((\mathrm{pH} - \mathrm{p}K_0 + e\psi)/kT)}} \tag{5}$$

where pH is the measured pH, p$K_0$ is the intrinsic p$K$ value of the ionisable groups of the macromolecule, $\psi$ is the electrostatic potential, $k$ is the Boltzmann constant and $T$ is the temperature.

Let us first discuss the extremes of the titration curve ($F^- = 0$ and $F^- = 1$). When a positively charged macromolecule is introduced into a solution containing mainly negatively charged macromolecules ($F^- = 1$), an increase in pH is observed (Fig. 9c). Because the macromolecule experiences a negative potential (5), this favours proton uptake by the polycation while protons are released by the polyanion

because of the positive potential of the polycations. The measured increase in pH indicates that the former effect dominates. At the other extreme of the titration curve, when a negatively charged macromolecule is introduced into a solution of positively charged macromolecules ($F^- = 0$), the opposite effect is seen. Proton release dominates and the bulk pH decreases.

In the intermediate regime, in the region where polyelectrolyte complex micelles are present in the system, the increasing and decreasing extremes are connected by a curve that crosses the initial pH value. The slope of the curve is steepest at $F^-_{\text{micelle}}$, which is also the "isoelectric point" of the complex. Here, the number of positive charges and negative charges at this composition are the same. Depending on the potential, the negatively charged groups deprotonate, and the positively charged groups protonate. The net effect depends on the differences between the pH and the p$K$ values of the charged groups of the macromolecules. For two isolated oppositely charged species, the effect is exactly symmetric for pH values halfway between the two p$K$s. In that case, the extra protonation of the positive species cancels deprotonation of the negative species and the pH will stay the same. Hence, for a symmetric system, at $\text{pH} = \frac{1}{2}(\text{p}K_{\text{anion}} + \text{p}K_{\text{cation}})$, one would expect the pH to be the same at $F^- = 0$, $F^- = 0.5$, and $F^- = 1$. At pH values that are not the average of the p$K$s of the system, the pH curve of a titration experiment can be totally different, but in all cases at $F^-_{\text{micelle}}$ the slope of the curve is the steepest because the buffering capacity of the system, which comes from free, uncomplexed polyelectrolyte, has a minimum in this point.

### 2.1.2 Polyelectrolyte Complex Micelles with Protein Molecules

In the previous section, the polyelectrolyte complex micelle formation of anionic diblock copolymers and cationic homopolymers was discussed. A simple way to obtain micelles filled with protein molecules is to replace the cationic homopolymer with positively charged protein molecules. Harada and Kataoka were the first to apply this procedure [64]. They formed protein-filled micelles by mixing lysozyme and poly(ethylene glycol)–poly(aspartic acid) block copolymers.

Polyelectrolyte complex micelles consisting of protein molecules and diblock copolymers only, contain thousands of protein molecules. One would expect that when used as nanoreactors, not all the protein molecules would be accessible to the substrate molecules. A way to down-regulate the number of protein molecules inside the polyelectrolyte complex micelles is by diluting them with like-charged homopolymers. Using this procedure it was found that an excess of homopolymer leads to the formation of stable micelles with protein molecules in the core [62]. Protein-filled micelles consisting of like-charged diblock copolymers together with protein molecules and homopolymers of opposite charge were unstable because of macroscopic complex formation between the homopolymer and protein molecules [1].

By making use of three components, the way the components are mixed may become important. Two different systems, one for incorporating negatively charged

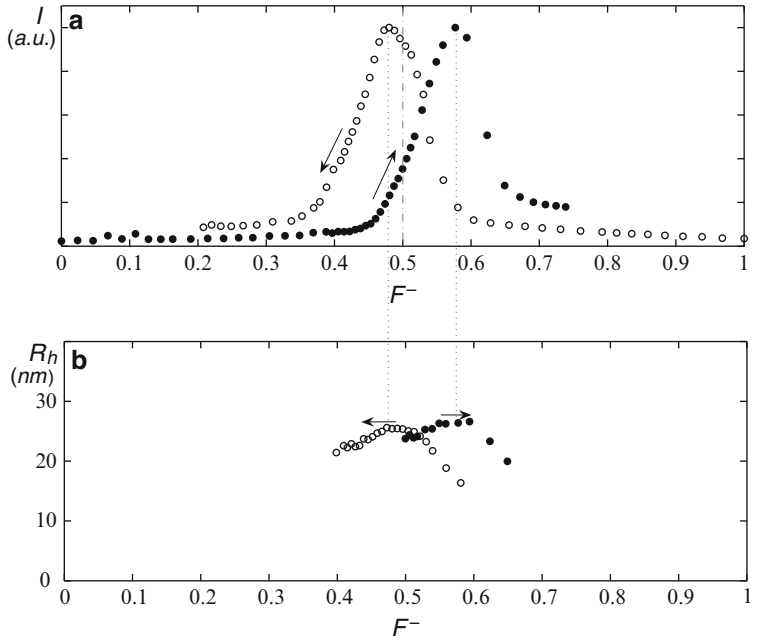


**Fig. 10** Composition titrations of system A: (**a**) $I(F^-)$ and (**b**) $R_h(F^-)$. *Solid circles* titrant is $PAA_{42}$-$PAAm_{417}$; *open circles* titrant is mixture of $PDMAEMA_{150}$ and lysozyme. The pH was fixed at 7 using a phosphate buffer. *Arrows* indicate the direction of the titration. Reprinted from [50] with permission. Copyright 2009, American Chemical Society

protein molecules (system B) and one for incorporating positively charged protein molecules (system A), were investigated to assess whether the order of mixing was important. These systems were $PAA_{42}$-$PAAm_{417}$, $PDMAEMA_{150}$ and lysozyme and $PAA_{139}$ (system A), and α-lactalbumin and quarternised poly(2-vinyl pyridinium)$_{41}$-*block*-poly(ethylene oxide)$_{205}$ ($P2MVP_{41}$-$PEO_{205}$) (system B). The two protein molecules lysozyme and α-lactalbumin are similar in size but oppositely charged at pH 7 [65]. The pH during these measurements was fixed at 7 using a phosphate buffer [50]. First, light scattering titrations were performed, starting at $F^- = 0$ and $F^- = 1$ (4). The results of these light scattering titrations [$I(F^-)$ and $R_h(F^-)$ ] are presented in Figs. 10 and 11.

One can directly see that the shapes of $I(F^-)$ are very different for the two systems. The shape of the $I(F^-)$ curves in Fig. 10 for system A strongly resemble the $I(F^-)$ curves presented in Fig. 9. This is no surprise because the same homopolymer and diblock copolymer were used. There is, however, a difference in the position of the maximum light scattering intensity.

$I(F^-)$ for system B, containing the negatively charged protein molecule (Fig. 11a, b), is not symmetrical, unlike the $I(F^-)$ of Fig. 10 and the schematic representation of $I(F^-)$ proposed by Van der Burgh et al. [61]. Interestingly, an

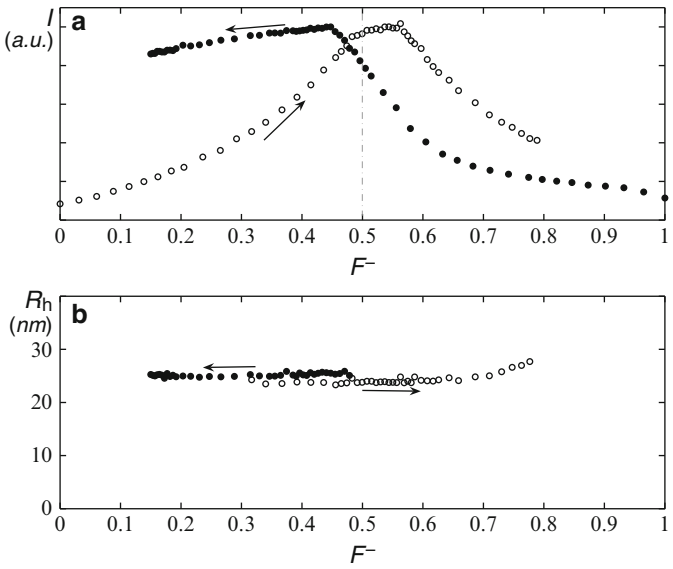


**Fig. 11** Composition titrations of system B: (**a**) $I(F^-)$ and (**b**) $R_h(F^-)$. *Open circles* titrant is a mixture of $PAA_{139}$ and α-lactalbumin; *solid circles* titrant is $P2MVP_{41}$-$PEO_{205}$ The pH was fixed at 7 using a phosphate buffer. *Arrows* indicate the direction of the titration. Reprinted from [50] with permission. Copyright 2009 American Chemical Society

accurate hydrodynamic radius (Fig. 11b) can be measured over a much broader composition interval than was found for system A (Fig 10b).

The second experiment that was performed consisted of mixing the three components (diblock copolymer solution, homopolymer solution and protein solution) in three different ways, and following the light scattering intensity and hydrodynamic radius as a function of time [50]. For system A, it was found that, independently of the way of mixing, the same light scattering intensity and hydrodynamic radius were found after 1 day. For system B, the intensity remained different for different preparation methods over a period of at least 10 days. The hydrodynamic radius remained the same from the start of the experiment.

These two measurements suggest that system A is not in full equilibrium during the light scattering titration, because the $I_{max}$ is different starting at $F^- = 0$ and $F^- = 1$, but the symmetry of $I(F^-)$ suggests that the complex formation is reversible: first soluble complexes are formed, then micelles, these micelles can disintegrate again into soluble complexes with an opposite charge to the complexes formed before the micelle formation. During the time-dependent measurements this system reached equilibrium in about a day. In contrast, the measurements on system B show that the complex formation was not reversible and that no equilibrium was obtained in about 10 days.

As discussed for PEM formation, where differences in kinetics of the systems show up as differences in growth rate, for polyelectrolyte complex formation in

solution the differences in kinetics show up as differences in reversibility of the polyelectrolyte complex formation. The lysozyme-containing micelles (system A) fall into the second kinetics category ($De \approx 1$) where relaxation phenomena are observed during the experiment. Therefore, the maximum intensity is dependent on the direction of the titration (see Fig. 10). By increasing the waiting time after each addition, the position of the maximum intensity becomes independent of the direction of the titration.

The α-lactalbumin-containing system (system B) belongs to the kinetically quenched category where $De \gg 1$. In this system, the polyelectrolytes do not rearrange or there is only little rearrangement of the polyelectrolytes within the micelles. If two oppositely charged polymers come into contact they stick. It is plausible that micelles that were formed starting at $F^- = 0$ are different from micelles that are formed starting at $F^- = 1$. The micelle formation is not reversible, therefore micelles are found at a much wider composition interval than for system A.

The reason why these two systems show different kinetics is probably that the lysozyme-containing system consists of two weakly charged polyelectrolytes (PAA and PDMAEMA), whereas the α-lactalbumin-containing system consists of the weakly charged homopolymer (PAA) and a strongly charged (quartenised) cationic polymer (P2MVP).

Differences between these two systems also are found when studying their salt-induced disintegration [51, 66]. This salt-induced disintegration can again be studied using light scattering titrations. In this case, a micellar solution is prepared into which a salt solution is titrated. The intensity and hydrodynamic radius can then be studied as function of the salt concentration.

In Fig. 12, the light scattering titrations with salt for system A, system B and micelles without incorporated lysozyme molecules (i.e., containing only the diblock copolymer and homopolymer) are presented. The $I(C_{\text{salt}})$ of system A first shows a gradual decrease in light scattering intensity (see Fig. 12), then the intensity levels off and a small plateau is found. The hydrodynamic radius decreases in the ionic strength interval at which $I(C_{\text{salt}})$ decreases. An increase in hydrodynamic radius is observed at the salt interval where the plateau is observed. For micelles without lysozyme, the hydrodynamic radius becomes too inaccurate to measure at this salt range. Above a certain salt concentration, the intensity starts decreasing again until the polyelectrolyte complexes disintegrate [66]. An explanation why this plateau is observed in the $I(C_{\text{salt}})$ plot may be that the critical salt concentration of polyelectrolyte complex formation is approached [67]. This behaviour has been observed not only with increasing salt concentration, but also with decreasing salt concentration [68].

Similar behaviour was also observed for PEMs. For two weakly charged polyelectrolytes at $\text{pH} = \frac{1}{2}(\text{p}K_{\text{anion}} + \text{p}K_{\text{cation}})$, the growth regime switches from linear to exponential upon a small increase in salt concentration; larger increases in the ionic strength may result in dissolution of the PEM and formation of whole polyelectrolyte complexes in solution [31]. In the pH regime where one of the polyelectrolytes is almost fully charged and the other partly charged, an increased

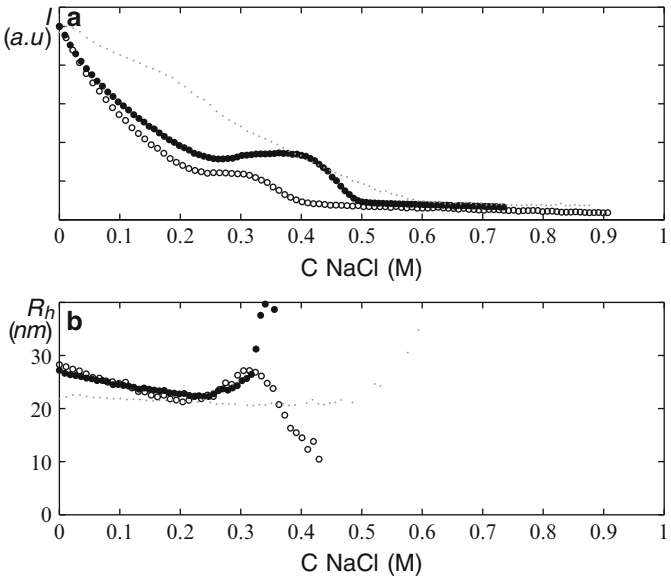


**Fig. 12** (**a**) Light scattering intensity ($I$) and (**b**) hydrodynamic radius ($R_h$) as a function of salt concentration for lysozyme-filled micelles (*open circles*) and normal micelles (*solid circles*). Only radii having a standard deviation of less than 1 nm are shown. *Light grey dots* are the results for the salt titration of the lipase-filled micelles consisting of $P2MVP_{41}$-$PEO_{204}$. The concentration of micelles was 1 g $L^{-1}$ and the starting volume was 9 mL. Reprinted from [66] with permission. Copyright 2009 American Chemical Society

salt concentration favours the formation of polyelectrolyte complexes in solution and no PEM formation is observed.

The polyelectrolyte complex micelles of system B in these DLS titrations with salt contained the enzyme lipase [51]. This protein molecule is also negatively charged at pH 7, but has about twice the size of α-lactalbumin and was chosen because we were interested in the effect on the enzymatic activity of lipase when incorporated into these micelles [69]. The light scattering intensity of this system shows a gradual decrease as a function of the ionic strength, until all the micelles are disintegrated and the intensity becomes constant [51]. The $I(C_{salt})$ for system B can also be seen in Fig. 13. The hydrodynamic radius remains constant during the titration, until all the micelles are disintegrated.

Both the lysozyme- and lipase-containing systems were studied by small angle neutron scattering (SANS) experiments as a function of the salt concentration. For the lipase-containing system (system B), both the light and neutron scattering intensity decreased as a function of the salt concentration, as can be seen in Fig. 13. The hydrodynamic radius was constant throughout the light scattering titration, but the size of the micelles determined using neutron scattering decreased as a function of the ionic strength. The contrast between the corona of the micelles and the solvent in neutron scattering is very low, so this technique gives information

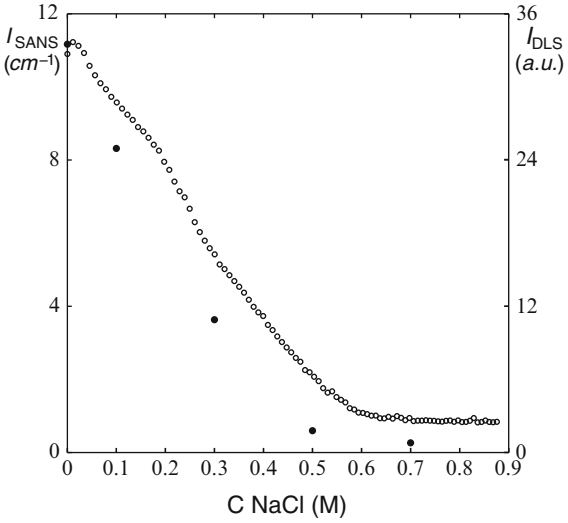


**Fig. 13** Neutron scattering intensity ($I_{SANS}$, *solid circles*) and light scattering intensity ($I_{DLS}$, *open circles*) as a function of the salt concentration ($C$) [51]. Reproduced by permission of The Royal Society of Chemistry

about the core of the micelles. An explanation for the decrease in core size and the decrease in intensity is that the mass of the micelles becomes smaller, most probably caused by the release of lipase molecules [51]. By assuming that the lipase molecules are released before the micelles disintegrate, it was found that at a salt concentration of 0.15 M all the lipase molecules were released.

For the system A, both $I(C_{salt})$ and $R_h(C_{salt})$ decrease from 0 to 0.2 M NaCl (see Fig. 12). This is an indication of rearrangement of the micelles. Because the electrostatic interactions between the negatively charged diblock copolymers and the (positively charged) lysozyme molecules are weak, one would expect that the enzymes are no longer incorporated above $C_{salt} = 0.12$ [62]. The plateau in the light scattering intensity between $C_{salt} = 0.2$ and 0.4 M (see Fig. 12), which is found for both the micelles with and without lysozyme, most probably indicates the presence of complexes between the positively charged homopolymer and negatively charged diblock copolymer.

Self-consistent field calculations have been used to study the free energy of interaction between protein molecules and the micelle. The electrostatic attractions in this case were modelled by nearest-neighbour interactions using a Flory–Huggins interaction parameter $\chi$. In this study, a molten globule protein structure mimicking lysozyme was constructed using the amino acid sequence of lysozyme. Each amino acid was approximated by being either hydrophobic, hydrophilic, negatively or positively charged [70]. This lysozyme-like object was placed in a two-gradient cylindrical coordinate system of which the micellar core formed the centre. The free energy of interaction between the micelle and the lysozyme-like structure was

**Table 1** Abbreviations for polymers discussed in this chapter

| Abbreviation | Full name | + or − |
|---|---|---|
| PAA | Poly(acrylic acid) | Anionic |
| PDMAEMA | Poly[2-(*N*,*N*-dimethyl amino)-ethyl methacrylate] | Cationic |
| $PAA_n$-$PAAm_m$ | Poly(acrylic acid)$_n$-*block*-poly(acryl amide)$_m$ | Anionic |
| PEG-P(Asp) | poly(ethylene glycol)-*block*-poly(aspartic acid) | Anionic |
| $P2MVP_n$-$PEO_m$ | Poly(2-vinyl pyridinium)$_m$-*block*-poly(ethylene oxide)$_m$ | Cationic |
| PLL | Poly(L-lysine) | Cationic |
| HA | Sodium hyaluronate | Anionic |
| PGA | Poly(sodium-L-glutamate) | Anionic |
| PAH | Poly(allylamine hydrochloride) | Cationic |
| PSS | Poly(sodium-4-styrene sulfonate) | Anionic |
| PDADMAC | Poly(diallydimethylammonium chloride) | Cationic |
| PEI | Poly(ethylene imine) | Cationic |
| PTMEAMA | Poly[2-(*N*,*N*,*N*-trimethyl amino)-ethyl methacrylate] | Cationic |
| PSPMA | Poly(3-sulfopropyl methacrylate) | Anionic |

calculated at different positions from the centre of the micelle. A minimum in the free energy was found at the core–corona interface and a maximum was found in the centre of the micellar core [70].

For both systems A and B it was found that the protein molecules are released from the micelles before the entire micelles disintegrate. An explanation for this behaviour is that the charge density of the protein molecules is much lower than the charge density of the polyelectrolytes, making the interactions between the protein molecules and the oppositely charged diblock copolymer much weaker than the interactions between the diblock copolymer and oppositely charged polyelectrolyte. Moreover, the protein molecules used were globular proteins, having a distinct 3D structure; this further hinders rearrangement of the protein molecules within the polyelectrolyte complex.

### 2.1.3 Turbidity

A procedure simpler than performing light scattering titrations is studying the correlation between multilayer growth and polyelectrolyte complexes in solution using turbidity measurements. Mjamed et al. studied turbidity as function of the mixing ratio and NaCl concentration of six different polyelectrolyte combinations (PLL/HA, PLL/PGA, PAH/PGA, PLL/PSS, PAH/PSS and PDAD-MAC/PSS) [71] (see Table 1 for list of abbreviations). A maximum in turbidity was found at mixing ratio of 1, which compares to $F^{-}_{\text{micelle}}$ in Fig. 7. Two different behaviours as function of the ionic strength were found. Depending on the chosen pair, the turbidity versus NaCl and the multilayer deposition as function of NaCl showed either a maximum or no maximum. Systems containing (weak) carboxylate as anion showed maxima, systems containing the strong PSS showed no maximum between an ionic strength

of 0.1 and 5 M, indicating that the complexes are still intact at 5 M NaCl. This indicates that the interaction strength between the polyelectrolytes is important for their behaviour in solution.

## 2.2 Force Measurements

Direct interactions between polyelectrolyte complexes can be studied using atomic force microscopy (AFM). When a colloidal probe coated with one type of polyelectrolyte is glued to a cantilever, the force measured as function of the distance to a surface coated with the oppositely charged polyelectrolytes can be measured. These force–distance curves give insight into the interactions between the oppositely charged molecules. This method has been used by Spruijt and coworkers. A colloidal probe was coated with an negatively charged polymer brush and its interactions with a positively charged brush attached to a flat silica surface were studied [72]. To study the forces between these two surfaces it is necessary to start at a high salt concentration (2–3 M) and gradually reduce the ionic strength. At low salt, the attractive force is too strong and separation of the two surfaces is impossible, i.e., the glue joint between the colloidal probe and the cantilever breaks when one tries to pull the surfaces apart. At 2–3 M salt, no attractive force is measured upon approach, and a weak adhesion force (0.1–1 nN) is measured upon separating the surfaces. Apart from an attractive force, a repulsive force due to compression of the polymers brushes is first measured at distances smaller than 50 nm [72]. An attractive force in both the approach and separation curve is measured at a salt concentration of 1.4 M. At this ionic strength no repulsive force is measured.

Some hysteresis in the force–distance curves is found due to slow processes occurring when the two surfaces are brought into contact (see Fig. 14). When the oppositely charged brushes come into contact, a thin polyelectrolyte complex layer is formed. Initially the brushes are compressed on both sides of this layer, but at a certain stage of the approach interpenetration of the polymer brushes takes place, resulting in growth of the polyelectrolyte complex phase. To separate the surfaces again, the chains have to be stretched until enough energy is stored to disrupt the complex phase. Once a few ion pairs are disrupted, this force is transferred to the remaining pairs until the whole complex has disintegrated and the brushes are completely separated. Now relaxation of the individual polymer chains occurs. Because relaxation takes place at a finite rate, the force–distance curve measured is dependent on the scan rate. An illustration of this process can be found in Fig. 14. At very low scan rates the approach and separation curve become almost identical, indicating a near-equilibrium process. From the hysteresis in the free force–distance curves, the true free energy of ion pairing can be derived using a kinetic model [72]. This model shows that ion pair formation and disintegration of the polyelectrolyte complex take place in a zipper-like fashion.

Johansson et al. performed AFM and surface force apparatus (SFA) measurements on PEMs. For the force measurements, the colloidal probe and the surface were both

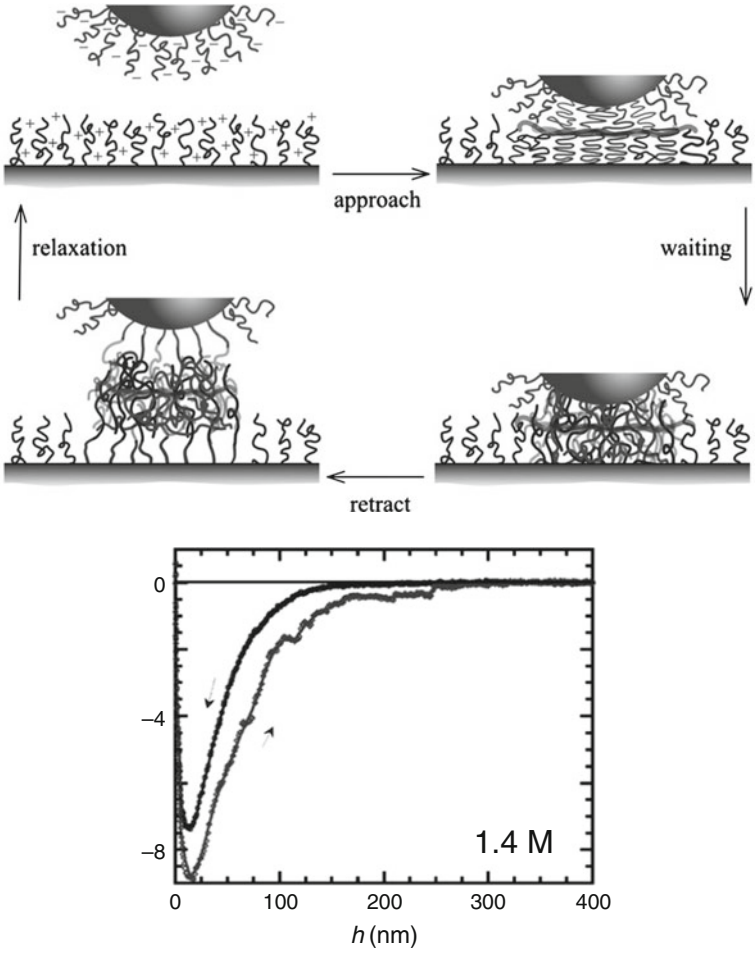


**Fig. 14** *Above*: interactions between oppositely charged polymer brushes during an AFM measurement. *Below*: force–distance curves between a surface covered with a PTMEAMA brush and a surface covered with a PSPMA brush at $C_{KCl} = 1.4$ M. Reprinted from [72] with permission. Copyright 2010, American Chemical Society

coated with PEM. Strong adhesive forces were found for large molecular contact areas, especially when the substrate was soft and when molecules can migrate across the interface, increasing the number of entanglements [73]. They found a polymer-dependent behaviour and, apparently, the degree of entanglements is determined by the chemistry of the polymer. Similar behaviour for the dissolution of PEMS was also found by Kovacevic and coworkers [31]. A chain length dependence of adhesive forces was also found whereby the adhesive forces for shorter polymers were higher [73]. This behaviour was explained by the argument that because the chain ends are more mobile than polymer loops, they could more easily form entanglements between the layers. Other studies, however, have found stronger adhesive forces

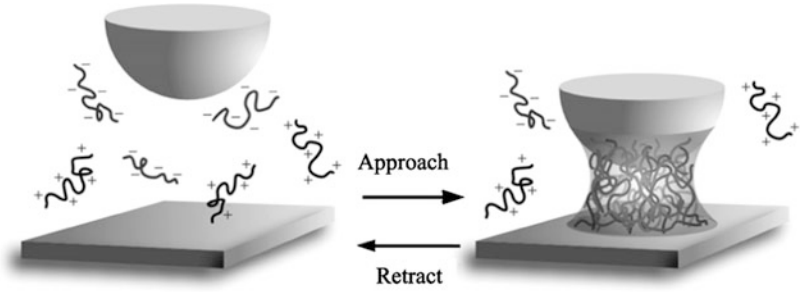


**Fig. 15** AFM measurement in which the interfacial tension of a polyelectrolyte complex is measured [75, 78]

for high molecular weight polymers [74]. This difference in observations is probably due to differences in experimental time scale. A longer equilibration time was used for the latter study, whereas the system of Johansson et al. was most probably not in equilibrium at the time scale of the measurements [73].

Force measurements can also be used to measure the interfacial tension between a polyelectrolyte complex and its coexisting phase [75] (Fig. 15). De Ruijter and Bungenberg de Jong tried to measure the interfacial tension of a polyelectrolyte phase and its coexisting phase using a capillary rise method and found interfacial tensions of ≈1 μN/M for an arabic gum and gelatin or whey protein system [76]. The accuracy of this method depends on the contrast between the polymer-rich and polymer-dense phase. Using a colloidal probe AFM method [77] on a polyelectrolyte complex consisting of two strong polyelectrolytes, Spruijt et. al. found an interfacial tension of ≈100 μN/M, which decreased with increasing ionic strength and became zero at the critical salt concentration for the system. At low salt, the kinetics is very slow, because almost all the polymers are present in the complex and there are very few present in the coexisting phase for polyelectrolyte exchange reactions. A critical scaling of the interfacial tension as function of the ionic strength was found, which was in agreement with the Voorn–Overbeek mean-field model for polyelectrolyte complex formation [14].

## *2.3 Rheology*

As has already been discussed, rheology is a powerful tool for studying the dynamical response of polyelectrolyte systems [43]. This experimental technique was also used to study transient networks of interconnected polyelectrolyte complex micelles [68, 79, 80]. These networks are formed by triblock copolymers having two like-charged end blocks, a neutral hydrophilic middle block and oppositely charged homopolymers. For low concentrations of these systems at $F^- = 0.5$, flower-like micelles are formed; the core of these micelles consists of the homopolymer and both charged end blocks of the triblock copolymer. Above a

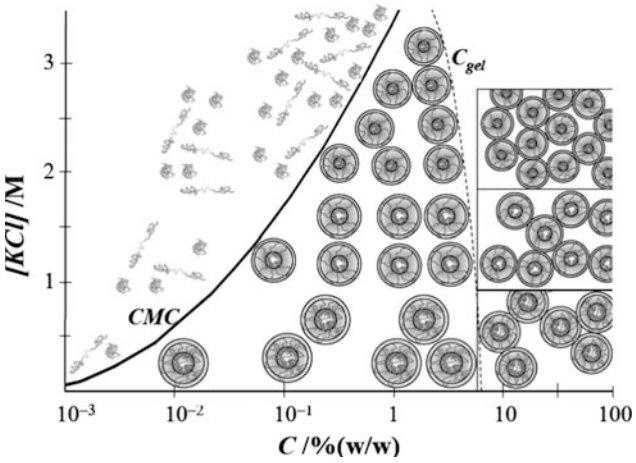


**Fig. 16** Phase diagram for stoichiometric polyelectrolyte complex formation of charged triblock copolymers and oppositely charged homopolymers. On the *horizontal axis* the polymer concentration is shown and the salt concentration can be found on the *vertical axis*. Flower-like micelles form above the critical micelle concentration (CMC). The aggregation number of these micelles is dependent on the ionic strength. The flower-like micelles become interconnected above the gel concentration ($C_{gel}$). The spacing between the micelles within the gel is independent of the salt concentration [68]. Reproduced by permission of The Royal Society of Chemistry

certain concentration, networks of micelles will form due to bridge formation between the micelles, whereby a triblock copolymer links two micelles together. These networks are macroscopic gels with visco-elastic properties. Increasing the ionic strength in these systems results in a decrease in aggregation number of the micelles. Simultaneously, there is an increases in the number density of the micelles. Because these two effects compensate each other, the number of bridges between the micelles remains equal at all salt concentrations and, therefore, the elastic response of these gels is virtually independent of the salt concentration [68]. A schematic representation of the phase diagram of the polymer versus the salt concentration can be found in Fig. 16.

These networks can also be tuned by adjusting the composition of the system [80]. For low polymer concentrations, the following structures are found as function of the composition: an excess of homopolymer results in soluble complexes, at charge-stoichiometry flower-like micelles are formed, and when the triblock copolymer is in excess the micelles stay intact. One block of the triblock copolymers in these micelles remains in the micelle and the other block forms a so-called dangling end in solution. At high polymer concentrations, first soluble complexes are formed when the homopolymer is in excess, a network is found at charge-stoichiometry ($F^- = 0.5$, see Fig. 16), and this network becomes disrupted when the triblock copolymer is in excess. Interestingly, an increase in viscosity is found in these systems due to repulsion between these micelles. This repulsion is due to the excess charge in the corona from the charged dangling end of the triblock copolymer.

## 3 Protein–Protein Complex Formation

Protein molecules are special polyelectrolytes in that their charge sign and charge density are a function of the pH (see Fig. 2). Moreover, the charge density of these molecules is rather low because there are only a few amino acids that are charged (arginine, histidine and lysine are positively charged; aspartic acid and glutamic acid are negatively charged). Most protein molecules form globular structures in an aqueous environment due to a delicate interplay between hydrophobic and hydrophilic amino acids. The specific folding of these globular structures enables protein molecules to perform special tasks as, e.g., enzymes or as building blocks.

Studying complex formation between protein molecules can give insight into biological processes. The cytosol of living cells is a complex mixture containing many different protein molecules that differ in size, charge (sign) and function. Electrostatic interactions between these proteins might play an important role in the stability of the cytoplasm. Also, in food, protein molecules are important for the structure and texture, and for the way the food is experienced in the mouth. In the context of this chapter we will discuss protein–protein complex formation as a special kind of polyelectrolyte complex formation.

Oppositely charged protein molecules could be an interesting model system for studying the interactions between similar, but oppositely charged nanoparticles. Biesheuvel et al. studied complex formation between lysozyme and succinylated lysozyme. The latter protein is a chemically modified form of lysozyme and has the opposite charge to lysozyme (i.e., negative instead of positive) at pH 7.5 [81]. At low salt concentration, mixtures of these two protein molecules form precipitates. These precipitates dissolve when the ionic strength or temperature is increased [82].

The redissolution of these +/− protein precipitates at elevated temperature indicates that attractive forces other than electrostatic attraction (e.g., hydrophobic interactions and hydrogen bonding) are important in this system because electrostatic attraction is not, or only minimally, dependent on temperature. This is not entirely surprising because many amino acids are hydrophobic or are able to form hydrogen bonds.

Figure 17 shows a plot of $F^+$ versus salt concentration for compositions with a fixed turbidity (measured as transmission of 95%). Like the plot of DLS intensity as a function of composition (see Sect. 2.1 on DLS), a maximum intensity is found at $F^+ = 0.5$. The experimental results of this system could theoretically be described using a heterogeneous Poison–Boltzmann cell model. This model assumes stronger correlations than, e.g., Voorn and Overbeek, taking the spatial structure within the complex into account [19]. It was developed to estimate the electrostatic free energy of strong complexes of oppositely charged flexible polyelectrolytes.

In cell models, each charged colloid, or in this case protein molecule, is surrounded by solvent and small (salt) ions, which form one cell. The Poison–Boltzmann equation is solved for the space between the protein molecule and the cell edge. In one-component cell models, the boundary conditions at each cell edge are fixed and each cell itself is electroneutral [83–86]. Here, we are dealing with a system

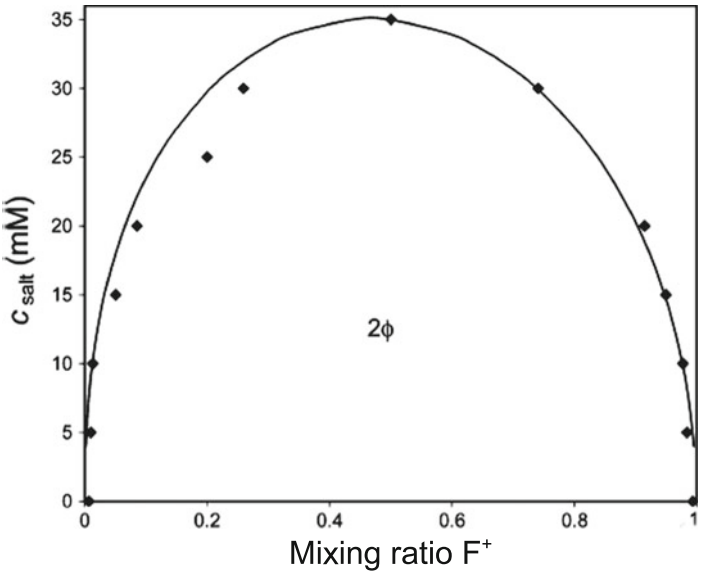


**Fig. 17** Critical ionic strength as function of the composition $F^+$. The protein concentration was 1 g $L^{-1}$; $2\Phi$ indicates the two-phase region. Experimental data were obtained via a turbidity experiment. A parameter $\chi = 14.8$ was used to describe the data theoretically. Reprinted from [82] with permission. Copyright 2006, American Chemical Society

containing two oppositely charged protein molecules and therefore a heterogeneous cell model has to be used. In this model, a mixture of colloidal spheres with fixed charged and volume in an aqueous environment containing small ions is considered. For the salt ions, a fixed chemical potential is assumed [82] (as if the system is in equilibrium with a large solution via a permeable membrane through which small ions and solvents can diffuse).

The non-electrochemical contributions are approximated using a Carnahan–Starling [87]–van der Waals equation of state. Figure 18 shows the phase diagram in the ionic strength versus protein concentration plane, at 1:1 mixing ratio and for various temperatures. To model the experimental results the only parameter that is not fixed is $\chi$. This parameter is used to model the non-electrostatic contributions. It can be seen in Fig. 18 that $\chi$ is temperature-dependent, which is expected because the precipitates dissolved when the temperature was increased.

By changing the pH, the number of charges on the protein molecules will be altered and asymmetric mixtures of lysozyme and succinylated lysozyme are obtained. These mixtures were also studied both experimentally and theoretically [88]. The heterogeneous cell model was further extended to include the ionisation of the protein molecules. In the model, the protein charge is not only considered a function of the pH and ionic strength, but also of the density and composition of the dilute and dense phases.

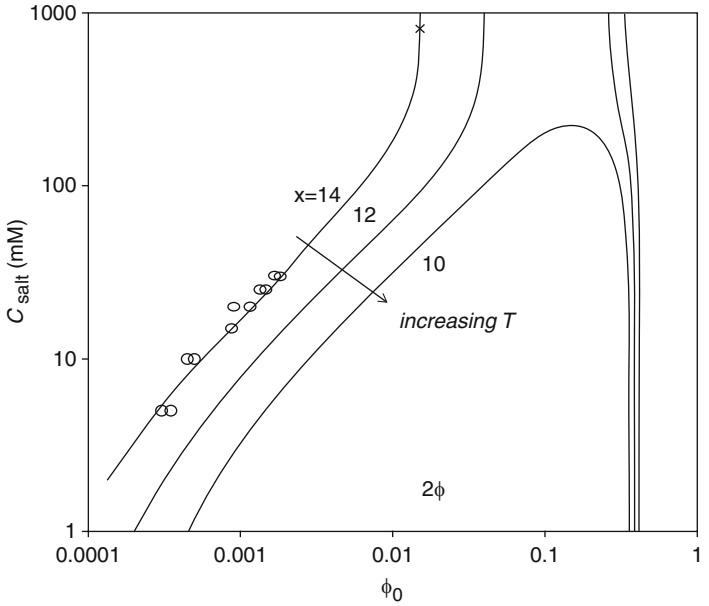


**Fig. 18** Phase diagram for ionic strength versus total protein concentration as a function of the temperature (*T*). Data points (*circles*) were obtained by determining the critical salt concentration and the data point marked by a *cross* was determined using light scattering (see [82] for more information). Reprinted from [82] with permission. Copyright 2006, American Chemical Society

Mixtures of lysozyme and succinylated lysozyme are not the only protein–protein systems that have been studied. Nigen et al. studied the formation of microspheres of calcium-depleted α-lactalbumin and lysozyme at 45°C and pH 7.5. These microspheres contain equimolar ratios of the two protein molecules. With confocal scanning laser microscopy (CSLM), and the two protein molecules labelled in different colours, the authors showed that the microspheres are built-up by binary assemblies of lysozyme and α-lactalbumin [89].

The ionic strength is important for the formation of α-lactalbumin–lysozyme microspheres. The equilibrium between free protein molecules and protein molecules in the microspheres depends on the ionic strength, as also found for the lysozyme–succinylated lysozyme system [82]. Increasing the salt concentration decreases the size of the microspheres; above 124 mM salt no microspheres are formed. Addition of salt to existing microspheres decreases the number of protein molecules within the spheres, but the protein aggregates remain spherical and monodisperse [90].

The protein molecules are able to exchange between different spheres. This was studied by CSLM using two different coloured batches (fluorescent green and red) of lysozyme molecules. Red fluorescent lysozyme molecules were added to

preformed microspheres containing the green fluorescent lysozyme molecules. A change in colour from green to red was observed when following the microspheres over time. It was further found that the protein molecules are able to diffuse within the microspheres [91].

It was also observed that formation of the microspheres follows a aggregation–reorganisation mechanism. First, α-lactalbumin–lysozyme heterodimers are formed, followed by the formation of protein nanospheres. These nanospheres form clusters that rearrange into microspheres. The total protein concentration has an effect on the final size of the microspheres [91]. The formation kinetics of calcium-depleted α-lactalbumin–lysozyme microspheres was investigated and it was found that the kinetics were independent of temperature, but at 25°C the clusters of nanospheres did not rearrange into microspheres and at 45°C they did. A possible explanation for this temperature effect is that calcium-depleted α-lactalbumin is in a molten globule state above 30°C. It was further observed that the kinetics depend on the protein concentration and ionic strength [92].

Microsphere formation was not only observed for lysozyme and α-lactalbumin; other oppositely charged protein couples (lysozyme/ovalbumin, ovalbumin/avidin and lysozyme/BSA) showed a similar behaviour. All these systems showed colocalisation of the protein molecules within the microspheres and were sensitive to the ionic strength. An analogy to the isoprotic point (see Fig. 2) of two weakly charged polyelectrolytes was found: the pH where optimal complexation occurred was $\frac{1}{2}(\mathrm{p}I_{\mathrm{protein}^+} + \mathrm{p}I_{\mathrm{protein}^-})$. Charge compensation was not observed in all systems, especially when there was a difference in protein size. In this case, the smaller protein molecule was in excess within the microsphere [93].

How do the relaxation phenomena of protein–protein complexes compare to polyelectrolyte complexes consisting of two polyelectrolytes? In Fig. 6, we sketched, the three distances ($d$, $r_{ij}$ and $h$) that are important for the relaxation behaviour of linear polyelectrolytes. The main difference between protein molecules and polyelectrolyte complexes is the distance $d$ because not only do most protein molecules have a very low charge density, they are 3D nanoparticles. The distance between opposite charges on different protein molecules is therefore expected to be larger because optimal 3D packing is more complicated than for linear polyelectrolytes. It is therefore not surprising that when two proteins are different in size, it is difficult to obtain charge compensation [93]. Rearrangement of the complexes was only found in systems where α-lactalbumin is in a molten globule state. A molten globule is more like a linear weakly charged polyelectrolyte. It is well known that weakly charged polyelectrolytes and protein molecules can form complex coacervate phases [8–12].

The ionic strength at which protein–protein complexes disintegrate is in general lower than for polyelectrolyte complexes. Probably because of the low charge density of the protein molecules and their less optimal packing within the complex. In some systems, an increase in temperature results in disintegration of the precipitates [82, 88]. This effect can be attributed to hydrophobic interactions and hydrogen bond formation between the amino acids. These interactions are known to be dependent on the temperature.

## References


1. Lindhoud S (2009) Polyelectrolyte complex micelles as wrapping for enzymes. PhD thesis, University of Wageningen, Wageningen
2. von Klitzing R (2006) Phys Chem Chem Phys 8(43):5012–5033
3. Zintchenko A, Rother G, Dautzenberg H (2003) Langmuir 19(6):2507–2513
4. Bakeev KN, Izumrudov VA, Kuchanov SI, Zezin AB, Kabanov VA (1992) Macromolecules 25(17):4249–4254
5. Hofs B, de Keizer A, Cohen Stuart MA (2007) J Phys Chem B 111(20):5621–5627
6. Itano K, Choi JY, Rubner MF (2005) Macromolecules 38(8):3450–3460
7. Bungenberg de Jong H (1949) In: Kruyt HR (ed) Complex colloid systems. Colloid science, vol 2. Elsevier, Amsterdam, pp 336–432
8. Weinbreck F, Tromp RH, de Kruif CG (2004) Biomacromolecules 5(4):1437–1445
9. Weinbreck F, Wientjes RHW (2004) J Rheol 48(6):1215–1228
10. de Kruif CG, Weinbreck F, de Vries R (2004) Curr Opin Colloid Interface Sci 9(5):340–349
11. Kaibara K, Okazaki T, Bohidar HB, Dubin PL (2000) Biomacromolecules 1(1):100–107
12. Kayitmazer AB, Strand SP, Tribet C, Jaeger W, Dubin PL (2007) Biomacromolecules 8:3568–3577
13. Spruijt E, Westphal AH, Borst JW, Cohen Stuart MA, van der Gucht J (2010) Macromolecules 43(15):6476–6484
14. Overbeek JTG, Voorn MJ (1957) J Cell Comp Physiol 49(S1):7–26
15. Cohen Stuart M, de Vries R, Lyklema H (2005) Polyelectrolytes. In: Lyklema J (ed) Soft colloids. Fundamentals of interface and colloid science, vol 5. Academic, New York, pp 1–84
16. Nakajima A, Sato H (1972) Biopolymers 11(7):1345–1355
17. Castelnove M, Joanny J-F (2001) Eur Phys J E: Soft Matter Biol Phys 6:377–386
18. Kramarenko E, Khokhlov A (2007) Polym Sci Ser A 49:1053–1063
19. Biesheuvel PM, Cohen Stuart MA (2004) Langmuir 20(11):4764–4770
20. Fuoss RM, Sadek H (1949) Science 110(2865):552–554
21. Michaels AS (1965) Ind Eng Chem 57(10):32–40
22. Schlenoff JB, Ly H, Li M (1998) J Am Chem Soc 120(30):7626–7634
23. Steitz R, Jaeger W, von Klitzing R (2001) Langmuir 17(15):4471–4474
24. Glinel K, Moussa A, Jonas AM, Laschewsky A (2002) Langmuir 18(4):1408–1412
25. Schoeler B, Kumaraswamy G, Caruso F (2002) Macromolecules 35(3):889–897
26. Voigt U, Jaeger W, Findenegg GH, Klitzing RV (2003) J Phys Chem B 107(22):5273–5280
27. Lavalle P, Gergely C, Cuisinier FJG, Decher G, Schaaf P, Voegel JC, Picart C (2002) Macromolecules 35(11):4458–4465
28. Lavalle P, Picart C, Mutterer J, Gergely C, Reiss H, Voegel JC, Senger B, Schaaf P (2004) J Phys Chem B 108(2):635–648
29. Hubsch E, Ball V, Senger B, Decher G, Voegel JC, Schaaf P (2004) Langmuir 20(5): 1980–1985
30. Shiratori SS, Rubner MF (2000) Macromolecules 33(11):4213–4219
31. Kovacevic D, van der Burgh S, de Keizer A, Cohen Stuart MA (2002) Langmuir 18(14):5607–5612
32. Picart C, Mutterer J, Richert L, Luo Y, Prestwich GD, Schaaf P, Voegel JC, Lavalle P (2002) Proc Natl Acad Sci USA 99(20):12531–12535
33. Lavalle P, Vivet V, Jessel N, Decher G, Voegel JC, Mesini P, Schaaf P (2004) Macromolecules 37:1159–1162
34. Sui ZJ, Salloum D, Schlenoff JB (2003) Langmuir 19(6):2491–2495
35. Burke SE, Barrett CJ (2003) Langmuir 19(8):3297–3303
36. Burke SE, Barrett CJ (2004) Pure Appl Chem 76(7–8):1387–1398
37. Yoo D, Shiratori SS, Rubner MF (1998) Macromolecules 31(13):4309–4318
38. Petrov AI, Antipov AA, Sukhorukov GB (2003) Macromolecules 36(26):10079–10086
39. Xie AF, Granick S (2002) Macromolecules 35(5):1805–1813

40. Izumrudov V, Sukhishvili SA (2003) Langmuir 19(13):5188–5191
41. Porcel C, Lavalle P, Ball V, Decher G, Senger B, Voegel JC, Schaaf P (2006) Langmuir 22(9):4376–4383
42. Porcel C, Lavalle P, Decher G, Senger B, Voegel JC, Schaaf P (2007) Langmuir 23(4):1898–1904
43. Spruijt E, Sprakel J, Lemmers M, Cohen Stuart MA, van der Gucht J (2010) Phys Rev Lett 105(20):208301
44. Jomaa HW, Schlenoff JB (2005) Macromolecules 38(20):8473–8480
45. Büscher K, Graf K, Ahrens H, Helm CA (2002) Langmuir 18(9):3585–3591
46. Tan HL, McMurdo MJ, Pan G, Van Patten PG (2003) Langmuir 19(22):9311–9314
47. Laugel N, Betscha C, Winterhalter M, Voegel J-C, Schaaf P, Ball V (2006) J Phys Chem B 110 (39):19443–19449
48. Hofs B, Voets IK, de Keizer A, Cohen Stuart MA (2006) Phys Chem Chem Phys 8(36):4242–4251
49. Ou ZY, Muthukumar M (2006) J Chem Phys 124(15):154902
50. Lindhoud S, Norde W, Cohen Stuart MA (2009) J Phys Chem B 113(16):5431–5439
51. Lindhoud S, de Vries R, Schweins R, Cohen Stuart MA, Norde W (2009) Soft Matter 5:242–250
52. Schönhoff M, Ball V, Bausch AR, Dejugnat C, Delorme N, Glinel K, Klitzing RV, Steitz R (2007) Colloids Surf A Physicochem Eng Asp 303(1–2):14–29
53. Farhat T, Yassin G, Dubas ST, Schlenoff JB (1999) Langmuir 15(20):6621–6623
54. Jaber JA, Schlenoff JB (2007) Langmuir 23(2):896–901
55. Glinel K, Prevot M, Krustev R, Sukhorukov GB, Jonas AM, Mohwald H (2004) Langmuir 20(12):4898–4902
56. Halthur TJ, Elofsson UM (2004) Langmuir 20(5):1739–1745
57. Kabanov AV, Bronich TK, Kabanov VA, Yu K, Eisenberg A (1996) Macromolecules 29 (21):6797–6802
58. Harada A, Kataoka K (1995) Macromolecules 28(15):5294–5299
59. Cohen Stuart MA, Besseling NAM, Fokkink RG (1998) Langmuir 14(24):6846–6849
60. Voets IK, de Keizer A, Cohen Stuart MA (2009) Adv Colloid Interface Sci 147–148:300–318
61. van der Burgh S, de Keizer A, Cohen Stuart MA (2004) Langmuir 20(4):1073–1084
62. Lindhoud S, de Vries R, Norde W, Cohen Stuart MA (2007) Biomacromolecules 8(7): 2219–2227
63. Biesheuvel PM, Cohen Stuart MA (2004) Langmuir 20(7):2785–2791
64. Harada A, Kataoka K (1998) Macromolecules 31(2):288–294
65. Galisteo F, Norde W (1995) Colloids Surf B Biointerfaces 4(6):389–400
66. Lindhoud S, Voorhaar L, de Vries R, Schweins R, Cohen Stuart MA, Norde W (2009) Langmuir 25:11425–11430
67. Yan Y, de Keizer A, Cohen Stuart MA, Drechsler M, Besseling NAM (2008) J Phys Chem B 112(35):10908–10914
68. Lemmers M, Voets IK, Cohen Stuart MA, van der Gucht J (2011) Soft Matter 7:1378–1389
69. Lindhoud S, Norde W, Cohen Stuart MA (2010) Langmuir 26(12):9802–9808
70. Lindhoud S, Cohen Stuart MA, Norde W, Leermakers FAM (2009) Phys Rev E 80(5):051406
71. Mjahed H, Voegel J-C, Chassepot A, Senger B, Schaaf P, Boulmedais F, Ball V (2010) J Colloid Interface Sci 346(1):163–171
72. Spruijt E, Cohen Stuart MA, van der Gucht J (2010) Macromolecules 43(3):1543–1550
73. Johansson E, Blomberg E, Lingström R, Wågberg L (2009) Langmuir 25(5):2887–2894
74. Creton C, Kramer EJ, Hui CY, Brown HR (1992) Macromolecules 25(12):3075–3088
75. Spruijt E, Sprakel J, Cohen Stuart MA, van der Gucht J (2010) Soft Matter 6(1):172–178
76. de Ruiter L, de Bungenberg de Jong H (1947) Proc Sect Sci (Koninklijke Nederlandse Akademie van Wetenschappen) 50:836–848
77. Sprakel J, Besseling NAM, Leermakers FAM, Cohen Stuart MA (2007) Phys Rev Lett 99:104504

78. van der Gucht J, Spruijt E, Lemmers M, Cohen Stuart MA (2011) J Colloid Interface Sci 361(2):407–422
79. Lemmers M, Sprakel J, Voets IK, van der Gucht J, Cohen Stuart MA (2010) Angew Chem Int Ed 49(4):708–711
80. Lemmers M, Spruijt E, Beun L, Fokkink R, Leermakers F, Portale G, Cohen Stuart MA, van der Gucht J (2012) Soft Matter 8:104–117
81. van der Veen M, Norde W, Cohen Stuart MA (2004) Colloids Surf B Biointerfaces 35(1): 33–40
82. Biesheuvel PM, Lindhoud S, de Vries R, Cohen Stuart MA (2006) Langmuir 22(3):1291–1300
83. Alexander S, Chaikin PM, Grant P, Morales GJ, Pincus P, Hone D (1984) J Chem Phys 80 (11):5776–5781
84. Hansson P (2001) Langmuir 17(14):4167–4180
85. Allen RJ, Warren PB (2004) Langmuir 20(5):1997–2009
86. Biesheuvel PM, Wittemann A (2005) J Phys Chem B 109(9):4209–4214
87. Carnahan NF, Starling KE (1972) AIChE J 18(6):1184–1189
88. Biesheuvel PM, Lindhoud S, Cohen Stuart MA, de Vries R (2006) Phys Rev E 73(4):041408
89. Nigen M, Croguennec T, Madec MN, Bouhallab S (2007) FEBS J 274(23):6085–6093
90. Nigen M, Croguennec T, Bouhallab S (2009) Food Hydrocolloids 23(2):510–518
91. Nigen M, Gaillard C, Croguennec T, Madec MN, Bouhallab S (2010) Biophys Chem 146(1):30–35
92. Salvatore D, Croguennec T, Bouhallab S, Forge V, Nicolai T (2011) Biomacromolecules 12(5):1920–1926
93. Desfougeres Y, Croguennec T, Lechevalier V, Bouhallab S, Nau F (2010) J Phys Chem B 114(12):4138–4144

Adv Polym Sci (2014) 255: 173–226
DOI: 10.1007/12_2012_182

Published online: 25 January 2013

# Advanced Functional Structures Based on Interpolyelectrolyte Complexes

**Dmitry V. Pergushov, Alexey A. Zezin, Alexander B. Zezin, and Axel H.E. Müller**

**Abstract** This review considers interpolyelectrolyte complexes, with a particular emphasis on advanced macromolecular co-assemblies based on polyionic species with nonlinear topology and on polymer–inorganic hybrids formed by interpolyelectrolyte complexes containing metal ions and/or metal nanoparticles.

**Keywords** Interpolyelectrolyte complexes · Interpolyelectrolyte reactions · Macromolecular co-assembly · Metal nanoparticles · Metallo-containing interpolyelectrolyte complexes · Nanostructures · Polyelectrolytes · Polymer–inorganic hybrids

## Contents



D.V. Pergushov (✉) and A.B. Zezin
Department of Chemistry, M.V. Lomonosov Moscow State University, 119991 Moscow, Russia
e-mail: pergush@genebee.msu.ru; pergushov@vms.chem.msu.ru; zezin@genebee.msu.ru

A.A. Zezin
Department of Chemistry, M.V. Lomonosov Moscow State University, 119991 Moscow, Russia

Institute of Synthetic Polymeric Materials, Russian Academy of Sciences, 117393 Moscow, Russia
e-mail: aazezin@yandex.ru

A.H.E. Müller
Makromolekulare Chemie II and Bayreuther Zentrum für Kolloide und Grenzflächen, Universität Bayreuth, 95440 Bayreuth, Germany

Present address: Institut für Organische Chemie, Johannes Gutenberg-Universität Mainz, 55099 Mainz, Germany
e-mail: axel.mueller@uni-bayreuth.de; axel.mueller@uni-mainz.de

## Abbreviations

| | |
|---|---|
| Cryo-TEM | Cryogenic transmission electron microscopy |
| EPR | Electron paramagnetic resonance |
| GPE | "Guest" polyelectrolyte |
| HPE | "Host" polyelectrolyte |
| IPEC | Interpolyelectrolyte complex |
| LbL | Layer-by-layer |
| NP | Nanoparticle |
| $P2VPH^+$ | Protonated poly(2-vinylpyridine) |
| P2VPQ | Quaternized poly(2-vinylpyridine) |
| P4VPQ | Quaternized poly(4-vinylpyridine) |
| PAA | Poly(acrylic acid) |
| PAH | Poly(allylamine hydrochloride) |
| PANa | Poly(sodium acrylate) |
| PB | Polybutadiene |
| PDADMAC | Poly(*N*,*N*-diallyldimethylammonium chloride) |
| PDMAEMA | Poly[2-(dimethylamino)ethyl methacrylate] |
| PDMAEMAQ | Quaternized poly[2-(dimethylamino)ethyl methacrylate] |
| PEI | Poly(ethylene imine) |
| PEO | Poly(ethylene oxide) |
| PIB | Polyisobutylene |
| PMAA | Poly(methacrylic acid) |
| PMANa | Poly(sodium methacrylate) |
| PPNa | Poly(sodium phosphate) |
| PS | Polystyrene |
| PSSNa | Poly(sodium styrene sulfonate) |
| TEM | Transmission electron microscopy |
| PNIPAAm | Poly(*N*-isopropylacrylamide) |
| DDA | Dodecylammonium |

## 1 Introduction

During recent decades, self-organization phenomena in macromolecular systems based on synthetic polyelectrolytes, as well as in complex systems containing natural macromolecules, have been extensively and successfully investigated. First of all, the studies have been aimed at gaining deeper understanding of self-organization mechanisms in biological systems. An example is the phenomenon of DNA compaction, which was revealed upon examination of the conformational behavior of double-helix DNA complexed with cationic surfactants in nonpolar solvents such as chloroform. The experimental results on such "null DNA," whose charge is fully compensated, under conditions pronouncedly different from those typical for common aqueous media, suggested that DNA compaction can be considered as intrinsic property of an uncharged double helix. Experts both in physical chemistry of polymers and in molecular biology have positively evaluated this concept [1–3].

Interpolyelectrolyte complexes (IPECs) resulting from coupling oppositely charged (or getting charged) polyelectrolytes obviously take an important and significant part in a domain of self-organizing polymer systems. Such macromolecular co-assemblies built up from linear polyions have attracted the attention of experts in polymer science for a long time [4–9]. Nowadays, one can confidently relate IPECs to smart and intelligent functional complex polymers having a pronounced tendency toward self-organization. Also of interest is the response of IPECs to minor variations in their environment (particularly to changes in pH, ionic strength, temperature, etc.) via considerable conformational changes and the whole spectrum of their physicochemical and mechanical characteristics. The unique simplicity of preparation of IPECs, together with an availability of linear polyelectrolytes, make such macromolecular co-assemblies and IPEC-based materials very promising for numerous applications.

IPECs have been demonstrated to act as effective flocculants and surface modifiers [10–13]. One can emphasize the successful application of IPECs as effective and available binders for soils and grounds in the aftermath of the accident in the Chernobyl atomic power station (Ukraine).These macromolecular co-assemblies were used to suppress erosion of soils and grounds and thus to prevent radionuclide contamination caused by spreading of radioactive particles [10, 14]. Twenty-five years later, IPECs have again attracted attention because of similar problems arising from the accident in the Fukushima Daiichi atomic power station (Japan) [15, 16]. Another attractive application of IPECs is for medical purposes in the design of pharmaceuticals for targeted drug delivery followed by controlled release, e.g., for a nonviral gene delivery into cells [17, 18].

Nowadays, we clearly see that the domain of interpolyelectrolyte interactions and IPECs is rapidly developing, involving relatively new areas of science and opening new possibilities for application of these macromolecular co-assemblies. With IPECs as templates, novel organic–inorganic complex systems and hybrid nanocomposites based on these are successfully being developed. During the last few years, studies on IPECs have been considerably extended as polyelectrolytes with new (nonlinear) topologies have become available. This becomes possible due

to remarkable advances in controlled radical polymerization techniques, such as atom-transfer radical polymerization (ATRP), stable free-radical polymerization (SFRP), and reversible addition-fragmentation transfer (RAFT) polymerization [19, 20]. As a result, well-defined star-shaped polyelectrolytes and star-like polyionic species (micelles of ionic amphiphilic block copolymers) as well as cylindrical polyelectrolyte brushes can now be utilized as polymeric components to be involved in interpolyelectrolyte complexation. This opens new possibilities for design of a novel generation of IPECs having a distinct compartmentalized structure. These problems and points will be considered in this review.

## 2 Formation and Basic Properties of Interpolyelectrolyte Complexes

### *2.1 Peculiarities of IPEC Formation*

During recent decades, considerable attention has been paid to interpolymer interactions and interpolymer complexes. This interest is motivated by a number of fundamental and application-oriented problems. In a fundamental aspect, interpolymer interactions are of significant importance because of the possibilities for design and fabrication of novel polymeric co-assemblies, structures, and materials. Such macromolecular co-assemblies (also referred to as interpolymer complexes) possess unique properties that are remarkably different from the properties of their polymeric components. In the simplest case, they result from "weak" mutual attraction of chemically and/or stereo-complementary macromolecules. Thus, "stereocomplexes" formed due to van der Waals interaction between stereoregular poly(β-propiolactone)s are well known [21]. Interpolymer complexes might also be stabilized via hydrogen bonds between monomer units of the polymeric counterparts [22, 23], for example, co-assemblies of poly(carboxylic acid)s with polyethers, i.e., poly[oxyethylene(propylene) glycol]s. Despite the low attraction energy between complementary monomer units, such interpolymer complexes are rather stable because of the cooperative character of interpolymer interaction. At the same time, they can reversibly dissociate to their polymeric components if certain conditions (temperature, pH, ionic strength, etc.) are met. This opens a unique opportunity for design and fabrication of new polymeric materials and structures of various scales and dimensions (ranging from nano- to macroscopic) with variable characteristics, which are determined by environmental conditions. Such materials and structures are referred to as functional, whereas the co-assemblies themselves are regarded as "smart." Similar principles for construction of complex polymeric structures are widely exploited and exemplified in nature by production of the most important biological architectures, such as double helices (i.e., DNA) and fibrillar proteins (e.g., collagen). Thus, the modern physical chemistry of polymers follows fundamental principles, which are widely used in nature.

Among interpolymer complexes, IPECs, which result from the interaction between oppositely charged polyelectrolytes, are of a special interest. Such macromolecular

co-assembly processes proceed with high rates, which are typical for diffusion-controlled reactions. As a result of collisions between oppositely charged macromolecular coils, contacts (referred to as ion–ion or salt bonds) are formed between their monomer units while low molecular weight counterions previously associated with charged groups of the polymeric components release into bulk solution (1). This release of low molecular weight counterions causes the entropy of the system to increase, i.e., $\Delta S > 0$. Calorimetric studies point to athermic character of interpolyelectrolyte complexation (in aqueous media). This fact indicates that co-assembly processes in such systems are predominantly driven by a gain in entropy.

(1)

Upon the formation of IPECs, the concentration of a low molecular weight salt ($a^-$, $b^+$) in the system increases. The increasing salt concentration shifts equilibrium (1) to the left, that is, it favors the dissociation of interpolymer salt bonds. This phenomenon is observed at high concentrations of the polymeric components and/or upon addition of low molecular weight salts to mixtures of oppositely charged polyelectrolytes and has been reported in numerous works [8, 24–26]. It is widely used when IPECs are applied.

At sufficient content of low molecular weight salts, the equilibrium, which can be shifted to one or another side by the changing salt concentration, is settled. There are numerous reports on fundamental aspects of interpolyelectrolyte reactions, in which equilibrium (1) is considered. Such equilibria are analyzed in terms of chemical thermodynamics, using equilibrium constants. For (1), the equilibrium constant $K_{eq}$ is given by:

$$K_{eq} = [\vdash A^{\ominus\oplus}B \dashv](b^+)(a^-)/[\vdash A^{\ominus}b^+][\vdash B^{\oplus}a^-] \tag{2}$$

If, for simplicity, $[\vdash A^{\ominus}b^+]_0 = [\vdash B^{\oplus}a^-]_0 = C_0$, that is, considering mixtures of oppositely charged polyelectrolytes at the stoichiometric (1:1) ratio between their ionic groups, then dividing the numerator and the denominator in Eq. (2) by the initial concentration ($C_0$) yields:

$$K_{eq} = (1/C_0) \cdot \{\Theta/(1-\Theta)^2\} \cdot (b^+)(a^-) \tag{3}$$

Here, $\Theta$ is a conversion in the reaction described by (1), such that $\Theta = [\vdash A^{\ominus\oplus}B \dashv]/C_0$, which equals the ratio of the concentration of the formed interpolymer salt bonds to the initial concentrations of ionic groups of the polymeric components. For nonstoichiometric mixtures, one takes as $C_0$ the initial concentration of ionic units of the minority polyelectrolyte.

From the above consideration, it follows that from the experimental point of view equilibrium (1) can be easily investigated for polyelectrolytes whose charged groups possess a strong specific affinity to counterions. Such systems comprising weak polymeric acids or weak polymeric bases have been studied in detail due to the

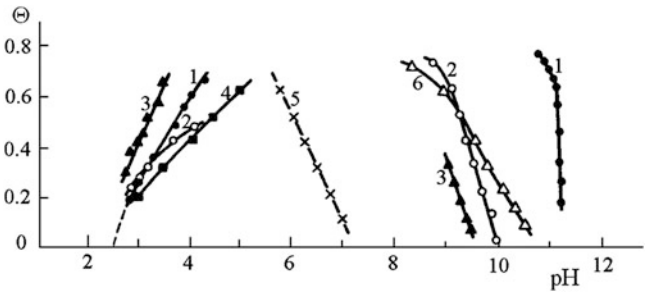


**Fig. 1** Plots of $\Theta$ versus pH for various polyelectrolyte systems: (*1*) poly(acrylic acid) (PAA) – poly(L-lysine); (*2*) PAA – poly[2-(dimethylamino)ethyl methacrylate] (PDMAEMA); (*3*) poly(L-glutamic acid) – PDMAEMA; (*4*) PAA – poly(*N*-ethyl-4-vinylpyridinium bromide) (P4VPQ); (*5*) poly(4-vinylpyridine) – poly(sodium styrene sulfonate) (PSSNa); (*6*) PDMAEMA – PSSNa. Reprinted from [27] with kind permission from MAIK Nauka/Interperiodica Copyright 1999

simplicity and availability of experimental techniques for study of interpolyelectrolyte reactions by means of potentiometric titration. As an illustration, one can consider equilibria (4) and (5):

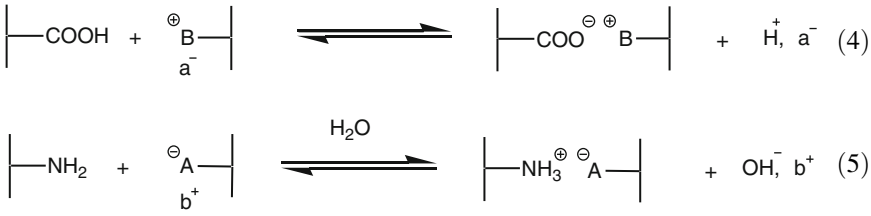


where (4) describes a reversible charging of a weak polyacid in the presence of polycations and (5) represents a reversible charging of a weak polybase in the presence of polyanions. Both charging reactions lead to the formation of IPECs. A detailed analysis of these equilibria in terms of $\Theta$ against the pH has been published [27]. A number of experimental $\Theta$ versus pH dependences for various polyelectrolyte systems are shown in Fig. 1.

The obtained findings point to a high stability of the formed IPECs, which in turn results from a high cooperativity of the coupling reactions (1), (4), and (5) between oppositely charged polyelectrolytes (also referred to as polyion addition reactions) [7, 8].

## 2.2 *Water-Soluble Nonstoichiometric IPECs*

IPECs have attracted significant attention mainly as novel amphiphilic materials, which are promising for applications in medicine, biology, and ecology [10, 28, 29]. A breakthrough and further progress in the domain of interpolyelectrolyte reactions and IPECs were achieved in the middle of the 1970s. They were associated with

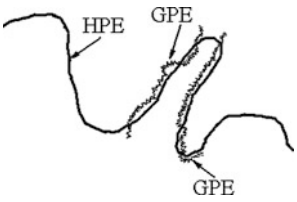


**Fig. 2** Structure of water-soluble nonstoichiometric IPECs formed by oppositely charged linear polyelectrolytes with $DP_{HPE} >> DP_{GPE}$ [31, 32]

the discovery of so-called water-soluble nonstoichiometric IPECs, which contain charged groups of the polymeric components in a nonequivalent ratio. For the first time, such macromolecular co-assemblies were reported [30]. Extensive studies of the water-soluble nonstoichiometric IPECs considerably advanced knowledge about the structure of these extremely interesting and promising macromolecular co-assemblies and their self-organization. It was found that the solution behavior of such IPECs decisively depends on their charge-to-charge stoichiometry. In particular, it was shown that IPEC species become compact if the ratio of oppositely charged groups of their polymeric components approaches 1:1 (i.e., stoichiometric).

These and other results allow one to consider water-soluble nonstoichiometric IPECs as peculiar amphiphilic block copolymers comprising a number of complex blocks assembled from the electrostatically coupled polymeric components. Such complex blocks are rather hydrophobic, thereby manifesting a tendency to a mutual segregation in aqueous media. Free (uncomplexed) segments of the excess polyelectrolyte are obviously hydrophilic and therefore grant IPEC species a solubility in aqueous media. This excess polyelectrolyte is typically referred to as a "host" polyelectrolyte (HPE). Its polymeric counterpart bearing opposite charge, which is incorporated into IPEC as a minority component, is generally referred to as a "guest" polyelectrolyte (GPE). The structure of water-soluble nonstoichiometric IPECs proposed by Kabanov and Zezin [31, 32] is schematically depicted in Fig. 2.

The unique behavior of water-soluble nonstoichiometric IPECs manifests itself, first of all, by polyion exchange reactions, which proceed between IPEC species and lead to transfer of a chain (or chains) of GPE from one HPE chain to another. These polyion exchange reactions cause such systems to undergo so-called disproportionation, which is known to result in phase separation of solutions of such macromolecular co-assemblies. The IPECs contained in coexisting phases considerably differ in their charge-to-charge stoichiometries: the insoluble phase is typically composed of a stoichiometric IPEC while a nonstoichiometric IPEC (or even a pure HPE) remains in the solution. Such phase separations can be caused by various factors, for example, by varying charge-to-charge stoichiometry of the mixture, by adding low molecular weight salts, by changing the temperature, etc.

These and other findings show that charge-to-charge stoichiometry of IPEC species can be remarkably different to the ratio between the amounts of monomer units of oppositely charged polymeric components in their mixture, i.e., the charge-to-charge stoichiometry of the mixture. To overcome this, one should introduce two independent parameters to characterize the charge-to-charge stoichiometry of the

mixture: first, $Z$ = [GPE]/[HPE] (here, the basemolar concentrations of the polymeric components in a reaction mixture are given in the brackets) and second, the stoichiometry of the formed IPEC, $\varphi = N_{GPE}/N_{HPE}$ (here, the amounts of monomer units of the polymeric components incorporated into an IPEC are given). These parameters are defined already in early works [31, 32] and will be used throughout this review.

Figure 3 illustrates transformations of the water-soluble nonstoichiometric IPECs upon increasing $Z$. Here, three regions (A, B, and C) are marked on the $Z$-axis, where $Z_{cr}$ and $Z_{lim}$ correspond to the boundaries between the regions A and B and B and C, respectively, with the stoichiometry of the IPEC changing differently in each region. This scheme describes the behavior of mixtures of oppositely charged polyelectrolytes with considerably different degrees of polymerization, where $DP_{HPE} \gg DP_{GPE}$ (here, DP is the degree of polymerization of the corresponding polyion) in the range $0 < Z \leq 1$.

In region A, $0 < Z \leq Z_{cr}$ and free (uncomplexed) macromolecules of HPE and IPEC species with stoichiometry being constant and equal to $\varphi_{cr} = DP_{GPE}/DP_{HPE}$ coexist in the solution. Numerous experimental results provide evidence that each of the IPEC species contains only one HPE chain. Disproportionation observed in region A results from an insufficient amount of GPE chains, which cannot occupy all HPE chains in the mixture. With increasing $Z$, the fraction of free HPE chains in the reaction mixture linearly decreases, with all HPE chains being incorporated into IPEC species at $Z = Z_{cr}$.

In region B, $Z_{cr} < Z \leq Z_{lim}$ and all HPE chains are occupied but they are able to host further GPE. Experimental results indicate that GPE chains, which are additionally incorporated into the IPEC species of stoichiometry $\varphi_{cr}$, are uniformly distributed among the macromolecular co-assemblies. However, a change of charge-to-charge stoichiometry of the IPEC species upon increasing $Z$ in the region B has not been investigated in detail so far. It was only found that IPEC species with $\varphi > \varphi_{lim}$ lose their solubility in aqueous media. This happens at $Z = Z_{lim} = \varphi_{lim}$.

On further addition of GPE to a mixture of oppositely charged polymeric components ($Z_{lim} < Z \leq 1$), the system becomes heterogeneous (the region C). As previously described [26, 33], IPEC species considerably differing in their charge-to-charge stoichiometries coexist in the mixture of oppositely charged polyelectrolytes. Particles of an insoluble IPEC in region C are present in a colloidally dispersed state and can be easily separated from the reaction mixture, for example, by centrifugation. A direct determination of their charge-to-charge stoichiometry by means of elemental analysis indicates that it remains constant and corresponds to the equimolar ratio between charged groups of HPE and GPE (i.e., $\varphi = 1$). At the same time, a water-soluble nonstoichiometric IPEC with stoichiometry $\varphi = \varphi_{lim}$ remains in the solution. At $Z = 1$, only a precipitate of a stoichiometric IPEC ($\varphi = 1$) is formed and the supernatant contains no polyions.

These insoluble stoichiometric IPECs have found their application as binders of various disperse systems, including soils and grounds, thus acting as effective agents for preventing wind and/or water erosion. Specifically, they have been used to suppress spreading of radioactive contamination in soils and grounds resulting from accidents in atomic power stations [10, 14–16].

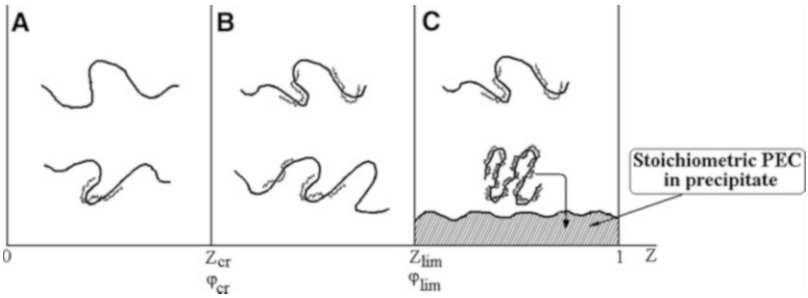


**Fig. 3** Behavior of mixtures of oppositely charged linear polyelectrolytes with $DP_{HPE} >> DP_{GPE}$ upon an increasing content of GPE. $Z$=[GPE]/[HPE]. For descriptions of regions *A*, *B*, and *C*, see text

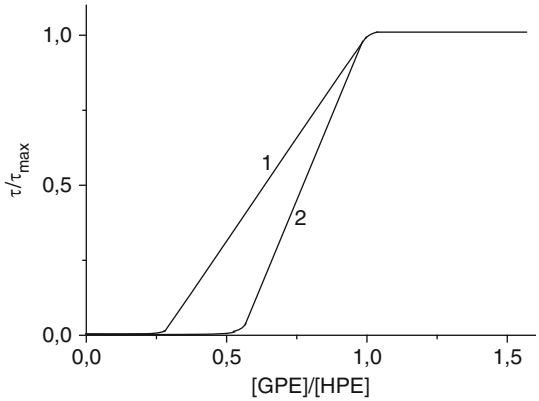


**Fig. 4** Turbidimetric titration curves of (*1*) an aqueous solution of sodium polyphosphate (PPNa) acting as HPE with an aqueous solution of 5,6-ionene bromide acting as GPE at pH 7.0 and 0.01 M NaBr; and (*2*) an aqueous solution of PDMAEMA·HCl (HPE) with an aqueous solution of PPNa (GPE) at pH 4.5 and 0.1 M NaCl

Addition of low molecular weight salts into mixtures of oppositely charged polyelectrolytes has a pronounced influence on the behavior of water-soluble nonstoichiometric IPECs. In particular, this manifests itself in a shift of the boundary between the regions A and B, that is, $Z_{cr}$, to lower values. The low molecular weight salts induce conformational transformations of particles of nonstoichiometric IPECs, (i.e., a coil–globule transition) followed by phase separation of the solution and macroscopic precipitation of a stoichiometric IPEC [31, 34].

The above phenomena, which are to be investigated for understanding of self-organization in multicomponent systems containing oppositely charged polyions, imply that IPEC species can exchange their polymeric components with each other. Turbidimetric titrations of aqueous solutions of various HPEs with aqueous solutions of different GPEs ($DP_{HPE} > DP_{GPE}$) provide evidence for such polyion exchange. The reaction mixture remains transparent until $Z = Z_{lim}$. When $Z$ exceeds

$Z_{lim}$, turbidity appears and then linearly increases with increasing $Z$ (in the range $Z_{lim} < Z < 1$). This is schematically illustrated by the turbidimetric titration curves given in Fig. 4.

These results undoubtedly point to the formation of a water-soluble nostoichiometric IPEC at low $Z$-values ($Z < Z_{lim}$), followed by the formation and the subsequent concentration of an insoluble stoichiometric IPEC at $Z > Z_{lim}$. This completely corresponds to the transformations of IPECs, which are described above (Fig. 3).

## 2.3 Polyion Transfer in IPEC Systems

The dynamic properties of IPECs have been considered in more detail by Kabanov and colleagues [7, 8, 35], who reported on the kinetics of interpolyelectrolyte exchange reactions. These reactions comprise a transfer of GPEs from some HPEs to other HPEs. The reaction represented by (6) illustrates this process:

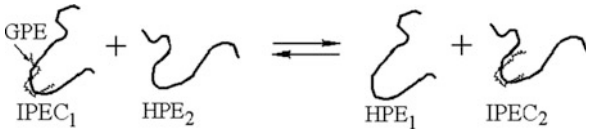


(6)

Here, $HPE_1$ and $HPE_2$ are chemically equal polyions with the same macromolecular characteristics. They exchange with each other by GPE. The reaction described by (6) represents a simple exchange process between particles of a nonstoichiometric IPEC (each containing one GPE chain) and free (uncomplexed) HPE chains. Such IPECs with $\varphi = N_{GPE}/N_{HPE} = DP_{GPE}/DP_{HPE}$ are formed in region A (see Fig. 3). It is obvious that the polyion exchange reaction proceeds for any $Z$-value and even not necessarily in homogeneous media. In the heterogeneous region (C), the reaction is matched to an interphase transfer of GPE chains.

From the basic point of view, the reaction represented by (6) is most suitable for fundamental investigations on the kinetics and mechanism of interpolyelectrolyte exchange reaction. Such studies provide key understanding of processes proceeding in self-organizing multicomponent systems comprising oppositely charged polyions. They are also necessary for deep insight into the structure and properties of a novel generation of amphiphilic polymeric materials based on IPECs.

The experimental investigation of interpolyelectrolyte exchange reactions described by (6) requires that $HPE_1$ and $HPE_2$, which participate in the process, are distinguishable. It is also necessary to be able to detect a transfer of GPE chains. The first was achieved by fluorescent labeling of $HPE_2$ or $HPE_1$ [8, 36]. As fluorescent labels, antracenyl or pyrenyl ones, were used and poly(methacrylate) ($PMA^-$) anions were exploited. The second problem was overcome by choosing GPEs, which are effective fluorescence quenchers. Typically, these are polymeric aromatic quaternary ammonium salts. Mostly, salts of poly(*N*-ethyl-4-vinylpyridinium) ($P4VPQ^+$) cations were used. Thus, a transfer of GPE-quenchers results either in fluorescence enhancing or

fluorescence quenching in the system, depending on which HPE (i.e., $HPE_2$ or $HPE_1$) is fluorescently labeled.

The kinetics of a single chain transfer, which is represented by (6), was studied more completely. In the simplest case, equal amounts of IPEC species, each containing only one HPE chain and one GPE chain, and free fluorescently labeled HPE (HPE*) are taken so that [HPE] = [HPE*]. Conversion ($q$) of the transfer was defined as the fraction of HPE* chains complexed with GPE chains. It was found that the kinetics of the transfer are well described in terms of a second-order reaction with respect to the concentrations of macromolecular reagents, i.e., IPEC {HPE-GPE} and HPE*. Accordingly, experimentally obtained kinetic curves were fitted as linear functions using Eq. (7):

$$\frac{q}{1-q} = k_2 \times [\mathrm{HPE}^*]_0 t. \tag{7}$$

Here, $k_2$ is the rate constant for the transfer of a GPE chain from one HPE chain onto another, $[HPE^*]_0 = [HPE]_0$ is the initial basemolar concentration of the reacting species in the system, and $t$ is time. It turned out that the measured values of $k_2$ are three to five orders of magnitude less than the calculated values for the rate constant, which is determined by diffusion-driven collisions [36]. This finding implies that indeed only one transfer of a GPE chain from an IPEC onto a HPE* chain takes place per $10^3$–$10^5$ collisions. The Scheme (8) below illustrates this process:

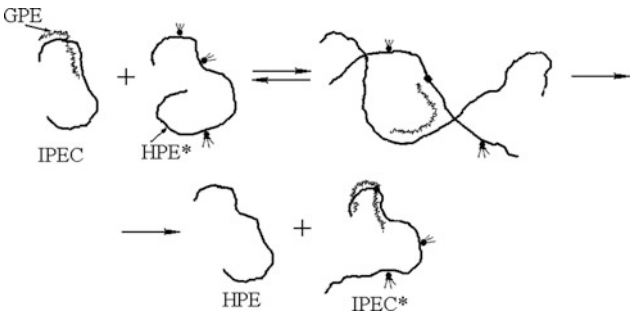


(8)

According to this scheme, transfer of a GPE chain from an IPEC onto a HPE* chain proceeds in a united macromolecular coil comprising three polyions (i.e., HPE, HPE*, and GPE) through redistribution of interpolymer contacts (interpolymer salt bonds). It was shown that the probability of the chain transfer strongly increases with increasing ionic strength of the solution [36]. This is explained by an enhanced segmental mobility of GPE (due to breakup of some interpolymer salt bonds) in the united macromolecular coil (an intermediate state).

Thus, the kinetics of polyion exchange reactions can be governed by varying the concentrations of a low molecular weight salt in the system. If the ionic strength of solutions is low, then macromolecular dissociation of IPECs to their polymeric components does not happen under such conditions. The rate of polyion exchange

reaction also strongly increases with the decreasing linear charge density of GPE as well as with the decreasing degree of polymerization of the latter [36].

The considered processes play an extremely important role during preparation of IPECs. Thus, mixing aqueous solutions of oppositely charged polyelectrolytes at charge-to-charge ratios at which water-soluble nonstoichiometric IPECs are to be finally formed results, at first, in appearance of turbidity in the system. However, the turbidity gradually disappears with time, depending on the mixing conditions, and particles of a nonstoichiometric IPEC with $\varphi = Z$ can be detected in the system [36]. The first, rapid stage of the reaction proceeds with a diffusion-controlled rate. It is accompanied by appearance of rather large aggregates, whose charge-to-charge stoichiometry differs from the charge-to-charge stoichiometry of the reaction mixture, i.e., $\varphi \neq Z$. The next, relatively slow stage is a polyion exchange between these aggregates and free HPE, leading to the formation of thermodynamically stable water-soluble nonstoichiometric IPECs.

The processes described above are also of importance for insoluble stoichiometric IPECs as well as for IPEC-based materials, including composites. This manifests itself in the fact that the swollen-in-water IPECs behave as viscous liquids and can creep. When incorporated into complex disperse systems (e.g., soils), they quickly recognize complementary sites on the surface of soil particles and strongly stick them together. In such systems, oppositely charged polyions constantly migrate relative to each other due to Brownian motion, remaining at the same time incorporated into the IPECs [8]. This behavior explains the fact that composites based on such macromolecular co-assemblies in a wet state exhibit pronounced self-healing behavior.

The results of studies on the kinetics of interpolyelectrolyte exchange reactions provide evidence that fluorescent labels of HPE*, which were taken to be hydrophobic, act as “anchors” for GPE-quenchers. It was found that an antracenyl label is a weak “anchor” compared to a pyrenyl label and that an increasing amount of labels in a HPE* chain leads to its more selective binding with GPE-quenchers [36, 37]. This is because of an additional gain of free energy upon formation of a contact between a label and a monomer unit of the polymeric quencher due to the donor–acceptor interaction and also because of incorporation of the label into a rather hydrophobic domain consisting of hydrophobic moieties of the coupled polyions. Such “recognition” plays an important role in biological systems.

Analysis of the equilibrium of interpolyelectrolyte coupling and kinetics of interpolyelectrolyte exchange led to the conclusion that IPECs are stable macromolecular co-assemblies. In aqueous media, IPECs do not dissociate to their polymeric components at concentrations of low molecular weight salts typically below about 0.5 M and, at the same time, retain high dynamics. At such salt concentrations, polyions building up macromolecular co-assemblies at ambient temperatures are able to easily migrate with respect to each other. In aqueous solutions of nonstoichiometric IPECs, GPE chains easily change their hosts through interpolyelectrolyte exchange reactions. These processes provide remarkable self-organization of IPECs. Being of a pronounced amphiphilic character, IPECs quickly find their optimal location in a complex environment. Thus, they “recognize” complementary sites on surfaces of particles in natural dispersions and anchor onto them, as depicted in Fig. 5.

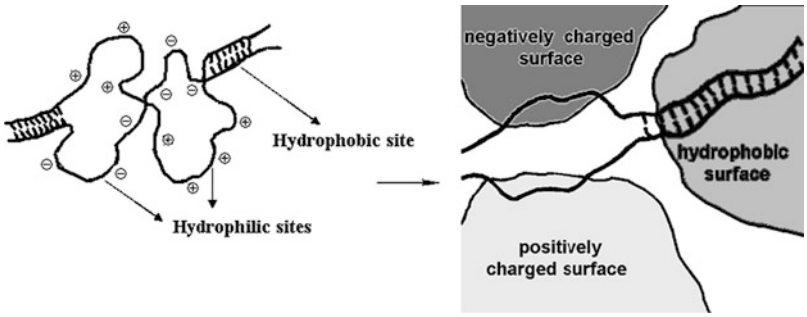


**Fig. 5** A fragment of an IPEC and a fragment of an IPEC in a soil pore

Nowadays, IPECs are typically considered to be self-organizing and ordered macromolecular co-assemblies. This concept is based not only on semi-intuitive understanding of such systems as products of the cooperative interpolyelectrolyte interaction but also on some supporting experimental findings.

Self-adjustment phenomena in IPECs manifest themselves on different scales: both within single particles in aqueous solutions of nonstoichiometric IPECs and in bulk insoluble stoichiometric IPECs. A transfer of GPE chains from some HPE chains to other identical chains has been considered above. It has been assumed that this transfer is possible because a GPE chain permanently changes its location in a HPE coil due to Brownian motion. In a united $\{HPE_1\text{-}GPE\text{-}HPE_2\}$ coil, it can "choose" another host within the lifetime of the coil and, therefore, migrate from the original $HPE_1$ to the added $HPE_2$. Besides, one assumes that all locations of the GPE chain in the HPE coil are equal because there is no available information about their preferable locations. At the same time, when the GPE chain is rather short it remains relatively strained on the oppositely charged longer HPE chain. This implies a certain order in mutual locations of the polymeric components in an IPEC particle. Such a consideration follows from numerous results on the conformational behavior of particles of water-soluble nonstoichiometric IPECs. Thus, the migration of GPE chains resembles a "worm"-like motion along a stretched thread, this motion being permanent and chaotic in nature.

The Brownian motion of GPE-quenchers becomes vectorized even if a minor amount of pyrenyl labels is attached to HPE chains; as little as about one label per 350 monomer units of HPE* is sufficient. This manifests itself in the fact that GPE-quenchers, as described above, predominantly occupy HPE* chains bearing the fluorescent labels. Considering a single particle of a water-soluble nonstoichiometric IPEC*, this also means that a random walk of a GPE chain in a HPE* coil is directed, with the GPE chain spending more time on sites of HPE*, which contain the anchoring label.

In the context of self-organization of IPECs, the so-called interpolyelectrolyte substitution reactions are of particular interest. In these reactions, $HPE_1$ chains coupled to GPE (i.e., forming $IPEC_1$) are substituted by $HPE_2$ chains, which are different in nature, thereby generating $IPEC_2$ as shown in (9)

$$\mathrm{IPEC_1\{HPE_1-GPE\} + HPE_2 \rightarrow IPEC_2\{HPE_2-GPE\} + HPE_1} \qquad (9)$$

Such reactions are described in terms similar to those that have been applied for consideration of polyion exchange reactions (6). A reaction with a participation of water-soluble nonstoichiometric IPECs comprising fluorescently labeled $PMA^-$ anions as HPE* and $P4VPQ^+$ cations as GPE-quenchers was studied. On addition of polyanions containing sulfo- or sulfonate groups to these systems, a full transfer of GPE chains from IPEC* particles onto polysulfo/sulfonate anions is observed, as illustrated by Scheme (10):

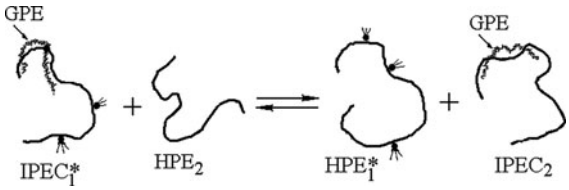


(10)

This process is accompanied by enhancing fluorescence, which is a measure of the shift of the equilibrium of the reaction shown in (10) from left to the right. Experimentally observed [7, 8] extremely high selectivity of interpolyelectrolyte interaction is explained by additional donor–acceptor interactions between the electron-donating sulfo/sulfonate groups of $HPE_2$ and the electron-accepting pyridinium groups of GPE. Even at rather low values of the energy of the non-Coulomb interaction between monomer units of the oppositely charged polymeric components, the total energy of the additional interaction of GPE chains with a $HPE_2$ chain, which is summed over all GPE monomer units, is sufficiently high to provide an error-free recognition and an almost complete selectivity of the interpolyelectrolyte coupling.

Published works [7, 38, 39] convincingly demonstrated that in a complex biological environment (e.g., in blood plasma) polycations find highly sulfated polysaccharides (e.g., heparin) in the system in an error-free manner. Polycations form stable IPECs with heparin, thereby suppressing its activity as a blood anticoagulant. Further detailed investigation on the kinetics and equilibrium of interpolyelectrolyte substitution reactions have provided a basis for the development of complex heparin antagonists with low toxicity and an improvement in systems for immunodiagnostics [7].

Thus, self-organization processes are widely represented in complex interpolyelectrolyte systems. The kinetics of such processes can be finely tuned by varying environmental conditions, in particular, by changing the concentration of low molecular weight salts. The course of the process can be controlled by incorporating “anchor” groups into the polymeric components of IPECs as well as by a directed choice of polyion competitors that differ in the chemical nature of their ionic groups. These phenomena have been considered on the nanometer scale, which corresponds to the typical size of charged macromolecules.

Self-organization processes proceeding in IPECs are not limited by the nanometer scale, pronouncedly manifesting themselves on the scale corresponding to mesostructures and in bulk. The self-organization can lead to the selective formation of highly ordered structures. An example of such a structure is stoichiometric IPEC formed by $PA^-$ anions and protonated linear poly(ethylene imine) (PEI) cations. The study of chemical transformations in such macromolecular co-assemblies provided evidence that more than about 80% (mol) of interpolymer salt bonds can be converted to covalent amide bonds, as illustrated by Scheme (11):

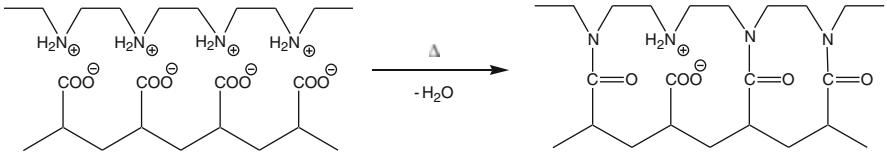


(11)

The reaction (11) proceeds at a temperature of 170–270°C in solid glassy specimens. The high yields are due to high ordering of both the original IPEC and the reaction product [8, 40, 41]. From an application point of view, these processes are extremely useful for chemical modification of such macromolecular co-assemblies with the aim of enhancing their stability in aggressive media and improving their mechanical properties. The structured IPECs {PAA-PEI} are found to be suitable macromolecular templates for the design of novel metallo-containing IPECs, which contain transition and/or heavy metal ions sandwiched between the polymeric components [42].

During the last decade, the potential for synthesis and construction of novel complex multicomponent self-organized IPEC-based structures has considerably increased as polyelectrolytes and polyionic species with nonlinear topology have become available. Among those are polymeric micelles with polyelectrolyte coronas, star-shaped polyelectrolytes, and cylindrical polyelectrolyte brushes. Polyionic species of such types themselves possess often a pronounced capability for self-organization, which is expected to be enhanced when they are incorporated into complex macromolecular structures such as IPECs. The advanced IPECs based on polyionic species with nonlinear topologies are considered in Sect. 3 of this review.

## 3 Advanced Interpolyelectrolyte Complexes

Further progress in the field of IPECs has been associated with involvement of more complex polyionic architectures, such as branched ionic (co)polymers (polyelectrolyte stars and cylindrical polyelectrolyte brushes) as well as self-assemblies of linear ionic diblock copolymers (polymeric micelles) (Fig. 6a–c), into interpolyelectrolyte complexation. Synthesis of well-defined polymeric architectures with nonlinear topology has become possible only recently due to considerable developments in living and controlled polymerizations. In this section, we briefly

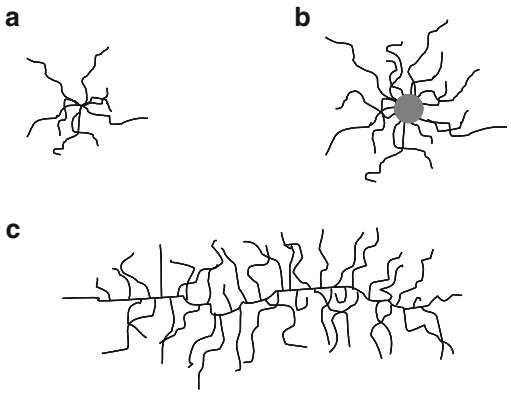


**Fig. 6** A polyelectrolyte star (**a**), a micelle with a polyelectrolyte corona (**b**), and a cylindrical polyelectrolyte brush (**c**)

consider and update the main achievements regarding the preparation and investigation of such advanced IPECs, which are also reported in a recent review [43].

The increasing interest to IPECs based on polyionic species of nonlinear topology is mainly due to the possibility of using them as a basis for building (optionally, to template) easily available and multifunctional polymeric architectures, which are of high potential for applications in rapidly developing nanotechnologies connected with such important areas as nonviral gene delivery, targeted/prolonged drug delivery, preparation of nanosized catalytic systems, etc.

## *3.1 IPECs Based on Star-Shaped (Co)Polymers*

Star-shaped polymers (also referred to as polymer stars or star polymers) represent isotropic centrosymmetric macromolecules, each containing a single branching point in a center of a macromolecule (Fig. 6a). They can be prepared via a "core-first" or an "arm-first" approaches. The branching point represents a small core remaining from an oligofunctional initiator ("core-first" approach), which is used to polymerize arms, or from a multifunctional cross-linker ("arm-first" approach), which is used to cross-link arms. The core determines the number of arms while the arms determine the overall size of the synthesized polymer star. Macromolecules of star-shaped polymers are characterized by a well-defined size (in the nanometer range) and a spherical morphology, both resulting from their inherent structuring.

Successful synthesis of well-defined star-shaped ionic (co)polymers [44] is a prerequisite for preparation of their IPECs. In connection with this, we consider papers [45, 46] that report on water-soluble IPECs with a star-shaped polyion, e.g., poly(sodium acrylate) (PANa) stars, acting as HPE. Water-soluble IPECs are formed when charged groups of the star-shaped HPE are in certain excess compared to charged groups of its polymeric counterpart (P4VPQ). Otherwise, macroscopic

phase separation (precipitation) is observed in mixtures of the oppositely charged polymeric components. It was found that the number of arms of the star-shaped HPE determines a window of Z-values, which correspond to the formation of water-soluble nonstoichiometric IPECs, this effect becoming more pronounced with increasing ionic strength of the surrounding solution [45].

A structural picture of complex species based on PANa stars was ascertained for the star-shaped HPE having a large number of arms (21 arms) coupled with a short linear polycation, quaternized poly(2-vinylpyridine) (P2VPQ), acting as a GPE [46]. The authors suggested that each complex particle formed has a compartmentalized structure of micellar (core–corona) type. A hydrophobic complex core is composed of oppositely charged segments of the polymeric counterparts while a hydrophilic corona, which grants to the whole macromolecular co-assembly solubility in aqueous media, is built up from excess segments of HPE (Fig. 7). If the total number of charged groups of the star-shaped HPE exceeds the degree of polymerization of the linear GPE, then typically one polyelectrolyte star, whose charge is partially compensated by chains of its polymeric counterpart, is incorporated into each complex particle formed [45, 46].

An examination of such systems by means of molecular dynamic simulations (Fig. 8) supported a proposed core–corona structure of nonstoichiometric IPECs based on star-shaped polyions and further refined their structural picture [47]. It was shown that some of the arms of the star-shaped HPE are completely charge-compensated by chains of the linear GPE and embedded into the core while the remaining arms are free and build up an ionic corona (Fig. 8b). This pronounced partition of arms between two populations explains an experimentally observed hydrodynamic size invariance (or a slight change in a hydrodynamic size) of the star-shaped HPE upon its loading with the oppositely charged linear GPE [45].

IPECs of very complex morphologies, such as long fibers forming fiber bundles or double wall vesicles tending to aggregate, were observed upon the interaction of oppositely charged cationic and anionic polyelectrolyte stars in extremely dilute aqueous solutions, e.g., quaternized poly[2-(dimethylamino)ethyl methacrylate] (PDMAEMAQ) stars and poly(methacrylic acid) (PMAA) stars, both having six arms [48]. By adjusting the molecular weights of the star-shaped polyelectrolytes, their concentrations, the matching degree of oppositely charged polymeric components, and preparation conditions, it is possible to tune different morphologies of the resulting IPECs.

To broaden the window of $Z$-values corresponding to the formation of water-soluble IPECs, star-shaped polyions can be complexed with double hydrophilic (bis-hydrophilic) diblock copolymers comprising an ionic block and a nonionic hydrophilic block. In this case, the formed macromolecular co-assemblies remain water-soluble even if oppositely charged groups of the polymeric counterparts are taken in 1:1 ratio ($Z = 1$) [49], provided that the length of hydrophilic nonionic block is sufficiently long. Apart from the enhanced water-solubility of the formed complex species, one can additionally impart new properties and desired functionalities, such as biocompatibility, thermosensitivity, etc., through the hydrophilic nonionic block of the copolymer.

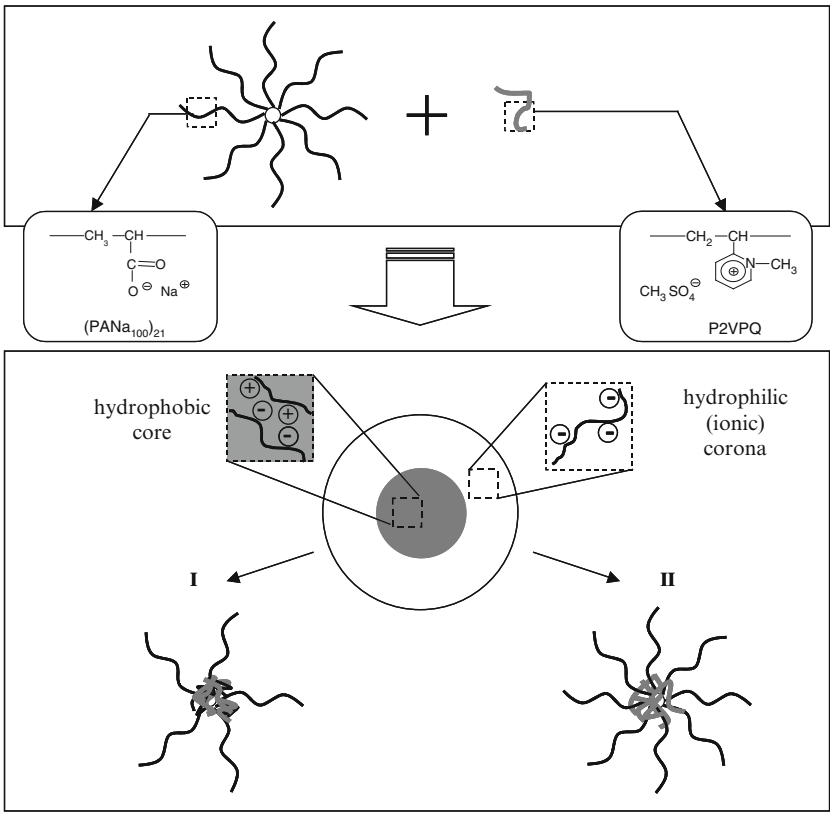


**Fig. 7** Core–corona structure of the water-soluble IPECs formed by the star-shaped PANa (HPE), having a large number of arms, with the linear P2VPQ (GPE). Reprinted with kind permission from Springer Science + Business Media from [46] Copyright 2009, MAIK Nauka/Interperiodica

It was found that each complex particle formed in mixtures of PANa stars and P2VPQ-*block*-poly(ethylene oxide) (P2VPQ-*b*-PEO) at $Z = 1$ is of a distinct micellar (core–corona) structure. Here, a hydrophobic complex core is composed of oppositely charged segments of the polymeric counterparts while a hydrophilic corona, which provides solubility in aqueous media to the whole macromolecular co-assembly, is built up from nonionic blocks of the bis-hydrophilic diblock copolymer (Fig. 9). In this case, several polyelectrolyte stars, whose charge is fully compensated by the ionic blocks of its polymeric counterpart, are typically (though not always) incorporated into each complex particle [49], their number being determined by the number of arms of the star-shaped polyion and degree of polymerization of the ionic block of the bis-hydrophilic diblock copolymer.

Similar micelle-like macromolecular co-assemblies were reported [50] for an anionic star-shaped bis-hydrophilic heteroarm copolymer PMAA-PEO coupled with a cationic bis-hydrophilic diblock copolymer, PDMAEMAQ-*block*-PEO (PDMAEMAQ-*b*-PEO), in alkaline media. In this case, however, the PEO blocks of both polymeric counterparts form a hydrophilic corona of each of the complex species formed.

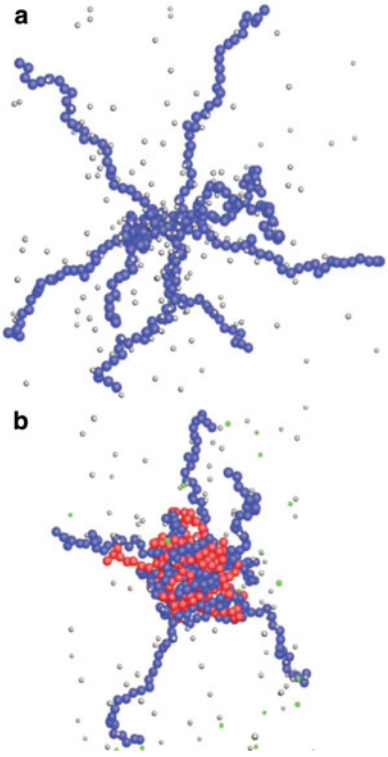


**Fig. 8** Snapshots of the typical conformations of (**a**) a bare (uncomplexed) polyelectrolyte star and (**b**) its IPEC with the linear GPE. Reprinted with permission from [47] Copyright 2009 American Chemical Society

During recent years, IPECs based on star-shaped (co)polymers with nucleic acids (also referred to as polyplexes) have attracted considerable attention in the context of nonviral gene delivery [51–56]. In particular, polyplexes of star-shaped PDMAEMA, having three and five arms, with DNA were shown to combine acceptable transfection efficiency with lower cytotoxicity [56].

## *3.2 IPECs Based on Star-Like Micelles of Diblock Copolymers*

Ionic amphiphilic diblock copolymers are well known to self-assemble into core–corona aggregates (micelles) in aqueous media. The micelle comprises a hydrophobic core formed by nonpolar blocks and a hydrophilic corona built up from polyelectrolyte blocks. The properties of such macromolecular self-assemblies are reviewed in detail elsewhere [57, 58]. In many cases, the micelles are characterized by a spherical morphology. When the radius of the hydrophobic core is considerably smaller than the thickness of the polyelectrolyte corona, such macromolecular self-assemblies are regarded as star-like micelles (Fig. 6b).

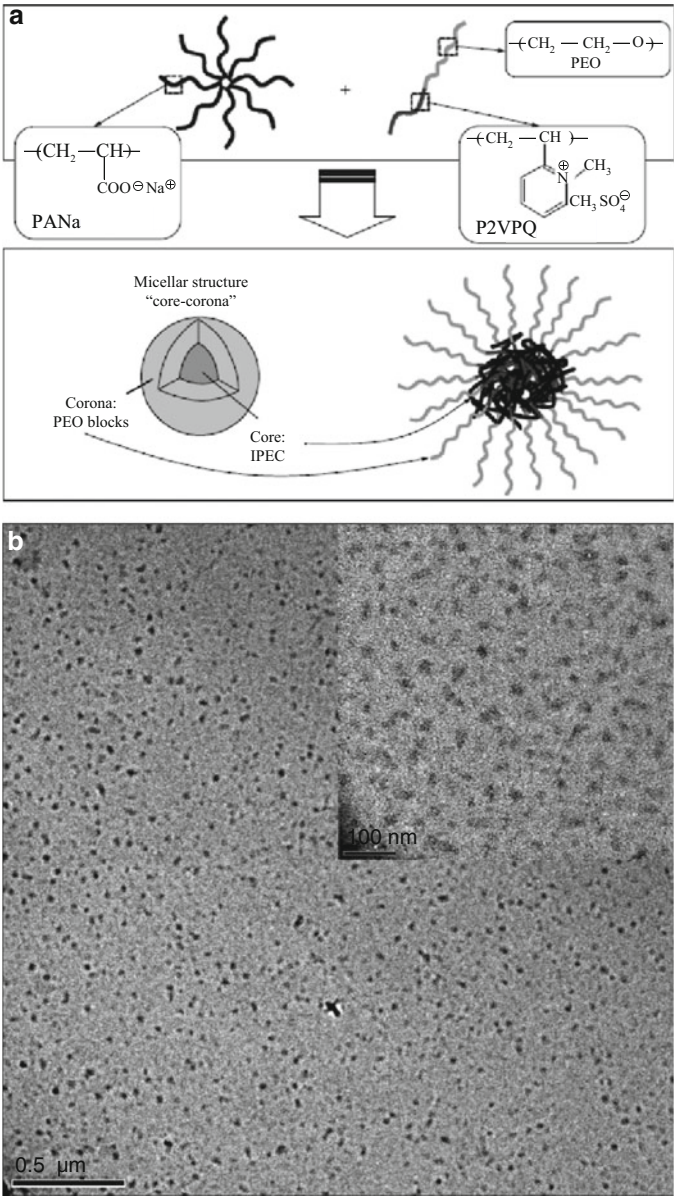


**Fig. 9** (**a**) Core–corona structure of IPECs formed by the star-shaped PANa fully charge-compensated with P2VPQ-*b*-PEO. (**b**) Cryogenic transmission electron microscopy (cryo-TEM) image of the IPEC cores. Reprinted with kind permission from Springer Science + Business Media from [49] Copyright 2011, Pleiades Publishing, Ltd.

They resemble star-shaped polyelectrolytes with a large number of arms, though the number of arms in such macromolecular self-assemblies might change if the micelles are of "dynamic" nature, that is, if they are able to change their aggregation numbers with variations in the environmental conditions. Historically, the micelles of ionic amphiphilic diblock copolymers were the first star-like polyionic species involved in interpolyelectrolyte complexation and their IPECs have attracted considerable attention during the recent years.

Because the micelles generated by ionic amphiphilic diblock copolymers in aqueous media possess polyelectrolyte coronas, they are naturally expected to form IPECs with oppositely charged polyions. To the best of our knowledge, the first attempt to study interpolyelectrolyte complexation in such systems was performed by Talingting et al. [59], who reported a study on the interaction of protonated polystyrene-*block*-poly(2-vinylpyridine) (PS-*b*-P2VPH$^+$) micelles with linear PSSNa of different molecular weights. Under a considerable excess of PSSNa to avoid any bridging or aggregation by linear polyions, the formation of macromolecular co-assemblies with a large mass excess (by a factor of ca. 5–6) of the charged groups of the PSSNa over charged groups of P2VPH$^+$ was found, thereby leading to charge inversion of the PS-*b*-P2VPH$^+$ micelles. This concomitant massive charge overcompensation resulting from the considerable molar excess (ca. 4.7–5.5) of sulfonate groups over pyridinium ones causes the formed IPECs to be colloidally stable.

Water-soluble (or colloidally stable) IPECs formed by oppositely charged micelles with polyelectrolyte coronas and linear polyions were subsequently found for a number of other systems. In particular, a detailed characterization of such macromolecular co-assemblies was performed for polyisobutylene-*block*-poly (sodium methacrylate) (PIB-*b*-PMANa) micelles complexed with a linear P4VPQ [60–62]. It was found that the formed IPECs remain water-soluble only when loading of the original micelles (acting as a HPE) by the linear polyion (acting as a GPE) does not exceed a certain threshold value. Such nonstoichiometric IPECs were thoroughly examined by means of various techniques, which provided evidence on their peculiar core–shell–corona (also referred to as "onion-like") structure (Fig. 10a). Specifically, each of the complex species comprises a hydrophobic core from nonpolar blocks, which is surrounded by a layer (inner shell) assembled from oppositely charged segments of the polymeric counterparts, and a hydrophilic corona (outer shell) from excess segments of ionic blocks, which do not form interpolymer salt bonds.

A similar multilayer structure with an inner complex shell was also proposed for IPECs formed by PS-*b*-P4VPQ, PS-*b*-PANa, and PS-*b*-PMANa micelles complexed with oppositely charged linear polyions [63–65]. In these cases, a polyelectrolyte corona is formed either by excess segments of ionic blocks of the copolymer (no overcharging of the original micelles by the linear polymeric counterpart) or by excess segments of the linear polyion (overcharging of the original micelles by the linear polymeric counterpart), depending on the actual ratio between molar concentrations of charged groups of the polymeric components in the system.

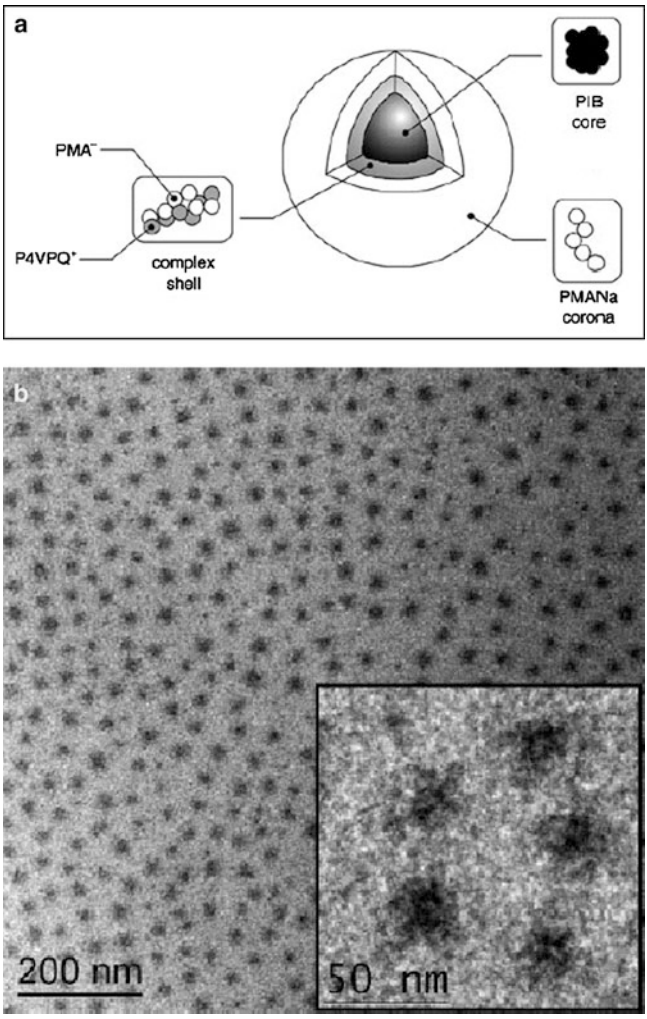


**Fig. 10** (**a**) "Onion-like" core–shell–corona structure of IPECs formed by the star-like PIB-*b*-PMACs micelles (HPE) with the linear P4VPQ (GPE). Reprinted from [61] Copyright 2004 with permission from Elsevier. (**b**) Cryo-TEM image of the micellar IPECs. Reprinted with permission from [62] Copyright 2008 American Chemical Society

As in the case of star-shaped polyelectrolytes described in Sect. 3.1, the micelles acting as HPE demonstrate only minor changes in their hydrodynamic size upon interaction with oppositely charged linear polyions [61–64]. This finding strongly suggests that, similarly to IPECs based on polyelectrolyte stars, the ionic blocks forming a polyelectrolyte corona of such complex species split into two populations: a certain number of such blocks are fully embedded into the complex inner shell, while the rest of the coronal blocks remain nearly free, thereby being responsible for solubility of the whole macromolecular co-assembly in aqueous media.

It was found that the aggregation numbers of the original micelles hardly changes upon their interaction with the oppositely charged linear polyions [61–64]. This remarkable invariance of the aggregation numbers was observed not only for "frozen" micelles such as PS-*b*-P4VPQ [63, 64] with a glassy PS block but also for "dynamic" micelles such as the PIB-*b*-PMANa [61, 62] with a soft PIB block, which can change their aggregation numbers with variations in environmental conditions [66]. This implies that the micelles act as peculiar macromolecular templates or "nucleating" particles for a buildup of core–shell–corona architectures. At the same time, it was shown that interpolyelectrolyte complexation does not render the dynamic PIB-*b*-PMANa micelles frozen as their aggregation numbers remain nevertheless sensitive to variations in the conditions of the surrounding solution (e.g., pH) [62].

Finally, we should mention that IPECs based on micelles of ionic amphiphilic diblock copolymers can participate in so-called polyion interchange (exchange and substitution) reactions, accompanied by a transfer of GPE chains from one to another HPE micelle. Such reactions were previously thoroughly investigated for aqueous mixtures of oppositely charged linear polyelectrolytes [8, 31, 36, 67]. It was found that the aggregation state of the polymeric component(s) involved in such polyion interchange reactions has a remarkable effect on the reaction rate [68]. Specifically, the rate of the polyion interchange reaction decreased in the following order: coil–coil (seconds) > coil–micelle (tens of seconds) > micelle–micelle (thousands of seconds). A similar tendency was also observed for polyion coupling (polyion addition) reactions, which result in the formation of IPECs, though in this case the complexation between oppositely charged micelles (a micelle–micelle system) was not examined [68].

### *3.3 IPECs Based on Cylindrical (Co)Polymer Brushes*

Cylindrical polymer brushes (also referred to as molecular polymer brushes or "bottle-brushes") represent anisotropic macromolecules with cylindrical symmetry, each containing a long linear backbone and a large number of rather short linear side chains, which are densely attached to the backbone (Fig. 6c). Therefore, they have a multitude of branching points located along the backbone. Cylindrical polymer brushes can be synthesized via "grafting-from", "grafting-to", or "grafting-through" approaches. Macromolecules of cylindrical polymer brushes exhibit a distinct worm-like morphology, which results from their pronounced anisotropic nature.

Recent advances in the synthesis of well-defined cylindrical ionic (co)polymer brushes, which represent another type of branched ionic polymers [44], offer the possibility of preparing their IPECs. An early attempt to obtain such macromolecular co-assemblies was made [69, 70] and describes formation of large complex aggregates with a rod-like cylindrical morphology resulting from the interaction of a PEO/PSSNa copolymer brush (so-called anionic prototype copolymer brush) with P4VPQ. These large rod-like co-assemblies are considered to be highly anisotropic supermicelles.

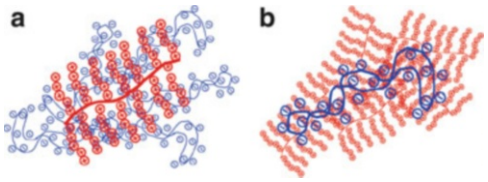


**Fig. 11** Charge mismatch for IPECs of cylindrical polyelectrolyte brushes with DNA: (**a**) excess of DNA and (**b**) excess of the cylindrical polyelectrolyte brush. Reprinted with permission from [71] Copyright 2007 American Chemical Society

IPECs formed between cylindrical polyelectrolyte brushes with P2VPQ or PEI side chains and DNA were examined [71]. It was found that, at a large excess of either of the polymeric counterparts, nanosized complex species coexist with the uncomplexed macromolecules of the excess polymeric component, thereby demonstrating an inhomogeneous distribution of macromolecules of the minority component among macromolecules of the excess one. This phenomenon was qualitatively explained in terms of the kinetically controlled formation of IPECs in such systems. The large charge density mismatch between the P2VPQ or PEI brushes and DNA was supposed to result in the formation of strongly positively charged complex species at an excess of the charged groups of the brushes and a slightly negatively charged complex species at an excess of the charged groups of DNA (Fig. 11).

It has been reported that IPECs based on cylindrical ionic (co)polymer brushes formed when macromolecular co-assemblies were prepared in organic solvents [72, 73]. To dissolve polymeric components to be involved in interpolyelectrolyte complexation in such solvents, a PSS brush with dodecylammonium counterions (PSS DDA) and a PEI/PEO copolymer brush were used. In particular, it was shown [72] that in dimethylformamide one can obtain both kinetically controlled and topologically controlled IPECs, depending on the "charge" of the PEI/PEO brush created by adding HCl. The interaction of the PSS DDA brush with the protonated PEI/PEO brush resulted in kinetically controlled IPECs whereas the interaction with the non-protonated PEI/PEO brush led to topologically controlled IPECs of a cylindrical morphology. The formation of similar topologically controlled IPECs was also observed for the PSS DDA brush interacting with a polyamidoamine dendrimer of the fifth generation in such organic solvents as dimethylformamide or *N*-methylformamide, whereas kinetically controlled macromolecular co-assemblies were formed in methanol [73].

Water-soluble nonstoichiometric IPECs formed by a cylindrical PAA brush (acting as a HPE) and linear P4VPQ (acting as a GPE) are described [74]. Similarly to the water-soluble IPECs based on PAA stars considered in Sect. 3.1, they are formed only when charged groups of the HPE brush are in a certain excess compared to charged groups of the linear GPE. Under this condition, IPECs based on the PAA brush exhibit a hydrodynamic size that is very close to that of the original brush, and P4VPQ chains are uniformly distributed among its macromolecules. Solubility of such macromolecular co-assemblies in aqueous media points to their core–corona

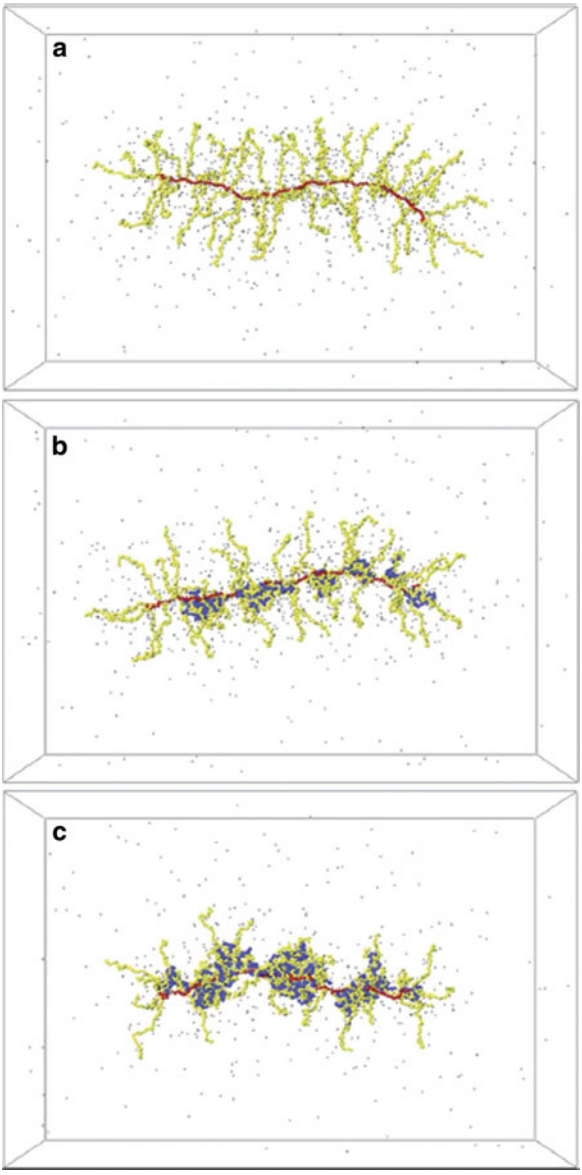


**Fig. 12** Snapshots of the typical conformation of (**a**) the bare (uncomplexed) cylindrical polyelectrolyte brush, and (**b,c**) its IPECs with the linear GPE at the degrees of charge compensation of 0.25 (**b**) and 0.5 (**c**). Reprinted from [74] with permission from the Royal Society of Chemistry Copyright 2009

structure. Their structural organization was further examined by means of molecular dynamics simulations [74]. The snapshots resulting from the simulations (Fig. 12) clearly demonstrate the formation of a necklace of core–corona pearls, each consisting of a hydrophobic complex core made from oppositely charged segments

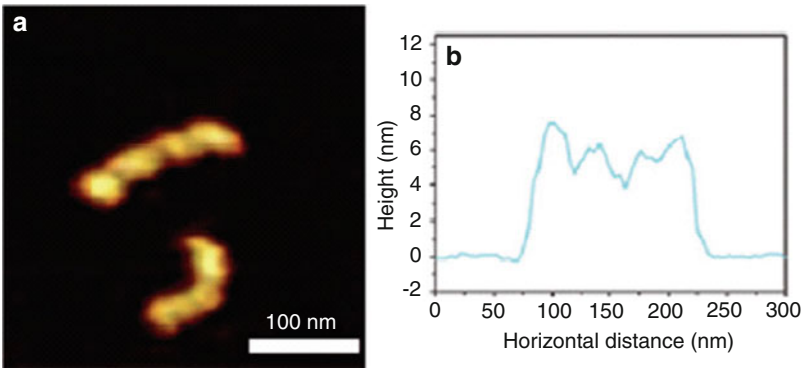


**Fig. 13** (**a**) AFM image of IPEC formed by the PDMAEMAQ brush (HPE) with linear PSSNa (GPE). (**b**) Section analysis of the upper species. Reprinted with permission from [75] Copyright 2010 American Chemical Society

of the polymeric counterparts, which is decorated by a hydrophilic corona built up from excess side chains of the cylindrical polyelectrolyte brush. This leads to a nanopatterned structure with longitudinal undulations. It is remarkable that such longitudinal undulations were experimentally observed for IPECs based on a PDMAEMAQ brush complexed with a short linear PSSNa [74, 75] (Fig. 13). Similarly to the IPECs based on PAA stars described in Sect. 3.1, side chains of the cylindrical polyelectrolyte brush demonstrate distinct repartitioning between the corona and the complex core domains; that is, some of the side chains of the HPE brush are nearly completely charge-compensated by chains of the linear GPE and embedded into the cores while the remaining side chains are free and build up coronas of the pearls (Fig. 12).

A possibility for manipulating the morphologies of cylindrical polyelectrolyte brushes via their complexation with oppositely charged linear polyions has been described [75]. In particular, it was found that increased loading of a PDMAEMAQ brush with a short linear PSSNa induces morphological changes of the original brush from a worm-like structure through an intermediate pear-necklace structure to fully collapsed spheres. However, an extremely long linear PSSNa resulted in a transition of the PDMAEMAQ brush to fully collapsed spheres, without intermediate states, even at very low loading by the linear GPE. As described previously [71], a pronounced inhomogeneous distribution of PSSNa chains (the minority component) among macromolecules of the PDMAEMAQ brush (the excess component) was observed.

Cylindrically shaped dendronized polymers resemble cylindrical polyelectrolyte brushes to a certain extent. The interaction of highly charged cationic dendronized polymers with DNA was examined [76]. It was shown that DNA wraps around such polymers, the overall charge of the formed IPECs and pitch size of the wrapped DNA being determined by dendron generation. These macromolecular co-assemblies might be used for development of novel nonviral gene delivery systems.

## 4 Metallo-Containing Interpolyelectrolyte Complexes

Polymer–metal hybrids based on polyelectrolyte systems have attracted growing interest during recent decades [77–79]. Metallo-containing compounds can provide polymer materials with special optical, electrical, magnetic, and mechanical properties as well as catalytic activity [77–81]. The capability of functional groups on polyelectrolytes to bind metal ions offers a possibility for their application as sorbing agents, ion-exchange materials, components of selective membranes [81–83], or as precursors for preparation of polymer–inorganic hybrids via reduction or precipitation of metal ions [81–85]. Polymer–inorganic nanocomposites are important candidates for construction of photonic devices, band-pass filters, components of nonlinear optical systems, optical limiters, elements of microcircuit chips, etc. [78, 79, 86]. Polyelectrolyte-based materials, including ultrafine particles of silver and noble metals, exhibit antibacterial properties and are therefore promising for application in medicine [87–90].

Metal ions coordinated with functional groups of polyelectrolytes may be used as a motif for assembling supramolecular and colloid systems [80, 91–93]. Polymer colloids and nanocomposites are very important as heavy metal carriers [80]. The dynamic nature of the coordination bonds between functional groups of polyelectrolytes and metal ions provides switchability to the system, mimicking the behavior of natural suprastructures [94]. The application of ionic amphiphilic block copolymers and terpolymers as templates for nanostructured systems or as precursors for synthesis of polymer–metal hybrids with different architectures [95–97] might be advantageous for design of prototypes for advanced catalytic, medicine-relevant, and electronic systems.

Sequences of interpolymer salt bonds built up by monomer units of oppositely charged polyelectrolytes form nanosized, structured domains from coupled functional groups. In some cases [8, 40, 41], even a perfect ladder-like arrangement of interpolymer salt bonds has been demonstrated. Such nanosized structured domains may act as scaffolds for sandwiching metal ions, which are incorporated (e.g., via the formation of coordination bonds with functional groups of the polymeric components) into the macromolecular co-assemblies with high selectivity [81]. The great variety of structures realized by IPEC-based systems, combined with the possibility of controlling the interaction of functional groups of the polymeric components with metal ions, has provoked a great interest in development of such novel functional materials.

This section describes, first, IPEC-based systems that contain metal ions. Then, a preparation of polymer–inorganic hybrids comprising metal nanoparticles (NPs) embedded into IPEC matrices is considered. Finally, advanced structures based on IPECs containing metal ions and IPEC-based hybrids containing metal NPs are reviewed.

## 4.1 IPECs Containing Metal Ions

The high dialysis permeability of IPECs allows transport of metal ions through the complex polymer matrix. An attractive possibility for an application of IPECs as sorbents or ion-exchange materials has stimulated considerable interest in the process of embedding metal ions into such macromolecular co-assemblies, distribution of metal ions throughout the complex polymer matrices, and their complexation with functional groups on the polymeric components. The preparation of nanocomposites in polyelectrolyte systems is another important stimulus for preparation of IPECs with a controlled content and regulated distribution of metal ions [81].

To study sorption of metal ions by IPECs and the formation of metallo-containing macromolecular co-assemblies based on them, both stoichiometric and nonstoichiometric IPECs {PAA-PEI} were used [81, 98, 99]. The interaction of metal ions with the IPECs implies sandwiching of these ions between PAA and PEI, being coordinated by their functional groups, which results in the formation of triple (tricomponent) macromolecular co-assemblies containing metal ions, as shown in (12):

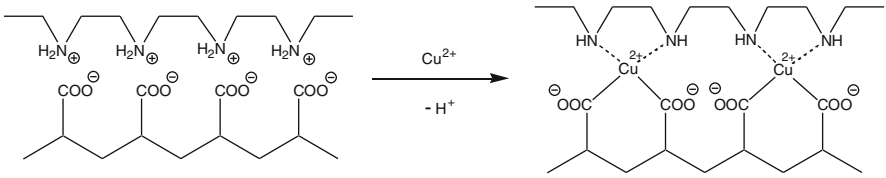


(12)

The scheme shown in (12) demonstrates that the sorption of metal ions by IPECs causes the pH of the environment to decrease. To shift the equilibrium, it is necessary to add alkali, which leads to structures with a high content of incorporated (sandwiched) metal ions.

Generally, the ligand environment of metal ions includes functional groups of both PAA and PEI. The formation of the triple macromolecular co-assemblies containing metal ions results in coloration of initially colorless IPECs. For example, IPEC films become deeply dark blue in the case of $Cu^{2+}$ whereas incorporation of $Ni^{2+}$ leads to a green coloration. Therefore, the coloration of the IPEC {PAA-PEI} films is a qualitative indicator of transformation of the IPEC into metallo-containing macromolecular co-assemblies. The structure of {PAA-$Cu^{2+}$-PEI} was revealed by means of electron paramagnetic resonance (EPR) [99]. The application of EPR provides direct information about coordination of paramagnetic metal ions with functional groups on the polymeric components. Figure 14 shows the characteristic EPR signals of $Cu^{2+}$ incorporated into IPEC {PAA-PEI} films with different stoichiometries in different ligand environments.

In the stoichiometric IPECs, $Cu^{2+}$ may exist in two ligand environments (Fig. 14b), i.e., 4 NH (see (13), structure A) or 2 NH and 2 $COO^-$ (see (13), structure B). However, the ligand environment with 2 NH and 2 $COO^-$ groups was shown to

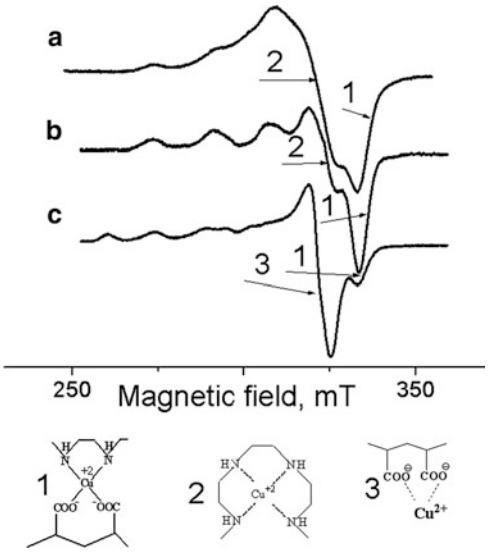


**Fig. 14** EPR spectra of the triple metallo-containing macromolecular co-assembly {PAA-$Cu^{2+}$-PEI} with $Cu^{2+}$ content of 6% (wt) where [PAA]:[PEI] = 1:9 (*a*), 1:1 (*b*), and 9:1 (*c*). *Arrows* point to different ligand environments: (*1*) 2 NH and 2 $COO^-$, (*2*) 4 NH, and (*3*) 2 $COO^-$

be preferable for $Cu^{2+}$. The ratio between structures A and B in the triple macromolecular co-assembly depends on the proportions of the reagents and the pH of the solution [81, 99]. The EPR spectra point to a gradual increase in the linewidth observed with rising of $Cu^{2+}$ content in IPECs, thereby suggesting a relatively uniform distribution of metal ions throughout the complex polymer matrices.

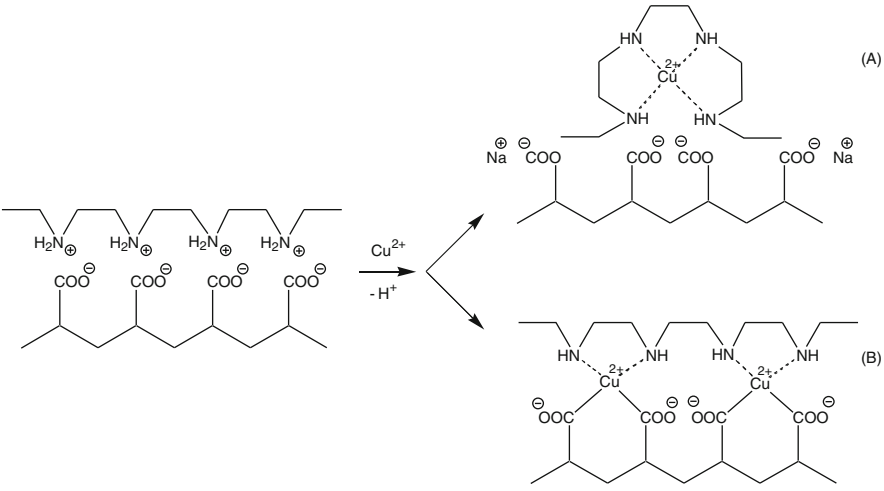


(13)

**Table 1** Sorption characteristics of the stoichiometric IPEC {PAA-PEI}

| Metal ion | Ion-exchange capacity % (wt) | Ion-exchange capacity mg-equivalent/g |
|---|---|---|
| $Cu^{2+}$ | 27 | 8.6 |
| $Co^{2+}$ | 20 | 6.8 |
| $Ni^{2+}$ | 20 | 6.8 |
| $Fe^{2+}$ | 6 | 3.0 |
| $Ag^{+}$ | 22 | 2.1 |

Table 1 demonstrates a high sorption capacity of the IPEC {PAA-PEI} films with respect to various metal ions. The largest capacity was found for $Cu^{2+}$ because the geometry of the functional groups of the polymeric counterparts in the IPEC fits suitably to that required for the ligand environment of the metal ion. The ion-exchange capacity in this case is as high as 8.6 mg-equivalent $Cu^{2+}$ per gram of the dry IPEC, that is, very close to that expected for structure B (13) of the triple macromolecular co-assembly {PAA-$Cu^{2+}$-PEI} with fully occupied ligand sites. Thus, IPECs may act as precursors for the further templated formation of polymer–inorganic hybrid structures containing metal ions. Such precursors are characterized by high regularity of an array of the metal-mediated coordination bonds between the polymeric components.

A transformation of IPECs into triple macromolecular co-assemblies containing metal ions leads to a considerable decrease in their degree of swelling in water (Table 2) and, accordingly, to a substantial increase in their durability. It was found that transition metal and silver ions sorbed by IPECs {PAA-PEI} are bound extremely strongly [81, 98, 99] due to the formation of coordination bonds with ligands of both polymeric counterparts and a chelating effect. For example, the IPEC {PAA-PEI} films were able to sorb $Cu^{2+}$ from aqueous solutions of $Cu(NO_3)_2$ at concentrations as low as $10^{-5}$ M. It is also the case for other metal ions, for example, $Co^{2+}$, $Ni^{2+}$, $Fe^{2+}$. This makes it possible to use the IPECs for effective extraction of metal ions from dilute aqueous solutions and for ion-exchange concentrating of metal ions for analytical purposes. The high sorption capacity of IPECs in combination with their stability both in alkali and acidic media (especially for thermally crosslinked IPECs {PAA-PEI}) provide the prerequisites for development of novel highly effective and easy-to-prepare sorbents or ion-exchange materials.

The method of a preparation of multilayer polyelectrolyte films by exposing a surface to solutions of a polyanion and a polycation in a cyclic (alternating) fashion was reported by Decher [100]. This became known as the “layer-by-layer” (LbL) technique, which fabricates free-standing multilayer polyelectrolyte films and films on solid substrates [101–103]. These polyelectrolyte-based systems arise from the cooperative ionic interaction between functional groups of polyanions and polycations at the interface. They may be considered as IPEC films with a heterogeneous distribution of the polymeric components. The incorporation of metal ions into such polyelectrolyte multilayer systems is a general approach for preparation of macromolecular co-assemblies containing metal ions. It was found that polyelectrolyte films prepared via the LbL technique are able to bind metal ions [82, 83, 103] as

**Table 2** The swelling degree of the stoichiometric IPECs {PAA-PEI} before and after incorporation of $Ni^{2+}$

| | Noncrosslinked IPEC | Crosslinked IPEC | IPEC, 10% (wt) $Ni^{2+}$, noncrosslinked | IPEC, 10% (wt) $Ni^{2+}$, crosslinked | IPEC, 20% (wt) $Ni^{2+}$, crosslinked |
|---|---|---|---|---|---|
| Degree of swelling | 160 | 44 | 42 | 45 | 36 |

they typically contain polyanions (such as PSSNa and PAA) and polycations [such as PEI, poly(allylamine hydrochloride) (PAH), and poly(*N*,*N*-diallyldimethylammonium chloride (PDADMAC)].

The functional groups of polyions can coordinate metal ions, thereby acting as ligands. The sorption of metal ions from solutions is a common way of embedding metal ions into multilayer polyelectrolyte films. For example, $Ag^+$ ions were incorporated into PAA/PAH multilayers from solutions of silver acetate [104]. A variation in the pH made it possible to change the content of metal ions in the films [105]. Also, palladium ions [104] were successfully included into PAA/PAH multilayers from aqueous solutions containing $[Pd(NH_3)_4]^{2+}$ ions. It should be mentioned that polyelectrolyte multilayers containing metal ions can be further used as precursors for preparation of polymer–metal nanohybrids [82, 83, 103–105].

Control of the assembly of multilayer polyelectrolyte films and the incorporation of metal ions provide the possibility for development of polymer matrices characterized by a varying content and distribution of the metal ions. The spatial localization of $Ag^+$ within multilayer polyelectrolyte films was realized using two different types of bilayer building blocks [104]. By adding fully ion-paired oppositely charged polyelectrolyte, a series of PAH/PAA bilayers, which do not include metal ions, can be inserted between the bilayers, which contain $Ag^+$. This technique allows one to prepare a sandwich-like metallo-containing film structure.

An alternative technique is based on a directed precoordination of metal ions with functional groups on polymers, which transforms them into polyions. This method was developed [106] for precursors of silver NPs synthesized in PEI/PAA films. Specifically, the PEI-$Ag^+$ polycation was used as a polymeric component for construction of polyelectrolyte multilayers with PAA.

Another approach for preparation of similar macromolecular co-assemblies containing metal ions, which is discussed in the literature [80, 92, 93, 107, 108], uses so-called “coordination polymers”. Use of bifunctional compounds with two terminal ligand groups, differing in a spacer length, demonstrates that chains and rings can be formed in aqueous solutions via coordinating metal ions [109]. An increasing solution concentration favors generation of chains (Fig. 15). This makes preparation of reversible coordination polymers possible [80, 109]. IPECs may include such coordination polymers as one of the polymeric components, though cationic molecules have been used so far. For example, LbL assemblies were obtained on planar substrates and surfaces of colloid particles using $Fe^{2+}$-metallo-supramolecular coordination polyelectrolytes (Fig. 16a) as polycations [108]. In this strategy, multilayer fabrication is achieved by repeated immersion of the substrates in solutions containing $Fe^{2+}$-metallo-supramolecular coordination polyelectrolytes and negatively charged polyions (Fig. 16b,c).

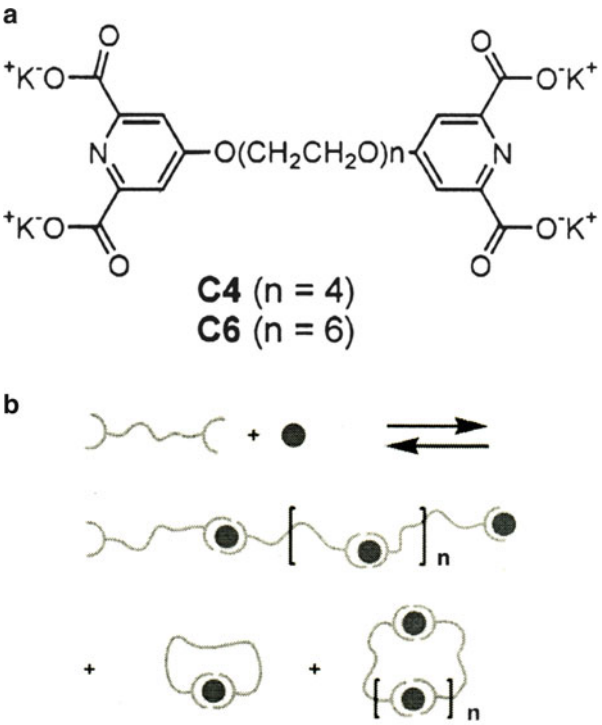


**Fig. 15** (**a**) Structure of water-soluble bifunctional ligands. (**b**) Schematic representation of the formation of coordination polymers and rings. Reprinted with permission from [109] Copyright 2003 American Chemical Society

## *4.2 IPEC Hybrids Containing Metal Nanoparticles*

A development of methods for preparation of polymer composites containing inorganic NPs is one of the hottest topics in nanoscience because of the unique electrophysical behavior, antibacterial and catalytic activity of such composites. During recent years, attention has been focused on elaboration of a simple single-stage method for production of polymer–metal hybrid materials directly in swollen polymer matrices via a reduction of metal ions incorporated into hydrogels [110–112] or bound to polyelectrolytes [81–85, 103–105, 113–117].

Due to simplicity, the chemical reduction of metal ions in a liquid phase is the most commonly applied approach for the preparation of NPs in aqueous and nonaqueous media. A number of compounds (aluminum hydrides, borohydride, hypophosphites, formaldehyde, salts of oxalic and tartaric acids, hydroquinone, hydrogen, hydrazine, etc. [77, 78]) can be used as reducing agents. A complete reduction usually requires multiple excess of a reducing agent. Generally, this approach is applicable for the synthesis of NPs of silver and noble metals. The NPs obtained through chemical reduction often contain impurities [78, 79]. A typical drawback of this approach is a broad size distribution of the generated NPs. However,

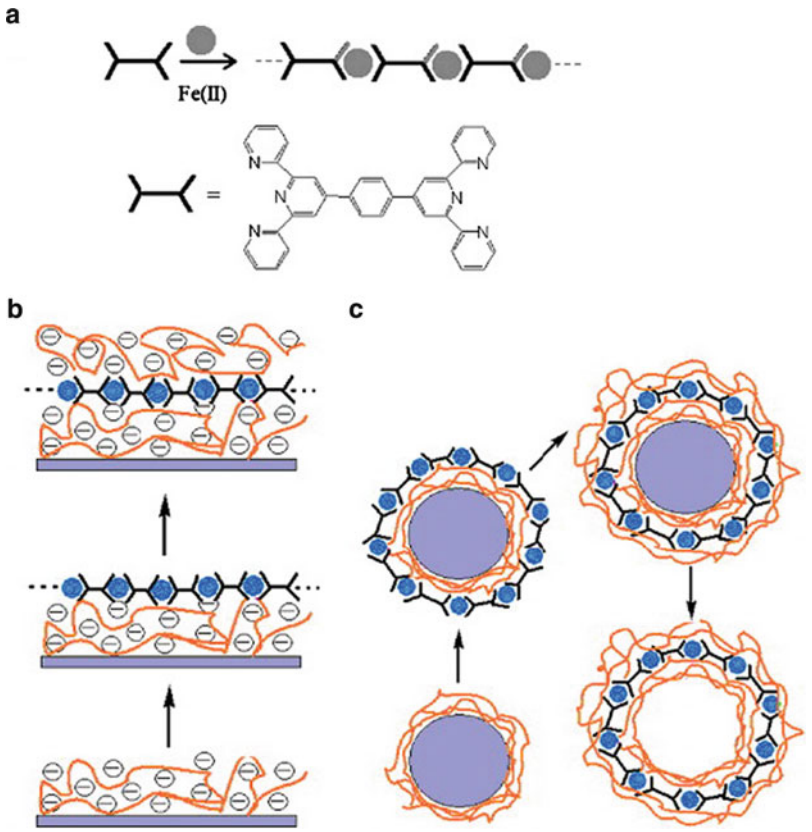


**Fig. 16** (**a**) Formation of $Fe^{2+}$-metallo-supramolecular coordination polyelectrolytes and a LbL assembly on planar (**b**) and spherical (**c**) surfaces derived from $Fe^{2+}$-metallo-supramolecular coordination polyelectrolytes and PSSNa. Reprinted from [80] Copyright 2010 with permission from Elsevier

chemical reduction in the presence of polymers may yield NPs of controlled sizes [78, 82–85, 103–105, 115, 116]. In this context, a specific technique [97, 112, 118, 119], whereby the polymers are used both as reducing agents of metal ions and for effective stabilization of the prepared NPs, should be mentioned.

Radiation–chemical approaches for the preparation of NPs were also found to be exceptionally useful, both for studying the processes that underlie the formation of NPs and for preparation of nanocomposites [81, 89, 90, 111, 114, 115, 120]. The main advantages of ionizing radiation for the preparation of NPs are control over the formation of reducing radiolysis products and controlled changes in the rate of reduction of metal ions in a broad interval [111, 120]. This method does not require any specific chemicals (reducing agents), thereby leading to NPs with high purity [78, 79, 111, 120]. Ionizing irradiation allows one to obtain NPs with a desired average size and a narrow size distribution [111, 120]. Due to high reduction potentials [121, 122] of radiolysis products, the radiation-induced

reduction makes it possible to prepare NPs from many metal ions (not only those of noble metals). The synthesis of copper NPs having a metal lattice is an illustrative example of the advantages of the radiation–chemical method, whereas chemical reduction, as a rule, leads to formation of copper protoxide [121].

Reduction or precipitation of metal ions is commonly applied for preparation of inorganic NPs by so-called intermatrix synthesis [81–85, 103–106, 113–117, 123–127] in polyelectrolyte matrices. Stabilization of inorganic NPs in polymeric matrices prevents their aggregation and, in addition, allows control of their growth rate and size. Polyelectrolytes or ion-exchange resins, which are filled by metal ions, are widely used precursors for fabrication of nanocomposites. The intermatrix synthesis technique has proved to be applicable for preparation of catalytically, electrocatalytically, and magnetically active composites with zero-valent metals (e.g., Cu, Pd, Ag, and others) via a chemical reduction of metal ions in matrices of cation-exchange resins. Due to the fact that functional groups of the polymeric component appear to be regenerated after each cycle (converted back into their initial ionic form), undertaking consecutive cycles with other metals will result in the formation of NPs with advanced structures (e.g., bimetallic core–shell, trimetallic core–sandwich, etc.) [116, 117]. A precipitation of metal ions opens the possibility to obtain nanocomposites on the basis of metal sulfide NPs [104, 116].

The advantages of synthesis of metal NPs in multilayer systems and their development are discussed in [103]. A number of studies [82–84, 104–106, 125–127] demonstrate that the LbL deposition of polyelectrolytes containing metal ions and subsequent reduction of these metal ions provides a straightforward technique for obtaining encapsulated NPs with a controlled size. Encapsulation into polymers appears to be advantageous because, apart from stabilization and protection of NPs, polymers offer unique possibilities for both a modification of the environment around catalytic sites and a change of access to these sites [103]. Various polyelectrolytes and metal ions with different binding activities can be used for assembling LbL-based hybrids, which are precursors for polymer–inorganic composites. Control of the precursor structure through conditions for a buildup of the LbL films and regimes of metal ion reduction provide prerequisites for the development of composites containing NPs with various sizes and even with different spatial distributions of NPs [105, 106]. The PAA/PEI films with silver NPs exhibit electrocatalytic behavior and antibacterial activity [106]. Palladium–nickel bimetallic core–shell NPs with magnetic properties were obtained by chemical reduction in the PAA/PAH films [123]. Through a chemical reduction, palladium NPs with a diameter of 2 nm were obtained as seeds for further growth of $Ni^{2+}$ shells, with control of their thicknesses (Fig. 17).

The LbL technique is widely applied for assembly of preformed NPs with oppositely charged polyelectrolytes [128–131]. The metal or semiconductor NPs of appropriate sizes in stabilizing media should be prepared before assembly of the LbL films. However, it appears to be quite difficult to realize an effective control over the concentration of NPs [103].

During the last few years, progress has been made in preparation of polymer–inorganic composites based on the LbL films, mainly related to membrane catalytic systems (Fig. 18). The LbL adsorption in porous polymeric membranes

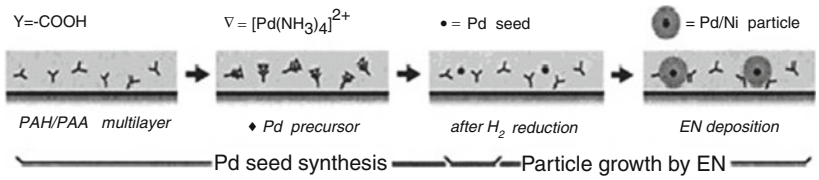


**Fig. 17** Intermatrix synthesis of palladium–nickel bimetal NPs in the multilayer film PAA/PAH. Reprinted with permission from [123] Copyright 2003 American Chemical Society

provides a simple way to create membrane catalysts. A universal approach for obtaining catalytic systems is a reduction of metal ions associated with charged groups of polyions, which constitute a film on the membrane, to obtain metal NPs [85, 125, 126] (Fig. 18c). On the other hand, the LbL adsorption of polyelectrolytes and a subsequent binding of preprepared gold or platinum NPs with charged groups on the polymers is an effective way of modifying the pores of hollow fibers and of developing catalytic membrane reactors [85, 125] (Fig. 18b).

IPECs containing metal ions swell in water and in water–organic media. Similarly to the precursor IPECs, they possess high permeability for polar low molecular weight substances and salts. These properties make it possible to reduce or precipitate metal ions directly in/into a polymeric matrix for a further preparation of inorganic NPs. Chemical and radiation–chemical approaches lead to composite materials with different structures [81, 114, 115, 132–134]. They contain NPs of metals or their oxides in matrices of IPEC {PAA-PEI}. The behavior of metallo-containing complex polymer materials is controlled by a size and a spatial distribution of the embedded NPs. An investigation of factors that regulate the formation of the metal NPs in the polymer matrices is of a key importance for a development of composites with required characteristics. Controlled variations in the content of the metal ions and their distribution in polymer samples [81, 115, 133] offer a unique opportunity to use IPECs to reveal such factors. The IPEC {PAA-PEI} loaded with metal ions has provided information about the main features of reduction of the metal ions, processes of nucleation and growth of the generated NPs as well as about the environmental conditions that control a spatial distribution of the NPs in the polymer matrices.

NPs of magnetic oxides show a pronounced superparamagnetic behavior. A polymer–inorganic hybrid material including particles of iron oxide was synthesized with the use of an IPEC and its magnetic properties were studied [134]. Alternative approaches were used for a preparation of metal nanoclusters. When IPEC films containing $Fe^{3+}$ are kept in an alkaline solution, iron hydroxide nanoclusters are formed. According to the low-temperature Mössbauer spectra, subsequent drying of the IPEC films at 60–70°C results in the formation of iron oxide NPs in the IPEC {PAA-PEI}:

$$\mathrm{PAA-Fe^{3+}-PEI + OH^- \rightarrow Fe(OH)_3 \text{ in IPEC } \{PAA-PEI\} \rightarrow Fe_2O_3}$$

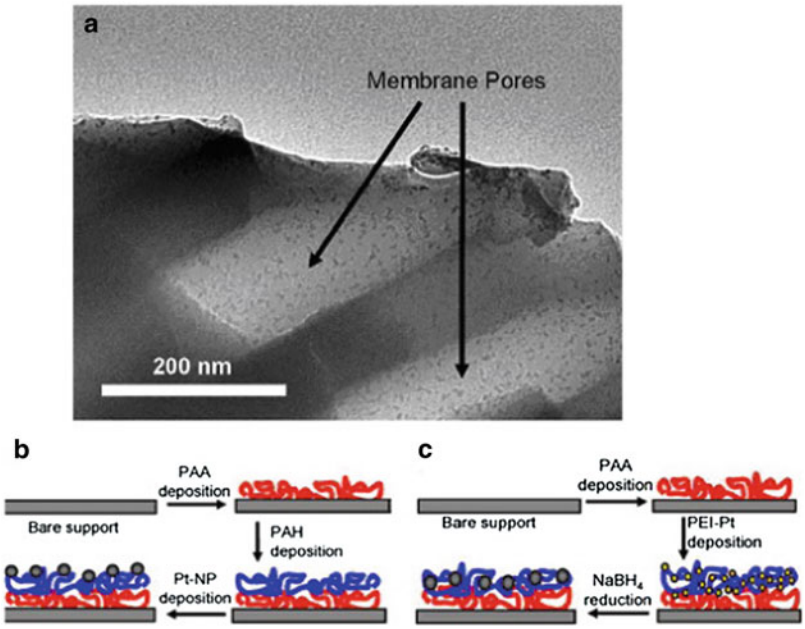


**Fig. 18** Membrane catalytic systems: (**a**) TEM images of pores of an alumina membrane modified with a PAA/PAH/(platinum NP) film. Modification of membrane pore surfaces using (**b**) the LbL deposition of PAA/PAH/(platinum NP) films, or (**c**) the LbL deposition of PAA/PEI-$Pt^{2+}$ films followed by a reduction. Reprinted from [125] Copyright 2009 with permission from Elsevier

The structure and properties of such polymer–inorganic hybrid materials substantially depend on the method of reduction of the metal ions [81, 114, 115, 132, 133]. The chemical reduction of $Cu^{2+}$ in IPEC matrices leads to the formation of copper protoxide NPs [81]. Micrographs of the irradiated film demonstrate that their size is of about 10 nm. The electric conductivity of the prepared hybrids is very low (Table 3).

The process of the reduction of $Cu^{2+}$ in IPECs {PAA-PEI} may be schematically described by the reaction:

$$NaBH_4 + PAA - Cu^{2+} - PEI + H_2O \rightarrow Na_3BO_3 + PAA - Cu^{+} - PEI + H_2 \uparrow$$

It is worth noting that the redox potential of $NaBH_4$ is $-1.24$ V [79]. The redox potential for $Cu^{2+}/Cu^{+}$ is $-0.15$ V, and that of a reduction of $Cu^{+}$ to metal atoms is $-2.9$ V [121]. For this reason, a chemical reduction of $Cu^{2+}$ leads to $Cu^{+}$ and, therefore, to the formation of copper protoxide NPs in an alkaline environment. Nanocomposites including $Cu_2O$ possess about the fivefold lower ion-exchange capacity of $Cu^{2+}$ in comparison to the initial IPEC films. The dramatic decrease in the ion-exchange capacity shows that considerable fractions of functional groups of PAA and PEI are blocked because of their interaction with copper prototoxide NPs, acting as active filler.

**Table 3** Electric conductivity of IPEC {PAA-PEI} and IPEC-based nancomposites

| Film | Conductivity $Ohm^{-1}\ cm^{-1}$ |
|---|---|
| IPEC {PAA-PEI} | $6 \times 10^{-10}$ |
| PAA-$Cu^{2+}$-PEI | $6 \times 10^{-7}$ |
| PAA-PEI-$Cu_2O$ | $3 \times 10^{-5}$ |
| PAA-PEI-Ni | 3.3 |

The chemical reduction of $Ni^{2+}$ in IPECs {PAA-PEI} results in metal NPs. The magnetization curves of dry films of the obtained nanocomposites qualitatively resemble those of metallic nickel [81], suggesting that the reaction proceeds as follows:

$$NaBH_4 + PAA - Ni^{2+} - PEI + H_2O \rightarrow Na_3BO_3 + Ni^0 + H_2 \uparrow$$

Table 3 demonstrates that this polymer–metal hybrid material shows a relatively high electric conductivity. The ion-exchange capacity of the obtained nanocomposite is several times lower than that of the IPEC precursor. This large effect indicates that nickel NPs strongly interact with the IPEC matrix as effectively as in the case of the IPEC-$Cu_2O$ nanocomposite. The swelling coefficient of PAA-PEI-Ni hybrids [10% (wt) Ni] obtained in matrices of noncrosslinked IPECs is about 100%. It considerably exceeds that for the triple metallo-containing IPEC {PAA-$Ni^{2+}$-PEI} (Table 2) but is lower than the value for the noncrosslinked IPEC {PAA-PEI}. This result proves the interaction between NPs and the IPEC matrix and shows that, similarly to copper protoxide NPs, ultrafine nickel NPs act as active filler.

The irradiation source and irradiation conditions influence the structure of the resulting hybrid materials [114, 115, 132, 133]. Microdifractograms (Fig. 19) and X-ray images show that copper, silver, nickel, and palladium NPs can be successfully obtained via reduction of the corresponding metal ions in the IPEC {PAA-PEI} films, using electron accelerators as well as X-ray and γ-radiation sources [81, 114, 115, 132, 133].

In the IPEC films irradiated in water–organic media, the species involved in the reduction of metal ions and the formation of NPs were primarily produced by the radiolysis of water [81, 114, 132, 133]:

$$H_2O \ \backslash/\backslash/ \rightarrow e^-_{aq}, {}^{\bullet}OH, {}^{\bullet}H,\ H_2,\ H_2O_2$$

The hydrated electrons, H atoms, and hydrogen can act as reducing agents. The OH radicals may oxidize metal atoms and ions in intermediate oxidation states. To increase the efficiency of the reduction processes, it is common to use scavengers of OH radicals (e.g., aliphatic alcohols):

$$CH_3CH_2OH + {}^{\bullet}OH \rightarrow CH_3{}^{\bullet}CHOH + H_2O$$

$$CH_3{}^{\bullet}CHOH \rightarrow CH_3CHO$$

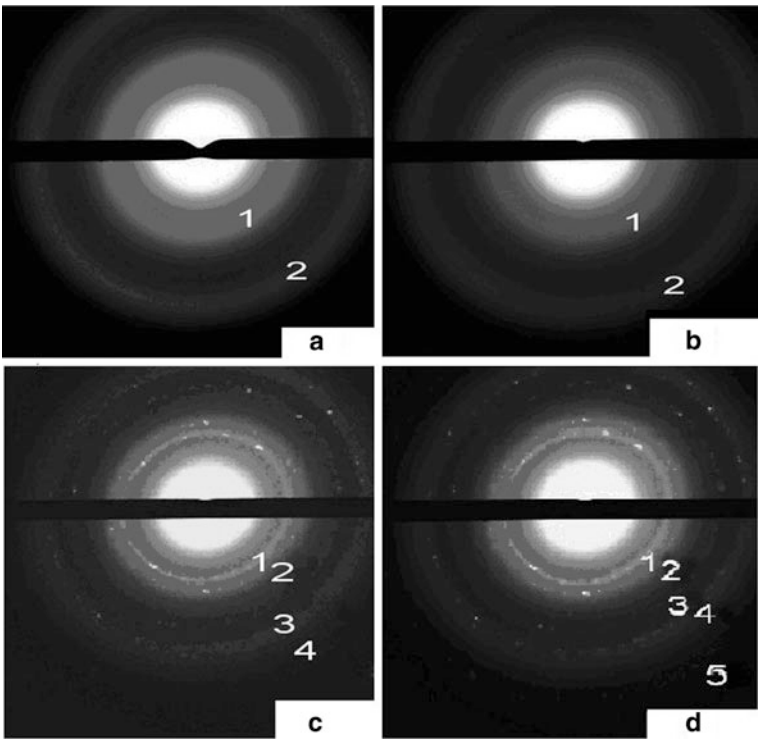


**Fig. 19** Microdifractograms of irradiated IPEC {PAA-PEI} film loaded with (**a**) $Cu^{2+}$ (initial content of 6% (wt), dose of γ-irradiation 320 kGy) Reprinted from [81] Copyright 2010 with permission from Elsevier; (**b**) $Ni^{2+}$ (initial content of 6% (wt), dose of γ-irradiation 400 kGy) Reprinted from [81] Copyright 2010 with permission from Elsevier; (**c**) $Cu^{2+}$ (initial content of 4% (wt), dose of e-beam irradiation 200 kGy) Reprinted with kind permission from Springer Science + Business Media from [115] Copyright 2011, Pleiades Publishing, Ltd.; and (**d**) $Ag^{+}$ (initial content of 16% (wt), dose of X-ray irradiation 800 kGy) Reprinted with kind permission from Springer Science + Business Media from [115] Copyright 2011, Pleiades Publishing Ltd. The numbers 1–5 signify reflexes

Both active species and stable radiolysis products can act as reducing species. The penetrating ability and dose rate are important parameters of ionizing irradiation. They influence the localization of the formation of reducing species as well as determine the contributions of processes related to generation and growth of NPs [111, 120].

The high penetrating ability of γ-irradiation and the EU-4 accelerator (Skobeltsyn Institute of Nuclear Physics, M.V. Lomonosov Moscow State University) [115, 133] provide a uniform generation of reducing species in the irradiated polymer system. The use of isotopic $^{60}Co$ sources for a reduction of $Cu^{2+}$ and $Ni^{2+}$ embedded into the IPEC {PAA-PEI} allows one preparation of a material containing rather small NPs (2–5 nm) [81, 115] that are uniformly distributed throughout the IPEC films (Fig. 20a). This accelerator offers an exceptionally high dose rate (more than 800 Gy/s). Under these conditions, the high rate of formation of metal

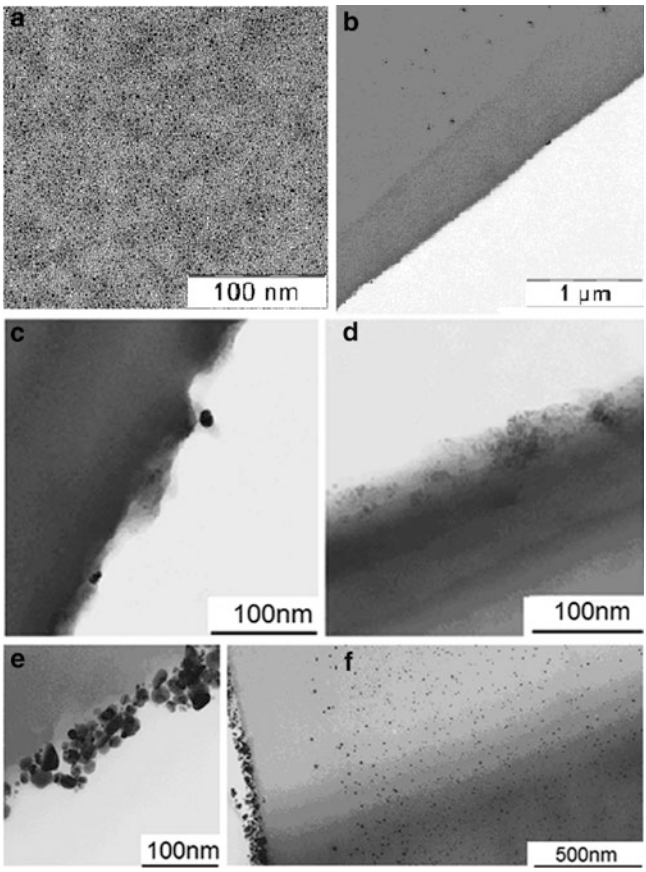


**Fig. 20** Transmission electron microscopy (TEM) micrographs of irradiated IPEC {PAA-PEI} film loaded with (**a**) $Cu^{2+}$ (initial content of 6% (wt), dose of γ-irradiation 320 kGy) Reprinted from [81] Copyright 2010 with permission from Elsevier; (**b**) $Cu^{2+}$ (initial content of 4% (wt), dose of e-beam EU-4 irradiation 200 kGy) Reprinted with kind permission from Springer Science + Business Media from [115] Copyright 2011, Pleiades Publishing, Ltd.; (**c**, **d**, **e**) $Cu^{2+}$ (initial content of 4% (wt), dose of X-ray irradiation 35, 70, and 140 kGy, correspondingly) Reprinted with kind permission from Springer Science + Business Media from [133] Copyright 2011, Pleiades Publishing, Ltd.; and (**f**) $Ag^{+}$ (initial content of 16% (wt), dose of X-ray irradiation 800 kGy) Reprinted with kind permission from Springer Science + Business Media from [115] Copyright 2011, Pleiades Publishing, Ltd.

clusters inside an IPEC film proceeds mainly via active particles formed in the swollen polymer matrix. The probability of cluster formation is high, and, in this case, the ratio between the rate of NP nucleation and the rate of NP growth determines the appearance of ultrafine NPs (less than 1.5 nm in size).

Use of the EU-4 accelerator (with electron energy of 250 keV) and the X-ray irradiator provide different regimes for NP nucleation and NP growth (Fig. 20b) on the surface and in bulk of the polymer matrix [115]. In the case of the EU-4 accelerator, particles of 2–10 nm in size are primarily formed on the film surface

whereas the particles generated inside the film are larger (~30–50 nm). In the case of X-ray irradiation, the nucleation of NPs is similarly controlled by the formation and transport of radiolysis products in the IPEC film and in the external water–alcohol medium. However, in this case, some other regimes of reduction come into play, being determined by specific features of the energy transfer from X-ray radiation to the substance [81, 132, 133]. The structure of the material depends on the nature of the reduced metal ions and their initial content in the sample. The unique ability of the IPEC matrices to stabilize NPs allows one to obtain information about peculiarities of their formation at different stages of X-ray irradiation (Fig. 20c–e) [115, 133]. A study of nanostructures obtained in IPECs {PAA-PEI} under the radiation–chemical reduction of $Cu^{2+}$ using X-ray irradiation demonstrated that the NPs are selectively formed in the subsurface layer of the IPEC films. The observed effect is due to favorable conditions for reduction of metal ions in the surface region because of the effective diffusion of radiolysis products from the outer water–alcohol medium and transport of $Cu^{2+}$ through the IPEC matrix to the ligand vacancies near the interface boundary. The specific feature of the interaction of X-rays with matter at the physical stage results in significant heterogeneity of energy absorption and increases the rate of formation of reducing radiolysis products near the surface of the IPEC films. The reduction of $Cu^{2+}$ is a slow, two-stage process [121]. The duration of the reduction of $Cu^{2+}$ and the formation of metal clusters provides an almost complete localization of NPs near the surfaces of the samples. In contrast to the formation of copper nanoclusters, single-stage radiation-induced chemical reduction of $Ag^{+}$ to silver atoms proceeds with a relatively high rate [122]. In this case, the efficient formation of NPs of 10–30 nm in size occurs not only at the surface of the IPEC film but also inside the IPEC film (Fig. 20f) [115].

Generation and transport of radiolysis products and the migration of metal ions across the polymer matrix control the formation of NPs in the irradiated IPEC films [115]. When irradiation is performed in a water–alcohol medium, metal clusters form via local processes, which proceed with participation of active species having high reduction potentials. Here, growth of NPs is provided by interfacial processes, in which the stable radiolysis products take part.

The ratio between the rates of NP nucleation and growth is determined by the dose rate and by the mechanisms of reduction of metal ions and formation of metal nanoclusters. The character of the formation of NPs is strongly controlled by the mechanisms of energy transfer from the ionizing radiation to the substance that determine the spatial distribution of radiolysis products. Variations in radiation parameters provide the different regimes for reduction on the surface of the IPEC film and inside the IPEC film. They make it possible to prepare composites both with NPs that are uniformly distributed throughout the polymer matrix and with a regular spatial distribution of NPs across the film thickness, including their localization in the subsurface layers.

Microdifractograms show a size effect on the packing of metal atoms in the prepared NPs. In the case of ultrasmall NPs with a mean size of 2–3 nm, the wide reflexes correspond to the interplane distances of ca. 1.20 Å and 2.00 Å for copper

NPs (Fig. 19a) and 1.16 Å and 2.00 Å for nickel NPs (Fig. 19b) [81]. This suggests only the short order of metal atoms and demonstrates the amorphous character of the NPs. In the case of larger NPs, distinct reflections of metal lattices (Fig. 19c,d) (copper, nickel, or silver) are clearly observed [115, 132, 133].

Since metal NPs act as active filler in the IPEC {PAA-PEI} matrix, their formation leads to the immobilization of carboxylate groups on their positively charged surfaces [115]. A high radiation–chemical yield for the reduction of metal ions [81, 114, 115, 132, 133] embedded into the IPEC matrices can be used for the development of single-stage methods for preparation of nanocomposites, applying various types of ionization radiation.

In general, one may conclude that both chemical and radiation–chemical approaches provide effective reduction of metal ions directly in IPEC matrices. This leads to the formation of stabilized NPs. However, it was found that the chemical method is applicable only for a preparation of NPs in thermally crosslinked IPECs. Apparently, a poor regularity of the chemical processes causes noncrosslinked matrices to disintegrate. In contrast, the irradiation technique allows one to derive nanocomposites from both crosslinked and noncrosslinked IPEC films due to specific control over the radiation-induced processes.

## *4.3 Advanced Structures Based on Metallo-Containing IPECs*

A controlled macromolecular assembly in solution is a universally exploited way for preparation of materials for nanotechnology. In particular, the LbL technology has been applied to the fabrication of coated core–shell particles and hollow capsules [103, 135, 136]. The fabricated core–shell and hollow particles may be used for various applications in catalysis, optics, drug delivery, and biosensing. They can serve as precursors for polymer–metal nanohybrids [103]. Reduction reactions are usually used for preparation of metal NPs inside of such multilayered polyelectrolyte systems. Specifically, polyelectrolytes whose charged groups are coordinated with metal ions may act as one of the components in the LbL systems. Alternatively, the sorption of metal ions from a solution leads to incorporation of metal ions into core–shell particles and hollow capsules [137]. Hollow capsules composed of PSS-doped polyaniline and PAH with bound $Ag^+$ were used for a preparation of capsules containing silver [138]. In this case, the PSS-doped polyaniline acts as reducing agent for $Ag^+$. Laser scanning during confocal microscope imaging can accelerate the reduction (Fig. 21a).

Micrometer-sized hollow spheres with metal NPs (10–30 nm) were obtained by photoreduction of $Ag^+$ in polyelectrolyte multilayers comprising $Ag^+$-PSS layers immobilized onto submicrometer-sized PS particles [138]. Hollow capsules with metal NPs can be formed either via a reduction of $Ag^+$ followed by a core dissolution or by a core dissolution with a subsequent reduction of $Ag^+$. The formed spherical nanocomposites with silver NPs were stable for long time (over 3 months). The silver-based core–shell particles and hollow spheres may find interesting applications in catalysis and molecular photoprinting. The PEI-$Pd^{2+}$

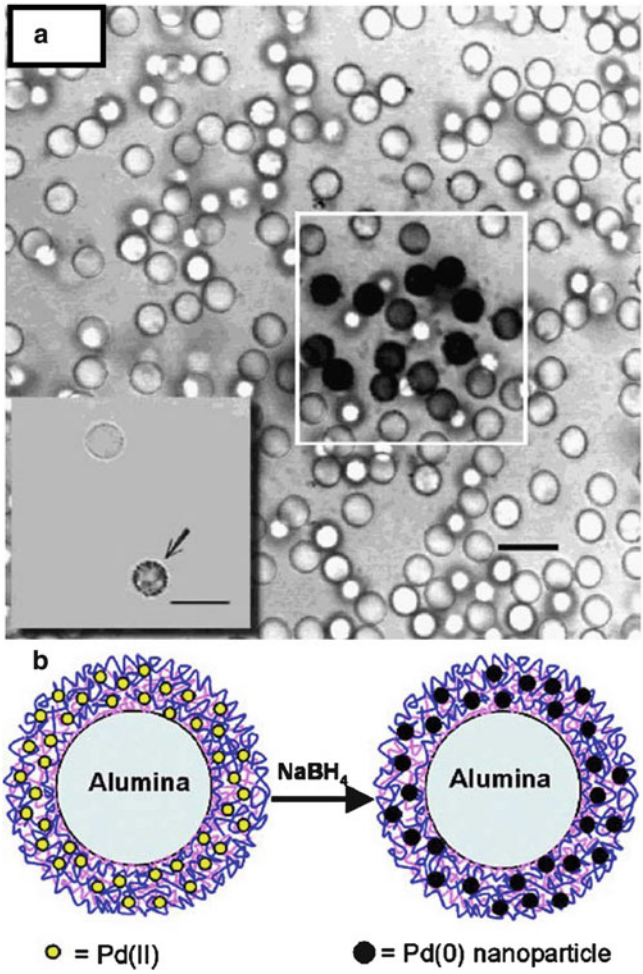


**Fig. 21** (**a**) Photoreduction of $Ag^+$ on the surface of the (polyaniline-PSS/PAH)$_4$ shells. *Inset*: (polyaniline-PSS/PAH)$_4$ capsules after the addition of $AgNO_3$ and photo-irradiation of the lower capsule (*arrow*). *Scale bar*: 10 mm. Reprinted with permission from [137] Copyright 2002 American Chemical Society (**b**) Formation of palladium NPs in a multilayered polyelectrolyte film on colloids. Reprinted with permission from [138] Copyright 2004 American Chemical Society

metallo-containing polycations were assembled by PAA interlayers onto alumina particles of 150 μm diameter [138]. Then, metal NPs (1–3 nm) with catalytic activity were obtained by a reduction of $Pd^{2+}$ with $NaBH_4$ in a multilayered polyelectrolyte matrix (Fig. 21b).

Micellar IPECs (also referred to as complex coacervate core micelles) [139, 140] are formed from bis-hydrophilic diblock copolymers comprising a charged and

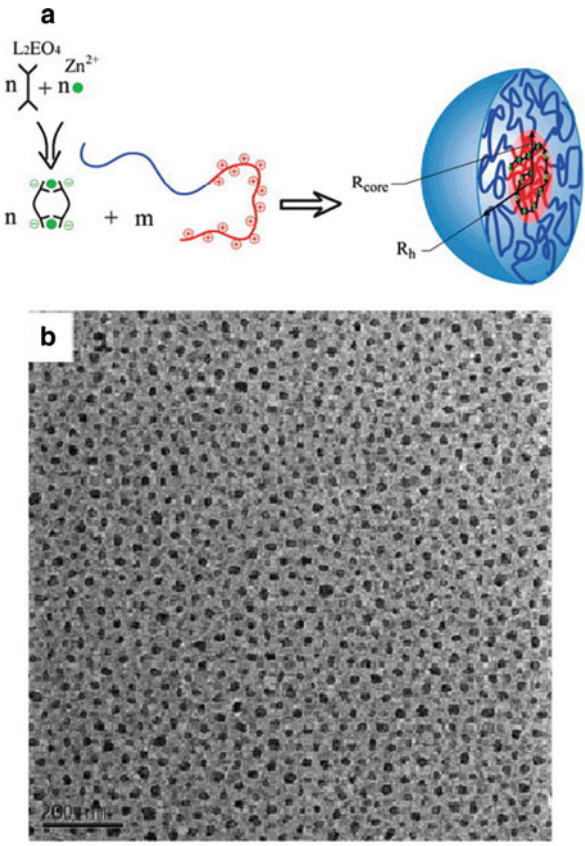


**Fig. 22** (**a**) Formation of IPEC micelles in Zn-$L_2EO_4$/P2VPQ-*b*-PEO. (**b**) Cryo-TEM image of the aggregates in the mixture of P2VPQ-*b*-PEO/Zn-$L_2EO_4$ (0.02% P2VPQ-*b*-PEO with 1:1 molar ratio between P2VPQ-*b*-PEO and Zn-$L_2EO_4$). *Scale bar*: 200 nm. Reprinted with permission from [92] with Copyright 2007 American Chemical Society

a nonionic hydrophilic block, which are complexed with oppositely charged macromolecules. One important application of such IPECs is their potential for mimicking biological phenomena or gene delivery using complexes of DNA with cationic bis-hydrophilic diblock copolymers. The incorporation of metal ions via their coordination with functional groups on the polymers is a particular approach for the assembly of micellar IPECs [80, 92]. In aqueous media, a bis-hydrophilic diblock copolymer P2VPQ-*b*-PEO forms on its chains a reversible supramolecular polyelectrolyte through coordination of metal ions to functional groups of the P2VPQ block (Fig. 22a). The reversible supramolecular polyelectrolyte acts as a homopolyelectrolyte in this system. It was mentioned in Sect. 4.1 that an increase in solution concentration results in the formation of chains, in the case of bifunctional ligands, with an extended spacer (Fig. 15). The negatively charged coordination compound consisting of $Zn^{2+}$ connected by ditopic ligands based on terdendate

ligand groups [92] (Fig. 22a) induces assembly of the cationic blocks. The formation of complex micelles in the system containing the coordination polymer involves two simultaneous synergistic processes [80]: the formation of micelles and polymerization of coordination supramolecules due to a sharp local increase in the concentration of metallo-containing units. The cryo-TEM images prove the formation of micelles with cores, which are highly contrasted by metal ions (Fig. 22b).

The morphology of micellar IPECs is under the control of mixture stoichiometry. By direct mixing of the components at a 1:1 charge-to-charge ratio, spherical micelles (Fig. 22) with a radius of ca. 25 nm are formed [80, 92]. Worm-like micelles (Fig. 23) with a hydrodynamic radius of over 150 nm were found in a mixture with excess positive charge [80, 92].

Design of advanced medicines and delivery drug systems has stimulated interest in microcapsulation of magnetic or antibacterial NPs incorporated into polymers [141, 142]. Fabrication of superfine catalytic or electronic devices is another reason for development of hierarchically organized metallo-containing polymer systems [95, 96, 143–145]. The nanostructured polymer systems give a fine tool for control of NP growth through variation of the interface interactions [143]. Immobilization of metal NPs into polymeric matrices such as micelles [146], microemulsions and microgels [147, 148], dendrimers [149, 150], block co-/terpolymer self-/co-assemblies [95, 96, 143, 145, 151], and spherical polyelectrolyte brushes [152, 153] provides a convenient approach for the fabrication of composites with various spatial orders of the NPs.

A method for preparation of a composite based on the three-dimensional nanosized copolymer template has been discussed [118]. The IPEC of the metallo-containing PEI-$Ag^+$ polycation with the ionic amphiphilic diblock copolymer PS-*b*-PAA was obtained for further synthesis of encapsulated metal NPs. The silver NPs with diameter 20–40 nm were successfully synthesized in coronas of micelles (Fig. 24). In this case, PEI was used as both reducing and stabilizing agent. The cryo-TEM images suggest that the $Ag^+$ content determines the size and spatial distribution of silver NPs.

Polymer-assisted synthesis and environment-sensitive stabilization of metal NPs can be achieved through the formation of IPECs based on diblock copolymers in the presence of $Ag^+$ [97]. Silver NPs were obtained in micellar IPECs consisting of P2VPQ-*b*-PEO and PAA-*block*-poly(*N*-isopropyl acrylamide) (PAA-*b*-PNIPAAm). Temperature was used to trigger the structural transition of a core–shell structure. The P2VPQ and PAA segments acted as containers for $Ag^+$ ions within micellar cores (25°C) or shells (60°C). PEO is supposed to ensure a spontaneous reduction of $Ag^+$ to Ag through oxidation of the oxyethylene groups [119] in the micellar IPECs. Control was demonstrated over the size of the formed silver NPs, over the size and shape of the micelles containing the metal NPs, and over the location of the silver NPs within the micellar IPECs. Spherical and elongated micelles with the metal NPs were observed. The authors suggested a potential application of such nanocomposites as environment-sensitive silver quantum dots and as antimicrobial agents in antifouling surface coatings that can be

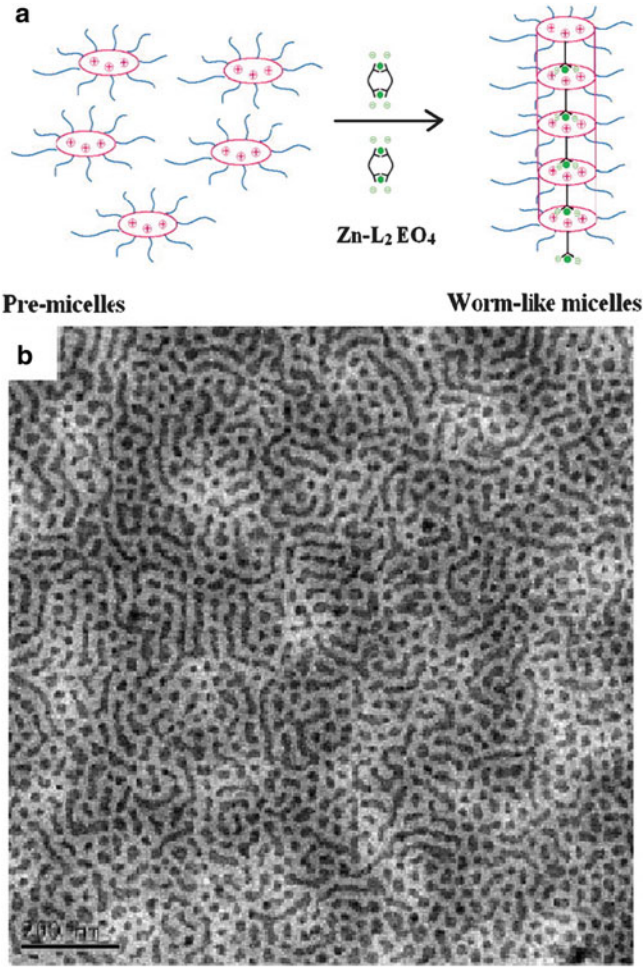


**Fig. 23** (**a**) Illustration of the bridging effect of Zn-$L_2EO_4$ coordination oligomers (*small rings*) between positively charged premicelles. (**b**) Cryo-TEM image of aggregates in the mixture of P2VPQ-*b*-PEO/Zn-$L_2EO_4$ (0.04% P2VPQ-*b*-PEO with 3:1 molar ratio between P2VPQ-*b*-PEO and Zn-$L_2EO_4$). *Scale bar*: 200 nm. Reprinted with permission from [92] Copyright 2007 American Chemical Society

prepared upon exposure of hydrophilic surfaces to a solution of micellar IPECs containing the silver NPs.

The IPECs based on triblock terpolymers containing polybutadiene (PB), P2VPQ, and PMAA blocks acted as scaffolds for the preparation of polymer–inorganic nanohybrids [96]. The IPEC shell on a hydrophobic PB core (Fig. 25a) was assembled from the P2VPQ and PMAA blocks while the excess segments of the PMAA blocks formed a hydrophilic corona. The PMAA blocks and the discontinuous (patchy) intramicellar IPEC {PMAA-P2VPQ} shell were loaded with $AuCl_4^-$

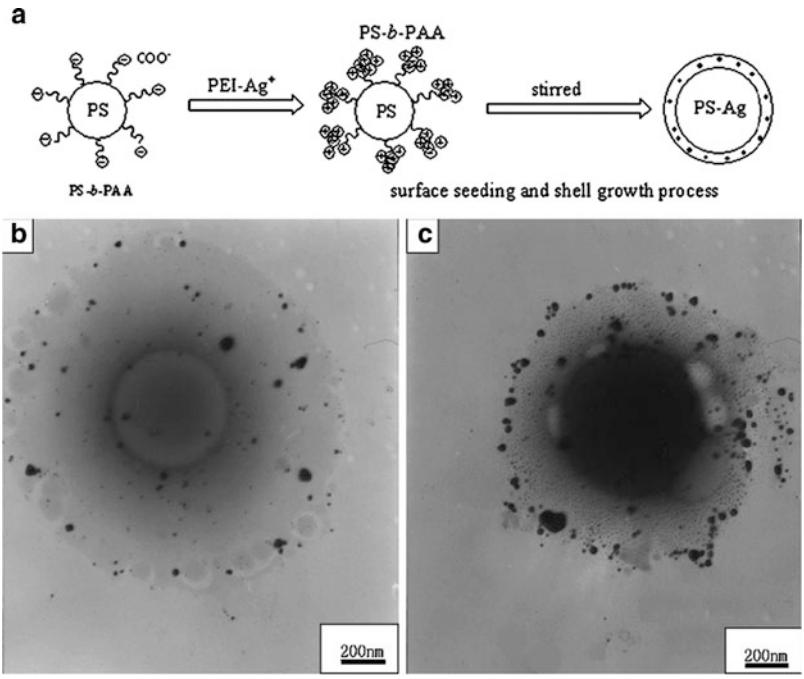


**Fig. 24** Synthesis of silver NPs in the triple metallo-containing macromolecular co-assembly {PS-*b*-PAA-$Ag^+$-PEI}. (**a**) Procedure for preparation of Ag/PS-*b*-PAA composite. (**b**, **c**) Typical TEM images of Ag/PS-*b*-PAA composites with different Ag content: (**b**) 0.012% (wt) PS-*b*-PAA, 0.02 mol/L $AgNO_3$; and (**c**) 0.012.% (wt) PS-*b*-PAA, 0.05 mol/L $AgNO_3$. Reprinted from [118] Copyright 2008 with permission from Elsevier

(Fig. 25a). The polymer micelles with coordinated $AuCl_4^-$ were exposed to UV irradiation to generate gold NPs with a narrow size distribution (3–4 nm in size). Interestingly, the formation of gold NPs takes place predominantly at the interface between the intramicellar IPEC and the PMAA corona as well as within the PMAA corona (Fig. 25b). Further addition of a bis-hydrophilic diblock copolymer P2VPQ-*b*-PEO to the PB-*b*-P2VPQ-*b*-PMANa micelles generated multilayered micellar IPECs (Fig. 25c). In this case, gold NPs obtained via reduction of $AuCl_4^-$ incorporated into such structures were located exclusively within the IPEC shell surrounded by the PEO corona (Fig. 25d).

The gold, platinum, and palladium NPs were generated within cylindrical micelles [95] of a PB-*b*-P2VPQ-*b*-PMANa triblock terpolymer. The PB cylindrical cores were covered by an intramicellar IPEC patchy shell assembled from the P2VPQ blocks complexed with PMAA segments while the excess PMAA segments formed a hydrophilic corona (Fig. 26c). The metal NPs were obtained using UV irradiation (gold) or reduction with $NaBH_4$ (platinum, palladium). TEM and cryo-TEM images demonstrate a difference in the localization of NPs within the polymer scaffold. The platinum and gold NPs (Fig. 26a,b) were randomly distributed all over the cylinders,

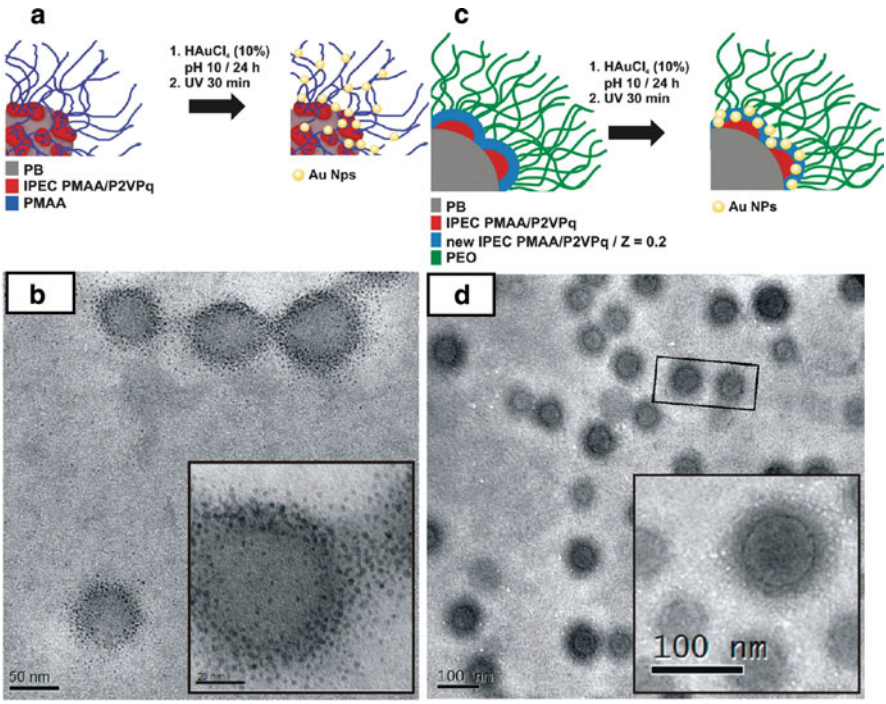


**Fig. 25** (**a**) Formation of gold NPs in PB-*b*-P2VPQ-*b*-PMAA triblock terpolymer micelles. (**b**) TEM micrograph of PB-*b*-P2VPQ-*b*-PMAA triblock terpolymer micelles loaded with gold NPs. (**c**) The IPEC from PB-*b*-P2VPQ-*b*-PMAA and P2VPQ-*b*-PEO. (**d**) Cryo-TEM micrograph of the IPEC from PB-*b*-P2VPQ-*b*-PMAA and P2VPQ-*b*-PEO, which is loaded with gold NPs. Reprinted with permission from [96] Copyright 2009 American Chemical Society

indicating a location within both the PMAA corona and the intramicellar IPEC domains (Fig. 26b). At the same time, the situation is different for palladium NPs in the PB-*b*-P2VPQ-*b*-PMANa micelles (Fig. 26d–f). Here, the palladium NPs are located in the IPEC patches distributed along the cylindrical PB core. Thus, the experiments with templates based on micelles of ionic amphiphilic triblock terpolymers have demonstrated that both hydrophilic (PMAA corona) and rather hydrophobic (IPEC domains) compartments present in such self-assembled structures can be used for deposition of NPs.

## 5 Conclusions and Perspective

Recent advances in controlled synthesis of macromolecules, in particular in controlled radical polymerization, have allowed the construction of polymers with various topologies and compositions. Successful design of star-shaped polymers, molecular polymer brushes, and amphiphilic block copolymers and terpolymers has

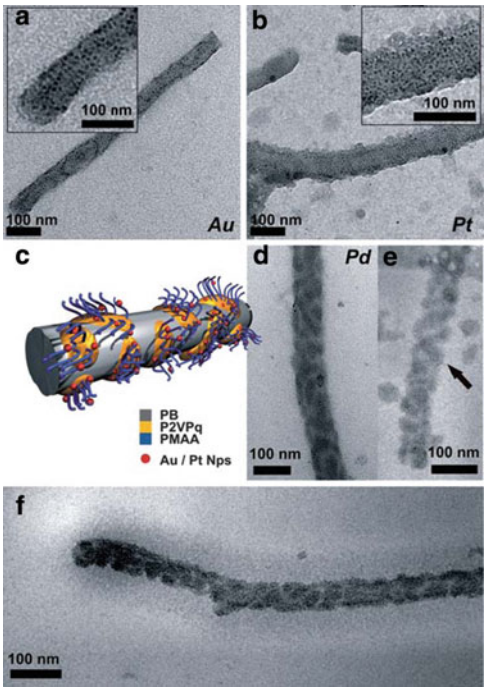


**Fig. 26** TEM micrographs of PB-*b*-P2VPQ-*b*-PMAA cylinders/metal NP hybrids deposited from aqueous solution: (**a**) gold , (**b**) platinum, and (**d**) palladium. (**c**) The proposed solution structure. (**e**, **f**) Cryo-TEM images from palladium-containing PB-*b*-P2VPQ-*b*-PMAA. *Insets* show a higher magnification. Reprinted from [95] with permission from the Royal Chemical Society Copyright 2011

stimulated extensive studies of self-organization phenomena in multicomponent macromolecular systems. Electrostatically driven co-assembly in such systems provides a simple route towards micelle-like polymeric structures with spatially separated domains (compartments) having different functionalities. An outer domain grants solubility in solution to the macromolecular co-assemblies while an inner domain (or domains) can accumulate from or release into the environment various compounds in response to variations in environmental conditions. Variations in the pH or in the ionic strength are an effective way to change the structure and properties of the formed IPECs. During the last few years, various advanced functional IPEC structures based on polyions (or polyionic species) with nonlinear (branched) topologies have been successfully prepared and thoroughly examined.

IPECs are proved to effectively bind metal ions. Such hybrid macromolecular co-assemblies containing noble and transition metal ions can be considered, therefore, as universal matrices for further preparation of polymer–metal nanocomposites with controlled and variable NP size as well as various spatial distributions of NPs in such polymer systems. In this context, the use of polyions (or polyionic species) with nonlinear (branched) topologies can be, beyond all doubt, advantageous and very

attractive. The IPECs based on such polyions (or polyionic species) act as autonomous nanoreactors and provide the prerequisites for successful directed design of promising hybrids for applications related to medicine, biotechnology, and catalysis. During the next few years, a breakthrough in this field is anticipated, resulting in the formation of novel families of nanosized advanced functional materials, which can be further applied for the needs of rapidly developing nanotechnologies.

**Acknowledgments** The support from the Deutsche Forschungsgemeinschaft within the framework of the Sonderforschungsbereich 840 "Von partikulären Nanosystemen zur Mesotechnologie" and from the Russian Foundation for Basic Research (project no. 12-03-00762) is gratefully acknowledged.

## References

1. Kabanov VA (1997) Journal of Journals 1:35
2. Manning GS (2001) Macromolecules 34:4650
3. Sergeyev VG, Pyshkina OA, Gallyamov MO, Yaminsky IA, Zezin AB, Kabanov VA (1997) Prog Polym Sci 107:198
4. Smid J, Fish D (1988) In: Mark HF, Kroschwitz JI (eds) Encyclopedia of polymer science and engineering, vol 11. Wiley, New York, p 720
5. Tsuchida E, Abe K (1982) Adv Polym Sci 45:1
6. Philipp B, Dautzenberg H, Linow K-J, Kötz J, Dawydoff W (1989) Prog Polym Sci 14:91
7. Kabanov VA (1994) Polym Sci 36:143
8. Kabanov VA (2005) Russ Chem Rev 74:3
9. Thünemann B, Müller M, Dautzenberg H, Joanny JF, Löwen H (2004) Adv Polym Sci 166:113
10. Kabanov VA, Zezin AB, Kasaikin VA, Yaroslavov AA, Topchiev DA (1991) Russ Chem Rev 60:288
11. Petzold G, Nebel A, Buchhammer HM, Lunkwitz K (1998) Colloid Polym Sci 276:125
12. Buchhammer HM, Kramer G, Lunkwitz K (1995) Colloids Surf A 95:299
13. Buchhammer HM, Petzold G, Lunkwitz K (1999) Langmuir 15:4306
14. Zezin AB (1999) Chemistry Today 6:30
15. Zezin AB, Rogacheva VB, Yaroslavov AA, Mikheikin SV (2012) Proceedings of international science symposium on combating radionuclide contamination in agro-soil environment, Korijama, Japan, 8–10 March 2012, p 438
16. Zezin AB, Rogacheva VB, Yaroslavov AA, Mikheikin SV (2012) Proceedings of symposium on the application and R & D of the technologies of decontamination, remediation, and restoration of environment, Tokyo, Japan, 3 February 2012, p 93
17. Kabanov AV, Kabanov VA (1994) Polym Sci 36:157
18. Kabanov AV, Kabanov VA (1998) Adv Drug Deliv Rev 30:49
19. Matyjaszewski K, Davis TP (2002) Handbook of radical polymerization. Wiley-Interscience, Weinheim
20. Müller AHE, Matyjaszewski K (2009) Controlled and living polymerizations. Wiley-VCH, Weinheim
21. Prud'homme RE (1989) In: Saegusa T, Higashimura T, Abe A (eds) Proceedings of the IUPAC 32nd international symposium on macromolecules "Frontiers of macromolecular science", Kyoto, Japan, 1–5 August 1988. Blackwell, Oxford, p 55
22. Kabanov VA, Papisov IM (1979) Vysokomol Soed Ser A 21:243
23. Baranovsky VY, Litmanovich AA, Papisov IM, Kabanov VA (1981) Eur Polym J 17:969

24. Michaels A (1965) Ind Eng Chem 57:32
25. Kalyuzhnaya RI, Volynskii AL, Rudman AR, Vengerova NA, Razvodovskii EF, Eltsefon BS, Zezin AB (1976) Vysokomol Soed Ser A 18:71
26. Gulyaeva ZG, Aldoshina IV, Zansokhova MF, Rogacheva VB, Zezin AB, Kabanov VA (1990) Vysokomol Soed Ser A 32:776
27. Zezin AB, Lutsenko VV, Rogacheva VB, Aleksina OA, Kalyuzhnaya RI, Kabanov VA, Kargin VA (1999) Polym Sci Ser A 41:1250
28. Zezin AB, El'tsefon BS, Rudman AR, Vengerova NA, Kalyuzhnaya RI, Valueva SP, Kopylova EM, Chepurov AK, Efimov VS, Kabanov VA (1987) Pharm Chem J 21:464
29. Zezin AB, Izumrudov VA, Kabanov VA (1989) Makromol Chem Macromol Symp 26:249
30. Tsuchida E, Osada Y, Sanada K (1972) J Polym Sci Polym Chem Ed 10:3399
31. Kabanov VA, Zezin AB (1984) Pure Appl Chem 56:343
32. Kabanov VA, Zezin AB (1982) In: Vol'pin ME (ed) Soviet Sci Rev Sect B Chem Rev, vol 4. Harwood Academic Publishing, p 207
33. Rogacheva VB, Ryzhikov SV, Zezin AB, Kabanov VA (1984) Vysokomol Soed Ser A 26:1674
34. Rogacheva VB, Ryzhikov SV, Shchors TV, Zezin AB, Kabanov VA (1984) Vysokomol Soed Ser A 26:2417
35. Kabanov VA, Zezin AB, Izumrudov VA, Bronich TK, Bakeev KN (1985) Makromol Chem Suppl 13:137
36. Bakeev KN, Izumrudov VA, Kuchanov SI, Zezin AB, Kabanov VA (1992) Macromolecules 25:4249
37. Izumrudov VA, Zezin AV, Kabanov VA (1991) Russ Chem Rev 60:792
38. Skorodinskaya AM, Kemenova VA, Chernova OV, Efimov VS, Lakin KM, Zezin AB, Kabanov VA (1983) Khim-Farm Zh 17:1463
39. Skorodinskaya AM, Kemenova VA, Efimov VS, Mustafaev MI, Kasaikin VA, Zezin AB, Kabanov VA (1984) Pharm Chem J 18:146
40. Zezin AB, Rogacheva VB, Komarov VS, Razvodovskii EF (1975) Vysokomol Soed Ser A 17:2637
41. Komarov VS, Rogacheva VB, Bezzubov BB, Zezin AB (1976) Vysokomol Soed Ser B 18:784
42. Zezin AB, Rogacheva VB, Valueva SP, Nikonorova NI, Zansokhova MF, Zezin AA (2006) Nanotechnol Russ 1:191
43. Pergushov DV, Borisov OV, Zezin AB, Müller AHE (2011) Adv Polym Sci 241:131
44. Xu Y, Plamper FA, Ballauff M, Müller AHE (2010) Adv Polym Sci 228:1
45. Pergushov DV, Babin IA, Plamper FA, Zezin AB, Müller AHE (2008) Langmuir 24:6414
46. Pergushov DV, Babin IA, Plamper FA, Schmalz H, Müller AHE, Zezin AB (2009) Dokl Phys Chem 425:57
47. Larin SV, Darinskii AA, Zhulina EB, Borisov OV (2009) Langmuir 25:1915
48. Ding J, Wang L, Yu H, Huo J, Liu Q, Xiao A (2009) J Phys Chem C 113:5126
49. Babin IA, Pergushov DV, Wolf A, Plamper FA, Schmalz H, Müller AHE, Zezin AB (2011) Dokl Phys Chem 441:219
50. Ge Z, Xu J, Wu D, Narain R, Liu S (2008) Macromol Chem Phys 209:754
51. Yin M, Ding K, Gropeanu RA, Shen J, Berger R, Weil T, Müllen K (2008) Biomacromolecules 9:3231
52. Xu FJ, Zhang ZX, Ping Y, Li J, Kang ET, Neoh KG (2009) Biomacromolecules 10:285
53. Nemoto Y, Borovkov A, Zhou Y-M, Talewa Y, Tatsumi E, Nakayama Y (2009) Bioconjug Chem 20:2293
54. Schallon A, Jérôme V, Walther A, Synatschke CV, Müller AHE, Freitag R (2010) React Funct Polym 70:1
55. Li D, Ping Y, Xu F, Yu H, Pan H, Huang H, Wang Q, Tang G, Li J (2010) Biomacromolecules 11:2221

56. Synatschke CV, Schallon A, Jérôme V, Freitag R, Müller AHE (2011) Biomacromolecules 12:4247
57. Förster S, Abetz V, Müller AHE (2004) Adv Polym Sci 166:173
58. Borisov OV, Zhulina EB, Leermakers FAM, Müller AHE (2011) Adv Polym Sci 241:57
59. Talingting MR, Voigt U, Munk P, Webber SE (2000) Macromolecules 33:9612
60. Pergushov DV, Remizova EV, Feldthusen J, Zezin AB, Müller AHE, Kabanov VA (2003) J Phys Chem B 107:8093
61. Pergushov DV, Remizova EV, Gradzielski M, Lindner P, Feldthusen J, Zezin AB, Müller AHE, Kabanov VA (2004) Polymer 45:367
62. Burkhardt M, Ruppel M, Tea S, Drechsler M, Schweins R, Pergushov DV, Gradzielski M, Zezin AB, Müller AHE (2008) Langmuir 24:1769
63. Chelushkin PS, Lysenko EA, Bronich TK, Eisenberg A, Kabanov AV, Kabanov VA (2004) Dokl Phys Chem 395:72
64. Lysenko EA, Chelushkin PS, Bronich TK, Eisenberg A, Kabanov VA, Kabanov AV (2004) J Phys Chem B 108:12352
65. Chelushkin PS, Lysenko EA, Bronich TK, Eisenberg A, Kabanov VA, Kabanov AV (2007) J Phys Chem B 111:8419
66. Burkhardt M, Martinez-Castro N, Tea S, Drechsler M, Babin IA, Grishagin IV, Schweins R, Pergushov DV, Gradzielski M, Zezin AB, Müller AHE (2007) Langmuir 23:12864
67. Kabanov VA (1994) In: Dubin P, Bock J, Davis R, Schulz DN, Thies C (eds) Macromolecular complexes in chemistry and biology. Springer, Berlin, p 151
68. Chelushkin PS, Lysenko EA, Bronich TK, Eisenberg A, Kabanov VA, Kabanov AV (2008) J Phys Chem B 112:7732
69. Ishizu K, Toyoda K, Furukawa T, Sogabe A (2004) Macromolecules 37:3954
70. Ishizu K (2005) Polym Degrad Stab 90:386
71. Störkle D, Duschner S, Heimann N, Maskos M, Schmidt M (2007) Macromolecules 40:7998
72. Duschner S, Störkle D, Schmidt M, Maskos M (2008) Macromolecules 41:9067
73. Krohne K, Duschner S, Störkle D, Schmidt M, Maskos M (2010) Macromolecules 43:8645
74. Larin SV, Pergushov DV, Xu Y, Darinskii AA, Zezin AB, Müller AHE, Borisov OV (2009) Soft Matter 5:4938
75. Xu Y, Borisov OV, Ballauff M, Müller AHE (2010) Langmuir 26:6919
76. Gössl I, Shu L, Schlüter D, Rabe J (2002) J Am Chem Soc 124:6860
77. Schubert US, Newkome GR, Manners I (eds) (2006) Metal-containing and metallo-supramolecular polymers and materials. ACS, Washington
78. Wohrle D, Pomogailo AD (2003) Metal complexes and metals in macromolecules: synthesis, structure and properties. Wiley-VCH, Weinheim
79. Pomogailo AD, Kestelman VN (2005) Metallopolymer nanocomposites. Springer, New York
80. Yan Y, Huang J (2010) Coord Chem Rev 254:1072
81. Zezin AB, Rogacheva VB, Feldman VI, Afanasiev P, Zezin AA (2010) Adv Colloid Interface Sci 158:84
82. Bruening ML, Dotzauer DM, Jain P, Ouyang L, Baker GL (2008) Langmuir 24:7663
83. Liu G, Dotzauer DM, Bruening ML (2010) J Membr Sci 354:198
84. Ruiz P, Macanás J, Muñoz M, Muraviev DN (2011) Nanoscale Res Lett 6:343
85. Macanás J, Ouyang L, Bruening ML, Muñoz M, Remigya J-C, Lahittea J-F (2010) Catal Today 156:181
86. Nicolais L, Carotenuto G (eds) (2005) Metal-polymer nanocomposites. Wiley-VCH, Weinheim
87. Shih C-M, Shieh Y-T, Twu Y-K (2009) Carbohydr Polym 78:309
88. Geng B, Jin Z, Li T, Qi X (2009) Sci Total Environ 407:4994
89. Yoksan R, Chirachanchai S (2009) Mater Chem Phys 115:296
90. Long D, Wu G, Chen S (2007) Radiat Phys Chem 76:1126
91. Landsmann S, Winter A, Chiper M, Fustin C-A, Hoeppener S, Wouters D, Gohy J-F, Schubert US (2008) Macromol Chem Phys 209:1666

92. Yan Y, Besseling NAM, de Keizer A, Drechsler M, Fokkink R, Cohen Stuart MA (2007) J Phys Chem B 111:11662
93. van der Gucht J, Spruijt E, Lemmers M, Cohen Stuart MA (2011) J Colloid Interface Sci 361:407
94. Lehn J-M (2007) Chem Soc Rev 36:151
95. Schacher FH, Rudolph T, Drechsler M, Müller AHE (2011) Nanoscale 3:288
96. Schacher F, Betthausen E, Walther A, Schmalz H, Pergushov DV, Müller AHE (2009) ACS Nano 3:2095
97. Voets IK, de Keizer A, Frederik PM, Jellema R, Cohen Stuart MA (2009) J Colloid Interface Sci 339:317
98. Zezin AB, Kabanov VA (1982) Sov Sci Rev B 4:207
99. Kabanov NM, Kokorin AI, Rogacheva VB, Zezin AB (1979) Vysokomol Soed Ser A 21:209
100. Decher G (1997) Science 277:1232
101. Sukhorukov GB, Donath E, Davis S, Lichtenfeld H, Caruso F, Popov VI, Möhwald H (1998) Polym Adv Technol 9:759
102. Lavalle P, Boulmedais F, Ball V, Mutterer J, Schaaf P, Voegel JC (2005) J Membr Sci 253:49
103. Shi X, Shen M, Möhwald H (2004) Prog Polym Sci 29:987
104. Joly S, Kane R, Radzilowski L, Wang T, Wu A, Cohen RE, Thomas LE, Rubner MF (2000) Langmuir 16:1354
105. Wang TC, Rubner MF, Cohen RE (2003) Chem Matter 15:299
106. Dai J, Bruening ML (2002) Nano Lett 2:497
107. Schutte M, Kurth DG, Linford MR, Cölfen H, Möhwald H (1998) Angew Chem Int Ed 37:2891
108. Yan Y, Harnau L, Besseling NAM, de Keizer A, Ballauf M, Rosenfeld S, Cohen Stuart MA (2008) Soft Matter 4:2207
109. Vermonden T, van der Gucht J, de Waard P, Marcelis ATM, Besseling NAM, Sudhölter EJR, Fleer GJ, Cohen Stuart MA (2003) Macromolecules 36:7035
110. Corain B, Burato C, Centomo P, Lora S, Meyer-Zaika W, Shmid G (2005) J Mol Catal A Chem 225:189
111. Chmielewski AG, Chmielewska DK, Michalik J, Sampa MH (2007) Nucl Instrum Methods Phys Res B 265:339
112. Porel S, Singh S, Harsha SS, Rao DN, Radhakrishnan TP (2005) Chem Mater 1:9
113. Ziolo RF, Giannelis EP, Weinstein BA, O'Horo MP, Ganguly BN, Mehrotra V, Russell MW, Huffman DR (1992) Science 257:219
114. Zezin AA, Feldman VI, Shmakova NA, Valueva SP, Ivanchenko VK, Nikanorova NI (2007) Nucl Instrum Methods Phys Res B 265:334
115. Zezin AA, Feldman VI, Abramchuk SS, Ivanchenko VK, Zezina EA, Shmakova NA, Shvedunov VI (2011) Polym Sci Ser C 53:61
116. Muraviev DN, Ruiz P, Muñoz M (2008) Phys Status Solidi A 205:1460
117. Ruiz P, Muñoz M, Macanás J, Turta C, Prodius D, Muraviev DN (2010) Dalton Trans 39:1751
118. Lei Z, Wei X, Zhang L, Bi S (2008) Colloids Surf A 317:705
119. Zhang DB, Qi LM, Ma JM, Cheng HM (2001) Chem Mater 13:753
120. Belloni J (2006) Catal Today 113:141
121. Ershov BG (1994) Russ Chem Bull 43:25
122. Ershov BG (2001) Russ Chem J 45:20
123. Wang TC, Rubner MF, Cohen RE (2003) Chem Mater 15:299
124. Ji T, Shi H, Zhao J, Zhao Y (2000) J Magn Magn Mater 212:189
125. Dotzauer DM, Abusaloua A, Miachon S, Dalmon J-A, Bruening ML (2009) Appl Catal B 91:180
126. Bhattacharjee S, Dotzauer DM, Bruening ML (2009) J Am Chem Soc 131:3602
127. Ouyang L, Dotzauer DM, Hogg SR, Macanás J, Lahitte J-F, Bruening ML (2010) Catal Today 156:100

128. Kotov NA, Dekany I, Fendler JH (1995) J Phys Chem 99:13065
129. Kleinfeld ER, Ferguson GS (1994) Science 265:370
130. Lvov Y, Ariga K, Onda M, Ichinose I, Kamitake T (1997) Langmuir 13:6195
131. Shmitt J, Decher G, Dressick WJ, Brandow SL, Geer RE, Shashidhar R, Culver JM (1997) Adv Mater 9:61
132. Zezin AA, Feldman VI, Dudnikov AV, Zezin SB, Abramchuk SS, Belopushkin SI (2009) High Energy Chem 43:100
133. Zezin AA, Feldman VI, Zezina EA, Belopushkin SI, Tsybina EV, Abramchuk SS, Zezin SB (2011) High Energy Chem 45:99
134. Suzdalev IP, Maksimov UV, Prusakov VE, Matveev VV, Imshennik VK, Novochihin SV, Zezin AB, Rogacheva VB, Valueva SP (2008) Nanotechnol Russ 3:729
135. Caruso F (2001) Adv Mater 13:11
136. Caruso F, Caruso RA, Möhwald H (1999) Science 282:1111
137. Antipov AA, Sukhorukov GB, Federik YA, Hartman J, Giersing M, Möhwald H (2002) Langmuir 18:6687
138. Kidami S, Dai J, Li J, Bruening ML (2004) J Am Chem Soc 126:2658
139. Cohen Stuart MA, Besseling NAM, Fokkink RG (1998) Langmuir 14:6846
140. Gohy JF, Varshney SK, Antoun S, Jérôme R (2000) Macromolecules 33:9298
141. Gubin SP (ed) (2009) Magnetic nanoparticles. Wiley-VCH, Berlin
142. De M, Ghost PS, Rotello VM (2008) Adv Mater 20:4225
143. Bronstein LM, Sidorov SN, Valetsky PM (2004) Russ Chem Rev 73:501
144. Saito H, Okamura S, Isuzu K (1992) Polymer 33:1099
145. Zhang J, Xu S, Kumacheva E (2004) J Am Chem Soc 26:7908
146. Ingert D, Pileni MP (2001) Adv Funct Mater 11:136
147. Manziek L, Langenmayr E, Lamola A, Gallagher M, Brese N, Annan N (1998) Chem Mater 10:3101
148. Antonietti M, Grohn F, Hartmann J, Bronstein L (1997) Angew Chem Int Ed 36:2080
149. Zhao M, Sun L, Crooks RM (1998) J Am Chem Soc 120:4877
150. Esumi K (2003) Top Curr Chem 227:31
151. Whilton NT, Berton B, Bronstein L, Hernze H, Antonietti M (1999) Adv Mater 11:1014
152. Sharma G, Mei Y, Lu Y, Ballauff M, Irrgang T, Proch S, Kempe R (2007) J Catal 246:10
153. Ballauff M, Lu Y (2007) Polymer 48:1815

# Index